THE UNIVERSITY *of* EDINBURGH

This thesis has been submitted in fulfilment of the requirements for a postgraduate degree (e.g. PhD, MPhil, DClinPsychol) at the University of Edinburgh. Please note the following terms and conditions of use:

- This work is protected by copyright and other intellectual property rights, which are retained by the thesis author, unless otherwise stated.
- A copy can be downloaded for personal non-commercial research or study, without prior permission or charge.
- This thesis cannot be reproduced or quoted extensively from without first obtaining permission in writing from the author.
- The content must not be changed in any way or sold commercially in any format or medium without the formal permission of the author.
- When referring to this work, full bibliographic details including the author, title, awarding institution and date of the thesis must be given.

Massive Binary Stars and the Kinematics of Young Massive Clusters

Vincent Hénault-Brunet

Doctor of Philosophy
The University of Edinburgh
July 2013

Abstract

Located in the Large Magellanic Cloud, R136 is a rare example of a nearby young and dense massive star cluster in which individual stars can be resolved. Often suggested as a globular cluster in formation, its study is of great interest and promises to provide insights into the early dynamical evolution of massive star clusters. This is crucial to understand more extreme and distant starburst clusters, which contribute to a significant fraction of all current star formation in the Local Universe, in particular in interacting galaxies.

The majority of this thesis is based on multi-epoch spectroscopic observations in and around R136 obtained as part of the VLT-FLAMES Tarantula Survey (VFTS), an ambitious programme which targeted nearly 1 000 massive stars in the intricate 30 Doradus star-forming region. The motivations and observing strategy of this survey, designed to address key questions about the evolution of massive stars and clusters, are first introduced. The data reduction procedures applied to VFTS data are described, with an emphasis on the tasks accomplished in the context of this thesis.

The VFTS data are first used to perform a detailed kinematic study of R136, determine its dynamical state, and evaluate the importance of gas expulsion in the early evolution of massive star clusters. Orbital motions of binary stars are found to dominate the line-of-sight velocity dispersion of the cluster, illustrating the risk of interpreting velocity dispersion measurements for unresolved extragalactic young massive clusters. However, once the detected binaries are rejected and the contribution of undetected binaries is accounted for through Monte Carlo simulations, the true velocity dispersion of the cluster is found to be low and consistent with it being in virial equilibrium. This suggests that gas expulsion has not had a dramatic effect on the early dynamical evolution of R136.

Using the velocity measurements of R136 as a test case, a maximum likelihood method that fits the velocity dispersion of a cluster from a single epoch of radial velocity data

is then tested. The method must be applied with care given the high binary fraction of massive stars and the large uncertainties in their binary orbital parameter distributions, but for typical velocity dispersions of young massive clusters ($\gtrsim 4$ km s^{-1}), it is shown that the velocity dispersion can be measured with an accuracy of 40% or better. This offers an efficient way of constraining the dynamics of these systems.

The radial velocity measurements of apparently single stars in R136 are also used to investigate the internal rotation of the cluster, a potentially important but largely unexplored characteristic of young clusters. Evidence is found, at the 95% confidence level, for rotation of the cluster as a whole. A simple maximum likelihood method is presented to fit rotation curves to the data, from which a typical rotational velocity of ~ 3 km s^{-1} is found. When compared to the low velocity dispersion of R136, this suggests that star clusters may form with as much as ~ 20% of their kinetic energy in rotation.

Finally, a smaller-scale survey of massive stars in the Wing of the Small Magellanic Cloud is introduced. As an example of the particularly interesting massive binaries that can be revealed by the synergy between large optical spectroscopic surveys of young clusters and observations at other wavelengths, the discovery of a new Be/X-ray pulsar binary and associated supernova remnant is reported. With a long spin period of over 1 000 seconds and a young age of $\sim 10^4$ years constrained by its association with the supernova remnant, the pulsar in this system is quickly emerging as a unique object that challenges our understanding of the spin evolution of accreting neutron stars.

Lay Summary

Stars often form in groups called clusters, which are sometimes considered as the building blocks of galaxies. Understanding in detail how these clusters form, evolve, and are destroyed can provide important insights on the properties and evolution of their host galaxies. The so-called globular star clusters, for example, typically contain hundreds of thousands of stars each and, given their very old ages of several billion years, are relics of the early assembly of galaxies. To understand the early phases of the evolution of such clusters, our best hope is to study much younger clusters that are similarly massive.

The central part of this thesis consists of a study of the velocities of stars in an important young massive cluster, called R136, one of the few nearby enough for individual stars to still be distinguishable with large telescopes. The stellar velocities hold precious information about the history of such systems. However, to successfully recover that history, care must be taken to isolate unwanted effects that could blur the information contained in the velocities. One particularly harmful effect is the rapid motions of stars orbiting each other in close binary systems. An important aspect of this thesis is to explore methods to take binary stars into account. Once this is done for the case of the young massive cluster R136, it is found that it had a quieter infancy than originally thought despite the rapid expulsion of gas from its natal cocoon. Consequently, it will probably be a long-lived cluster. It is also shown that R136 is probably rotating, and the implications of that for the formation and evolution of star clusters are discussed.

Finally, as an example of the interesting objects that can be unveiled when studying young clusters in detail, the discovery of a pulsar in a binary system is presented. This pulsar is the compact rotating remnant of a massive star that died at a young age in a supernova explosion. The age of the remnant could be constrained by studying the shell of gas swept by the explosion, which was also discovered as part of this thesis. The pulsar is intriguingly found to be rotating much slower than expected given its young age, and promises to reveal important clues about the physics of such stellar remnants.

Résumé en français pour les non-spécialistes

Les étoiles sont souvent formées en groupes appelés amas, qui peuvent être considérés comme des composantes fondamentales des galaxies. Comprendre en détails comment ces amas naissent, évoluent et sont détruits peut fournir d'importants indices sur les propriétés et l'évolution des galaxies dans lesquelles ils se trouvent. Les amas dits *globulaires*, par exemple, contiennent typiquement plusieurs centaines de milliers d'étoiles chacun et, compte tenu de leur âge de plusieurs milliards d'années, constituent des reliques d'une époque lointaine de la formation des galaxies. Pour comprendre les débuts de l'évolution de tels amas, notre meilleur espoir est d'étudier des amas beaucoup plus jeunes mais tout aussi massifs.

La partie central de cette thèse est portée sur l'étude des vitesses des étoiles dans un important amas jeune et massif situé dans le Grand Nuage de Magellan, une galaxie voisine de notre Voie Lactée. Appelé R136, cet amas est un des rares qui soit assez proche pour que des étoiles individuelles puissent être discernées avec l'aide de grands télescopes. Les vitesses des étoiles contiennent de précieuses informations sur l'histoire de tels systèmes. Par contre, pour en profiter, il faut prendre bien soin d'isoler certains effets indésirables qui pourraient brouiller ces informations. Un effet particulièrement néfaste est le mouvement rapide d'étoiles en orbite dans des systèmes binaires. Un aspect important de cette thèse consiste à explorer des méthodes pour prendre en compte les mouvements des étoiles dans ces systèmes binaires. Une fois ces méthodes appliquées à R136, il est démontré que l'amas a eu une enfance plus calme qu'autrefois anticipée, et ce malgré l'expulsion rapide du gaz de son cocon natal. En conséquence, R136 devrait survivre pour plusieurs milliards d'années. Il est aussi démontré que R136 montre un taux de rotation élevée, et les implications de cette découverte pour la formation et l'évolution des amas sont discutées.

Finalement, en tant qu'exemple d'astres intéressants qui peuvent être dévoilés par

l'étude détaillée de jeunes amas, la découverte d'un pulsar membre d'un système binaire est présentée. Ce pulsar est le cadavre stellaire compact d'une étoile beaucoup plus massive que le Soleil morte à un jeune âge suite à son explosion en supernova. L'âge du pulsar a pu être estimé en étudiant la coquille de gaz balayée par l'explosion, également découverte dans le cadre de cette thèse. La rotation anormalement lente du pulsar compte tenu de son jeune âge est intriguante et promet de révéler d'importants indices sur la physique de tels cadavres stellaires.

Declaration

I declare that this thesis was composed by myself, that the work contained herein is my own except where explicitly stated otherwise, and that this work has not been submitted for any other degree or professional qualification. Where the work was done in collaboration with others, I made a significant contribution. Parts of the work contained in this thesis have been published in refereed scientific journals or submitted for publication. These are listed below:

- Chapter 2 draws upon work published in "*The VLT-FLAMES Tarantula Survey. I. Introduction and observational overview*", Evans, Taylor, Hénault-Brunet et al. 2011, A&A, 530, 108.
- Chapter 3 is based on work presented in "*The VLT-FLAMES Tarantula Survey VI. A low velocity dispersion for the young massive cluster R136*", Hénault-Brunet et al. 2012, A&A, 546, 73. The framework for the analysis of variability and the identification of binaries was developed in partnership with Hugues Sana. The discussion of the dynamical state of R136 was written in collaboration with Mark Gieles.
- Chapter 4 draws upon work from "*The velocity dispersion of OB stars from single- and multi-epoch radial velocities: the R136 cluster as a test case*", Cottaar & Hénault-Brunet 2013, submitted to A&A. The code used for the analysis presented in this chapter was developed by Michiel Cottaar and the paper was written in collaboration with Michiel Cottaar.
- Chapter 5 is based on work presented in "*The VLT-FLAMES Tarantula Survey VII. Evidence for rotation of the young massive cluster R136*", Hénault-Brunet et al. 2012, A&A, 545, L1. The discussion of the origin of rotation in star clusters in Sections 5.1 and 5.4 was written in collaboration with Mark Gieles.
- Chapter 6 is based on work initially published in "*Discovery of a Be/X-ray pulsar binary and associated supernova remnant in the Wing of the Small Magellanic Cloud*, Hénault-Brunet et al. 2012, MNRAS, 420, L13. The reduction of X-ray data used in this work was performed by Wei Sun, Martin Guerrero, and Lidia Oskinova, and the analysis of these X-ray data was done in partnership with the same people. The analysis of the supernova remnant in Section 6.5.2 was done in partnership with You-Hua Chu, Jay Gallagher, and Robert Gruendl.
- Additionally, the discussion in Chapter 7 about the connection between rotation and the formation of R136 is based on the ESO VLT proposal "*Unveiling the*

origin of internal rotation in the young massive cluster R136", PI: V. Hénault-Brunet. The N-body calculations on which part of the argumentation is based were performed by Mark Gieles and Anna-Lisa Varri.

Vincent Hénault-Brunet
July 2013

Acknowledgements

First of all, I would like to thank Chris Evans for making all of this possible by allowing me to join the Tarantula Survey team four years ago. His guidance, trust, and enthusiasm, added to the freedom he gave me to pursue my evolving research interests, have made a real positive impact on my work and research career.

It has been truly fulfilling to work with the members of the VLT-FLAMES Tarantula consortium. Our meetings, often informal, but where ideas were debated with rigour and passion, encapsulate the very essence of a collaborative scientific endeavour. In particular, thanks to Mark Gieles for patiently guiding my first steps in the world of stellar dynamics and giving me the opportunity to continue this adventure in his new research group at the University of Surrey. Thanks also to Hugues Sana, whose approach to data reduction and statistical analysis has become for me an example to follow, to Nate Bastian for his awareness of the "bigger picture" (be it about star clusters or scientific careers), and to ROE colleague William Taylor for his precious expertise with the reduction of FLAMES data and his contagious passion for all things scientific.

I would like to extend my thanks to other collaborators outside the Tarantula consortium, including Lida Oskinova for the opportunity to observe at Paranal and work on this intriguing Be/X-ray pulsar binary, as well as Michiel Cottaar for a fruitful collaboration. I was also fortunate to attend the Vatican Observatory summer school, from which I will certainly remember, among other things, Douglas Heggie's beautifully taught lectures on the N-body problem.

I am very grateful to the Scottish Universities Physics Alliance (SUPA) and the Natural Science and Engineering Research Council of Canada (NSERC) for their financial support.

Greetings to all the colleagues who have made the ROE a great place to work, and to all the friends who have contributed to make Edinburgh such a fantastic city to live in.

Finalement, merci à mes parents de m'avoir donné tout ce dont j'ai toujours eu besoin pour réussir, ainsi qu'à toute ma famille pour nous faire sentir chez nous chaque fois que nous sommes de retour au Québec. Et bien sûr, mille mercis à Maude, mon amoureuse et complice, pour son support incomparable et de formidables années partagées en terre écossaise et à la découverte de l'Europe.

Contents

Abstract i

Lay Summary iii

Résumé en français pour les non-spécialistes iv

Declaration vi

Acknowledgements viii

Contents ix

List of Figures xiv

List of Tables xviii

1 Introduction 1

1.1 30 Doradus: a look back in history 1

1.2 Star clusters 4

1.2.1 Star clusters as laboratories 4

1.2.2 Young massive clusters 6

1.3 The dynamics of star clusters 7

1.3.1 Dynamical timescales 7

1.3.2 "Infant mortality" and mass loss from star clusters 10

1.3.3 Weighing star clusters 19
1.3.4 The rotation of star clusters 21
1.4 Massive stars and binaries 23
1.5 This thesis 27

2 Spectroscopic surveys of massive stars: overview and data reduction 32
2.1 Introduction 32
2.2 The VLT-FLAMES Survey of Massive Stars 32
2.3 The VLT-FLAMES Tarantula Survey 34
2.3.1 30 Doradus 34
2.3.2 Motivations 38
2.3.3 The FLAMES instrument 39
2.3.4 Observing strategy for the VFTS 41
2.3.5 Highlights from the VFTS 46
2.4 Data reduction: VLT-FLAMES MEDUSA 51
2.4.1 General procedure 51
2.4.2 Cross-contamination 55
2.4.3 Atmospheric refraction effects 56
2.4.4 Line-of-sight gas velocities 56
2.5 Data reduction: VLT-FLAMES ARGUS 58
2.6 A survey of massive stars in SGS-SMC 1 63

3 A low velocity dispersion for the young massive cluster R136 64
3.1 Introduction 64
3.2 ARGUS data 65

3.3 Radial velocity and variability analysis 67
3.3.1 Zero-point errors 67
3.3.2 Variability criteria 69
3.3.3 Absolute radial velocities 73
3.4 Spectral classification of ARGUS non-variable sources 75
3.5 Supplementary MEDUSA data 79
3.6 Velocity dispersion 81
3.6.1 Velocity dispersion upper limit 81
3.6.2 Contamination by "halo" stars 84
3.6.3 The contribution of cluster rotation 86
3.6.4 The velocity dispersion when including binaries/variable stars ... 86
3.6.5 The contribution of errors and undetected binaries 87
3.7 Discussion 91
3.8 Summary 96

4 The velocity dispersion of OB stars in young clusters from a single epoch of radial velocities: R136 as a test case 97

4.1 Introduction 97
4.2 Method 99
4.2.1 Outline of the maximum likelihood method 99
4.2.2 Current constraints on the binary properties of OB stars..... 101
4.2.3 Review of the binary properties of OB stars 106
4.3 Data 108
4.3.1 R136 108
4.3.2 Simulated data 110

4.4 Results 111

4.4.1 Systematic biases: Monte Carlo simulations 111

4.4.2 Analysis of R136 radial velocity data 113

4.5 Discussion 117

4.6 Summary 119

5 Evidence for rotation of the young massive cluster R136 120

5.1 Introduction 120

5.2 Data 121

5.3 Analysis 122

5.3.1 The "globular cluster" method 122

5.3.2 Maximum likelihood method 124

5.4 Discussion 131

5.5 Summary 133

6 Discovery of a Be/X-ray pulsar binary and associated supernova remnant in the Wing of the SMC 134

6.1 Introduction 134

6.2 Background 135

6.2.1 Be/X-ray binaries 135

6.2.2 BeXRBs in the SMC 137

6.2.3 The NGC 602 region 138

6.3 X-ray observations 139

6.3.1 Spectral analysis 140

6.3.2 Timing analysis 143

6.4 Optical spectroscopy 144

6.5 Discussion 147

6.5.1 The properties of SXP 1062..... 147

6.5.2 The environment of SXP 1062 149

6.5.3 A slowly rotating pulsar in a young supernova remnant 151

7 Conclusions and future prospects 155

7.1 New constraints on the dynamics of R136 155

7.2 Towards quantitative dynamical analysis of young massive clusters 157

7.3 Confirming the rotation of R136 and unveiling its formation 159

7.4 Binaries, velocity dispersion, and rotation: connecting the dots..... 161

7.5 SXP 1062: the Rosetta Stone of accreting neutron stars? 162

A Log of radial velocity measurements and variability tests 164

B Notes on individual ARGUS sources 174

Bibliography 180

List of publications 191

List of Figures

1.1 The Dorado constellation in the southern sky, with the location of the LMC and 30 Doradus indicated 2

1.2 30 Doradus on different scales, from the broader region to the resolved components of R136a 3

1.3 Radius-mass diagram of Milky Way open clusters, young massive clusters, and old globular clusters 5

1.4 Observed frequency distribution of ages for open clusters and embedded "clusters" within 2 kpc of the sun 11

1.5 Illustration of the relative change in the radius of a cluster following impulsive mass loss and adiabatic mass loss 15

1.6 Surface brightness profiles for three young clusters and two N-body simulations which include the rapid removal of gas which was left over from a non-100% star formation efficiency 17

1.7 The light-to-dynamical mass ratio of young clusters compared to predictions from SSPs and gas expulsion models 18

1.8 The measured velocity dispersion of young clusters squared, presented as a function of a prediction for this quantity, and shown along with a prediction of the effect of binaries 19

1.9 The dependence of η on the slope γ of the EFF profile 21

1.10 Typical parameter space for massive binaries and corresponding detection techniques 25

1.11 Schematic representation of the orbital parameters of a binary system . 26

2.1 Distribution of stellar generations of differing age in 30 Doradus 36

2.2 The GIRAFFE spectrograph, its fibre positioner, and one of the two plates of the fibre positioner 40

2.3 A schematic of ARGUS in the Ozpoz fibre positioner and the ARGUS fibre geometry 41

2.4 Typical detection probability of an O-type spectroscopic binary for the MEDUSA observations of the VFTS 44

2.5 ARGUS reconstructed pointings overlaid on an HST-WFC3 F555W image of R136, with the location of the VFTS MEDUSA and UVES targets in the central region of 30 Dor also shown 45

2.6 Combined *YJKs*-band image of 30 Doradus from the VISTA Magellanic Clouds (VMC) Survey with the O-type and Wolf-Rayet stars observed by the VFTS indicated 46

2.7 Example CCD images from different reduction steps for one MEDUSA LR02 observation of a field in SGS-SMC 1. 54

2.8 Reduced spectra of two consecutive exposures for an O-type star observed as part of the FLAMES survey of massive stars in SGS-SMC 1, showing the effect of differential atmospheric refraction on the continuum slope 57

2.9 Nebular emission-line spectrum (LR03 and HR15N settings) for one line of sight of the VFTS sample 57

2.10 Example of a multiple Gaussian fit to the S II λ6717 line profile of one line of sight from the VFTS 58

2.11 ARGUS reconstructed images overlaid on an F555W HST-WFC3 image with individual extracted ARGUS sources identified 61

2.12 A close-up on the reconstructed ARGUS image in the surroundings of VFTS 1033 and the spectra associated to the different spaxels of that source 62

3.1 Distribution of zero-point velocity shifts from the cross-correlation of ARGUS calibration arc spectra and from the cross-correlation of nebular lines 68

3.2 Example of a simultaneous Gaussian fit to the He II λ4200, He I λ4388, and He II λ4542 absorption lines for an individual epoch of the ARGUS source VFTS 1026 70

3.3 Weighted mean spectrum and Temporal Variance Spectrum for the ARGUS sources VFTS 1028 and VFTS 1025 72

3.4 Difference between the absolute RVs measured from He II λ4542 and from other stellar absorption lines 74

3.5 RVs from this work compared to the RVs from Sana et al. 2013 80

3.6 Distribution of ARGUS and MEDUSA sources used in this work overlaid on an F555W HST-WFC3 image of R136 81

3.7 Observed line-of-sight velocity dispersion of stars within a given distance from the centre of R136 83

3.8 Observed line-of-sight velocity dispersion of R136 with spectral subtypes divided in two subsamples 85

3.9 Estimate of the contributions to the line-of-sight velocity dispersion for massive stars in the inner 5 pc of R136 88

3.10 Estimates of the contribution to the line-of-sight velocity dispersion of R136 from undetected binaries for different assumptions about the period distribution 90

4.1 The observed radial velocity distribution for a single epoch drawn from the multi-epoch radial velocity dataset of R136 along with the best-fit radial velocity distribution and intrinsic velocity distribution of the cluster 101

4.2 Illustration of the period and mass ratio distributions considered in this chapter, along with the corresponding unprojected and projected velocity distributions 103

4.3 Probability distribution of velocity offsets for massive binaries with different orbital periods 105

4.4 Two-component EFF fit to the surface brightness profile of R136 and distribution of velocities for the stars within 10 pc from R136 109

4.5 The systematic offset induced in the best-fit velocity dispersion due to the uncertainties in the orbital parameter distributions of OB stars . . . 112

4.6 The random uncertainties in the measured velocity dispersion as a function of the sample size N for single-epoch observations of a cluster with a velocity dispersion of 5 $\mathrm{km\,s^{-1}}$ 114

4.7 The best-fit binary fraction, velocity dispersion, and mean velocity for five single-epoch radial velocity datasets of the O-type stars in R136 . . 116

5.1 Illustration of the positions and RVs of the stars considered in this chapter along with the best-fit rotation axis determined for different models 122

5.2 Difference between the mean radial velocities on each side of R136 as a function of position angle 123

5.3 RV (in the system of the cluster) as a function of distance X from the optimal rotation axis for different models, along with best-fit rotation curves 126

5.4 Distributions of fitted parameters from 10 000 simulated datasets with the same rotation curves as the best-fit rotation curves determined from the R136 dataset 127

5.5 Likelihood contours around the best-fit parameters for the rotation curve of the R136 dataset 128

5.6 Distribution of amplitudes $V_{\rm rot} \sin i$, Ω, and A from 10 000 Monte Carlo simulations of RV distributions with no rotation 130

5.7 Distribution of PA_0 from 10 000 Monte Carlo simulations of RV distributions with no rotation 130

6.1 Hα image of the supergiant shell SGS-SMC 1 and close-ups on NGC 602 and SXP 1062 136

6.2 Chandra ACIS-I and XMM-Newton EPIC-pn spectra of SXP 1062 . . . 140

6.3 Spectral model fits to the X-ray spectra of SXP 1062 142

6.4 XMM-Newton and Chandra power density spectra in the soft and hard energy bands 143

6.5 Pulse profiles folded with a period of 1 062 s in different energy bands . . 144

6.6 Optical VLT-FLAMES and 2dF spectra of 2dFS 3831 146

6.7 Hα, [S II], and [O III] images of the nebula detected around SXP 1062 . . 150

7.1 Possible positions of new ARGUS pointings around R136 and comparison of the best-fit rotation curve of R136 with rotation curves from different formation scenarios 160

B.1 Spectra of ARGUS sources that did not show spectroscopic variability . 175

B.2 Non-variable ARGUS sources displaying composite spectra 177

List of Tables

2.1 Observational details of the different settings used in the VFTS for the three observing modes of FLAMES 42

3.1 Rest air wavelengths adopted for the principal helium lines in the ARGUS spectra 74

3.2 Coordinates, RVs, and spectral types of ARGUS and MEDUSA sources showing no significant variability 77

4.1 Constraints on the distributions of orbital parameters of massive binaries from the literature 102

5.1 Best-fit parameters for the rotation curve and confidence level for the detection of rotation for different subsamples of stars in and around R136 131

6.1 Best-fit parameters of the models fitted to the X-ray spectra of SXP 1062 141

A.1 Individual epochs of the ARGUS observations 165

A.2 Results of the variability tests for the ARGUS sources 166

A.3 Radial velocities for individual epochs for all the ARGUS sources suitable for radial velocity analysis 172

Chapter 1

Introduction

1.1 30 Doradus: a look back in history

The Tarantula Nebula, in the Large Magellanic Cloud (LMC), has a long history of hiding its true nature. The nebulosity was originally thought to be a star which seventeenth century astronomers named "30 Doradus", corresponding to the 30th brightest star in the constellation Dorado (the Spanish name for dolphinfish; Figure 1.1). In 1751, Abbé Nicolas Louis de Lacaille undertook a journey to the Cape of Good Hope to document the stars of the southern sky. In one of his reports, published in 1755, he catalogued 30 Doradus as a nebula and was the first to establish its non-stellar nature.

Jumping more than two centuries later, it was the turn of R136a (the very central region the Tarantula Nebula; see Figure 1.2 and Chapter 2) to be interpreted as something it is not. In the early 1980s, only ground-based imaging was available to determine its size, and it was interpreted as a single stellar object. Its high luminosity and temperature, much larger than that of any other star, pointed to a very large mass. For more than a decade, it was suggested to be the most massive known single star, with a spectacular mass over 2000 $M_{\odot}$ (e.g. Cassinelli et al. 1981), although this scenario also drew some criticism (e.g. Moffat & Seggewiss 1983). The alternate hypothesis that R136a could be the dense stellar core of a populous cluster was however considered by many as too contrived or unlikely and was therefore rejected (we will come back to this later). R136a thus continued to masquerade as a "supermassive" star (at least for a big part of the astronomical community) until Weigelt & Baier (1985) resolved it into eight components based on higher spatial resolution imaging using holographic

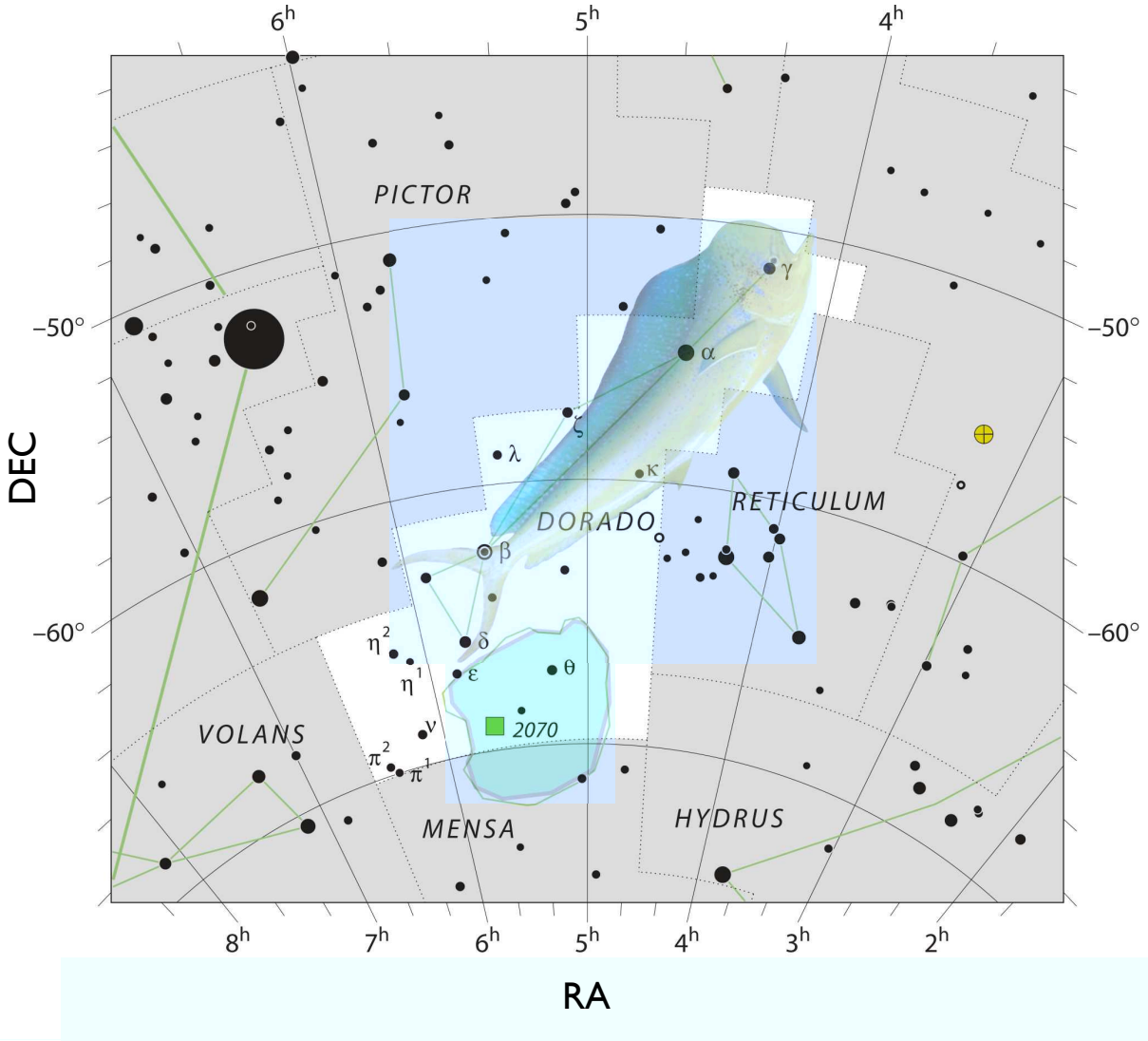

Figure 1.1 The Dorado constellation in the southern sky, with the location of the LMC shown in light green to the south. The position of 30 Doradus (labeled as '2070') is also indicated. Credit for the background map: IAU and Sky & Telescope magazine.

speckle interferometry (a more recent image of R136a using adaptive optics is shown in Figure 1.2). Amusingly, these eight objects include the current record holder for the most massive star known (R136-a1) and a few other very massive stars which have been reported to exceed the commonly assumed upper stellar mass limit of ~ 150 $M_{\odot}$, although their mass is nowhere near the claims made for R136a in the 1980s (Crowther et al. 2010).

While the points discussed above are mainly historical curiosities, they remind us that great care must be taken when interpreting distant stellar systems. Just like the compactness of R136a could mimic a single stellar source when looked at using traditional ground-based imaging, binary systems can easily appear as single stars at

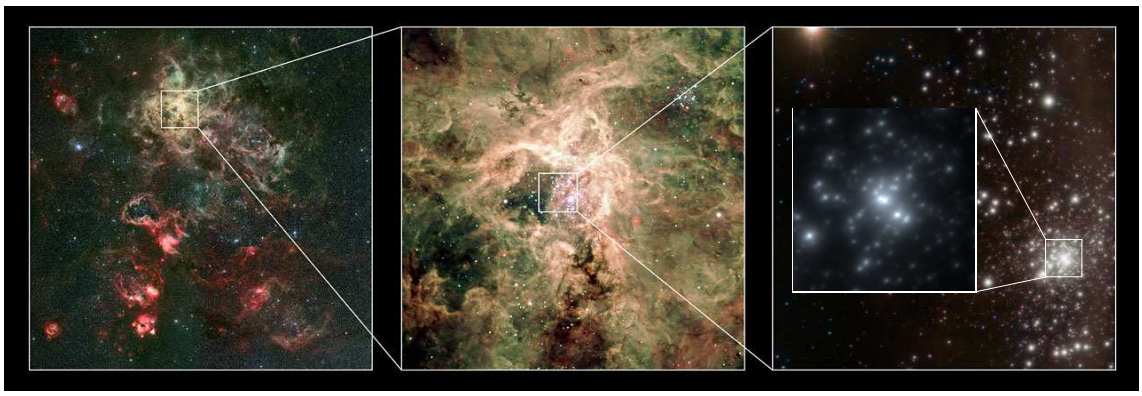

Figure 1.2 A visible-light image of the 30 Doradus region as seen with the Wide Field Imager on the MPG/ESO 2.2-metre telescope (left) along with a zoomed-in visible-light image of the Tarantula Nebula from the Very Large Telescope (middle). An image of the R136 cluster with the near-infrared MAD adaptive optics instrument on the Very Large Telescope is shown in the right-hand panel, with the smaller image on the right showing a close-up on R136a. Credit: ESO/P. Crowther/C.J. Evans.

the distance of the LMC (for which a separation of $1''$ on the sky corresponds to a projected distance of 50 000 AU).

With this in mind, the work presented in this thesis looks at the kinematics of stars in R136, the massive cluster at the centre of 30 Doradus, with a particular emphasis on the effect of unresolved binaries on the measured velocities. Like previous work that has unveiled the true nature of 30 Doradus or its constituents, we take advantage of cutting-edge instrumentation, in this case multi-object (and in particular integral-field unit) spectroscopy with an 8-m telescope.

Most of the work presented in the next chapters is a component of a larger project looking at nearly 1 000 massive stars in 30 Doradus, a region small enough on the sky to have once been considered a single star. This is presented exactly 250 years after a catalogue of nearly 10 000 stars in the entire southern hemisphere was published posthumously under the name of Nicolas Louis de Lacaille, the man himself who established 30 Doradus as a nebula.

The present chapter introduces the context and basic theory relevant to the studies presented in the main chapters of this thesis, with an emphasis on the dynamics of young massive star clusters and on massive stars/binaries.

1.2 Star clusters

1.2.1 Star clusters as laboratories

In the current paradigm of star formation, stars form predominantly in groups or clustered environments (Lada & Lada 2003; Bressert et al. 2010), which has led star clusters to be considered as the building blocks of galaxies. In practice, however, only a minority of these groups will evolve to form bound clusters (e.g. Bastian 2012, and references therein). That said, the small number of stars forming in bound clusters is still of great interest as these clusters are important astrophysical laboratories. Star clusters are still the best approximation to "simple stellar populations", with all stars having approximately the same age, making them unique systems to test models of stellar evolution. With their stars bound by mutual gravitational attraction and relatively high stellar densities, clusters are also ideal laboratories where we can study a range of dynamical effects like stellar collisions and binary formation or disruption.

Traditionally, studies of star clusters have unsurprisingly focused on our own backyard, the Milky Way. Two distinct groups appeared to emerge (see Figure 1.3), with open clusters having relatively young ages (less than a few Gyr), low masses ($\sim 10^2 - 10^4$ $M_\odot$), and being found in the disc of the Galaxy, while globular clusters are part of the Galactic halo/bulge, are massive ($\sim 10^4 - 10^6$ $M_\odot$), very dense, and are almost as old as the Universe. Both groups have effective radii (see below) of typically $\sim 2 - 4$ pc, which implies a large spread between the central densities of open and globular clusters ($10^1 - 10^6$ $M_\odot$ pc^{-3}).

At the present time, the most extreme young clusters in the Milky Way and Magellanic Clouds are forming a few 10 000 stars, and partly occupy the gap between open and globular clusters. In the Milky Way, these are clearly associated with the disc, like open clusters, although their masses are more closely related to globular clusters. These rare clusters, which are close enough for individual stars to be resolved, can provide important insight into extreme star-formation events in the local Universe and shed light on the formation of globular clusters in the distant past of the Milky Way (Elmegreen & Efremov 1997). They are also ideal places to study the distribution of stellar masses, from solar-type stars up to the most massive stars known. These young rich clusters appear to be the only places where the most massive stars can be observed. They are also important laboratories to investigate the birth of stars and the dynamical evolution of dense stellar systems.

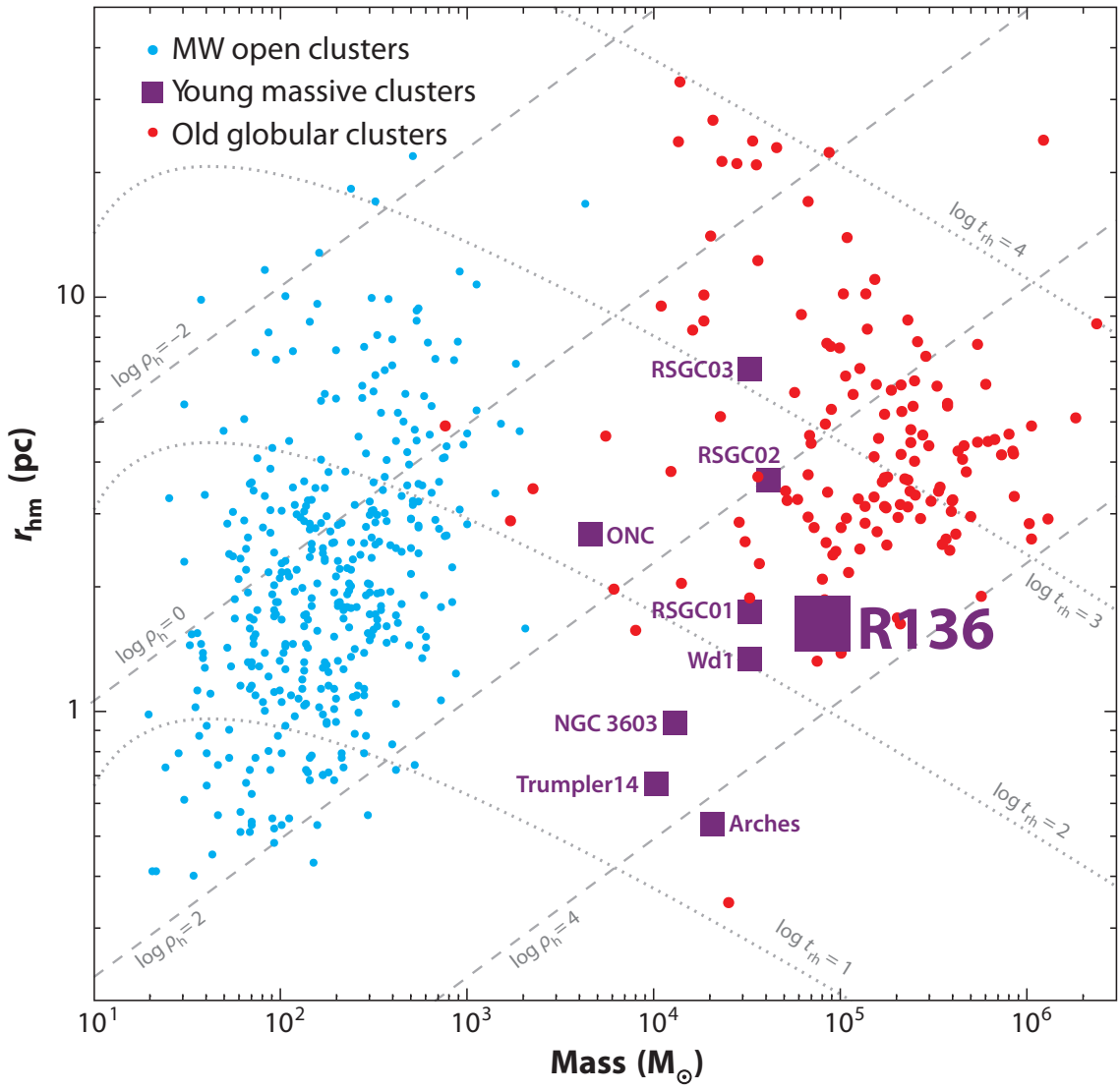

Figure 1.3 Radius-mass diagram of Milky Way open clusters, young massive clusters, and old globular clusters, with R136 (in the LMC) also indicated (adapted from Portegies Zwart et al. 2010). The gray dashed and dotted lines trace constant half-mass density $\rho_{\rm h}$ and half-mass relaxation time $t_{\rm rh}$, respectively.

In addition to a few Galactic examples, the idea that the formation of clusters with masses comparable to old globular clusters is not restricted to the early Universe is supported by the population of massive clusters found in the Magellanic Clouds, which span a broad range of ages (e.g. de Grijs & Anders 2006). The apparent gap between the properties of open and globular clusters was also somewhat closed by the discovery of extragalactic Young Massive Clusters (YMCs) from observations with the Hubble Space Telescope in the early 1990s (Holtzman et al. 1992). These clusters were found to have masses on a par with globulars, but with ages comparable to open clusters.

1.2.2 Young massive clusters

YMCs have gained a lot of interest in recent years as they might help us to understand the formation of old globular clusters in the early universe. To realise just how much of a revolution this represents, it is worth quoting Lyman Spitzer, who in his 1987 seminal book on the dynamical evolution of globular clusters mentioned that "the origin and early evolution of globular clusters is ignored [in the book] because so little is known about this important early phase". Interestingly, Spitzer was the driving force behind the development of the Hubble Space Telescope, which soon started to unveil these extragalactic YMCs, observable up to large distances ($\lesssim$ 100 Mpc) due to the high light-to-mass ratio of young stellar populations.

YMCs are commonly defined as being younger than about 100 Myr, more than a few crossing times old, and more massive than 10^4 $M_\odot$ (Portegies Zwart et al. 2010). The requirement that the age of the cluster exceeds its current dynamical time (the orbit time of a typical star) by a factor of a few, as we will explain below, effectively ensures that we are dealing with bound clusters rather than unbound associations. The upper limit on the age in the above definition means that YMCs are still in an early phase of significant mass loss due to stellar evolution. The adopted mass limit is such that lower-mass clusters are unlikely to survive for more than 1 Gyr. The masses and projected lifetimes of YMCs are therefore comparable to those of the old globular clusters that populate the bulges and halos of many galaxies, including the Milky Way, although the extent to which the YMCs that we observe today will eventually resemble globular clusters remains uncertain (see e.g. Portegies Zwart et al. 2010).

While only a few examples of YMCs are known in the Milky Way, as alluded to previously, they are particularly abundant in starburst and interacting galaxies (e.g. Holtzman et al. 1992; Miller et al. 1997; Whitmore et al. 1999). They have also been found and studied in several quiescent spirals (e.g. Larsen 2004; Cantiello et al. 2009). In nearby young starburst galaxies, at least 20% and possibly all of the UV light appears to come from young star clusters (Meurer et al. 1995). These large populations of distant unresolved clusters are useful to study the cluster luminosity function, the cluster initial mass function, and the cluster formation efficiency, which is in turn important when considering YMCs as tracers of star formation in galaxies. For a review of YMC populations, we refer for example to Larsen (2010).

The few YMCs that are close enough to be resolved are still extremely important to constrain the dynamical evolution of these systems. In this thesis, we focus on this aspect rather than on populations of distant clusters. We will be mostly concerned

with the phase in the evolution of clusters just after most of the ambient gas left over from the star formation process has been ejected due to feedback from massive stars. This phase is crucial as it provides the initial conditions for the longer-term evolution of the cluster, i.e. for the later stages driven first by stellar mass loss and then purely by stellar dynamical processes. Yet, the first few million years of the evolution of star clusters is still poorly understood.

1.3 The dynamics of star clusters

In this section, we review some basic aspects of the dynamics of star clusters, in particular those relevant to their early evolution. We start by introducing the fundamental timescales of a self-gravitating system.

1.3.1 Dynamical timescales

The dynamical timescale is the time required for a typical star to cross the system, and also the timescale on which the system (re)establishes dynamical equilibrium. We can estimate this timescale from a typical circular orbit using the virial radius ($r_{\rm vir}$) as the scale of the system[1]

$$\begin{aligned} t_{\rm dyn} \sim \frac{r_{\rm vir}}{v} &= \frac{r_{\rm vir}}{\sqrt{GM/r_{\rm vir}}} = \left(\frac{GM}{r_{\rm vir}^3}\right)^{-1/2} \\ &\sim 2\times10^4 \text{ yr} \left(\frac{M}{10^6 \text{ M}_\odot}\right)^{-1/2} \left(\frac{r_{\rm vir}}{1 \text{ pc}}\right)^{3/2} , \end{aligned} \tag{1.1}$$

We can see that $t_{\rm dyn}$ is relatively short for a typical massive cluster. This dynamical timescale can be compared to the age of a system to estimate if it is a bound cluster or an unbound association. Gieles & Portegies Zwart (2011) proposed that a cluster should be defined as stellar grouping whose age is greater than a current dynamical crossing time, which naturally includes bound stellar groupings and excludes unbound expanding associations. For unbound stellar agglomerates expanding into the field, the ratio age/$t_{\rm dyn}$ is indeed expected to remain small and stay constant or to decrease as

[1] $r_{\rm vir} = GM^2/(2|U|)$ as shown in Section 1.3.2. M is the total cluster mass, U is the potential energy, and G is the gravitational constant. Note that because massive star clusters tend to be approximately spherically symmetric in space, or at least look circular on the sky, the radius is a meaningful measure of their size.

a function of time, while for bound clusters this ratio should be large and will increase with time. An implication of this definition is that very young systems (commonly referred to as embedded clusters) are not included since their stars have not yet had time to cross from one side of the system to the other. This avoids the complication of defining "clusters" at very young ages, where it is hard to know if systems are bound, and where the surface density distribution of stars can anyway not be clearly divided into "clustered" and "distributed" modes (Bressert et al. 2010, but for words of caution about the difficulty to distinguish these modes, see Gieles et al. 2012).

The other fundamental timescale is the relaxation time ($t_{\rm rl}$), which corresponds to the time required for the kinetic energies of the cluster members to roughly equalize via two-body encounters. It is the timescale on which the spatial distribution and velocities (i.e. the orbits) of individual stars evolve, and on which stars tend to establish a Maxwellian velocity distribution. The local relaxation time is given by (Spitzer 1987)

$$t_{\rm rl} = \frac{\langle v^2 \rangle^{3/2}}{15.4\ G^2\ m\ \rho\ \ln\Lambda}, \tag{1.2}$$

where $\langle v^2 \rangle$ is the mean square velocity, m is the local mean mass and ρ is the local density. The value of Λ depends on the range of stellar masses and the number of stars, but for simplicity we adopt $\ln\Lambda = 10$ as an appropriate value for the YMCs considered here (see Portegies Zwart et al. 2010).

For a cluster in virial equilibrium ($U = -2\ T$, where T is the total kinetic energy of the cluster stars), we have $T/M = \frac{1}{2}\langle v^2 \rangle$. We can replace the quantities in equation 1.2 above by their cluster-wide averages and write $\langle v^2 \rangle = GM/2r_{\rm vir}$ and $\rho \approx 3M/8\pi r_{\rm vir}^3$, and also make the approximation that $r_{\rm vir}$ is equal to the half-mass radius ($r_{\rm hm}$; the distance from the cluster centre containing half of the total mass). We then obtain the half-mass two-body relaxation time (Spitzer 1987)

$$\begin{aligned} t_{\rm rh} &\approx \frac{0.0065\ \langle v^2 \rangle^{3/2}}{G^2\ \langle m \rangle\ \bar{\rho}} \\ &= 0.014 \frac{N^{1/2}\ r_{\rm vir}^{3/2}}{G^{1/2}\ \langle m \rangle^{1/2}} \\ &\approx 0.014\ N\ t_{\rm dyn}\ , \end{aligned} \tag{1.3}$$

where $\langle m \rangle \equiv M/N$ is the global mean stellar mass and N is the total number of stars

in the cluster. We can also rewrite the above as

$$t_{\rm rh} \sim 2 \times 10^8 \ {\rm yr} \left(\frac{M}{10^6 \ {\rm M}_\odot} \right)^{1/2} \left(\frac{r_{\rm vir}}{1 \ {\rm pc}} \right)^{3/2} \left(\frac{\langle m \rangle}{M_\odot} \right)^{-1}. \tag{1.4}$$

This is typically much longer than $t_{\rm dyn}$ for massive clusters, which implies that the mean free path of stars greatly exceeds the size of the system, or equivalently that stars make many orbits almost unaffected by two-body encounters.

One consequence of two-body encounters is dynamical friction and a trend towards equipartition of kinetic energy, in which the velocity dispersions of stars of different masses would have $m\langle v^2 \rangle \sim$ constant. Heavier stars will tend towards lower mean velocities, and sink to the centre of the cluster. Lower-mass stars will acquire higher velocities and preferentially occupy the outer regions of the cluster, and may even escape. The timescale for this process, called mass segregation, is related to the relaxation timescale by (Spitzer 1969)

$$t_{\rm s} \sim \frac{\langle m \rangle}{m} t_{rl}. \tag{1.5}$$

The timescale for stars of mass m to segregate is therefore shorter for higher values of m. Numerical simulations also show that the trend towards equipartition is accelerated as the mass spectrum of stars is widened (e.g. Farouki & Salpeter 1982). The mass segregation timescale can be reduced to a few Myr when the maximum mass is 20 $M_\odot$, implying that mass segregation is effective over the lifetime of massive stars. Note however that full equipartition is probably never reached in young clusters, which have a wide range of masses, due to the Spitzer instability (Spitzer 1969). In this case, the heavier stars form a sub-cluster at the centre of the system which is dynamically decoupled from the rest of the cluster.

Mass segregation can lead to an increase in the mass-to-light ratio with increasing distance from the cluster centre because low-mass stars are then relatively more abundant in the outer parts of the cluster. Clearly, the timescales discussed above suggest that dynamical mass segregation generally needs to be taken into account, and not only for older clusters, so the common assumption that light traces mass (such that the half-light and half-mass radii are identical) may well be inaccurate. Even if a cluster is much younger than the timescale for mass segregation, there might be primordial mass segregation. The possibility that a cluster formed with massive stars preferentially closer to the centre is consistent with simulations of cluster formation

(e.g. Bonnell & Bate 2006). For a review of the observational evidence found for mass segregation in a few Galactic YMCs, we refer to Portegies Zwart et al. (2010).

Note that a star cluster never reaches full "thermal" equilibrium. A fraction $\xi_{\rm e}$ of the stars in the tail of the velocity distribution have velocities larger than the escape velocity $v_{\rm esc}$. If we assume that these stars escape and that the high-velocity tail is refilled every t_{rh}, the timescale for the cluster to dissolve is $t_{\rm dis} = t_{\rm rh}/\xi_{\rm e}$. An isolated cluster has an escape velocity $v_{\rm esc} = 2\langle v^2\rangle^{1/2}$. For a Maxwellian velocity distribution, a fraction $\xi_e = 0.0074$ has $v_{\rm esc} > 2\langle v^2\rangle^{1/2}$. The corresponding dissolution timescale can be estimated as $t_{\rm dis} = 135\ t_{\rm rh}$. This is how we estimate that a cluster with an initial number of stars $N \approx 10^5$ would survive for ~ 10 Gyr. However, for clusters in a tidal field, $v_{\rm esc}$ would be lower and $\xi_{\rm e}$ would therefore be higher, such that the dissolution timescale and the lifetime would be reduced. For example, YMCs such as the Arches and Quintuplet systems, near the Galactic centre (see e.g. Portegies Zwart et al. 2010), are likely to dissolve within ~ 1 Gyr.

With the above in mind, it is worth digressing from the main topic of this section to revisit the controversy about the status of R136a that emerged in the 1980s. One important argument of the authors arguing for an extraordinary stellar object of $\sim$ 2000 $M_\odot$ was that the cluster of a few tens of massive stars required to explain the spectrum of R136a (if it was not a single star) would have a short relaxation time of $\sim 1\,000$ yr and therefore evolve (and dissolve) way too rapidly (e.g. Savage et al. 1983). They were however ignoring the presence of the much more numerous lower-mass stars, which have since been detected down to ~ 1 $M_\odot$ all the way through the core of R136 (Sirianni et al. 2000; Andersen et al. 2009). That led to a significant underestimation of the relaxation time, which depends on the number of stars.

Finally, we note that one other timescale, independent of the dynamical properties of clusters, will influence their evolution. This is the stellar evolution timescale (~ 10 Myr for YMCs; Portegies Zwart et al. 2010), which is driven by mass loss.

1.3.2 "Infant mortality" and mass loss from star clusters

The expression "infant mortality" of star clusters was initially coined by Lada & Lada (2003) to describe the discrepancy between the number of observed open clusters and the number of embedded "clusters" (i.e. still partly or completely enshrouded in the molecular cloud from which they formed). These authors argued that there are about ten times fewer open clusters than expected if all embedded clusters evolve into open

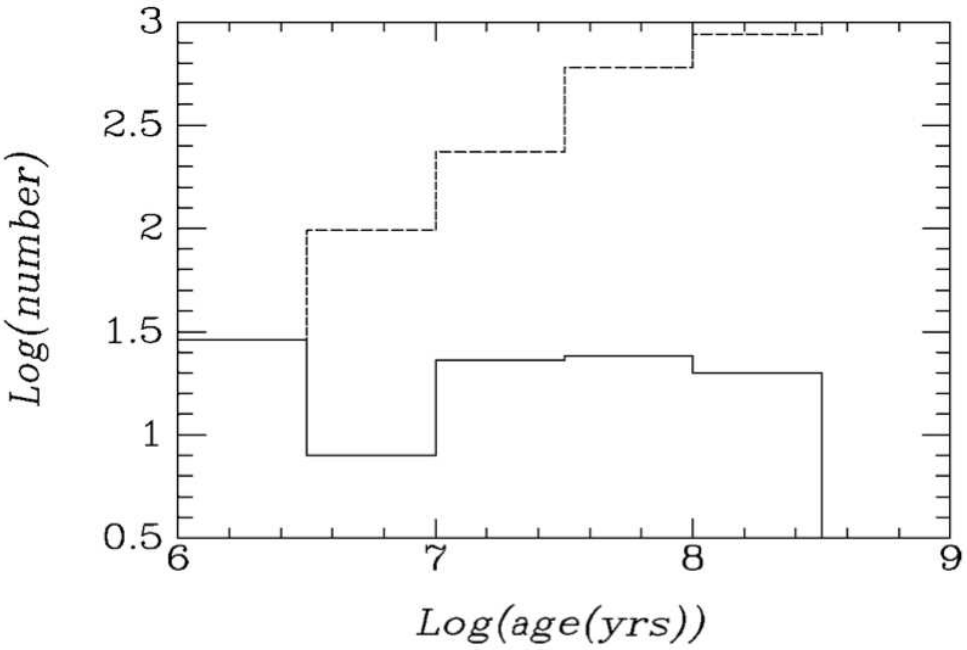

Figure 1.4 Figure from Lada & Lada (2003) showing the observed frequency distribution of ages for open clusters and embedded "clusters" within 2 kpc of the sun (solid line) compared to that predicted for a constant rate of star formation adjusted for cluster luminosity evolution (dotted line). All embedded "clusters" fall into the first bin.

clusters (see Figure 1.4).

The rapid removal of gas left-over from star formation by stellar winds from massive stars or supernovae explosions was suggested to leave young clusters in a super-virial state, making them vulnerable to dissolution, and thus explaining the apparent disruption of such a large fraction of clusters (e.g. Geyer & Burkert 2001; Kroupa & Boily 2002; Bastian & Goodwin 2006). The importance of the infant mortality scenario however depends on the definition adopted for embedded clusters (Bressert et al. 2010; Bastian 2011), with more conservative criteria requiring less than 50% of clusters to be destroyed to match the observed number of open clusters. But no matter which definition is adopted, the question of whether or not gas expulsion plays a significant role in the early evolution/disruption of star clusters still needs to be addressed.

Star clusters have been observed to expand in their first 100 Myr (Mackey & Gilmore 2003; Bastian et al. 2008; Portegies Zwart et al. 2010), but this expansion is not direct evidence for the importance of gas expulsion. There are two ways for clusters to expand as a response to mass loss (e.g. Hills 1980): (i) expansion following impulsive mass loss, e.g. change of potential due to removal of mass faster than the crossing time of the cluster, leaving the cluster in a super-virial state for a few crossing times, or

(ii) adiabatic expansion, e.g. driven by stellar evolution on a slow timescale compared to the crossing time of the cluster ($\sim$ 10 Myr for YMCs), in which case the cluster remains in virial equilibrium. Thus, the best way to evaluate the importance of rapid gas expulsion (case i) and the implications for the formation and early evolution of star clusters is to determine the dynamical state of young clusters. In particular, it is important to verify if clusters are in virial equilibrium from a young age.

We summarize below the theory behind the gas expulsion phase. We start by considering the idealized case of instantaneous mass loss from a virialized system (Hills 1980), and then discuss how a more realistic treatment would change this picture. Assuming that the gas expulsion timescale $t_{\rm exp}$ is much smaller than the dynamical timescale $t_{\rm dyn}$ of the cluster, which is true for many young clusters (Portegies Zwart et al. 2010), then we can also assume that the mass loss is instantaneous and does not affect the positions and velocities of the stars in the system, so the velocity dispersion is the same after the impulsive mass loss as it was before. If the cluster was in dynamical equilibrium before the onset of gas expulsion, then its initial velocity dispersion can be derived from the virial theorem, which is simply

$$U + 2\ T = 0. \tag{1.6}$$

From the above equation, it is straightforward to show that the total energy is

$$\begin{aligned} E = U + T = U + \left(\frac{-U}{2}\right) = \frac{U}{2} \\ = -2\ T + T = -T, \end{aligned} \tag{1.7}$$

For an idealized cluster containing N stars of equal mass m, we have

$$U = -\sum_{\rm pairs} \frac{G\ m^2}{|\vec{r}_i - \vec{r}_j|} = -\frac{N(N-1)}{2}\frac{G\ m^2}{r_{\rm vir}}, \tag{1.8}$$

where $r_{\rm vir}^{-1} \equiv \langle |\vec{r}_i - \vec{r}_j|^{-1} \rangle$. $r_{\rm vir}$ is therefore an estimate of the average distance between particles in the system. For large values of N, we have $N(N-1) \approx N^2$. Thus,

$$U \approx -\frac{N^2}{2}\frac{G\ m^2}{r_{\rm vir}} = -\frac{GM^2}{2r_{\rm vir}}, \tag{1.9}$$

where we have used $M = Nm$.

If we assume that the velocities of stars are isotropic, then

$$\langle v_x^2 \rangle = \langle v_y^2 \rangle = \langle v_z^2 \rangle = \frac{1}{3}\langle v^2 \rangle, \tag{1.10}$$

and the mean-square velocity along the line-of-sight is then also $\langle v_r^2 \rangle = \frac{1}{3}\langle v^2 \rangle$. We can then write the kinetic energy term of equation 1.6 as

$$\begin{aligned} T = \frac{1}{2}\sum_i m_i v_i^2 &= \frac{m}{2} N \frac{\sum_i v_i^2}{N} \\ &= \frac{m}{2} N \langle v^2 \rangle \\ &= \frac{3}{2} M \langle v_r^2 \rangle \\ &= \frac{3}{2} M \sigma_{\rm 1D}^2 \ , \end{aligned} \tag{1.11}$$

where in the last step we have used the fact the mean-square line-of-sight velocity is in fact the square of the line-of-sight velocity dispersion (because the average line-of-sight velocity is zero). The same also applies to all other directions.

The virial theorem (equation 1.6) allows us to write the (3D) velocity dispersion prior to mass loss as

$$\sigma^2 = \frac{GM}{2r_{\rm vir}}. \tag{1.12}$$

Only a fraction of the gas is turned into stars during the collapse and fragmentation of a giant molecular cloud forming a star cluster (e.g. Lada & Lada 2003). This is described as the star formation efficiency and is simply

$$\epsilon \equiv \frac{M_{\rm stars}}{M_{\rm stars} + M_{\rm gas}}, \tag{1.13}$$

where $M_{\rm stars}$ and $M_{\rm gas}$ are the contributions from the stars and gas to the total initial mass of the system. We expect most of the residual gas to be expelled by stellar winds and supernovae, so we will assume here that the mass loss is $\Delta M = M_{\rm gas}$. We also assume that the distribution of the gas that is removed is homologous to the distribution

of the stars. The energy of the star cluster immediately after gas expulsion is

$$E = T + U = \frac{1}{2}\left[M_{\rm stars}\ \sigma^2 - \frac{GM_{\rm stars}^2}{r_{\rm vir}}\right]. \tag{1.14}$$

On a timescale comparable to $t_{\rm dyn}$ the cluster expands to find a new equilibrium radius $r_{\rm vir}^{\rm new}$ satisfying the virial theorem for this new energy. The total energy after virial equilibrium is reached again can be expressed in terms of the potential energy by the following equation

$$E = T + U = \frac{U}{2} = -\frac{GM_{\rm stars}^2}{4r_{\rm vir}^{\rm new}}. \tag{1.15}$$

We can use equations 1.12, 1.14, and 1.15 to relate the initial and final radius by the equation

$$\frac{r_{\rm vir}^{\rm new}}{r_{\rm vir}} = \frac{M_{\rm stars}}{M_{\rm stars} - M_{\rm gas}} = \frac{\epsilon}{2\epsilon - 1}, \tag{1.16}$$

which is illustrated with the red curve in Figure 1.5. The cluster expands to a new equilibrium radius because the velocity dispersion of the stars is too large for their new potential once the gas is removed. Note that stars with a velocity greater than the new escape velocity just after gas expulsion will be lost (e.g. Bastian & Goodwin 2006). The above argumentation is reasonable if the star formation efficiency is high ($\epsilon \gtrsim 0.5$), but equation 1.16 tells us that in the simple case discussed above, the system is disrupted if half of the mass of the system or more is lost instantaneously (i.e. $t_{\rm exp} \ll t_{\rm dyn}$). When $\epsilon \leq 0.5$, the equation indeed does not have a solution. In this case, the cluster cannot find a new equilibrium radius and is left in a super-virial state, implying that gas expulsion leads to the complete dissolution of the cluster in a few dynamical timescales. A similar behaviour is seen in N-body simulations, which show that in the case of instantaneous gas removal, clusters need to form with star formation efficiencies of $\epsilon \gtrsim 30\%$ in order to survive gas expulsion (e.g. Baumgardt & Kroupa 2007). In these simulations, the time needed for a cluster to completely dissolve, or to find a new virial equilibrium after gas expulsion, is about $\sim 20-30\ t_{\rm dyn}$, where $t_{\rm dyn}$ is the initial dynamical time (i.e. when both the gas and stars were still present). Note that it is possible for a bound core to remain even with $\epsilon < 50\%$, as stars escaping with high velocities can carry away a significant fraction of the energy of the cluster and leave the remaining stars more strongly bound (Baumgardt & Kroupa

2007). Also, because the dynamical timescale depends on the density, gas expulsion is less instantaneous in the core compared to the outskirts of a concentrated cluster. The stars in the core might therefore respond adiabatically (see below), which increases the survival probability of clusters.

Clusters with much lower star formation efficiencies of about 10% could also survive if the gas was not lost instantaneously but adiabatically ($t_{\rm exp} \gg t_{\rm dyn}$; Baumgardt & Kroupa 2007). In this case, the cluster stars can adjust to the change in potential even though a large fraction of the gas is lost, expanding through a series of virial equilibria. This is actually what happens as clusters lose mass through stellar evolution. If we go back to the result for the impulsive mass loss (equation 1.16) and assume a very small ΔM, then we can write

$$\frac{\delta r_{\rm vir}}{r_{\rm vir}} = \frac{\delta M}{M}, \tag{1.17}$$

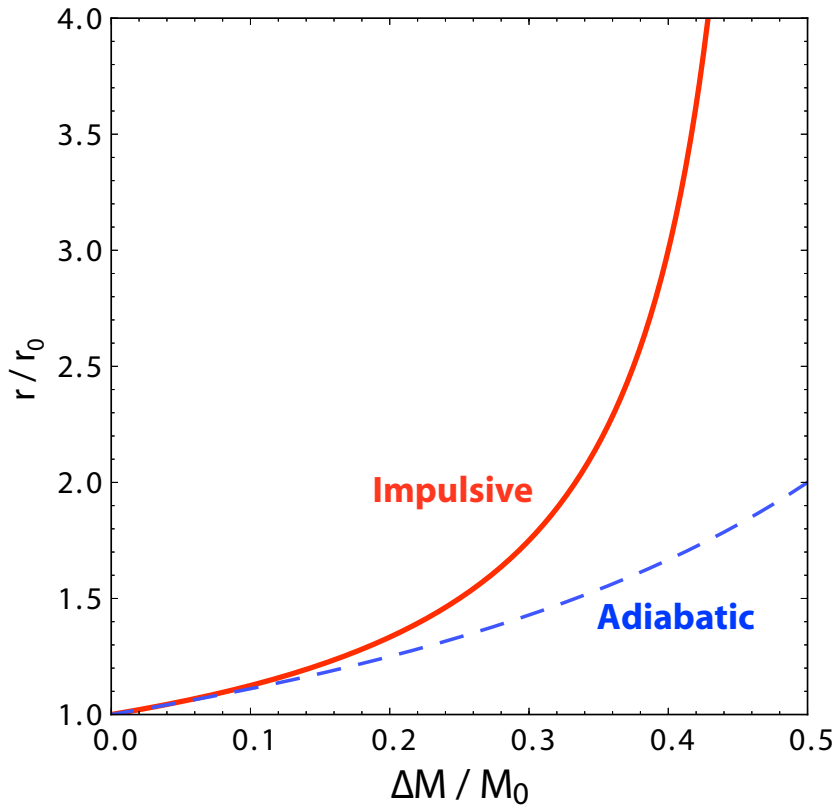

Figure 1.5 Illustration of the relative change in the radius of a cluster following impulsive mass loss (solid red line) and adiabatic mass loss (dashed blue line).

which is easily solved to obtain

$$\frac{r_{\rm vir}}{r_{\rm vir}(t=0)} = \frac{M(t=0)}{M}. \tag{1.18}$$

This result is illustrated with the blue curve in Figure 1.5. Even when losing half of the cluster mass through stellar evolution (which is roughly what is lost from a canonical initial mass function over a Hubble time), the cluster would only expand by a factor of two.

The discussion above might lead to believe that a low star formation efficiency could explain the majority of disrupted young clusters. However, in reality the physics of the gas expulsion phase is much more complex than suggested, and the models contain several simplifications and free parameters which can be tweaked to give different outcomes. These include not only the star formation efficiency, but also tidal fields, the exact timescale of gas removal, and the precise form of feedback responsible for gas removal (e.g. Baumgardt & Kroupa 2007; Baumgardt et al. 2008; Fall et al. 2010). Clearly this is a topic where observational constraints are welcome. A very useful constraint can come from verifying a simple prediction of the gas expulsion scenario: the fact that young clusters that have just cleared their natal gas should have been left super-virial and expanding for several crossing times.

The interest in gas expulsion as an explanation for infant mortality was partly stimulated by the observations of Bastian & Goodwin (2006). These authors found an excess of light at large radii in a number of extragalactic YMCs and interpreted it as a signature of an over-density of stars that could be a halo of unbound, escaping stars, resulting from gas expulsion. They fitted two analytical profiles to the observed luminosity profiles. The King template (King 1962) is commonly used to fit the luminosity profile of globular clusters, and the EEF profiles (Elson et al. 1987) have been shown to yield good fits for the structure of young clusters in the LMC as well as YMCs in distant galaxies (Larsen 2004). The fits were very good for both profiles at small radii, but clear excesses in the observed profiles were found at large radii (see Figure 1.6). Such excess light at large radii has also been found in many young LMC clusters (e.g. Mackey & Gilmore 2003) and in young clusters in the Antennae galaxies (Whitmore et al. 1999). This behavior is also seen in N-body simulations of clusters including the effects of gas removal, which show an unbound halo of stars that is removed, although still appearing to be associated with the cluster (Bastian & Goodwin 2006). These results must however be interpreted with care, as we are dealing (in most cases) with distant clusters in which stars are not resolved, and also

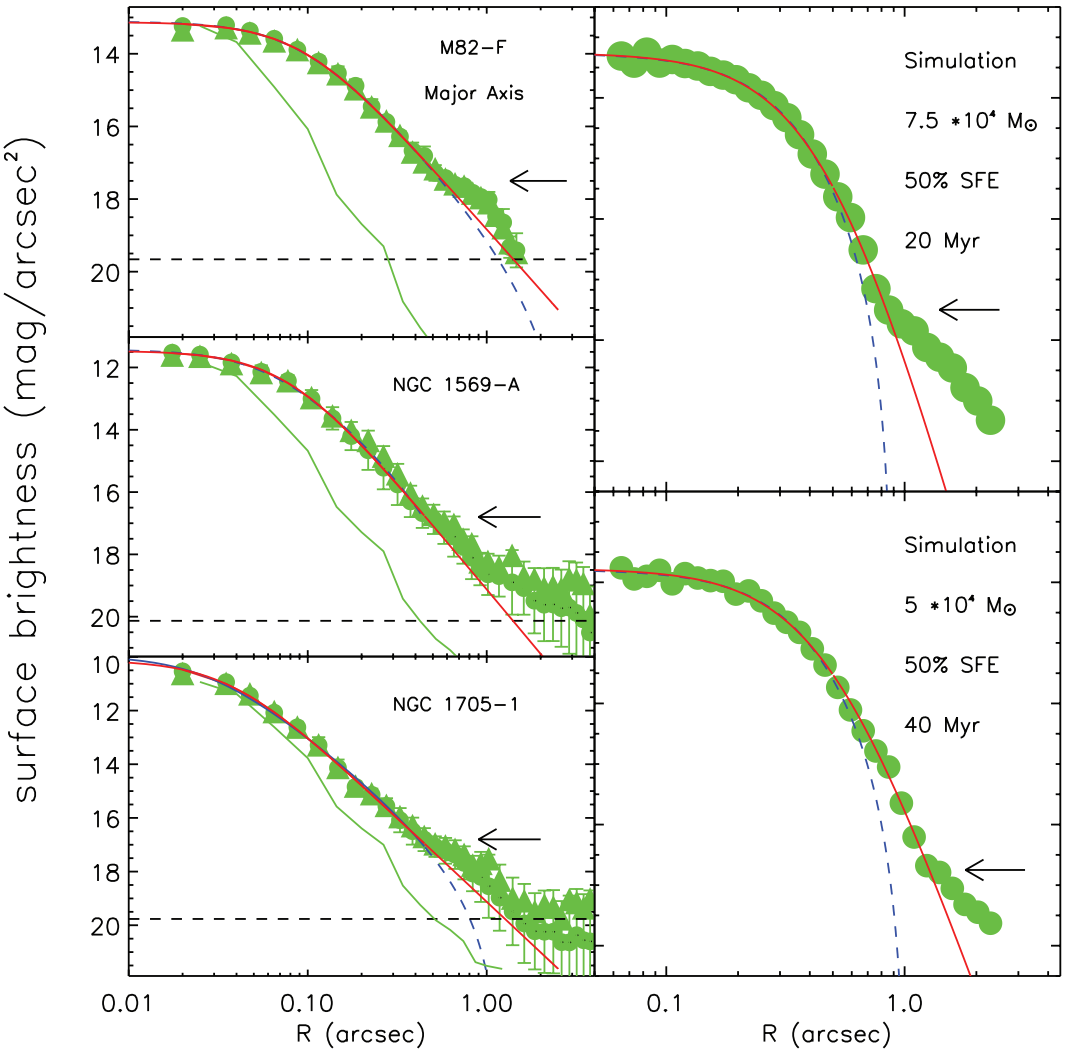

Figure 1.6 Surface brightness profiles for three young clusters (left) and two N-body simulations which include the rapid removal of gas which was left over from a non-100% star formation efficiency (right). The solid (red) and dashed (blue) lines are the best fitting EFF (Elson et al. 1987) and King (King 1962) profiles respectively. Figure reproduced from Bastian & Gieles (2006) and based on results from Bastian & Goodwin (2006).

because an excess of light at large radii can, at least in some cases, be interpreted as an additional component coming from a larger-scale OB association in which the young cluster would be located (see Chapter 3 for more details in the specific case of R136).

Attempts to determine the dynamical state of young clusters have been made by comparing dynamical masses (obtained through measuring the velocity dispersion and size of a cluster; see Section 1.3.3) and photometric masses (estimated from the age and integrated luminosity). For several unresolved extragalactic star clusters with ages of less than $\sim$ 10 Myr, the dynamical mass has been found to be up to ten times larger than the photometric mass (e.g. Bastian et al. 2006, see Figure 1.7). This led

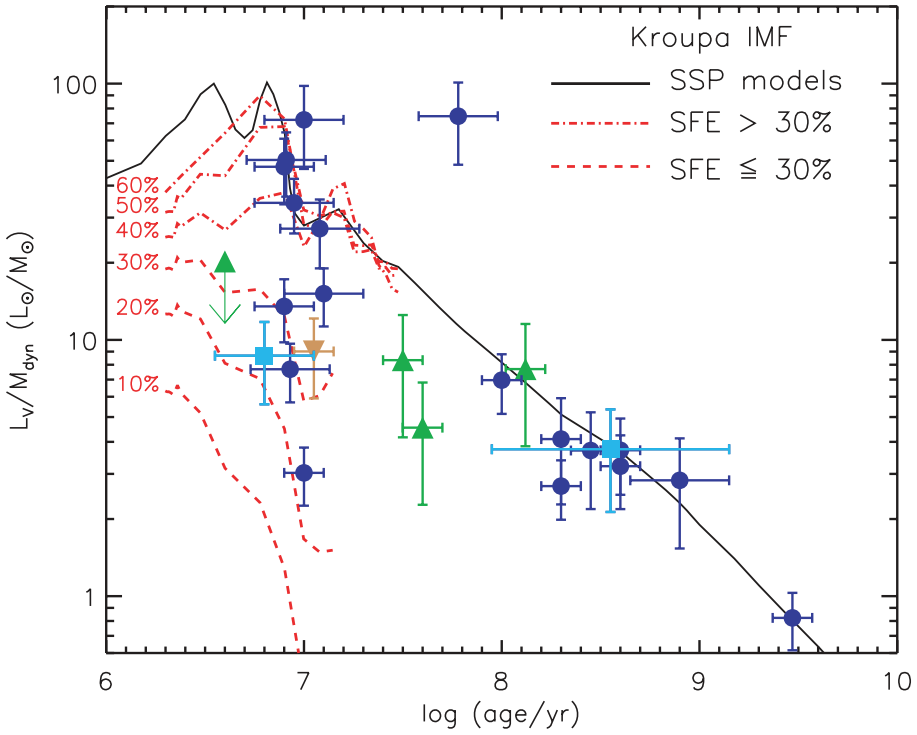

Figure 1.7 The light-to-dynamical mass ratio of young clusters (Figure from Goodwin & Bastian 2006). The solid (black) line is the prediction of simple stellar populations (SSPs) with a Kroupa stellar IMF and solar metallicity. The dashed and dash-dotted lines (red) are the SSP model tracks folded with the effects of rapid gas removal following non-100% star formation efficiencies. Dashed lines represent cases where the clusters would become completely unbound according to the simulations.

to the suggestion that these clusters might be super-virial and expanding following gas expulsion (Goodwin & Bastian 2006).

However, a more promising explanation is the contribution to the velocity dispersion from the internal orbital motions of massive binary stars, leading to an overestimate of the velocity dispersion. Kouwenhoven & de Grijs (2008) showed that for older open clusters, this effect can only account for at most a factor of ~ 2 increase of the dynamical mass, but the light of young star clusters at ~ 10 Myr is dominated by luminous red supergiants with initial masses $\sim 13 - 22$ $M_\odot$, which have a relatively high binary fraction. Gieles et al. (2010b) showed that the increase in the measured line-of-sight velocity dispersion in these young clusters could be produced by the orbital motions of massive binaries (Figure 1.8). This shows that the role of gas expulsion cannot be investigated unambiguously through observations of unresolved extragalactic clusters. It also highlights the importance of studying stellar dynamics in nearby YMCs, where individual stars can be resolved, in order to properly take binaries into account.

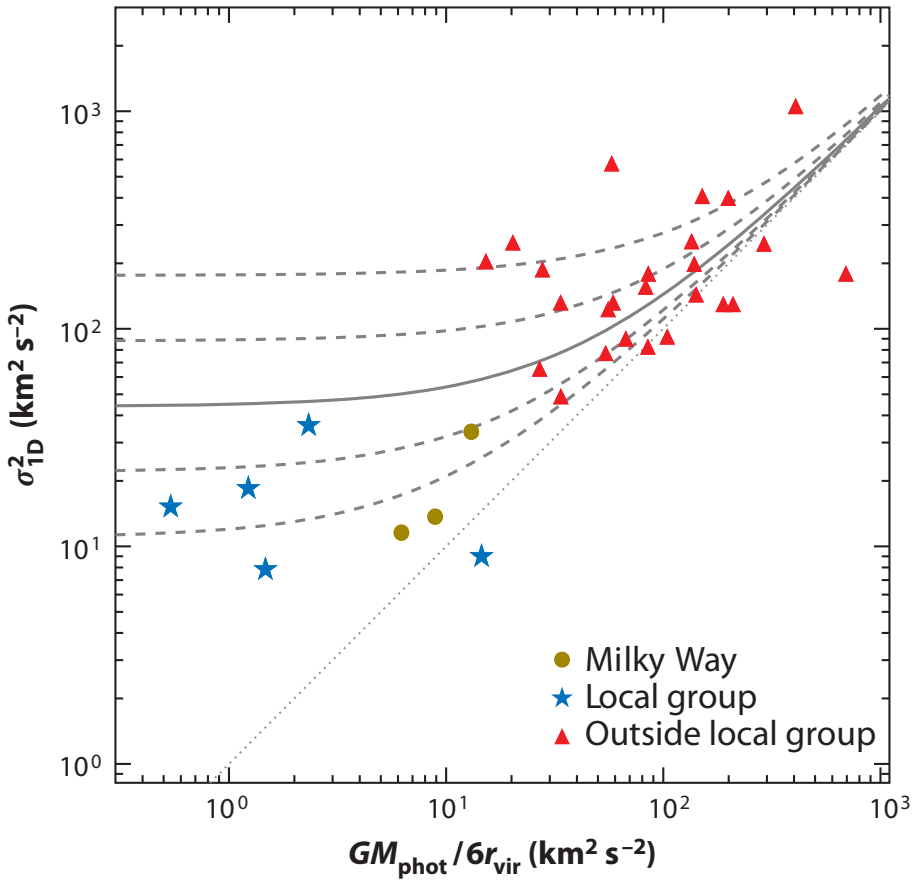

Figure 1.8 The measured velocity dispersion squared for the clusters of Figure 1.7, presented as a function of a prediction for this quantity (see the equation for the dynamical mass in Section 1.3.3). The solid line is a prediction of the effect of binaries on $M_{\rm dyn}$, with $1\,\sigma$ and $2\,\sigma$ variations due to stochastic fluctuations shown as dashed lines based on the results of Gieles et al. (2010b).

1.3.3 Weighing star clusters

We present here a few additional details on the determination of dynamical masses of clusters, which can be compared to photometric masses to probe the dynamical state of these systems and check the assumptions on which both results are based. As mentioned previously, the photometric mass ($M_{\rm phot}$) is obtained by converting the observed luminosity, age and distance directly to mass using the age dependent mass-to-light ratio (M/L) taken from an SSP model. This method requires an estimate of the cluster age, which itself also depends on the metallicity and stellar IMF. In young clusters, dominated by the light of massive stars, the lower-mass end of the IMF is not directly probed, and so the inferred $M_{\rm phot}$ depends on what is assumed for the IMF (through the M/L).

The equation for the dynamical mass ($M_{\rm dyn}$) can be obtained by simply combining equations 1.9 and 1.11 from above, and introducing the parameter $\eta \equiv 6r_{\rm vir}/r_{\rm eff}$, where $r_{\rm eff}$ is the effective (half-light) radius of the cluster, i.e. the distance from the cluster centre containing half of the total light in projection. This yields

$$M_{\rm dyn} = \eta \frac{\sigma_{\rm 1D}^2 \, r_{\rm eff}}{G}, \tag{1.19}$$

where $\sigma_{\rm 1D}$ is the line-of-sight velocity dispersion in the cluster, which is readily determined either through the broadening of spectral lines in integrated-light spectra, or through the measurement of the individual radial velocities of stars in the cluster. As discussed extensively in this thesis, the effect of binaries on $\sigma_{\rm 1D}$ must be taken into account, especially for young clusters, because massive stars tend to have a high binary fraction. The radius may be measured directly from images if the cluster is resolved, which is possible up to distances of $10 - 20$ Mpc with high-spatial resolution HST imaging. However, since bright massive stars dominate the light but contribute to a small fraction of the total mass, the observed $r_{\rm eff}$ can be considerably smaller than the half-mass radius if young clusters are mass segregated.

The constant η depends on the density profile. For example, for the Plummer model (Plummer 1911), which is often used for the construction of initial conditions for N-body models because of its analytical convenience, it can be shown that the ratio of $r_{\rm vir}$ and $r_{\rm eff}$ is such that $\eta \simeq 10$. It turns out that a similar value of $\eta = 9.75$ is commonly used in dynamical mass estimates, as a variety of reasonable models providing good fits to the observed profile also yield values of η close to 10. In that case, we can rewrite equation 1.19 in the following form

$$M = 1.2 \times 10^6 \left(\frac{\sigma_{\rm 1D}}{10 \text{ km/s}} \right)^2 \left(\frac{r_{\rm eff}}{5 \text{ pc}} \right) M_\odot. \tag{1.20}$$

In Figure 1.9, we show the dependence of η on the parameter γ in an EFF surface brightness profile (Elson et al. 1987). As mentioned previously, the observed profiles of LMC clusters are well represented by EFF profiles, which have cores and power-law halos and are defined as

$$\Sigma(r) = \Sigma_0 \left(1 + \frac{r^2}{a^2} \right)^{-\gamma/2}, \tag{1.21}$$

where a is a scale parameter. A Plummer (1911) density profile has $\gamma = 4$ (see

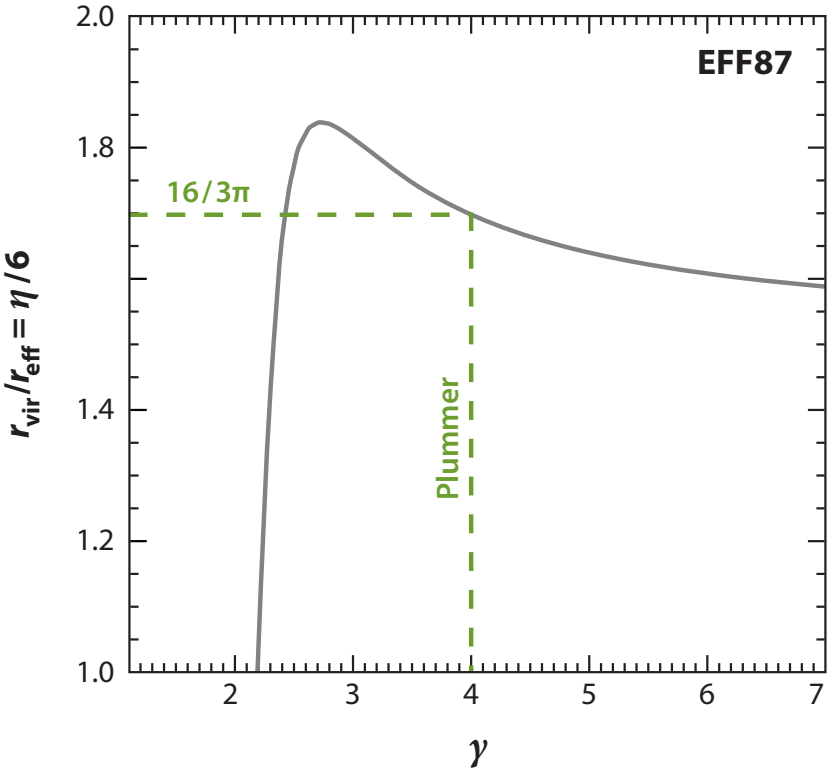

Figure 1.9 The dependence of η (related to $r_{\rm vir}/r_{\rm eff}$) on the slope γ of the EFF profile. η is used to convert an observed line-of-sight velocity dispersion and half-light radius into a dynamical mass. Figure from Portegies Zwart et al. (2010).

Figure 1.9). For $\gamma \leq 2$, the mass of the EFF profile diverges, and for $\gamma \lesssim 2.5$, the ratio $r_{\rm vir}/r_{\rm eff}$ drops rapidly, illustrating that care must be taken when applying the dynamical mass equation, especially for clusters with shallow density profiles. A typical range for the power-law index is $2.2 \lesssim \gamma \lesssim 3.2$ for LMC clusters (Mackey & Gilmore 2003). Similar slopes are also found for extragalactic clusters (Larsen 2004). Finally, we note that mass segregation can also have a severe effect on η, resulting in a variation of more than a factor of ~ 3 (Fleck et al. 2006).

1.3.4 The rotation of star clusters

Early studies of the structure and morphology of Galactic globular clusters (GCs) have shown that the small deviations from spherical symmetry observed in this class of stellar systems are frequently initiated by the presence of internal rotation (e.g., see Geyer et al. 1983; White & Shawl 1987). Even if their shape appears nearly spherical, Milky Way GCs rotate with amplitudes up to half the 1D velocity dispersion ($0 \lesssim V_{\rm rot} \sin i \, / \sigma_{\rm 1D} \lesssim 0.5$, e.g. Meylan & Heggie 1997), so their amount of rotational energy is typically not dominant but also not negligible. If clusters rotate from a young age, it can have

important consequences on their dynamical evolution. Numerical simulations have indeed shown that rotation can accelerate the dynamical evolution of star clusters by speeding up the collapse of the core through the gravogyro instability or by significantly increasing the escape rate for clusters in a strong tidal field (e.g. Einsel & Spurzem 1999; Kim et al. 2002; Ernst et al. 2007; Hong et al. 2013).

Most of the rotational signatures are found through radial velocity (RV) studies, but rotation has also been confirmed in the plane of the sky for ω Centauri and 47 Tucanae from proper motion studies (van Leeuwen et al. 2000; Anderson & van der Marel 2010, respectively). RV studies are now able to measure rotational amplitudes in GCs below 1 $\mathrm{km\,s^{-1}}$ and despite these precise measurements there are some clusters in which no rotation has been detected (e.g. Lane et al. 2010c), although this could also be an inclination effect.

The physical origin of the internal rotation measured in these old clusters is still unclear, as the role played by angular momentum during the initial stages of star cluster formation is only partly understood. N-body simulations of the merging process of two star clusters have shown that the resulting stellar system may be characterized by a significant amount of global angular momentum (Makino et al. 1991; Baumgardt et al. 2003). Therefore, in some cases, the presence of relatively strong internal rotation has been interpreted as a signature of a past merger event (for a recent example, see Lane et al. 2010a).

In turn, rotation in clusters could be imprinted during their formation process. In the context of a formation scenario by dissipationless collapse, relatively few investigations have considered the role of angular momentum in numerical experiments of "violent relaxation" (Gott 1973; Aguilar & Merritt 1990). In this respect, giant molecular clouds (GMCs), the birth sites of young massive clusters, have been observed to rotate (e.g. Rosolowsky et al. 2003), but we do not know if this translates into significant rotation in clusters.

Observational input is now getting sufficiently abundant to look for correlations between rotational amplitude and other cluster properties. Bellazzini et al. (2012) report a correlation between horizontal branch (HB) morphology and $V_{\mathrm{rot}} \sin i \,/\sigma_{\mathrm{1D}}$ in a sample of 20 globular clusters. Given that metallicity is the first parameter determining HB morphology, this in turn suggests a correlation between $V_{\mathrm{rot}} \sin i \,/\sigma_{\mathrm{1D}}$ and metallicity, such that clusters with higher metallicity have greater fractions of energy in rotation. Since a higher metallicity in a gas implies a higher efficiency of energy dissipation by atomic transitions, this then hints at a significant role of dissipation in the process of

cluster formation (e.g. Bekki 2010).

Mackey et al. (2013) recently detected a significant degree of systemic rotation in the intermediate-age LMC cluster NGC 1846, which also shows an extended main-sequence turnoff suggested to be linked to the formation of multiple stellar generations. They argued that their observations are in qualitative agreement with the predictions of simulations modeling the formation of multiple populations of stars in globular clusters, where a dynamically cold, rapidly rotating second generation is a common feature. While somewhat speculative, this is nevertheless interesting. The points discussed above certainly suggest that rotation may be intimately linked to the formation of clusters.

1.4 Massive stars and binaries

As previously mentioned, the study of YMCs is naturally connected to the study of massive stars, which dominate the light of these systems with their high luminosities. Massive stars are commonly defined as those with an initial mass of more than about 8 $M_\odot$, the limit above which they end their life in core-collapse supernovae (as opposed to white dwarfs for intermediate and low-mass stars). This includes stars of spectral type O and B, as well as their evolved phases like Luminous Blue Variables (LBVs) and Wolf-Rayet stars. The most common system of modern spectral classification builds upon that of Morgan et al. (1943), MK, which uses a scheme with letters and numbers to define spectral types/subtypes and roman numerals to refer to the luminosity class. For more massive stars (O and early B), this scheme was first modified and defined by Walborn (1971) and Conti & Alschuler (1971). Intermediate-mass stars of $\lesssim 8$ $M_\odot$ correspond roughly to spectral types B1.5 or cooler on the main sequence. Thus, stars with O and early B spectral types are the ones which we are concerned with in this thesis. We will not review the extensive literature on the spectral classification of OB stars since the early 1970s, but simply mention that spectral classification is a useful way to estimate some of physical properties of massive stars from the morphology of their spectral lines when a detailed atmospheric analysis is not available or possible, although the relation between spectral types/subtypes and physical properties is not necessarily straightforward.

Massive stars are both rare and short-lived. There is indeed only about one O-type star for every 10 000 solar-type stars and the most massive stars only live a few million years (e.g. Conti et al. 2008). Nevertheless, it is these rare massive stars that dominate the

ecology of the Universe by shaping the dynamical and chemical evolution of galaxies. Via their intense ionizing radiation fields, their fast and dense stellar winds, and ultimately their spectacular death as core-collapse supernovae, they effectively act as powerful cosmic engines by injecting heavy elements and energy into the surrounding medium. They play a central role in a broad range of astrophysical situations, not only locally but also in the distant Universe. For example, numerical simulations of the collapse of primordial gas clouds suggest that the first generation of stars in the history of the universe (Population III stars) was biased towards high mass stars (Bromm et al. 1999). The deaths of massive stars appears to be connected to long-duration gamma-ray bursts (GRBs) as several nearby GRBs show the signature of a massive star undergoing core-collapse (Woosley & Bloom 2006). Massive stars dominate the rest-frame ultraviolet spectra of star-forming Lyman-break galaxies at high redshifts (Douglas et al. 2010), and it is even thought that they could have been a major factor in the reionization of the early Universe (Haiman & Loeb 1997). All tracers of star formation also rely on massive stars in one way or another (e.g. Conti et al. 2008).

One of the most important aspects of massive stars, which has consequences on many of the topics outlined above, can be summarized very simply: most O- and early B-type stars are found in binaries and multiple systems. The multiplicity fraction of massive stars (see e.g. Sana & Evans 2011) appears even higher than that of solar-type stars (Duquennoy & Mayor 1991). Even single massive stars may well have been part of a multiple system in the past, before being ejected by a supernova kick or dynamical interaction, or even merging with their companion. It is important to take into account this high binary fraction in models of star formation and stellar evolution. In particular, if the stars in a binary system are sufficiently close to interact during their lifetime (through stellar winds, expansion, tides, mass transfer, and mergers), this can have a significant impact on their physical properties, for example on their rotation rate (e.g. de Mink et al. 2013), which itself is thought to be a major factor in the evolution of massive stars. As emphasized throughout this thesis, it is also crucial to take into account the multiplicity of massive stars when studying the kinematics of YMCs.

More in-depth discussions of the binary fraction and orbital parameters of massive stars, as well as their effect on the kinematics of young clusters, will be presented in later chapters. We present here some basic background information that will be useful to understand the typical parameter space that we are investigating in the studies presented in this thesis.

Binary systems can be divided into four main groups: (1) visual binaries, in which

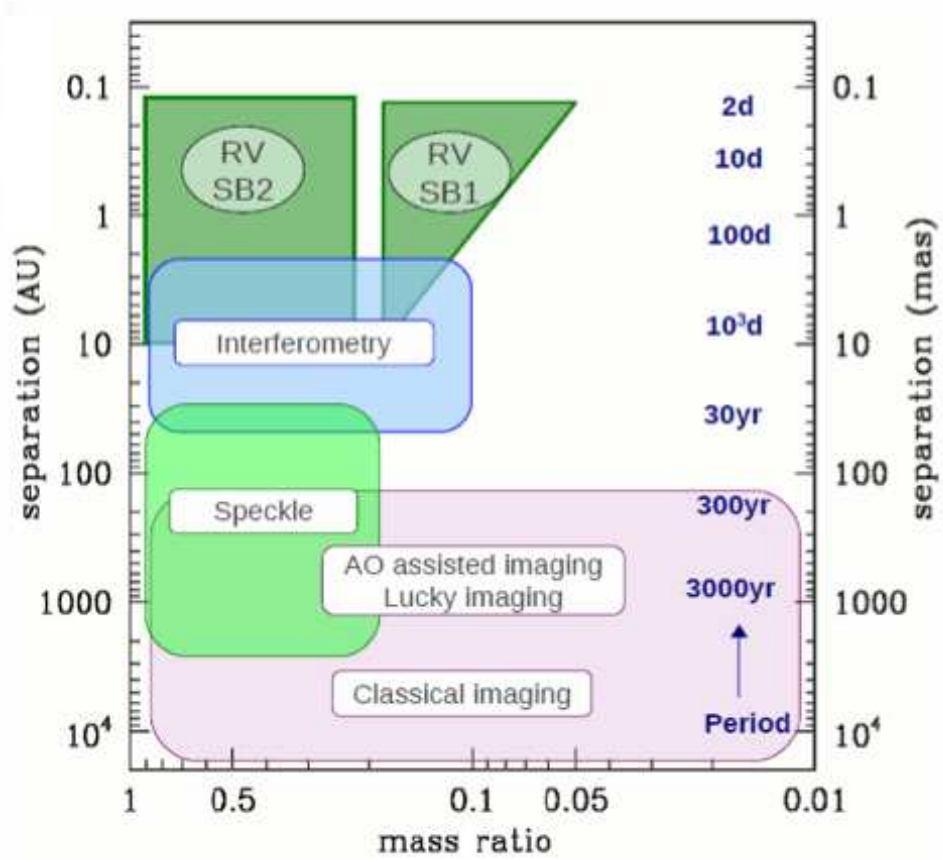

Figure 1.10 Typical parameter space for massive binaries, assuming a primary of 40 $M_\odot$ *at a distance of 1 kpc.* The relevant regions for various detection techniques are overlaid. Figure reproduced from Sana & Evans (2011).

individual stars can be resolved, (2) eclipsing binaries, where one star passes in front of the other and causes a variation in the observed magnitude, (3) single-lined spectroscopic binaries (SB1), in which periodic Doppler shifts of spectral lines due to orbital motions can be seen in the more luminous of the two stars while its companion remains undetected, (4) double-lined spectroscopic binaries (SB2), in which the lines of two distinct stars are seen in the spectrum, and these sets of lines are seen to shift with respect to each other due to the relative motion of the two stars in the system.

The different types of binary systems can be probed with different techniques. While many parameters are needed to describe the orbit of a binary, the two main parameters influencing their detection are the separation (or equivalently the orbital period) and the mass ratio of the two components. Figure 1.10 (from Sana & Evans 2011) illustrates the regions of parameter space that can be probed by different observing techniques for a typical binary with a primary mass of 40 $M_\odot$ at a distance of 1 kpc. This assumes that observations with appropriate time sampling are available, and ignores the (smaller)

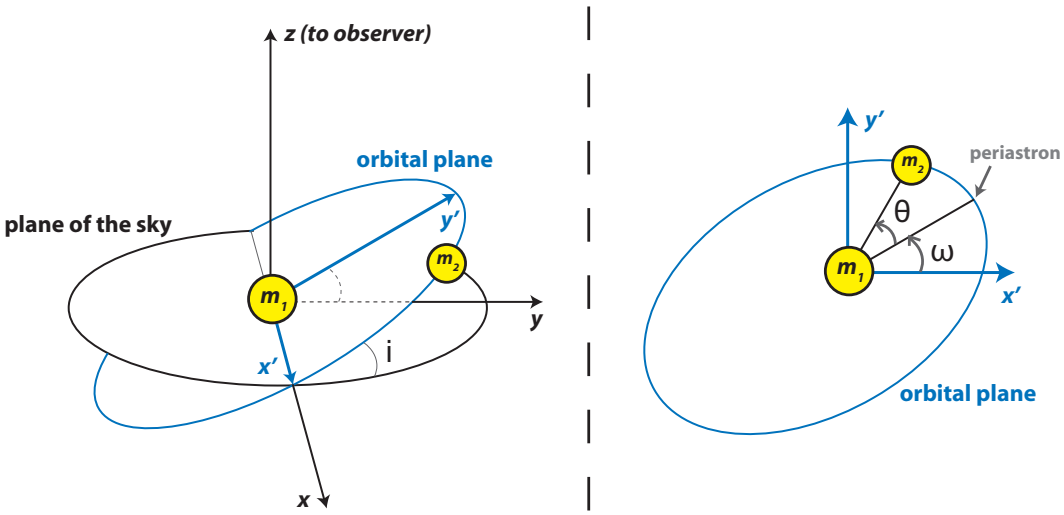

Figure 1.11 Schematic representation of the orbital parameters of a binary system. See the main text for the definition of these parameters.

effect of orbital inclination and eccentricity on the detection probability. The techniques considered include radial velocity studies from spectroscopy, interferometry, speckle interferometry, adaptive optics assisted imaging, lucky imaging, and classical imaging. Note that at the distance of the LMC (50 kpc), only radial velocity studies are still able to detect close binaries and are not influenced by the larger distance (as long as the quality of the spectra obtained is good enough for radial velocity measurements). All the other techniques would only be sensitive to much larger separations than indicated in Figure 1.10 (which assumes a distance of 1 kpc). The radial velocity studies considered in this thesis can generally detect binaries with mass ratios between 0.1 and 1, and orbital periods between ~ 1 and 10^3 days.

To fully describe the orbit of a binary system, which will be useful in later chapters to assess their contribution to the kinematics of clusters, several orbital parameters are needed (see Figure 1.11 for a schematic representation). These parameters are:

- P: the orbital period.
- e: the orbital eccentricity.
- ω: the argument of periastron.
- i: the orbital inclination.
- θ: the true anomaly (or equivalently T, the time of periastron passage). θ is a function of the orbital phase $(t - T)/P$, where t is the time of the observation.
- m_1: the mass the primary.

- q: the secondary to primary mass ratio (m_2/m_1).

The radial velocity of the primary (as we will be mainly concerned with SB1 systems) with respect to the centre of mass of the system then varies as:

$$V_{r,1} = \left(\frac{2\pi G}{P}\right)^{1/3} \frac{m_2 \sin i}{m_1^{2/3}} \frac{1}{\sqrt{1-e^2}} \left[\cos\left(\theta + \omega\right) + e\cos\left(\omega\right)\right]. \tag{1.22}$$

The detection of spectroscopic binaries is obviously biased towards systems showing large radial velocity shifts. From the equation above, we can see that these will preferentially be systems with close to edge-on orientations, short periods, and with components of similar mass. Low inclinations or long-period binaries, on the other hand, produce smaller radial velocity shifts that are harder to detect. Eccentricity can also introduce biases if only a fraction of the orbit is sampled.

In practice, when simulating radial velocity shifts introduced by a population of binaries, we can simplify the choice of orbital parameters above by assuming that the orbital plane is randomly oriented in three-dimensional space, and also by assuming that the time of periastron passage is uncorrelated with respect to the time at which the radial velocity is measured.

1.5 This thesis

Despite their importance in a wide range of astrophysical situations, many questions still persist about the evolution of massive stars and clusters. Using data from the VLT-FLAMES Tarantula Survey, this thesis addresses some of these questions. The main chapters focus on the kinematics of young massive clusters, with an emphasis on the analysis of spectroscopic data of massive stars in Radcliffe 136 (R136; Feast et al. 1960). This cluster is by far the youngest massive cluster in the Magellanic Clouds and has often been suggested as a globular cluster in formation (e.g. Kennicutt & Chu 1988). Its study promises to provide great insight into the earliest dynamical evolution of YMCs.

After introducing the VLT-FLAMES Tarantula Survey and presenting the data reduction procedures performed in the context of this thesis in Chapter 2, a detailed study of the kinematics of R136 is presented in Chapter 3. This work looks at the initial conditions for the longer-term evolution of such a young massive cluster. In particular, we address whether the assumption of virial equilibrium used in all studies

of star clusters is justified. We also use this study of a resolved young massive cluster to evaluate the importance of gas expulsion in early cluster evolution. In order to obtain the first measurement of the velocity dispersion of R136, we analyse multi-epoch spectroscopic data of the inner regions of 30 Doradus in the LMC obtained as part of the VLT-FLAMES Tarantula Survey. Following a quantitative assessment of the variability, we use the radial velocities of non-variable sources to place an upper limit of 6 $\mathrm{km\,s^{-1}}$ on the line-of-sight velocity dispersion of stars within a projected distance of 5 pc from the centre of the cluster. After accounting for the contributions of undetected binaries and measurement errors through Monte Carlo simulations, we conclude that the true velocity dispersion is likely between 4 and 5 $\mathrm{km\,s^{-1}}$ given a range of standard assumptions about the binary distribution. This result is consistent with what is expected if the cluster is in virial equilibrium, suggesting that gas expulsion has not had a dramatic effect on its dynamics. We find that the velocity dispersion would be ~ 25 $\mathrm{km\,s^{-1}}$ if binaries were not identified and rejected, confirming the importance of the multi-epoch strategy and the risk of interpreting velocity dispersion measurements of unresolved extragalactic YMCs.

After having clearly illustrated the large effect of massive binaries on the observed line-of-sight velocity distribution of R136 and with a measurement of its true velocity in hand from our multi-epoch approach, we then use our data and results to test an alternative method of determining the velocity dispersion of a cluster (Chapter 4). Cottaar et al. (2012b) presented a maximum likelihood procedure to recover the true velocity dispersion of a cluster from a single epoch of radial velocity data by simultaneously fitting the intrinsic velocity distribution of the single stars and the centres of mass of the binaries along with the velocity shifts caused by orbital motions. They showed that this procedure can accurately reproduce velocity dispersions below 1 $\mathrm{km\,s^{-1}}$ for solar-type stars. We test this method using Monte Carlo simulations and our stellar radial velocity data in R136 as an example for which the velocity dispersion of O-type stars is known from a multi-epoch approach, taking into account the large uncertainties in the binary orbital parameter distributions of OB stars. For typical velocity dispersions of young massive clusters ($\gtrsim 4$ $\mathrm{km\,s^{-1}}$) we demonstrate that the method can distinguish between a cluster in virial equilibrium and an unbound cluster despite the higher spectroscopic binary fraction and more loosely constrained distributions of orbital parameters of OB stars compared to solar-type stars. This offers a promising mean of estimating the velocity dispersion of the massive star population in other young clusters and associations, in particular in YMCs, whose light is dominated by OB stars.

In Chapter 5, our radial velocity measurements of apparently single stars in R136 are used to investigate the internal rotation of the cluster. Although it has important ramifications for both the formation of star clusters and their subsequent dynamical evolution, rotation remains a largely unexplored characteristic of young star clusters (few Myr). From the radial velocities of 36 apparently single O-type stars within a projected radius of 10 pc from the centre of the cluster, we find evidence, at the 95% confidence level, for rotation of the cluster as a whole. We present a simple maximum likelihood method to fit simple rotation curves to our data, which we argue improves upon the method traditionally used to detect and quantify rotation in clusters. We apply this method to find a typical rotational velocity of $\sim$3 km s^{-1}. When compared to the low velocity dispersion of R136, these result suggests that star clusters may form with at least $\sim$20% of their kinetic energy in rotation.

After having looked at the effect of a population of massive binaries on the kinematics of young massive clusters in the first part of this thesis, we then turn our attention to an individual massive binary system in Chapter 6. The discovery of this system was made as part of a survey of massive stars in a young star-forming region in the Wing of the Small Magellanic Cloud (SMC). The survey is introduced, and the properties of this new Be/X-ray pulsar binary are presented. The strong pulsed X-ray source was discovered with the Chandra and XMM-Newton X-ray observatories. The X-ray pulse period of 1062 s is consistently determined from both Chandra and XMM-Newton observations, revealing one of the slowest rotating X-ray pulsars known in the SMC, and the optical counterpart is confirmed as a Be star from optical spectroscopy. The detection of a shell nebula around the system is also presented and identified as a supernova remnant, from which the age of the pulsar is estimated to be $(2-4) \times 10^4$ yr. The peculiar properties of the system (the young age and long spin period of the pulsar) are discussed as well as the challenges they pose to our understanding of the spin evolution of accreting neutron stars.

While Chapter 6 may seem slightly disconnected from the main focus of this thesis, it provides a nice example of the particularly interesting massive binaries that can be revealed by spectroscopic surveys of young clusters and star-forming regions. It also serves as a reminder of the importance of understanding binarity among massive stars, not only for the dynamics of clusters, but also to understand stellar evolution and the fate of massive stars. Be/X-ray binaries are clear manifestations of the interplay between binary interaction and the rotation of massive stars. There is indeed compelling evidence that the Be star in such systems has been spun up by mass transfer from the progenitor of the neutron star (see de Mink et al. 2013).

Finally, the main results from this thesis are summarized in Chapter 7, along with possible avenues for future research directly inspired by these results.

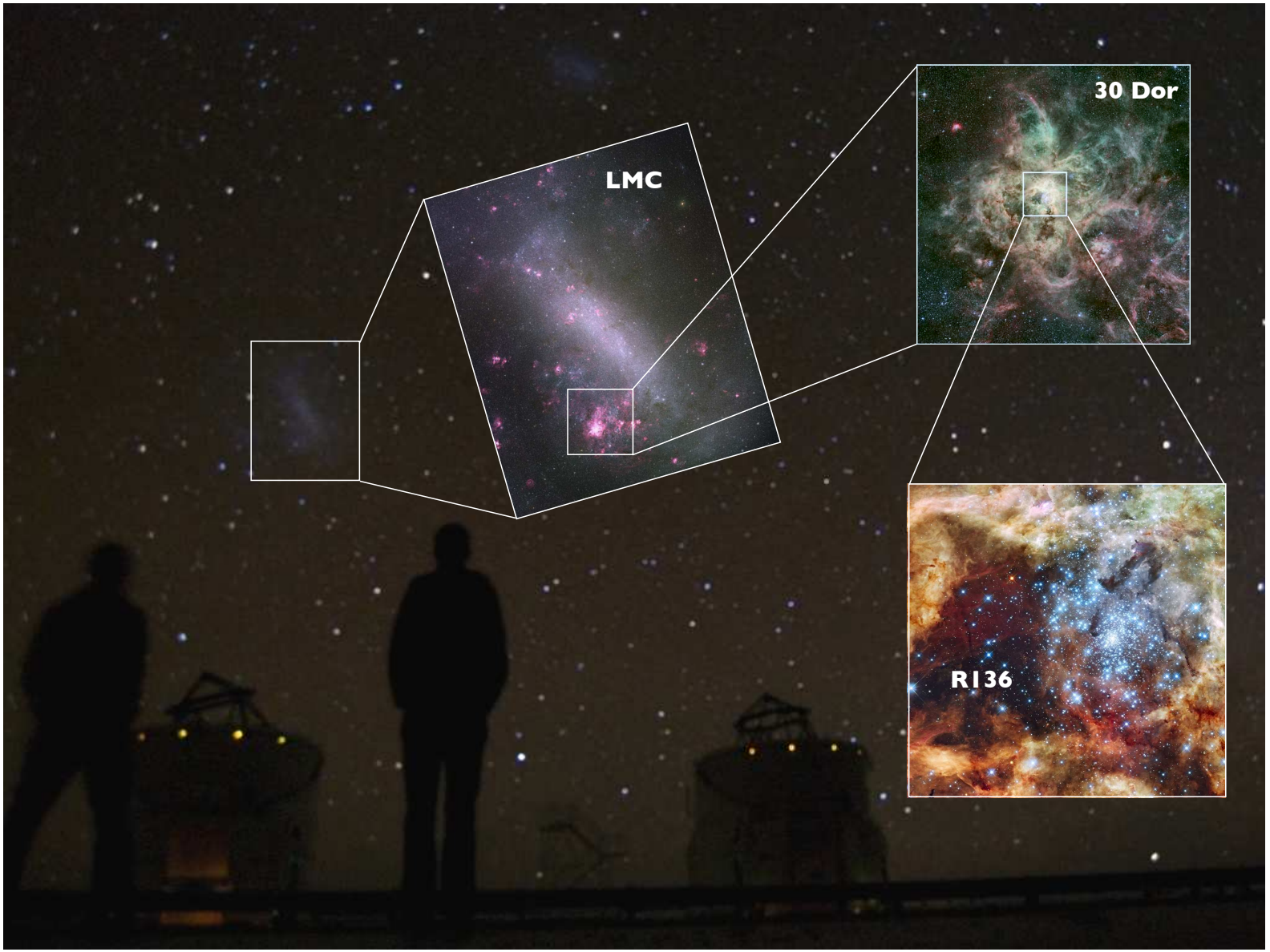

Night sky from Cerro Paranal with close-ups on the LMC, 30 Doradus, and R136. The images of the LMC, 30 Doradus, and R136 are respectively from the Anglo-Australian Observatory, ESO's WFI on the 2.2-m ESO/MPG Telescope, and HST WFC3.

Chapter 2

Spectroscopic surveys of massive stars: overview and data reduction

2.1 Introduction

Our understanding of massive stars has improved significantly in recent years, notably because of large surveys like the VLT-FLAMES Survey of Massive Stars (FSMS) and parallel theoretical developments (e.g. Evans et al. 2008). Yet, many fundamental questions persist regarding their formation, evolution, and impact on their environment. The VLT-FLAMES Tarantula Survey (VFTS; Evans et al. 2011) has been designed to address many key outstanding questions about massive stars and the early evolution of massive clusters. It targets the intricate 30 Doradus region in the LMC, a star-forming region hosting hundreds of massive stars and home to the young massive cluster R136.

In this chapter, we review the motivations behind spectroscopic surveys of massive stars, with an emphasis on the VFTS, on which the main part of this thesis is based. Some highlights from the VFTS relevant to the formation and dynamics of massive star clusters are presented. We also introduce the datasets used in the following chapters and describe the data reduction procedures performed.

2.2 The VLT-FLAMES Survey of Massive Stars

Before describing the VFTS, we first briefly review its predecessor. The FSMS was an ESO Large Programme which provided important insights into the evolution of massive

stars. It was specifically designed to understand the rotational velocities, rotational mixing and mass loss of these stars in different metallicity environments. To obtain these crucial constraints on massive star evolution, high-quality spectra of over 800 stars in seven stellar clusters of the Milky Way and Magellanic Clouds were gathered with the Fibre Large Array Multi-Element Spectrograph (FLAMES; Pasquini et al. 2002) on the Very Large Telescope (VLT), for a total of over 100 hours (Evans et al. 2005a,b, 2006). Over 50 O-type stars and over 500 B-type stars were observed. This sample of massive stars of unprecedented size, along with the theoretical developments that it catalysed, made the following breakthroughs possible.

The first highlight of the FSMS was to provide quantitative evidence for the reduced wind intensities of massive stars at lower metallicities. The driving mechanism for the relatively dense winds observed in massive stars is now commonly accepted to be the transfer of momentum from the radiation field of the star to metallic ions in their extended atmospheres (Castor et al. 1975). A corollary of that theory is that the intensity of the outflows should vary with metallicity, a prediction quantified by Vink et al. (2001). The SMC and LMC are considered as metal-poor, with metallicities of respectively $\sim$ 25% and $\sim$ 50% of the solar metallicity. An atmospheric analysis of the O-type stars in the survey yielded estimates for their temperature, luminosity, helium abundance, as well as for the velocity structure and mass-loss rate of the wind. From this it was shown that the wind intensities of LMC O-type stars are intermediate to those of O-stars in the SMC and Milky Way (Mokiem et al. 2006, 2007a,b). The observational confirmation of this effect has fundamental implications in many areas of astrophysics. For example, because their mass-loss rates are lower, O-type stars in lower metallicity environments should lose less angular momentum over the course of their evolution. It is thus expected that a larger fraction of these stars would undergo chemically-homogeneous evolution (e.g. Meynet & Maeder 2000), which has been proposed as a channel for the progenitors of long-duration GRBs (e.g. Yoon et al. 2006). Such chemically-homogeneous evolution may drastically affect age estimates for the youngest star clusters. Understanding the dependence of stellar winds on metallicity is also a necessary step to predict the properties of Population III stars, which must have had very low metallicities.

As we just glimpsed, rotation is a key factor influencing the evolution of massive stars. Models of the interiors of massive stars that include the effects of stellar rotation predict surface enhancements of nitrogen and helium, which should be higher for higher masses and rotational velocities (e.g. Meynet & Maeder 2000; Brott et al. 2011). A good understanding of the surface enrichment of these stars is therefore useful to

constrain their evolutionary paths. The atmospheric analysis of about 400 B-type stars observed in the LMC and SMC as part of the FSMS allowed to determine their physical parameters, rotational velocities, and nitrogen abundances (Trundle et al. 2007; Hunter et al. 2007, 2008a,b). This showed that SMC stars are characterised by faster rotational velocities (Hunter et al. 2008b), supporting the idea that stars should rotate faster at lower metallicity. It also surprisingly revealed that rotational mixing alone cannot account for the observed nitrogen abundances in massive stars. Some very slowly rotating stars show significant nitrogen enrichment, while some rapidly rotating seem to have undergone very little chemical mixing. This poses challenges to the theory and suggests that other mechanisms like binary interactions and the effect of magnetic fields are probably important (Hunter et al. 2008a).

We outlined above only some of the results that were obtained as part of the FSMS, which themselves represent only a fraction of the advances made in massive star research in recent years. Those FSMS results illustrate the power of large surveys of massive stars and the advantage of gathering statistically significant samples of these otherwise rare objects. They however also highlight the fact that several aspects of the evolution of massive stars are still not well understood.

2.3 The VLT-FLAMES Tarantula Survey

Building on the success of the FSMS, but also motivated by the many fundamental questions that it contributed to raise, a new survey was designed. The VFTS (Evans et al. 2011), another ESO Large Programme with a total of 160 hours of observing time, is a multi-epoch spectroscopic survey of over 800 massive stars (including ~ 300 O-type stars) in the 30 Doradus star-forming region of the LMC.

2.3.1 30 Doradus

30 Doradus ("30 Dor"), also often referred to as the Tarantula Nebula, is the best studied and arguably the most famous giant H II region. Located to the north-east of the main LMC disk, it is also the nearest extragalactic giant H II region. With a total stellar mass in excess of $\sim 10^5$ $M_\odot$, 30 Dor is one of the largest concentrations of massive stars and one of the largest star-forming regions in the Local Group (e.g. Conti et al. 2008), making it a prime target to understand unresolved young stellar populations, star formation, and starburst phenomena much farther away. At its centre, the young massive cluster R136 harbors the largest known concentration of O2-3 stars (Melnick

1985; Parker 1993; Walborn & Blades 1997; Massey & Hunter 1998; Walborn et al. 2002a) as well as several hydrogen-rich Wolf-Rayet (WN-type) stars, some of which are thought to have current masses in excess of 150 $M_{\odot}$ (Crowther et al. 2010). These densely packed hot stars are responsible for illuminating the surrounding gas with their ionising radiation that is absorbed and re-emitted in a rich nebular emission spectrum.

Note that a distinction is often made between the 30 Doradus region and the 30 Doradus nebula. The "region" ($\sim$ 1 kpc in diameter) comprises all the stars and nebulosities visible on deep images and thought to be physically related to the star formation event in the surroundings, while the "nebula" ($\sim$ 200 pc in diameter) defines the location of the bulk of the ionised gas (Conti et al. 2008). The 30 Dor nebula is sometimes referred to as NGC 2070, but more often this designation is used to refer to the centre of 30 Dor ($\sim$ 40 pc in diameter) where most of the ionising radiation originates. This central region is in turn commonly called the NGC 2070 or 30 Doradus "cluster", but this designation is misleading as the region is typically younger than its crossing time (assuming an age of a few Myr and a velocity dispersion similar to that found in Chapter 3 for R136) and therefore, strictly speaking, cannot be considered as a cluster according to the definition discussed in Chapter 1. We argue in Chapter 3 that only the inner $\sim$ 5 pc of R136, where the age of stars exceeds the crossing time, can realistically be referred to as being bound. Finally, R136a (the very central region of R136; 0.25 pc in diameter) is the smallest distinct substructure in 30 Doradus other than individual stars.

Walborn & Blades (1997) identified at least five distinct populations across 30 Doradus, reminiscent of cluster complexes observed well beyond the Local Group (e.g. Bastian et al. 2006). These five populations include (1) the central concentration of very young stars associated to R136, (2) an even younger population of embedded massive stars to the north and west of the central cluster where there is significant molecular gas (Werner et al. 1978; Johansson et al. 1998), (3) a population of early-type supergiants throughout the central region, (4) an older population containing cooler and more evolved supergiants in the cluster Hodge 301 about 40 pc in projection to the north-west, and finally (5) another population of early-type supergiants in the association surrounding the luminous blue variable R143.

The different stellar populations of 30 Doradus were also discussed by Grebel & Chu (2000). Their schematic presenting the different generations, reproduced in Figure 2.1, illustrates the past, present, and future of this star-forming region. The four quadrants show the same optical HST image, but different stellar generations are highlighted in each quadrant. Stellar winds and supernovae from the oldest generation in 30 Doradus,

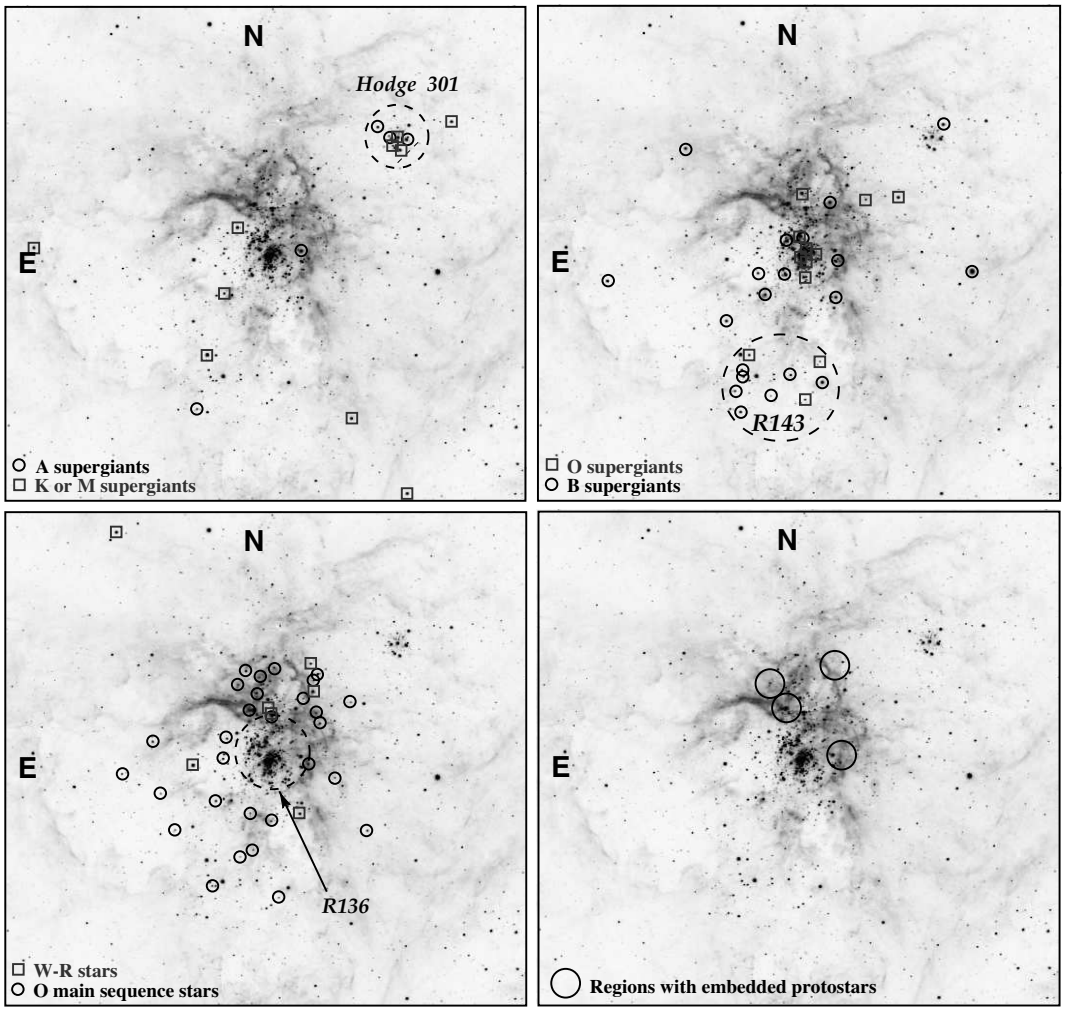

Figure 2.1 Figure adapted from Grebel & Chu (2000) illustrating the distribution of stellar generations of different ages in 30 Doradus. The ~ 20 Myr and oldest generation traced by K, M, and A supergiants is shown in the upper left quadrant. The upper right quadrant shows O and B supergiants. O-type main-sequence and Wolf-Rayet stars are shown at the lower left, and some of the regions with embedded protostars at the lower right. Note that R136 contains a large number of young O-type and Wolf-Rayet stars which are not marked individually. The VFTS will help to refine and better understand this picture.

found primarily in the ~ 20 Myr cluster Hodge 301 (Figure 2.1, top left quadrant), have possibly triggered subsequent star formation and led to the formation of R136. Younger stars, the present generation, are found towards the centre of the region and are shown in the upper right and lower left quadrants of Figure 2.1. These are O supergiants ($\lesssim 3$ Myr) and B supergiants ($\lesssim 10$ Myr), as well as main-sequence O-type stars and Wolf-Rayet stars ($\lesssim 5$ Myr), including the early O-type stars and hydrogen-rich Wolf-Rayet stars in R136 ($\sim 1-2$ Myr). Finally, some of the regions containing the future generation of stars are shown in the lower right quadrant of Figure 2.1. These regions

with dust-embedded protostars are found around R136 along shells and filaments of nebular gas which appear to be rich stellar nurseries, possibly triggered by feedback from R136 (Walborn & Blades 1997; Walborn et al. 1999, 2002b). Studying these young objects at optical wavelengths is generally difficult because of the large dust obscuration, but observations in the near-infrared reduce dust attenuation by up to a factor of 10. Imaging at near-infrared wavelengths has revealed many new sources, including high-mass young stellar objects and embedded clusters (e.g. Walborn et al. 2013) which may eventually evolve into bound clusters.

The feedback from massive stars in 30 Doradus can be seen in the network of filaments and shells originating from the centre of the nebula. Spectroscopic measurements have shown that the shells have velocities of tens to hundreds of $\mathrm{km\,s^{-1}}$ (e.g. Chu & Kennicutt 1994). The spatial correlation between these shells and the shock-heated X-ray emitting gas suggests that they are the result of feedback from stellar winds and supernova (Wang 1999; Townsley et al. 2006). The gas left-over from star formation will eventually leave the region as the total kinetic energy in the shells exceeds the gravitational binding energy of the region by a large factor (Chu & Kennicutt 1994).

In this thesis, we focus on the region in and around R136, which is dominated by the young population of O-type stars, but it is important to keep in mind that the cluster is part of a wider and complex environment where we witness multiple generations of star formation. This complexity is also what makes the richness of 30 Doradus, as it provides an opportunity to study massive stars in different evolutionary stages (e.g. main sequence, Wolf-Rayet stars, transition Of/WN stars) and across a wide range of ages within a single region. O-type stars span a wide range of masses ($\gtrsim$ 20 $\mathrm{M_\odot}$), effective temperatures ($\sim$ 30 000 to 50 000 K) and wind properties, and can be split into several morphological subgroups. Thus, the number of massive stars contained in the region is obviously another advantage, as it not only makes it possible to gather an unprecedently large sample of these rare and short-lived objects, but also to understand the most massive stars as a population and explore the evolutionary connections between subgroups. 30 Doradus is actually the only place (within a single region) where so many massive stars spanning a wide range of intrinsic luminosities can be resolved and observed spectroscopically with current ground-based facilities. Conveniently, its distance is also well-constrained[1] and the foreground extinction is significantly lower than towards the most massive young clusters in the Milky Way.

[1] In this thesis, we adopt a distance modulus to the LMC of 18.5 (e.g. Gibson 2000; Pietrzyński et al. 2013).

2.3.2 Motivations

Based on the previous sections and Chapter 1, it is clear that fundamental questions concerning the formation and evolution of massive stars and clusters remain unanswered, and that 30 Doradus constitutes an ideal laboratory to address many of these. Its rich stellar populations can shed light on the physical properties, multiplicity properties, and chemical enrichment of the most massive stars. Moreover, the study of the central cluster R136 promises to provide insights into the formation and early dynamical evolution of massive star clusters, in which mass loss from massive stars plays a role.

The VFTS was designed to tackle these outstanding issues relating to the evolution of massive stars and clusters by using the multi-object capability of the FLAMES instrument. Combined with the light-gathering power of the VLT, this allowed us to collect a statistically significant and unbiased sample of high-quality data of the massive star population of the Tarantula Nebula, enabling the largest homogeneous spectroscopic study of extragalactic early-type stars undertaken to date.

In the context of recent results pointing to a high multiplicity fraction among massive stars (e.g. Sana & Evans 2011, and references therein), one of the primary motivations of the VFTS was to detect massive binary/multiple systems via variations in their radial velocities. With 30 Doradus already known to harbour a rich population of massive binaries (Bosch et al. 2009), the multi-epoch approach - with time-sampling designed to optimize the detection of binaries - is one of the most important aspects of the observing strategy. This does not only allow us to provide strong constraints on the spectroscopic binary fraction and address the role of binarity in the evolution of massive stars, but is also crucial to disentangle the contribution of the orbital motions of binaries in the determination of the velocity dispersion of R136, one of the original goals of the survey (Chapter 3).

Once binaries are identified, a quantitative analysis of the spectrum of each star can be performed to obtain its stellar parameters, wind properties, and chemical abundances. These results will be used to perform the first large-scale study of nitrogen enrichment in O-type stars and revisit the role of rotational mixing on the surface nitrogen enrichment of B-type stars, which was one of the puzzling results of the FSMS (see above). The differences in the wind properties of early O-type stars, Wolf-Rayet stars and Of/WN stars will be studied, potentially revealing information about the differences in the mechanism driving these winds. Measurements of the rotational velocities of such a large sample of OB stars will also provide insight into the influence of rotation on their

evolution (and vice versa) and serve as useful tests for models of rotating massive stars (Brott et al. 2011). This is particularly important for O-type stars, in which this has not been thoroughly explored in the past due to limited sample sizes.

As discussed above, 30 Doradus is a complex system and more than just a convenient region to sample a large number of massive stars. It is an ideal place to study the feedback from massive stars on their environment, and it can be used as a template for starburst regions much farther away, which can only be studied via their integrated properties because stars cannot be individually resolved. The VFTS data will allow the first comprehensive census of the hot massive stellar content within the archetypal starburst that is 30 Dor. Estimates of the stellar feedback (e.g. ionising luminosity and stellar wind luminosity) from individual stars can then be compared to that inferred from the nebular properties or predicted by population synthesis codes such as Starburst99 (Leitherer et al. 1999), providing a fundamental calibration that ties together local star-forming regions with more distant ones. R136, in particular, is one of the few resolved massive clusters that is well-suited to test the reliability of synthetic predictions given its high mass and young age, which ensures that the upper end of the stellar mass function is well populated and that stochastic effects are minimal (Cerviño et al. 2002).

2.3.3 The FLAMES instrument

FLAMES is the multi-object, intermediate and high resolution spectrograph mounted at the Nasmyth A platform of Unit Telescope 2 (UT2) of the VLT (see Figure 2.2). It is fibre-fed, meaning that it uses optical fibres to feed the light from objects to a spectrograph, where it is dispersed and detected. It comprises three main components:

- **A Fibre Positioner** (OzPoz; see Figure 2.2) hosting two plates, such that one is observing while the fibre positions are configured on the second for the subsequent observations. These plates consist of a curved metallic disc (to match the curvature of the focal surface) on which the magnetic buttons holding the fibres are attached. The magnetic side of these buttons sticks to the plate while the other side is open to let the light from the target enter the button where it is coupled into the fibres by a tiny prism. Each of the two plates has a hole in the centre, and in one of the plates this hole hosts ARGUS (see below).

- **A medium-high resolution optical spectrograph, GIRAFFE**, with three types of feeding fibre systems: MEDUSA, IFU, and ARGUS. It is equipped with two gratings (high and low resolution) and several order sorting filters are

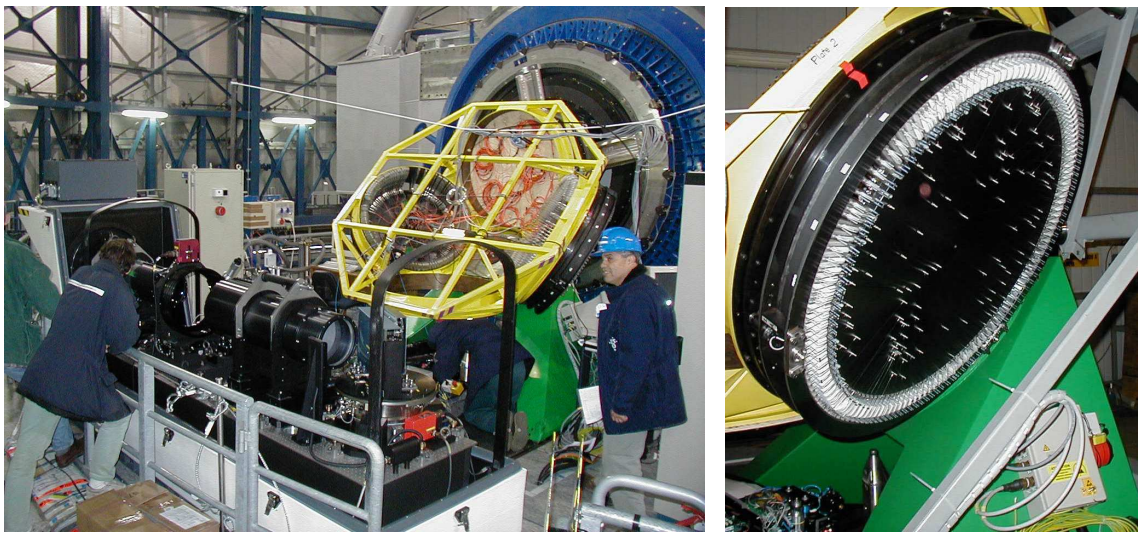

Figure 2.2 *Left*: The GIRAFFE spectrograph as seen during the integration on the Nasmyth A platform of UT2. The fibre positioner OzPoz is visible behind the spectrograph (the picture was taken when the OzPoz enclosure had not been installed yet). *Right*: One of the two plates of the fibre positioner OzPoz, where we can see the magnetic buttons attaching the fibres to the plate. Credit: ESO.

available to select the required spectral range. Five additional fibres, distributed evenly across the CCD, can be illuminated at the start of an observation with a Th-Ar light source to allow simultaneous (and more precise) wavelength calibration of every exposure and monitoring of the instrument drifts (although this option was not employed for the VFTS).

There are two sets (one for each positioner plate) of up to 132 MEDUSA fibres available for science (or sky) observations, deployable within a $25'$ diameter field-of-view through the use of the pick-and-place magnetized fibre buttons mentioned above, each with an aperture diameter of $1\farcs2$ on the sky.

For each plate, there is also a set of 15 deployable Integral Field Units (IFUs) dedicated to science observations, and another 15 dedicated to sky measurements (with only the central fibre present in this case). Each IFU consists of a rectangular array of 20 microlenses (also called spaxels for **spa**tial pi**xels**) with a sampling of $0\farcs52$ per microlens, resulting in an almost rectangular aperture of $2'' \times 3''$ on the sky. The microlenses are used to couple the light into the fibres and ensure that there are no losses between fibres. These deployable IFUs were however not used for the VFTS.

Finally, ARGUS is the large IFU mounted at the centre of one plate of the fibre positioner (shown schematically in Figure 2.3). It consists of a 22×14 array

of microlenses coupling the light into fibres. For the "1:1" magnification scale used for the VFTS, this provides an almost rectangular total field-of-view of $11.5'' \times 7.3''$ on the sky for a single pointing. In parallel, 15 deployable ARGUS single sky fibres can be positioned in the $25'$ field.

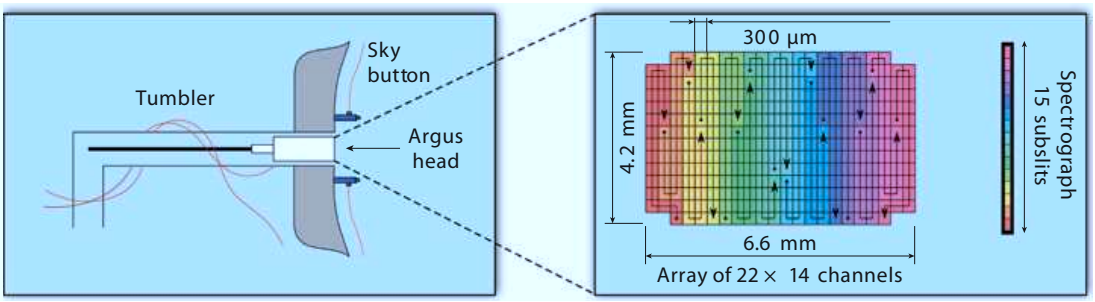

Figure 2.3 *Left*: A schematic of ARGUS in the Ozpoz fibre positioner. *Right*: The ARGUS fibre geometry and the allocation of fibres into subslits feeding the GIRAFFE spectrograph, with the arrows • → indicating the orientation of the subslits in the array. Figure adapted from Lützgendorf et al. (2012).

- **A link to the Red Arm of the Ultraviolet and Visual Echelle Spectrograph (UVES)**, the high-resolution spectrograph mounted at the Nasmyth platform B of UT2 of the VLT. Although UVES was originally designed to operate in long slit mode only, it has been modified such that it is also possible to use a fibre mode (with up to 8 fibres) fed by the FLAMES positioner to its Red Arm. Each UVES fibre has an aperture on the sky of $1''$.

2.3.4 Observing strategy for the VFTS

The VFTS employed three different observing modes of the FLAMES instrument:

- **MEDUSA**: The majority of observations were obtained using the MEDUSA fibre-feed to the GIRAFFE spectrograph. The field-of-view of the instrument means that spectra across the whole 30 Dor nebula can conveniently be obtained with one central telescope pointing.

- **ARGUS**: This mode was used to probe the more densely populated regions around the core of R136, the minimum object separation of $11''$ of the MEDUSA fibres (limited by the size of the magnetic buttons) being too large to survey these inner regions. Five pointings of the ARGUS unit were observed in the central part of 30 Dor. A seeing constraint of $\leq 0''.8$ was imposed for these observations.

- **UVES**: A small number of objects were finally observed in the inner part of 30 Dor, in parallel to the ARGUS pointings, with the fibre-feed to UVES, which delivers a greater spectral resolving power than that of GIRAFFE.

The observational details and different wavelength settings used for the three observing modes used for the VFTS are listed in Table 2.1. Note that all the observations were performed in back-to-back pairs of exposures to allow for removal of spikes from cosmic ray hits, with each pair of exposures of a given configuration with a given instrument setting forming a single Observation Block (OB). The exposure times were chosen to ensure sufficient signal-to-noise ratio (S/N $\geq$ 50 per resolution element, for precise radial velocity - RV - measurements) in the combined spectra of individual OBs. More details about the MEDUSA and ARGUS observations and their data reduction are given below and in the following subsections, but the UVES data are not discussed further as they are not used in the analyses presented in this thesis.

Table 2.1 Summary of the exposure time, wavelength coverage, spectral resolution ($\Delta\lambda$, determined by the mean full-width at half-maximum of arc lines in the wavelength calibration exposures), effective resolving power for the central wavelength of the setting ($R \equiv \lambda/\Delta\lambda$) and minimum number of OBs for the different FLAMES modes and settings used in the VFTS.

Mode	Setting	Exp. time/OB [s]	λ [Å]	$\Delta\lambda$ [Å]	R	minimum # of OBs
MEDUSA	LR02	2×1815	3960 – 4564	0.61	7 000	6
MEDUSA	LR03	2×1815	4499 – 5071	0.56	8 500	3
MEDUSA	HR15N	2×2265	6442 – 6817	0.41	16 000	2
ARGUS	LR02	2×1815	3960 – 4570	0.40	10 500	5
UVES	520	2×1815	4175 – 5155 ; 5240 – 6200	0.10	53 000	5

MEDUSA observations

The target selection for the MEDUSA observations and associated photometry are discussed in detail in Evans et al. (2011). Note that no colour cuts were employed on the input target lists to avoid selection biases, and that a magnitude cut of $V \leq 17$ mag was imposed to ensure that the S/N in the observed spectra was high enough.

Exactly 1000 targets were observed with nine different configurations of the MEDUSA fibre-feed to the GIRAFFE spectrograph. For every MEDUSA configuration, a minimum of ten fibres distributed relatively evenly across the field were reserved for 'sky fibres' (i.e. not placed on objects). The three wavelength settings used for the MEDUSA mode were chosen to provide intermediate-resolution spectra of the lines

commonly used in classification and quantitative analyses of massive stars (including RV measurements) in the $3960 - 5070$ Å region and higher-resolution spectra of the Hα line as a diagnostic of the stellar wind intensity. The wavelength regions covered also encompass strong nebular forbidden emission lines ([O III] λ4959, [O III] λ5007, [N II] λ6549, [N II] λ6583, [S II] λ6717, [S II] λ6731) and several nebular recombination emission lines of hydrogen and helium (e.g. Hα, Hβ and Hγ), allowing us to trace gas velocities along the line of sight of each star.

To build up sufficient S/N for the quantitative atmospheric analysis of each star, three OBs of the LR02 and LR03 settings were observed, as well as two OBs of the HR15N setting (Table 2.1), with no time constraints enforced for the execution of these OBs (although most sequences for a given setting were observed consecutively). The details of each OB and their modified Julian Dates are listed in Evans et al. (2011). Perhaps the most important observational feature of the VFTS is that three additional OBs were obtained at the LR02 setting to detect RV variables (both true binaries and multiple systems). A minimum of 28 days were imposed between the execution of the third and fourth LR02 epochs, and similarly between the fourth and fifth. The sixth epoch was obtained in October 2009, approximately one year after the first epoch, in order to significantly increase the probability of detecting intermediate- and long-period binaries. A small number of OBs at the LR02 wavelength setting were repeated for operational reasons (e.g. deterioration of the seeing beyond the required constraints during the exposure). In cases where such problems occurred but the full exposures (1815 s) were completed, these observations were retained as they can still provide useful RV measurements (especially for the brighter targets) despite lower S/N.

The binary detection probability as a function of orbital period for a given time sampling can be calculated using Monte Carlo simulations as in Sana et al. (2009). Figure 2.4 shows the typical detection probability for an O-type spectroscopic binary given the time sampling of the LR02 MEDUSA observations in VFTS. We can see that the detection rate is larger than 90% for periods shorter than 10 days, and larger than 50% for periods shorter than 200 days. The drops in the detection probability for periods around one month and 300 days are aliases caused by the specific time sampling adopted for the VFTS. This time sampling is such that the radial velocity of binaries with a period close to one month or 300 days varies nearly in phase with the time of the observations, making them more difficult to detect.

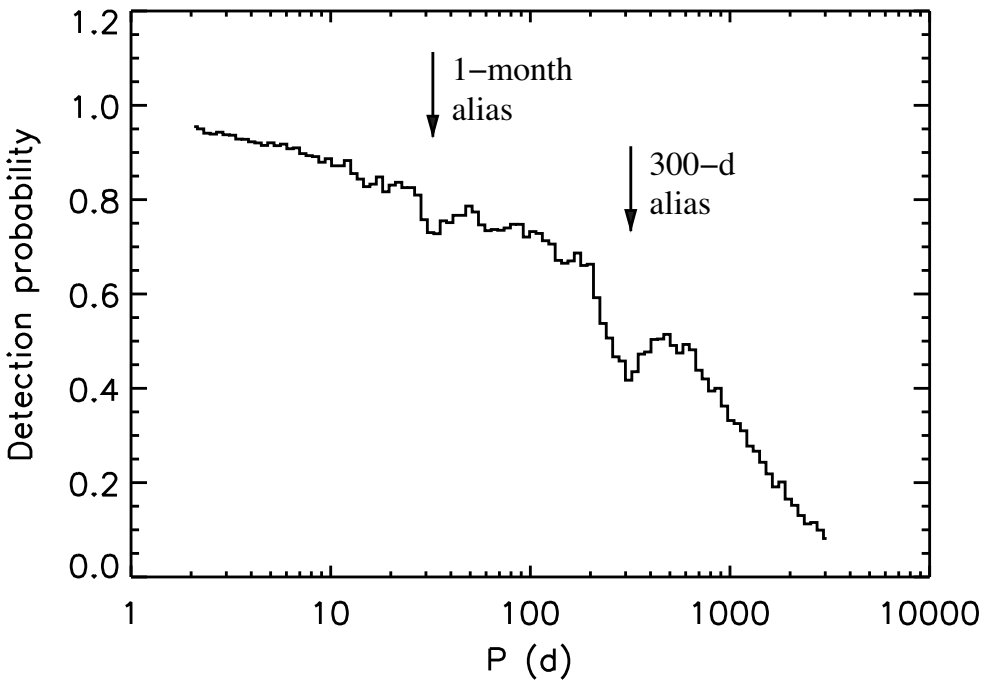

Figure 2.4 Detection probability of an O-type spectroscopic binary as a function of its orbital period P given the accuracy of the RV measurements and the typical time sampling provided by the MEDUSA observations of the VFTS. The arrows indicate the 1-month and 300-day aliases. Figure reproduced from Sana et al. (2013b).

ARGUS observations

As introduced above, the MEDUSA data were complemented by five pointings within the central arcminute of R136 with the ARGUS IFU (see Figure 2.5). The first ARGUS pointing ("A1") was located on the core, with three pointings ("A2" to "A4") immediately adjacent. The fifth pointing ("A5") was located to the NNE of R136 to target a reasonable number of stars at a slightly larger radius from the core.

Full spectral coverage for quantitative analysis in the densely populated region in and around R136 is best obtained with AO-corrected or HST spectroscopy, but the main intention here was to probe the kinematics of these inner regions, again with follow-up observations to identify binary systems. Thus, only the LR02 wavelength setting of the GIRAFFE spectrograph was used for the ARGUS observations. The resulting wavelength coverage was comparable to that from the MEDUSA observations with the same wavelength setting, but at greater resolving power ($\sim 10\,500$; see Table 2.1) because of the smaller aperture size of the ARGUS fibres.

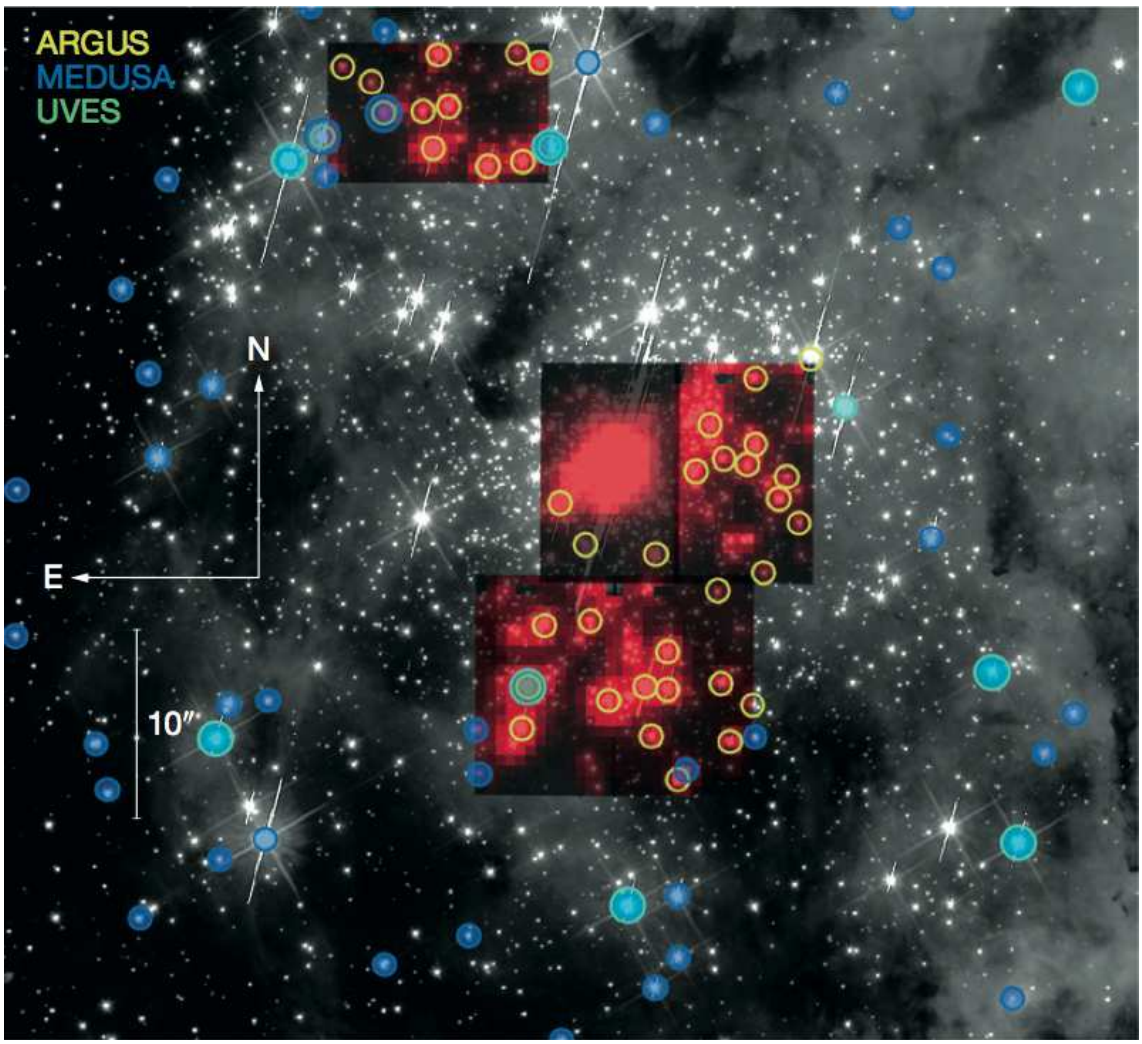

Figure 2.5 ARGUS reconstructed pointings (and extracted sources) for a single epoch overlaid on an HST-WFC3 F555W image of R136 (De Marchi et al. 2011). The location of the VFTS MEDUSA and UVES targets in the central region of 30 Dor are also shown.

For each ARGUS pointing, two OBs were observed without time restrictions and, similar to the multi-epoch strategy for the MEDUSA observations, the follow-up epochs (third and fourth) were observed with a minimum interval of 28 days. All these data were obtained over the period between October 2008 and March 2009, with a final (fifth) epoch observed in December 2009 or January 2010. As with the MEDUSA observations, a number of the ARGUS OBs were re-observed owing to changes in conditions and other operational issues, and the observations were retained when full exposures were completed as useful RV measurements can still be obtained under poorer seeing conditions for the bright targets extracted from the ARGUS observations. The full list of completed exposures for the ARGUS pointings are given in Evans et al. (2011). Note that given the very similar constraints on the execution of the different

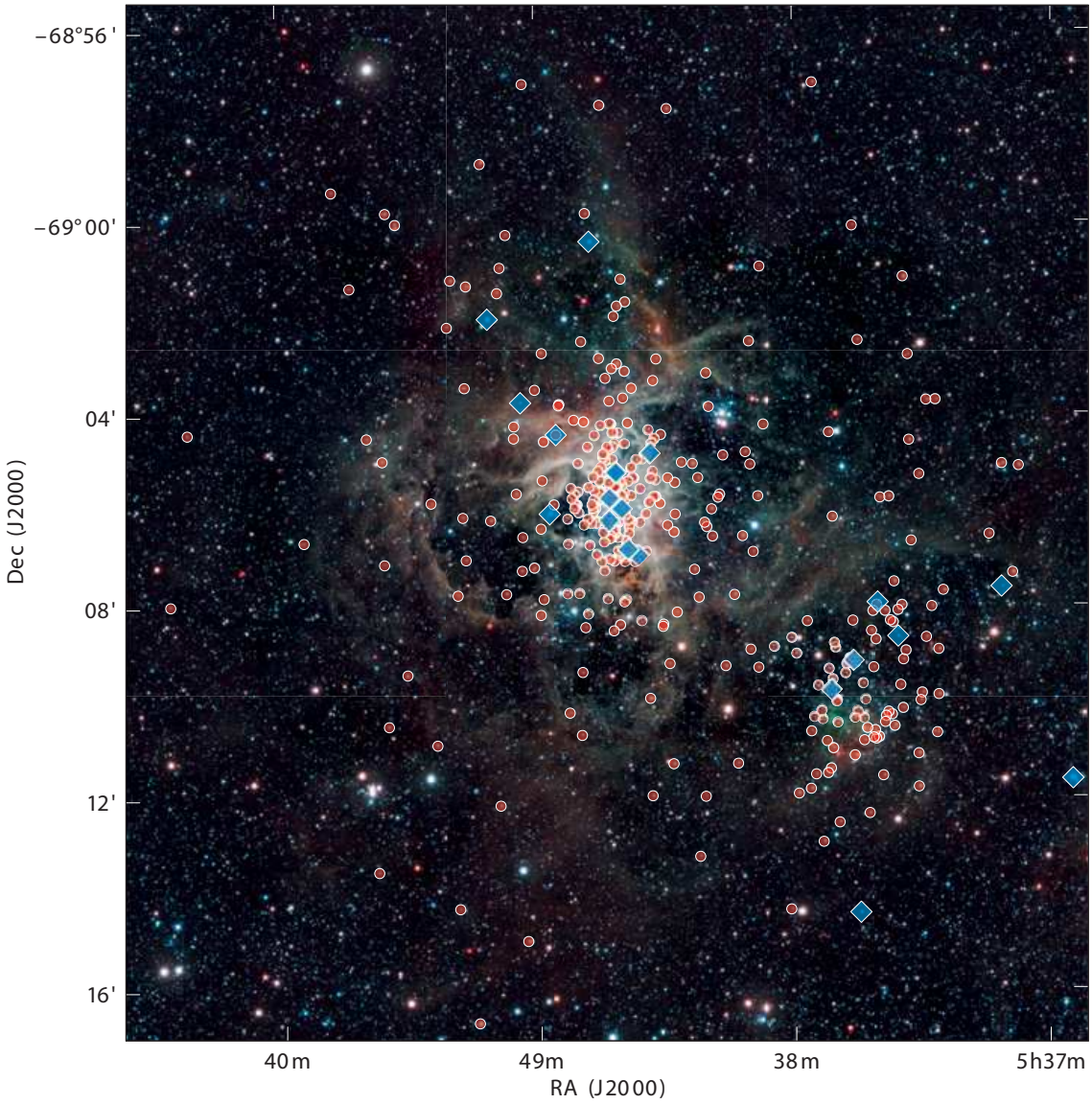

Figure 2.6 Combined *YJKs*-band image of 30 Doradus from the VISTA Magellanic Clouds (VMC) Survey (Cioni et al. 2011). The O-type (red circles) and Wolf-Rayet stars (blue diamonds) observed by the VFTS are indicated.

epochs for the ARGUS and MEDUSA observations, the binary detection probability for the ARGUS observations is very similar to what is shown in Figure 2.4 for the MEDUSA observations.

2.3.5 Highlights from the VFTS

In total, the VFTS has observed over 500 B-type stars, over 300 O-type stars and 20 emission-line stars (Wolf-Rayet and Of/WN stars). The sample of B-type stars is comparable in size to that of the FSMS, but the VFTS sample has the added benefit

of multi-epoch data to investigate multiplicity. There are also about 90 stars with classifications of A-type or later with radial velocities consistent with them being members of the LMC. The remaining foreground stars or objects with data quality issues were not retained in the final sample. There are 893 objects with MEDUSA and/or UVES spectra catalogued in Evans et al. (2011), along with 41 ARGUS targets (see the extraction procedure below), 4 of which were also observed with MEDUSA or UVES. All these objects have been assigned an identifier of the form VFTS+'number' based on ascending RA position, with MEDUSA/UVES targets starting at VFTS 001 and ARGUS-only sources starting at VFTS 1001.

As an indication of the spatial distribution of the VFTS targets, the positions of the O-type and Wolf-Rayet stars observed as part of the survey are shown in Figure 2.6 on a *YJKs*-band mosaic of 30 Doradus from the VISTA Magellanic Clouds (VMC) Survey. The majority of targets lie in the central region surrounding R136, and a large number of stars were also observed in the surrounding regions of NGC 2060 to the south-west.

Although many important results from the VFTS are yet to come (e.g. about the physical parameters of OB and Wolf-Rayet stars, or the census of hot luminous stars and their feedback as a template for distant starbursts), the survey is already providing new insights into the formation, evolution, and multiplicity of massive stars. We now summarise some of the results that are not presented in detail in the next chapters, but which are still relevant to the formation and early dynamical evolution of massive clusters and also make use of the RV measurements (of either the stars or gas) performed in the context of this thesis.

A massive runaway star from 30 Doradus

One of the exciting early results emerging from the VFTS was the discovery of a massive runaway star that was likely dynamically ejected from the young massive cluster R136 (Evans et al. 2010). The massive O2 star VFTS 016, located at a projected distance of about 120 pc to the west of R136, illustrates the power of the multi-epoch strategy adopted for the VFTS, which not only allows us to detect binaries but also makes it possible to quantify the probability that a star is actually single.

VFTS 016 was first observed several years ago with the 2-degree Field (2dF) instrument at the Anglo-Australian Telescope. It was noticed then that its RV was 85 $\mathrm{km\,s^{-1}}$ lower than the local systemic velocity, which could still have indicated a large-amplitude binary. However, no significant RV variations were seen in the multiple epochs of

VFTS data. From this, a massive companion with a period shorter than one year was excluded at the 98% level.

The significantly different RV of VFTS 016 compared to nearby stars and gas suggests that it is a runaway star, which could have been ejected from its formation site either by dynamical interactions in a dense cluster or by the kick received from the supernova explosion of a companion in a binary system. Spectral analysis of the star pointed to a mass of ~ 90 $M_{\odot}$, which in turn suggests that its runaway status is due to interactions with even more massive stars in R136 (e.g. Fujii & Portegies Zwart 2011). Given that R136 is thought to be too young for a supernova explosion to have occurred, VFTS 016 becomes a very strong candidate for dynamical ejection if it did originate from there. However, note that the star is also at a projected distance of 70 pc from the less massive and older cluster NGC 2060. High-quality proper motion measurements will be needed to reach final conclusions about the origin of VFTS 016 and other candidate runaways identified by the VFTS. The GAIA mission should provide useful information in that respect. An ongoing multi-epoch imaging programme of 30 Doradus with HST (PI: D.J. Lennon) will also allow us to measure proper motions and assess the status of these runaway candidates.

The multiplicity properties of massive stars in 30 Doradus

The main scientific motivations for the VFTS include testing evolution theories for massive stars, providing a near-complete census of the closest starburst template, and investigating the dynamics of 30 Doradus. In order to achieve each of these goals, a first crucial ingredient to consider is the multiplicity of massive stars.

Sana et al. (2013a) analysed the multiplicity properties of the O-type star population in 30 Doradus based on the multi-epoch RV measurements performed on VFTS data, which were used to identify spectroscopic binaries. The RV measurements of 28 O-type stars observed with ARGUS (see Chapter 3 for details) were incorporated in this analysis. By modeling (with Monte Carlo simulations) simultaneously the observed binary fraction, the distributions of the amplitudes of the RV variations and the distribution of the time scales of these variations, the intrinsic binary fraction and period and mass-ratio distributions were derived. After correcting for observational biases in this way, the observed spectroscopic binary fraction of $35 \pm 3\%$ (i.e. the fraction of objects displaying statistically significant RV variations with an amplitude of at least 20 $\mathrm{km\,s^{-1}}$) was found to correspond to an intrinsic binary fraction of $51 \pm 4\%$. A preference was also found for short-period systems (compared to a flat distribution

in $\log_{10}(P/\mathrm{day})$; see Chapter 4 for a more detailed discussion of the binary fraction and distributions of orbital parameters of massive binaries).

Given the multiplicity properties derived in Sana et al. (2013a) for the O-type stars in 30 Doradus, it was estimated from simple evolutionary considerations that more than 50% of all the stars born as O-type stars belong to a binary system with a period less than 1 500 days, and will therefore exchange mass with their binary companion[2]. This highlights the significant effect of binary interaction on the evolution and fate of massive stars, and suggests that it is important to take binarity into account to interpret young unresolved populations whose light is dominated by massive stars.

The even larger sample of B-type spectra from the VFTS is also being investigated for RV variations in order to constrain the multiplicity properties in the lower mass regime of B-type stars (Dunstall et al., in preparation). Preliminary results (based on a cross-correlation analysis, rather than Gaussian fitting as in Chapter 3 and Sana et al. 2013a) point to similar observed and intrinsic binary fractions to what was found for the O-type stars.

Candidates for isolated high-mass star formation

'Competitive accretion' and 'monolithic collapse' are currently the main theories of star formation, and each implies a different environment for the formation of the most massive stars in a young system. In the competitive accretion scenario (e.g. Bonnell & Bate 2006), the potential well of a cluster of lower-mass stars attracts surrounding gas into the cluster, which allows some stars to accrete mass and become more massive. In this case, massive stars are expected to be found within clusters of lower-mass stars. In the monolithic collapse scenario (e.g. Krumholz et al. 2009), the stellar masses are set by the gas core from which they form and star formation traces the gas, so while some massive stars can still form in a clustered distribution, others will form in relative isolation (i.e. not strongly influenced by the gravitational potential of nearby stars). Depending on how stars form, the initial mass function (IMF) will be sampled in different ways. In the framework of competitive accretion, some authors have suggested that massive stars only form in clusters, in which case the IMF would be sampled in a "sorted" way, with enough low mass stars needing to be present before higher mass

[2]Note that the binary fraction is defined as the ratio of the number of binaries to the total number of systems (single stars and binaries), i.e. a binary fraction of 50% means that two stars out of three are part of a binary system. Although it might appear contradictory at first glance, the claim that over 50% of the current O-star population in 30 Doradus will exchange mass with its companion is therefore consistent with the inferred intrinsic binary fraction of 51%.

stars can form (e.g. Weidner et al. 2010). On the other hand, in the case of monolithic collapse, massive stars could form in relative isolation, such that the IMF would be sampled stochastically (e.g. Oey et al. 2004). This has important implications on the mass distribution and numbers of massive stars in different galaxies (e.g. Bastian et al. 2010).

The VFTS sample can provide insights into theories for the formation of massive stars. Bressert et al. (2012) identified 15 stars observed as part of the survey outside of R136 and NGC 2060 which are strong candidates for being high-mass stars that have formed in isolation, suggesting that stochastic sampling of the IMF and the formation of massive stars by monolithic collapse does occur in at least some situations. The multi-epoch strategy of the VFTS was key to improve upon previous attempts to find O-type stars that formed in isolation, as it allowed to test the possibility that apparently isolated massive stars are merely runaways from clusters (in which case they would not have formed in isolation).

Based on the VFTS data and complementary optical to mid-infrared imaging, the candidates identified were chosen to satisfy several criteria including (1) not showing RV variability, (2) have a RV within $1\,\sigma$ of the mean of apparently single O-type stars in 30 Doradus (i.e. not runaways along the line-of-sight), (3) show no evidence of a surrounding cluster, and (4) be associated with gaseous and/or dusty filaments. As an additional constraint on the association between stars and gas, the line-of-sight gas velocities (see section 2.4 for more details on these measurements) from the [N II] λ6583, [S II] λ6717, [S II] λ6731, and Hα nebular emission lines were compared to the stellar radial velocities and found to be within ~ 5 km s^{-1} for 7 of the 15 candidates and within ~ 15 km s^{-1} for most candidates.

VFTS 682, a new hydrogen-rich Wolf-Rayet star discovered as part of the survey and located 29 pc north-east of R136 (Evans et al. 2011), was also added to the list of candidates for high-mass stars formed in isolation even though it does not meet all the adopted criteria. It appears single, but its RV, estimated from fits of atmospheric models, is not within $1\,\sigma$ of the mean of 30 Doradus. RV measurements for emission-line stars are however very uncertain, so it is still possible that it was formed in situ. Even if it was a runaway ejected from R136 (Banerjee et al. 2012), this would represent an exciting scenario given its very young age (1 to 1.4 Myr) and high mass (~ 150 M$_\odot$; Bestenlehner et al. 2011). In any case, its presence outside of a cluster is certainly intriguing as its spectrum resembles those of very luminous stars in the core of R136 (Crowther et al. 2010) and such massive stars had previously only been found in the cores of dense clusters. Again, proper motions from GAIA and HST will be crucial

to reach strong conclusions as to whether these high-mass stars have truly formed in isolation.

2.4 Data reduction: VLT-FLAMES MEDUSA

Apart from the extraction of sources/stellar spectra from the ARGUS IFU data cubes (see section 2.5) and the gas velocity measurements (see below) which were performed in the context of this thesis, the bulk of the data reduction and processing for the VFTS was performed by William Taylor (2012). The same procedure as that used for the VFTS MEDUSA data was however also adopted by the author of the present thesis to reduce all the MEDUSA data from a survey of massive stars in SGS-SMC 1 (see section 2.6 and Chapter 6). We therefore outline here this common data reduction procedure for the MEDUSA data of both surveys.

2.4.1 General procedure

The initial data processing steps were performed with the ESO Common Pipeline Library (CPL) FLAMES reduction routines (v2.8.7). These basic reduction steps are standard for any fibre-fed multi-object spectrograph and include:

- **Bias subtraction**: A bias voltage is usually applied to CCD detectors to ensure that they operate as much as possible in a linear manner, and as a result a non-zero count is recorded in all pixels. Several bias frames are taken everyday as part of the standard day-time calibration of FLAMES. The median of these frames is subtracted from each raw science frame. Note that the subtraction of the signal from the dark current (arising from the thermal energy within the silicon lattice comprising the CCD) can safely be skipped for observations with the most recent CCD installed on GIRAFFE, as is the case for the data used in this thesis.

- **Flat fields and fibre localization**: Flat fields are also obtained as part of the standard day-time calibration of FLAMES by positioning all the fibres in a spiral pattern on the focal plate and uniformly illuminating each one in turn with a featureless white light source with the help of the fibre-positioning robot. The fibres are arranged side by side along the slit of the spectrograph, so after being dispersed by the grating, the spectra from all these fibres are also recorded side by side on the CCD. The first function of the flat-field images is to detect and trace the central position and width of the spectra across the two-dimensional

CCD image, which is then useful for the extraction of the science frames (the S/N of science observations is generally much lower and the position of the fibres on the CCD much harder to trace). As the pipeline knows where a given fibre should approximately lie, broken fibres can also be identified when the localization algorithm cannot measure any signal at the expected position of a fibre. Once the location of the science data on the CCD has been constrained, the flat-field frames are also used to extract the flat-field spectra following the same extraction procedure as outlined below for the science frames. Flat-field corrections are done in one dimension, i.e. the extracted science spectrum for a given fibre (see below) is divided by the normalised flat-field spectrum of that same fibre. This corrects the data for the pixel-to-pixel variations. In a flat-field frame, the amount of light entering the fibres is supposed to be the same for all fibres, so differences in the intensity of the extracted flat-field spectra also trace differences in the fibre relative transmission. Finally, the inter-fibre flux values of the flat-field frames serve to model the contamination from light scattered inside the spectrograph and detected across the CCD, which is then subtracted from the extracted spectra.

- **Wavelength calibration**: In order to establish the wavelength scale of the spectra, calibration frames are taken by passing the fibre-positioning robot over the fibre tips and illuminating them with a Thorium-Argon arc lamp. Starting from the fibre positions obtained from the flat-field frames, the arc lamp spectra are extracted. These spectra contain a large number of emission lines whose wavelengths are known from laboratory tests and which are used as a reference to provide a wavelength calibration for the observed sources.

- **Extraction of the spectra**: There are two main methods for extracting the spectra, i.e. turning the 2D fibre profiles into 1D spectra by moving along the dispersion direction and combining all the flux from a given fibre. The simplest method, called summed extraction, consists of summing all the flux across the width of the fibre profile for each column of the CCD. This procedure ignores the fact some pixels contain more counts (better quality information) than others because all contribute with equal weight to the final spectrum, which effectively adds noise to the final spectrum. The alternative, called optimal extraction, consists of using the shape of the fibre profile (created from the flat-field reduction) as a weighting function when adding flux from different pixels, thereby giving a higher contribution to the final spectrum to better pixels. This also has the advantage of directly identifying and removing unexpected deviations from the smooth and continuous distribution of pixel intensities, as these spikes are likely due to cosmic ray hits. For the data used in this thesis (including

the FLAMES data in SGS-SMC 1), the more basic summed extractions were however performed because optimal extractions for the VFTS data did not yield an improved data product and instead introduced further problems. It was indeed found that optimal extractions sometimes led to negative counts in the reduced sky spectra (which by design have the faintest signals), a problem that is not present with summed extractions (Taylor 2012). This problem is possibly linked to the treatment of the background (and its small-scale variations) in the optimal extraction procedure (for more details see Taylor 2012).

As a result of the reduction steps outlined above, the science observations are processed and the pipeline routines provide bias corrected, extracted and wavelength calibrated spectra, corrected for fibre-to-fibre transmission and pixel-to-pixel variations. There is some curvature at a given wavelength across the CCD (see Figure 2.7) due to natural distortions in the camera of the spectrograph, so the wavelength coverage is slightly shifted (by a few Å) between the fibres at the edge and the fibres at the centre of the slit. The pipeline automatically truncates to a common point at the blue end of each setting but not the red. For consistency, all spectra are additionally truncated to a common point at the red end of each setting. Some example CCD images used in the reduction procedure are shown in Figure 2.7. We can see from that figure that the GIRAFFE spectra are parallel in dispersion along the long side of the detector, and the short side is along the slit direction. The lines of constant wavelength are arranged on low-curvature arcs.

After the basic reduction, the following additional reduction stages, which are not taken into account by the pipeline routines, were performed:

- **Heliocentric correction**: All the spectra are corrected to the heliocentric frame using the IRAF packages RVCORRECT and DOPCOR.

- **Sky subtraction**: Each sky fibre is inspected for signs of an on-sky source or cross-contamination from bright spectra/emission lines from adjacent fibres on the detector. Although they are very rare, contaminated sky fibres are rejected prior to creation of a median sky spectrum for each observation. This median sky spectrum is then subtracted from all the objects in that observation. Note that the sky subtraction for fibre spectra is rarely optimal, especially at the distance of the Magellanic Clouds, due to the spatially-varying nebular emission (as seen from long-slit HST spectra in 30 Dor; e.g. Walborn et al. 2002b). Also, as the fibres collect light coming from both extended nebular emission and stellar flux from a point source, the relative intensity of the nebular contamination can vary

Figure 2.7 Example CCD images from different reduction steps for one MEDUSA LR02 observation of a field in SGS-SMC 1. From top to bottom, a flat-field, wavelength calibration Th-Ar arc lamp, and raw science frame are shown. A few hydrogen Balmer lines and helium absorption lines are visible in the science frame, as well as bright spots originating from cosmic-ray events. The GIRAFFE spectrograph subslits (packets of fibres) can also be distinguished.

with changing seeing conditions. Care is therefore required when analysing lines that are more likely to suffer from nebular contamination.

- **Error spectrum**: An error spectrum is produced by the pipeline for each fibre as part of the reduction process, recording for each wavelength bin the statistical error arising from different stages in the reduction, e.g. bias level, detector gain, read-out noise. We combine this error spectrum with the errors on the median sky spectrum to obtain an estimate of the overall error for each spectrum. The median sky error adopted takes into account the variance in the real fluxes of the sky fibres used to create the median, yielding considerably larger errors for the nebular lines, therefore providing a realistic estimate of the accuracy (or lack of) of the sky subtraction (for more details see Taylor 2012).

- **Cosmic-ray rejection**: To clean the extracted spectra of cosmic rays, we employ the following technique. For each spectrum, the ratio of the two back-to-back exposures composing each OB is calculated. A boxcar 4-σ clip, over 100 wavelength bins, is then performed on this ratio. Any unexpected and significant deviations in the ratio points to a feature present in only one of the exposures. Since the exposures were consecutive, it is safe to assume that such a transient feature was a cosmic ray. The pixels identified in this way as likely affected by a cosmic-ray hit were rejected, then replaced with the value from the sister exposure, appropriately scaled by the ratio of the surrounding region.

2.4.2 Cross-contamination

In addition to the reduction procedure described above, inspection of individual fibre profiles is necessary to make sure that the spectra do not suffer from cross-contamination. The wings of the fibre profile for particularly bright emission-line objects (in particular Wolf-Rayet stars) can indeed be sufficiently broad to extend into the profile of nearby fibres and affect the extracted spectra, especially if those nearby fibres correspond to much fainter stars. Using the observations performed under the best seeing conditions (and therefore with the strongest signal and broadest fibre-profile wings) for each MEDUSA configuration and wavelength setting, the fibres adjacent to the brighter targets were therefore inspected. Fortunately, cross-contamination between fibres was generally found to be minimal for the VFTS dataset, with only a small number of fibres contamined by bright stars (for more details and notes about which stars are contaminated, see Evans et al. 2011). Even in those cases, the spectral regions used for RV measurements are generally not affected. For the survey of massive stars in

SGS-SMC 1, cross-contamination was never found to be an issue given that the region does not contain stars comparable to the brightest emission-line stars in 30 Doradus.

2.4.3 Atmospheric refraction effects

Some of the spectra of the same object are seen to have distinctly different continuum shapes for different observations/exposures (see Figure 2.8). This is not an artefact of the reduction procedure, but a real variation attributed to the effect of differential atmospheric refraction combined with a small drift in on-sky fibre position caused by field rotation (e.g. Taylor 2012). This differential effect is due to the fact that the atmospheric refraction index, and hence the direction of propagation of the light from a given stars, changes with wavelength and distance from the zenith. As a consequence, the red and blue parts of a spectrum do not hit the fibre at the same position, and part of the stellar spectrum can fall outside the fibre entrance. This effect is more important when observing over a wide spectral range and in the blue part of the spectrum, so observations with GIRAFFE in the blue low resolution setup are more affected. The software controlling FLAMES accounts for the change in zenith distance of the field and offsets the position of the telescope by the appropriate amount. However, because the field is rotating, the variation in the zenith distance is not constant across the field, and the fibres gradually become misaligned with their intended objects, causing different relative contributions of blue and red light to enter the fibres.

Thankfully, this differential atmospheric refraction effect only impacts the underlying gradient of the continuum, and if the spectra are rectified before stacking, there is no impact on the integrity of the data. Therefore, it does not compromise the science goals of the VFTS or the survey of massive stars in SGS-SMC 1, for which absolute flux levels are not important.

2.4.4 Line-of-sight gas velocities

Although not strictly part of the reduction procedure, we briefly describe below some additional operations that were performed by the author of this thesis on the MEDUSA spectra from the VFTS. The aim was to measure the line-of-sight gas velocities in 30 Dor and use them as a reference to which stellar velocities can be compared (see Section 2.3.5 for example).

For each object and exposure for which this was possible (e.g. not contaminated by broad stellar emission lines), the stellar spectrum (usually the continuum) was fitted

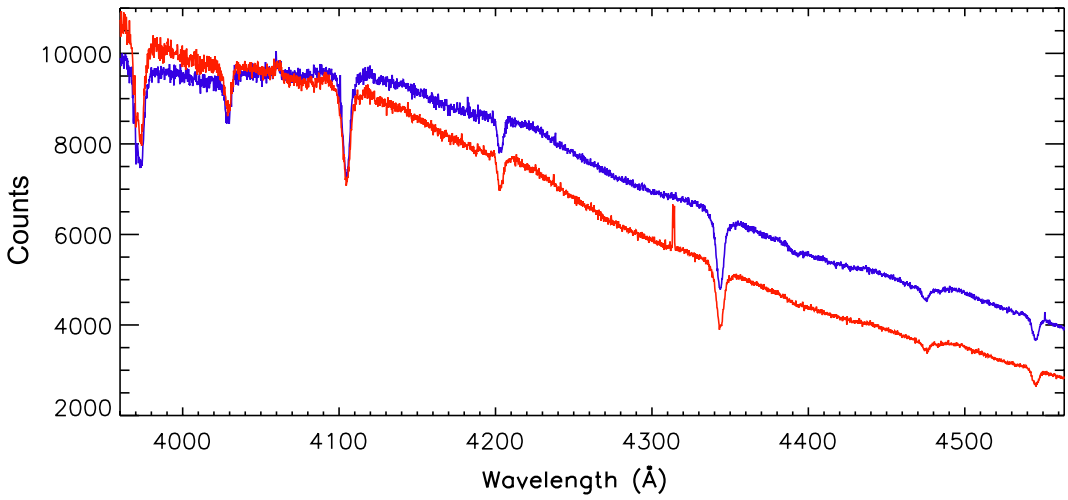

Figure 2.8 Reduced spectra of two consecutive exposures for an O-type star observed as part of the FLAMES survey of massive stars in SGS-SMC 1, showing the effect of differential atmospheric refraction on the continuum slope.

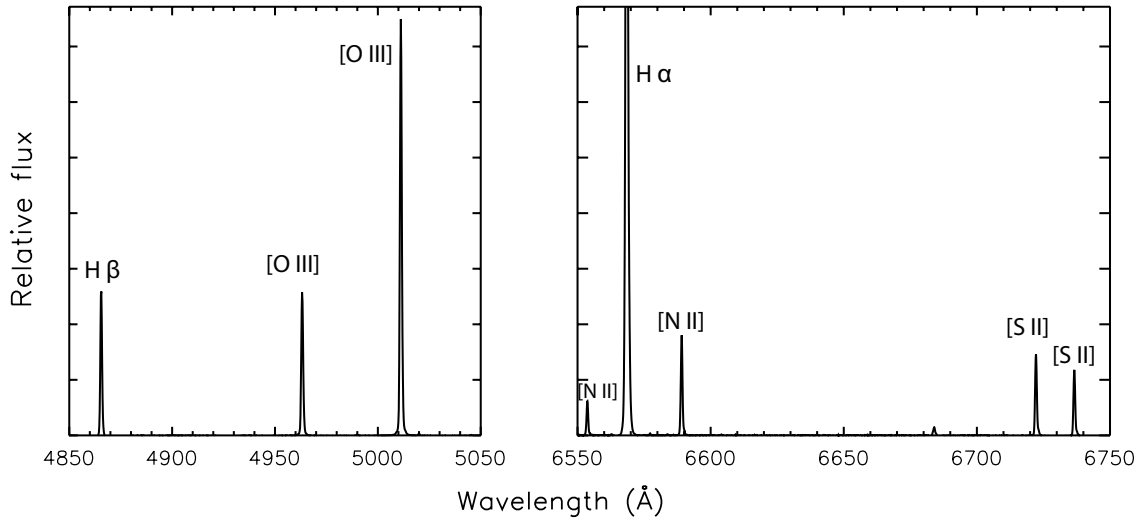

Figure 2.9 Nebular emission-line spectrum (LR03 and HR15N settings) with all epochs/exposures co-added for one line of sight of the VFTS sample. The strongest lines are identified.

on either side of the most prominent nebular emission lines (Figure 2.9). The stellar component was then subtracted from these spectra, leaving only the nebular spectrum in the spectral regions of interest. The nebular spectra from all the epochs/exposures of a given line of sight were finally co-added to maximize the S/N.

The spectral resolution of our data ($R \sim 10\,000$) is high enough to resolve the nebular line profiles, which are often complex and show multiple components (see an example in Figure 2.10). Following the methodology presented by Westmoquette et al. (2007), multiple Gaussian profiles were fitted to the strongest nebular lines using an IDL

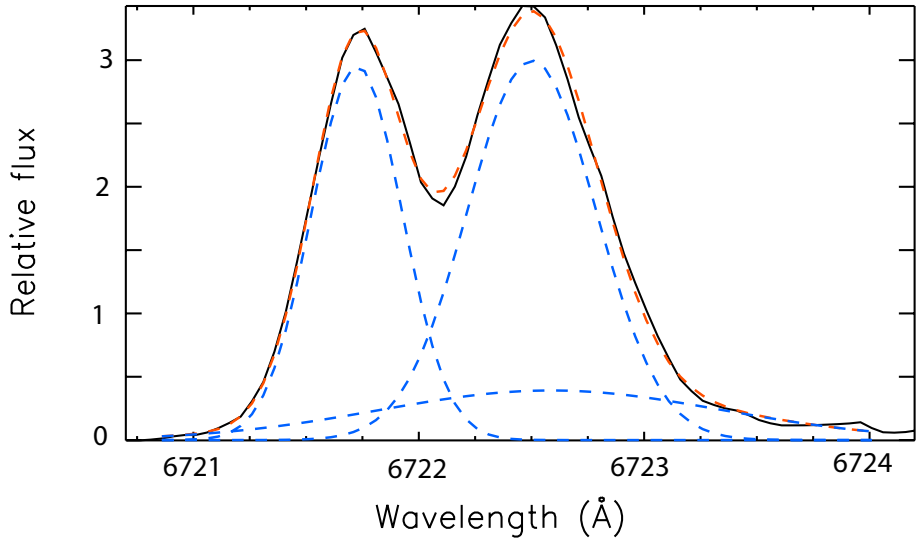

Figure 2.10 Example of a multiple Gaussian fit to the [S II] λ6717 line profile of one line of sight from the VFTS. The total fit is shown in red and the contribution of individual components in blue.

χ^2 fitting package called PAN[3] (Peak ANalysis; see Westmoquette et al. 2007). The centroids of the best-fit Gaussians were then used to calculate the line-of-sight gas velocities. Velocities measured from different lines typically agree within a few km s^{-1}.

2.5 Data reduction: VLT-FLAMES ARGUS

The ARGUS fibres are smaller than the MEDUSA fibres (0.″8 on the sky compared to 1.″2). They are also packed closer together, with over 300 spectra in a single ARGUS frame (given the dimensions of the array of microlenses), compared to 132 or less for MEDUSA. Cross-contamination is therefore potentially more of a problem and needs to be checked carefully. Fortunately, it did not appear to affect the stellar spectra that we extracted from the ARGUS observations. Otherwise, the reduction techniques for ARGUS and MEDUSA data are almost identical. The main difference is that in the case of 3D spectroscopic observations with ARGUS, a data cube containing the spatial information (i.e. mapping spaxels onto their appropriate on-sky position) for each wavelength bin has to be generated, as well as an error cube. A different kind of flat field (Nasmyth screen flat fields or so-called attached flats) is also available for ARGUS observations. They are obtained by illuminating the closed Nasmyth shutter with halogen lamps after the observations. For these flat fields, the sky and UVES fibres are not moved at all from their observing positions, which should ensure minimal

[3]R. Dimeo, 2005, PAN User guide: ftp://ftp.ncnr.nist.gov/pub/staff/dimeo/pandoc.pdf

differences between observing and calibration conditions. However, the attached flats were not used as noticeable differences were found between these flats and the 'standard' flats, possibly due to scattering within the instrument when the attached flats are taken (Taylor 2012).

The ARGUS frames for the VFTS were thus reduced using the same methods as for the MEDUSA data, apart from the sky subtraction and the combination of spectra from adjacent spaxels on the sky (individual stars typically extend over several spaxels). The extracted (cosmic-ray clipped) spectra were corrected to the heliocentric frame, and then combined as explained below. We note that the extraction of spectra of individual objects from integral field spectroscopic data can be done at different levels of sophistication. While complex techniques have been developed to deal with very crowded regions (e.g. Kamann et al. 2013), we adopted a straightforward approach which consists of identifying spatial pixels that are dominated by the contribution of a single star and obtain a spectrum of that star by summing the spectra in only those pixels. This simple method was found to perform well in the moderate crowding conditions around R136.

Sources were selected if they appeared isolated in the reconstructed ARGUS images and if they could be matched to a star (or multiple, densely-packed stars) in an archival HST F555W image (from the early release science observations of 30 Dor taken with the Wide-Field Camera Three, WFC3; De Marchi et al. 2011). Less isolated sources were also extracted if their spectra could be distinguished from those of their surroundings, and if they had a matching bright source in the WFC3 image. Some sources are obviously multiple in the WFC3 image but their spectra were retained because they might still prove useful in the analysis of the velocity dispersion of R136.

The spaxels to be combined for a given source were selected on the basis that they showed the same spectral features (and relative strengths) as the brighest/central spaxel of that source[4]. There are small positional shifts of approximately one spaxel between the different epochs of a given pointing. These shifts were taken into account when defining (for each frame) the spaxels that contribute to a given source. Spectra were extracted for a total of 41 sources from the ARGUS frames. The 37 unique ARGUS sources are listed in Evans et al. (2011), along with their coordinates determined from the centroids of matching sources in the WFC3 image (and transformed - for consistency - to the same astrometric system as the Selman-Skiff catalogue used for the MEDUSA targets; see Evans et al. 2011). As mentioned previously, these sources are

[4]Note that one disadvantage of ARGUS is that the spaxel size is relatively large compared to the field-of-view, such that the point spread function is not well sampled.

given a separate series of RA-sorted identifiers, starting with VFTS 1001, in order to distinguish them from targets observed with MEDUSA and/or UVES. Note that four MEDUSA/UVES sources were also observed with ARGUS (VFTS 542, 545, 570, and 585), as noted in Evans et al. (2011). The five ARGUS pointings and the location of the extracted sources are shown in Figure 2.11. More details about the spectral content of the ARGUS sample are given in Chapter 3 and Appendix B.

The four or five spaxels with the lowest counts in each pointing were used as local sky spectra. Even so, for most sources the nebular subtraction is still far from perfect given the small-scale variations mentioned previously. Before combining the sky spectra, a $5\,\sigma$ clip (compared to the noise of the median spectrum) was employed to remove remaining cosmic rays or artefacts. A weighted-average sky spectrum was created, then subtracted from the spectra from each of the source spaxels.

The effects of differential atmospheric refraction are clearly visible in the ARGUS spectra, with adjacent spaxels apparently dominated by the same source often having very different continuum profiles (e.g. see Figure 2.12). Thus, each spectrum was normalised individually before combining the contribution of different spaxels. This normalisation was done by a spline-fit across carefully selected continuum regions, then division of the spectrum by the resulting smooth curve. This method generally gave an excellent fit to the continuum, but is less certain for spectra with broad emission lines, for which the continuum is hard to define. The final spectrum of each source is a weighted average of the normalised spectra from the individual spaxels, again employing a $5\,\sigma$ clip around the median to remove spurious pixels.

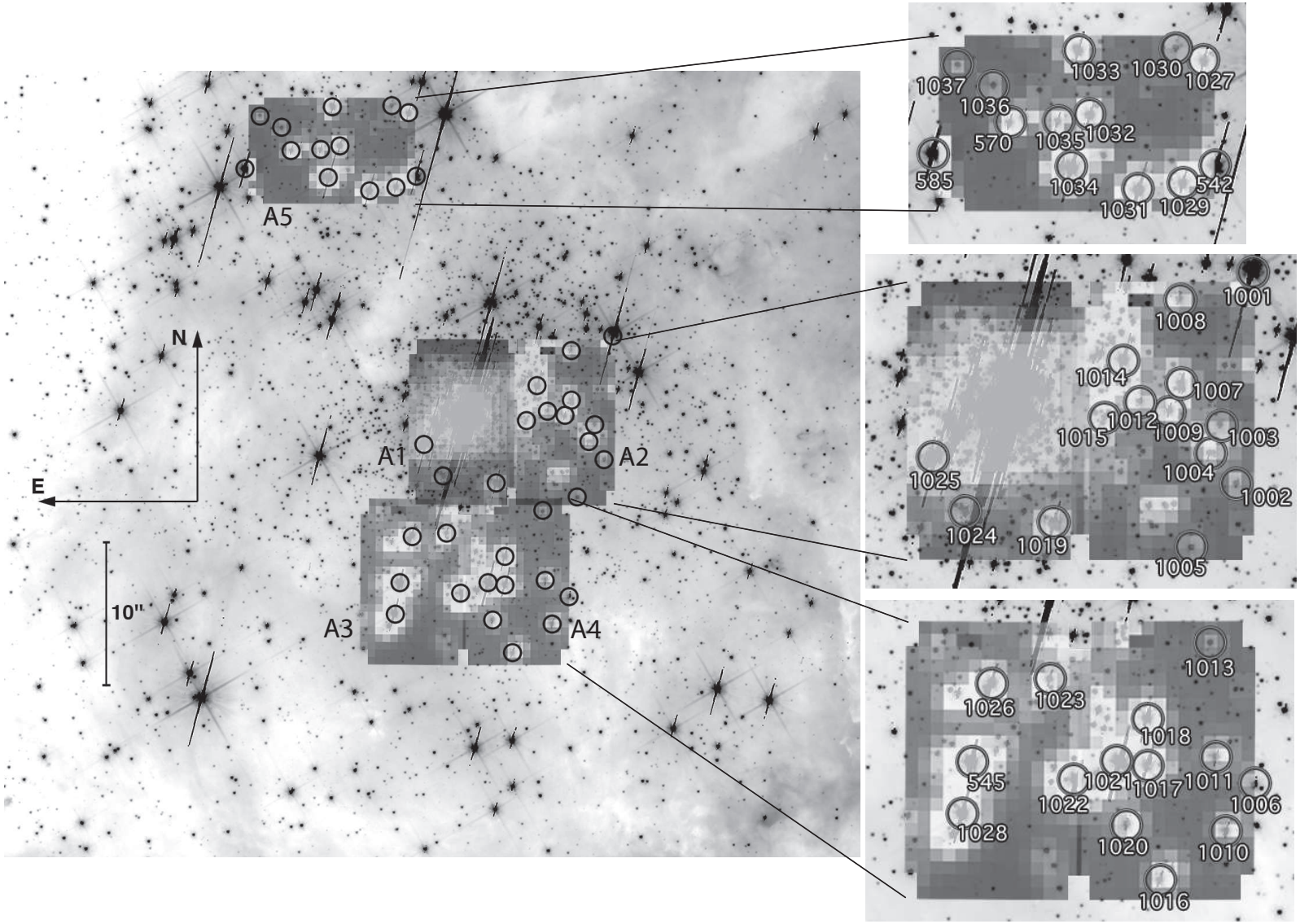

Figure 2.11 *Main image*: reconstructed images of the five ARGUS pointings overlaid on an F555W HST-WFC3 image (De Marchi et al. 2011). *Right-hand panels*: identification of individual extracted sources – *upper panel*: Field A5; *central panel*: Fields A1 (eastern pointing) and A2; *lower panel*: Fields A3 (eastern pointing) and A4.

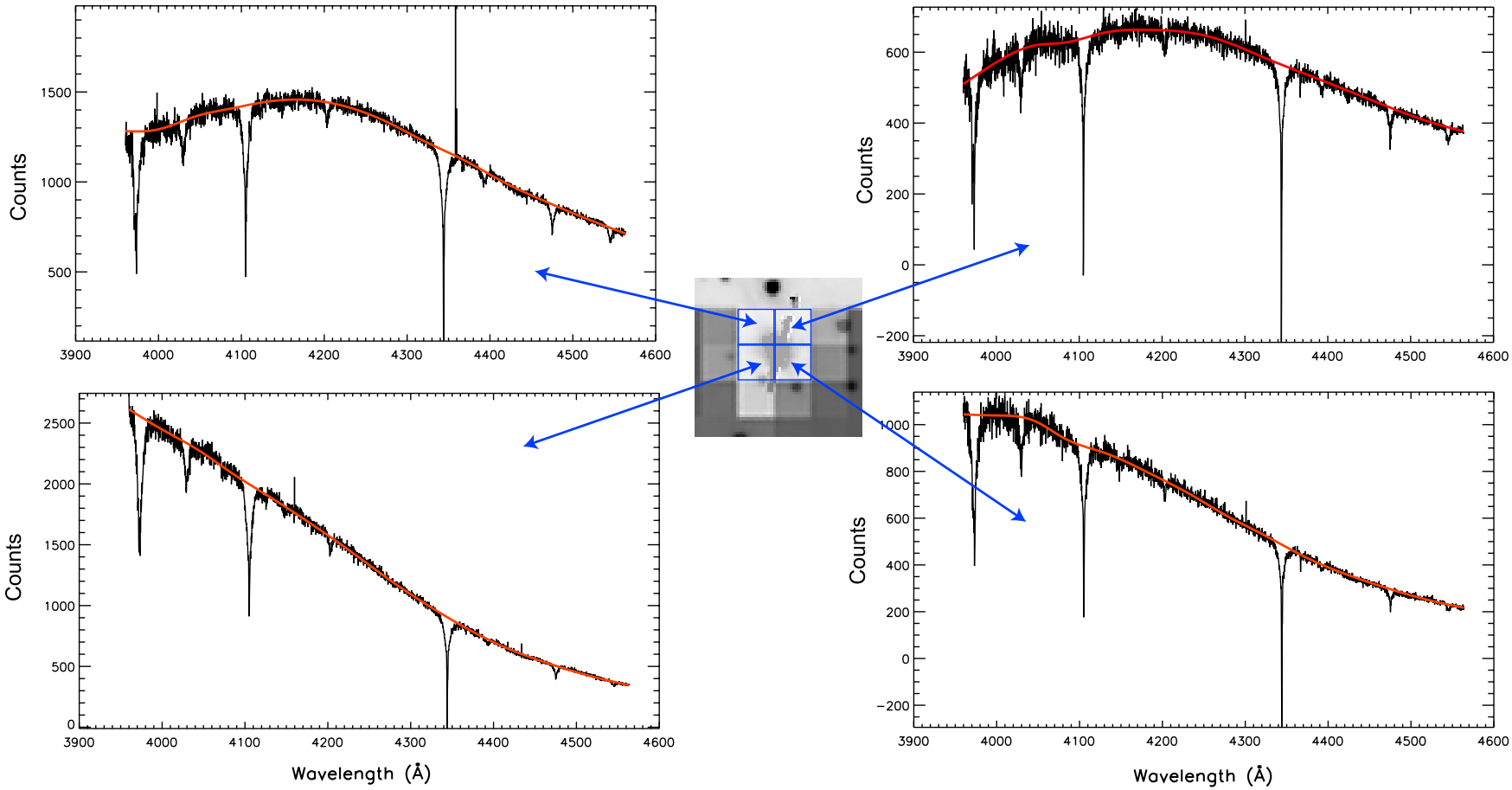

Figure 2.12 A close-up on the reconstructed ARGUS image (of one exposure) in the surroundings of VFTS 1033 (see Figure 2.11) and the spectra associated to the different spaxels of that source. The fitted continuum for each source is shown as a red curve, clearly showing the effect of differential atmospheric refraction. We can also see that the nebular emission for this source has been oversubtracted, illustrating that sky subtraction from fibre data is often not optimal.

2.6 A survey of massive stars in SGS-SMC 1

The data reduction for the FLAMES survey of massive stars in SGS-SMC 1 that will be discussed further in Chapter 6 was performed exactly in the same way as outlined above for the VFTS. The wavelength settings used were the same as the VFTS (although with exposure times of 2×1800 s for all the settings). Six MEDUSA configurations (with significant overlap between different configurations) were observed across the region of the supergiant shell SGS-SMC 1 in the SMC. The targets, initially selected from R-band photometry by simply imposing a magnitude cut $R < 17$, include about 20 O-type or early B-type stars, 300 later B-type stars, 11 A-type stars, and about 200 cooler types, 66 of which have a velocity consistent with the SMC. In total, 542 unique stars were observed in three nights of observations. All of these stars have been observed with the LR02 setting, and a large fraction of them with the LR03 and HR15N settings as well. At least two epochs were obtained for all of the targets, but the very short baseline makes studies of multiplicity limited compared to what was possible for the VFTS. The main objective of this survey of massive stars in the SMC was however different, and more specifically aimed at obtaining spectroscopy for the optical counterparts of X-ray sources detected in the region.

Chapter 3

A low velocity dispersion for the young massive cluster R136

3.1 Introduction

As we argued in Section 1.3.2, detailed dynamical studies of individual resolved clusters (i.e. in the Galaxy, SMC, or LMC) are necessary to make progress and understand the role of gas expulsion in the evolution of star clusters. In the case of radial velocity (RV) surveys, multi-epoch observations make it possible to detect binaries, which can then be removed and allow a cleaner estimate of the velocity dispersion (unless the orbital solution is known, in which case the centre-of-mass velocity can be included in the dispersion calculation). The young massive cluster R136 ($M \sim 10^5$ $M_\odot$, Andersen et al. 2009), in the 30 Doradus region of the LMC, is an ideal target to perform such a study and test the impact of gas expulsion given its young age of less than 2 Myr (de Koter et al. 1998; Massey & Hunter 1998; Crowther et al. 2010). It has recently carved a cavity in the surrounding ionised gas and its dynamics could have been affected by gas expulsion.

The identification of binaries was central to the study of stellar dynamics in 30 Doradus with the Gemini Multi-Object Spectrograph by Bosch et al. (2009), who found that the velocity dispersion of NGC 2070 went down from ~ 30 km s^{-1} to 8.3 km s^{-1} after correcting for binaries, confirming their prediction (Bosch et al. 2001) that the high velocity dispersion of NGC 2070 could be due to the orbital motions of undetected binaries. In order to perform a similar study for the dense surroundings of R136, a different observational approach was required because this region is too crowded for

fibre spectroscopy. As outlined in Chapter 2, a key component of the VLT-FLAMES Tarantula Survey (Evans et al. 2011) is multi-epoch spectroscopy in the inner part of 30 Dor with the FLAMES–ARGUS integral-field unit, which we use in the present chapter to obtain an estimate of the velocity dispersion of 'single' stars in R136. The central velocity dispersion is an important proxy for the dynamical state of the cluster and is required to estimate, for example, the central potential and relaxation time-scale, both of which are required for detailed numerical (N-body) calculations of R136-like objects (e.g. Portegies Zwart et al. 1999; Gieles et al. 2010a). As a result of the same study, the identification of massive binaries could eventually provide important clues to the star-formation process and the subsequent dynamical evolution of R136, in which binaries can be formed, ejected and destroyed. Our measurements will also serve as useful empirical input for the modeling of stellar interactions in dense clusters, such as the recent studies of Fujii & Portegies Zwart (2011) and Banerjee et al. (2012).

We report in this chapter on a velocity dispersion estimate for the young massive cluster R136 which was originally published in Hénault-Brunet et al. (2012a). In Section 3.2, we provide additional comments on the FLAMES–ARGUS IFU data for which the reduction procedure was described in Chapter 2. In Section 3.3, we present our RV and variability analysis of the stars observed with ARGUS. In Section 3.4, we discuss the spectral classification of the non-variable ARGUS sources. In Section 3.5, we briefly introduce the VFTS MEDUSA data complementing the ARGUS data. We calculate the velocity dispersion from the stars showing no variability and also estimate the contribution of errors and undetected binaries to the velocity dispersion in Section 3.6. The implications of the measured velocity dispersion for the dynamical state of R136 are discussed in Section 3.7. Finally, we summarize the results of this chapter in Section 3.8.

3.2 ARGUS data

The main data used in this chapter consist of the five ARGUS IFU pointings in the central arcminute of 30 Doradus (see Chapter 2; Figure 2.5), for which at least five epochs were obtained. This central region is relatively gas free, so the nebular contamination in the ARGUS spectra is not as important as in other regions of 30 Doradus. Spectra of 41 different sources, corrected to the heliocentric frame, were extracted from the data cubes. The LR02 setting of the GIRAFFE spectrograph ($\lambda = 3960 - 4570$ Å, $\Delta\lambda = 0.40$ Å, $R \equiv \lambda/\Delta\lambda \sim 10\,500$) is well-suited to probe the stellar dynamics of R136. This setting gives access to several stellar absorption lines suitable for RV analysis (see section 3.3) at the typical signal-to-noise ratio (S/N)

of $\sim$ 85 of our single-epoch spectra. To optimize the detection of binaries, the first two epochs were observed without time restrictions, and the third and fourth were observed with a minimum interval of 28 days between both the second and third, and third and fourth epochs. The fifth epoch was observed at least one year after the first epoch. Some observations were then repeated due to changes in conditions and other operational issues, providing additional epochs for three of the five pointings. Note that expanding the time baseline of the observations enhances the chances of detecting longer period binaries, but these binaries have a smaller impact on the velocity dispersion enhancement. Further details on the ARGUS data, the reduction and the extraction procedure can be found in Chapter 2 (see also Evans et al. 2011).

For the analysis presented in this chapter, individual exposures were considered to belong to the same epoch if their start time was separated by less than one hour. The multiple exposures composing a single epoch were then averaged using the errors (propagated throughout the reduction process) as weights and performing a $5\,\sigma$ clip around the median to remove remaining cosmic features. The spectra from individual exposures had already been normalised as part of the extraction procedure (see Chapter 2). The resulting epochs, their modified Julian date, and the corresponding ARGUS pointings and exposures are listed in Table A.1.

An effort was made to extract spectra preferably for sources that appeared single by comparing the ARGUS data cubes with an archival HST Wide-Field Camera Three (WFC3) F555W image (De Marchi et al. 2011) and identifying matching sources (see Chapter 2). Out of 41 ARGUS sources, 23 are dominated by one bright source from the WFC3 image. For these 23 ARGUS sources, only stars at least a factor of ten fainter (in data counts) are visible in the WFC3 image within the region covered by the ARGUS spatial pixels from which the spectrum was extracted. Even if those fainter stars were contaminating the ARGUS spectrum, it is doubtful that they would contribute significantly to the helium absorption lines used for our RV analysis (section 3.3.2). The ARGUS spatial elements for a further 11 extracted sources are dominated by one bright object from the WFC3 image, but could suffer from more significant contamination from nearby stars (typically at a level of $\sim 20\%$). The remaining seven ARGUS sources appear multiple in the WFC3 F555W image, with two or more densely-packed bright stars contributing at a comparable level to the flux in the region of the ARGUS source. These seven ARGUS sources were retained because they could still prove useful to our analysis (see below).

Note that even the spectrum of apparently single ARGUS sources (based on the WFC3 image) could contain contributions from multiple stars. The inner part of R136 is

densely populated with stars. Two stars could be several thousand AU apart and, given the distance to the LMC, still appear as a single source in the WFC3 image. The HST point spread function (PSF) of $\sim 0.1''$ indeed corresponds to a physical separation of about 5×10^3 AU at the distance of R136. HST probes a very different and non-overlapping separation range to the spectroscopic binaries discussed in this chapter, and we would not expect to detect the motion of unresolved binaries with such large separations given our spectral resolution and time coverage. These considerations are however not real concerns for our study because we can identify shorter period binaries from RV variations (section 3.3.2) and estimate the residual contribution of undetected binaries to the velocity dispersion using Monte Carlo simulations (section 3.6.5). Stars showing double/asymmetric line profiles or inconsistent absolute RVs between different lines can also be flagged as multiple (either true binaries or a chance alignment of stars along the line of sight). On the other hand, we can still use the sources which appear multiple in the WFC3 image if they show none of the above spectroscopic signs of binarity/multiplicity. In that case, one star could be dominating the spectrum, or several stars could be contributing without showing any apparent RV difference, and the source would still be valid to study the dynamics of the cluster.

3.3 Radial velocity and variability analysis

3.3.1 Zero-point errors

To check that zero-point errors do not affect our multi-epoch RV measurements significantly, we first cross-correlated the ARGUS calibration arc spectra of each epoch/exposure with the arc spectrum of the corresponding fibre from the first exposure of the first epoch. We then determined the zero-point velocity shifts from the peak of the resulting cross-correlation functions. The corresponding distribution of zero-point errors for over 20 000 such measurements is shown in Figure 3.1 (top panel). The vast majority of the measurements lie between -0.5 and $0.5\ \mathrm{km\,s^{-1}}$ with a peak at $\sim 0\ \mathrm{km\,s^{-1}}$, suggesting that the instrument wavelength calibration is remarkably stable and does not introduce spurious variations of stellar radial velocity between the different epochs.

To investigate possible issues with the telescope and/or instrument not accounted for in the arc spectra, we also performed a similar analysis on the nebular lines (Hγ and Hδ) from selected spaxels with minimum stellar contamination. The resulting distribution of velocity shifts for over 500 measurements peaks near $0\ \mathrm{km\,s^{-1}}$ and has a small

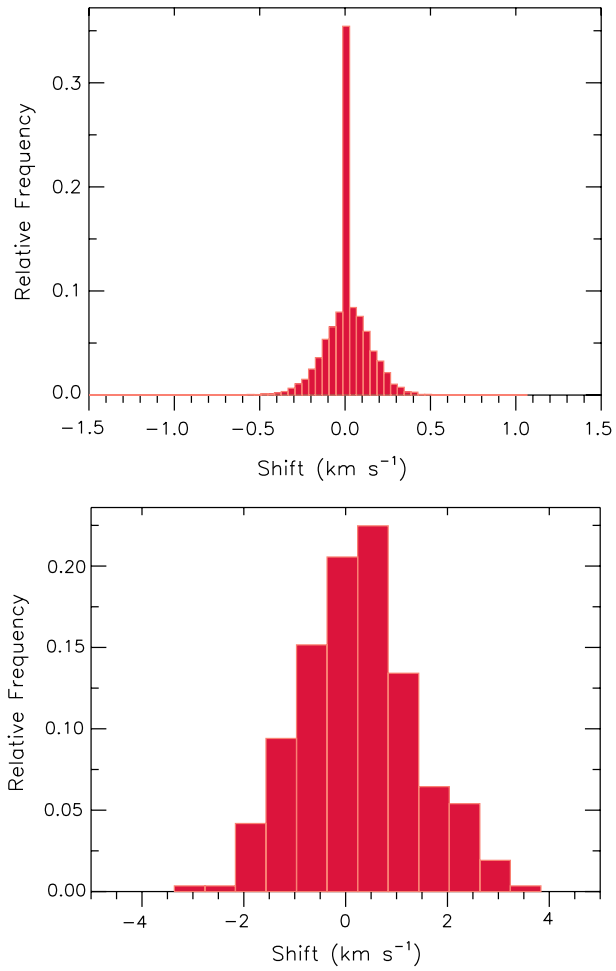

Figure 3.1 Distribution of zero-point velocity shifts from the cross-correlation of ARGUS calibration arc spectra (top) and from the cross-correlation of nebular lines (bottom) between different epochs/exposures.

standard deviation of $\sim 1\,\mathrm{km\,s^{-1}}$ (Figure 3.1, bottom panel), which again suggests that there are no significant systematic shifts between epochs. Note that the nebular line profiles are not as narrow as the lines from the arc spectra due to ubiquitous multiple components from the complex gas kinematics in the region, which means that the cross-correlation using nebular lines is less accurate. The small pointing shifts between different exposures and epochs (see Chapter 2) also means that the same spaxel can actually sample slightly different regions (where the gas velocities might differ) from one exposure/epoch to the next. This might contribute to increase the width of the distribution shown in the bottom panel of Figure 3.1.

3.3.2 Variability criteria

In order to exclude the stars exhibiting RV variations from our calculation of the velocity dispersion, we implemented the following quantitative assessment of the variability.

For each star and epoch, we started by fitting Gaussian profiles to individual stellar absorption lines (He II λ4200, He II λ4542, He I+He II λ4026, He I λ4143, He I λ4388 and He I λ4471, or a subset when some of these lines were too weak or the S/N too low). In principle, the profiles of the helium lines are not Gaussian, particularly in the wings. However, given the moderate S/N of our spectra and the noise in the line wings, the use of Gaussians provided good fits to the line profiles (see Figure 3.2) and did not affect the results. We used the MPFIT IDL least-squares fitting routine (Markwardt 2009) and Gaussian profiles defined by their central radial velocity, width, depth, and continuum value. An example fit is shown in Figure 3.2 for the ARGUS source VFTS 1026. The resulting $1\,\sigma$ error on the measured RV in this case is ± 2.1 km s^{-1}, illustrating the precision that can be achieved for a single epoch with a good quality spectrum. To check if errors in the normalisation of the continuum could influence the RV measurements, we also performed the fits allowing for a linear component instead of a constant continuum, but this did not affect the results. We chose the Gaussian fitting approach (as opposed to cross-correlation for example) because it can provide reliable error estimates on the velocities and directly yields absolute RVs, which we need to compute the velocity dispersion if different lines are used for different stars (see section 3.3.3). This method is also well suited to our data set, for which the quality of spectra varies significantly between stars and even from one epoch to the next.

The lines listed above are characteristic of the O-type stars composing the vast majority of our sample (see Table 3.2 for the spectral types of the sources showing no spectroscopic variability). These lines were the only lines generally strong enough to perform satisfactory RV measurements on the spectra of individual epochs. Metallic lines were not considered because they were generally too weak, and Balmer lines were ignored because their profiles and apparent RVs can be affected by stellar winds or strong/variable nebular contamination. When one of the fitted lines appeared significantly contaminated by nebular emission it was also rejected, unless the nebular component could be clearly identified and the fit could be performed on the wings of the line only. The most affected line was He I λ4471, but it was also occasionally a problem for the other He I lines.

From close inspection of all the fitted profiles, we first identified the stars showing double-lined spectroscopic binary (SB2) profiles. Four of the 41 ARGUS sources show

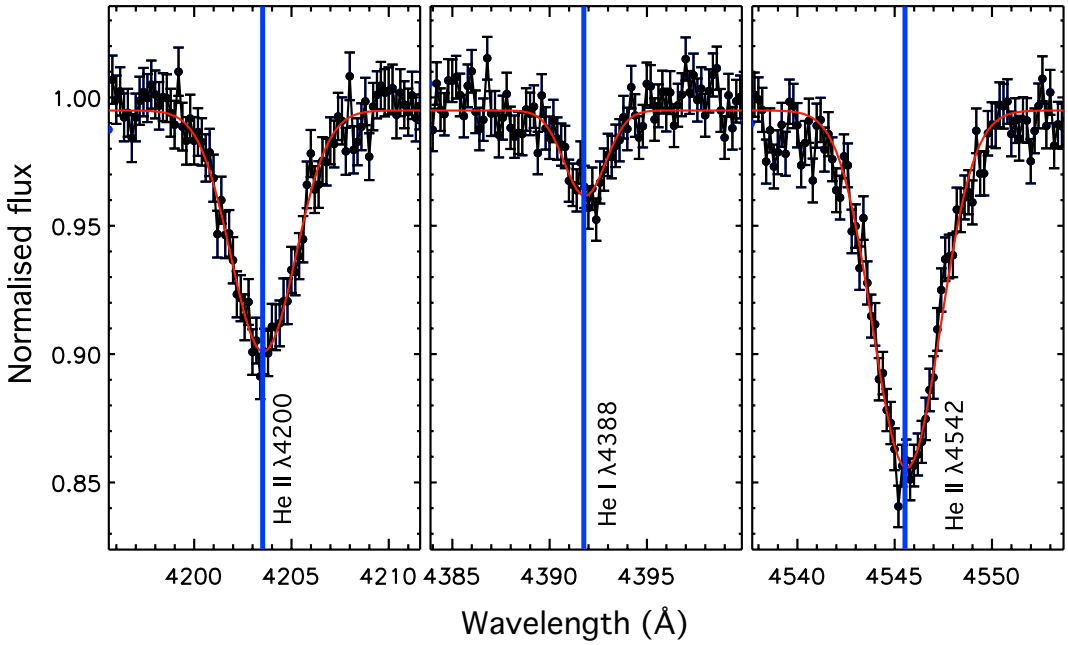

Figure 3.2 Example of a simultaneous Gaussian fit (i.e. same RV for all lines) to the He II λ4200, He I λ4388, and He II λ4542 absorption lines for an individual epoch of the ARGUS source VFTS 1026 (O2-4.5 + mid/late O, see Section 3.4).

SB2 profiles (VFTS 1016, 1019, 1031 and 1033), and none of them had a primary component with a constant RV throughout all epochs (based on the criteria below), suggesting that they are genuine multiple systems and not just the result of the alignment of two stars with different RVs along the line of sight. The epochs at which SB2 profiles are observed in these sources are indicated in Table A.2.

We considered a star as a radial velocity variable if the series of RV measurements of any of the fitted lines of that star contained at least one strongly deviant point, which we defined as

$$\left| \frac{RV_i - \mu}{\sigma_i} \right| > 4, \tag{3.1}$$

where RV_i and σ_i are the radial velocity and its $1\,\sigma$ error at epoch i, and μ is the weighted mean RV over all the epochs. If the above condition was fulfilled for at least one individual line, then the null hypothesis of constant RV was rejected.

For each star and each line, we also computed the value of χ^2 assuming a constant RV,

i.e.

$$\chi^2 = \sum_i \frac{(RV_i - \mu)^2}{\sigma_i^2}, \tag{3.2}$$

and rejected the constant RV hypothesis when the goodness of fit of a constant RV model to the data was poor, which we defined as

$$1 - P(\chi^2, \nu) < 10^{-4}, \tag{3.3}$$

where $P(\chi^2, \nu)$ is the probability that, in a χ^2 distribution with ν degrees of freedom (ν = number of epochs -1), the value of χ^2 is less than or equal to the value computed in equation 3.2. The thresholds adopted in equations 3.1 and 3.3 were chosen so that the probability of a false variability detection in our sample (given the sampling and accuracy of our measurements) remained negligible. In the analysis of the multiplicity properties of the O-type stars in the VFTS, Sana et al. (2013a) adopted slightly different variability criteria, but mention that their results are generally equivalent to those of a variability test based on the goodness of fit of a constant RV model like that of equations 3.2 and 3.3.

As a further check, we investigated line profile variations (LPV) by computing Time Variance Spectra (TVS; Fullerton et al. 1996). The only difference with the method of Fullerton et al. (1996) is that we used the known error bars at each pixel to define a wavelength-dependent threshold instead of using a flat threshold based on continuum noise. This has the advantage of taking into account the varying S/N as a function of wavelength. The TVS at wavelength λ is given by

$$\mathrm{TVS}(\lambda) = \frac{1}{N-1} \frac{N}{\sum_i 1/\sigma_i^2(\lambda)} \sum_i \frac{(f_i(\lambda) - \langle f(\lambda) \rangle)^2}{\sigma_i^2(\lambda)}, \tag{3.4}$$

where N is the number of spectra in the time series, $f_i(\lambda)$ and $\sigma_i(\lambda)$ are the flux and $1\,\sigma$ error at wavelength λ for epoch i, and $\langle f(\lambda) \rangle$ is the weighted average flux of all epochs at wavelength λ. The threshold for variability at a confidence level of 99% is

$$\mathrm{TVS}(\lambda) > \frac{N}{\sum_i 1/\sigma_i^2(\lambda)} \frac{P_{\chi^2}(0.01, N-1)}{N-1}, \tag{3.5}$$

where $P_{\chi^2}(0.01, N-1)$ is the cutoff value in a χ^2 distribution with $N-1$ degrees of

freedom such that the probability that a random variable is greater than this cutoff value is equal to 0.01. The cases for which significant variability is inferred from the TVS are indicated in Table A.2. These results generally confirm those obtained from the other variability tests, and in two cases help to establish significant variability in emission-line stars with no or only weak absorption lines. Figure 3.3 shows examples of TVS for two stars of our ARGUS sample, one revealing no variability and the other showing significant LPV. Note that the TVS often shows variability in nebular emission lines due to changes in conditions affecting the sky subtraction, but we ignore these spectral regions when assessing the variability of a star. The quantity $TVS^{1/2}$ is plotted in Figure 3.3 because it scales linearly with the size of the spectral flux deviations and gives a direct estimate of the amplitude of the variations.

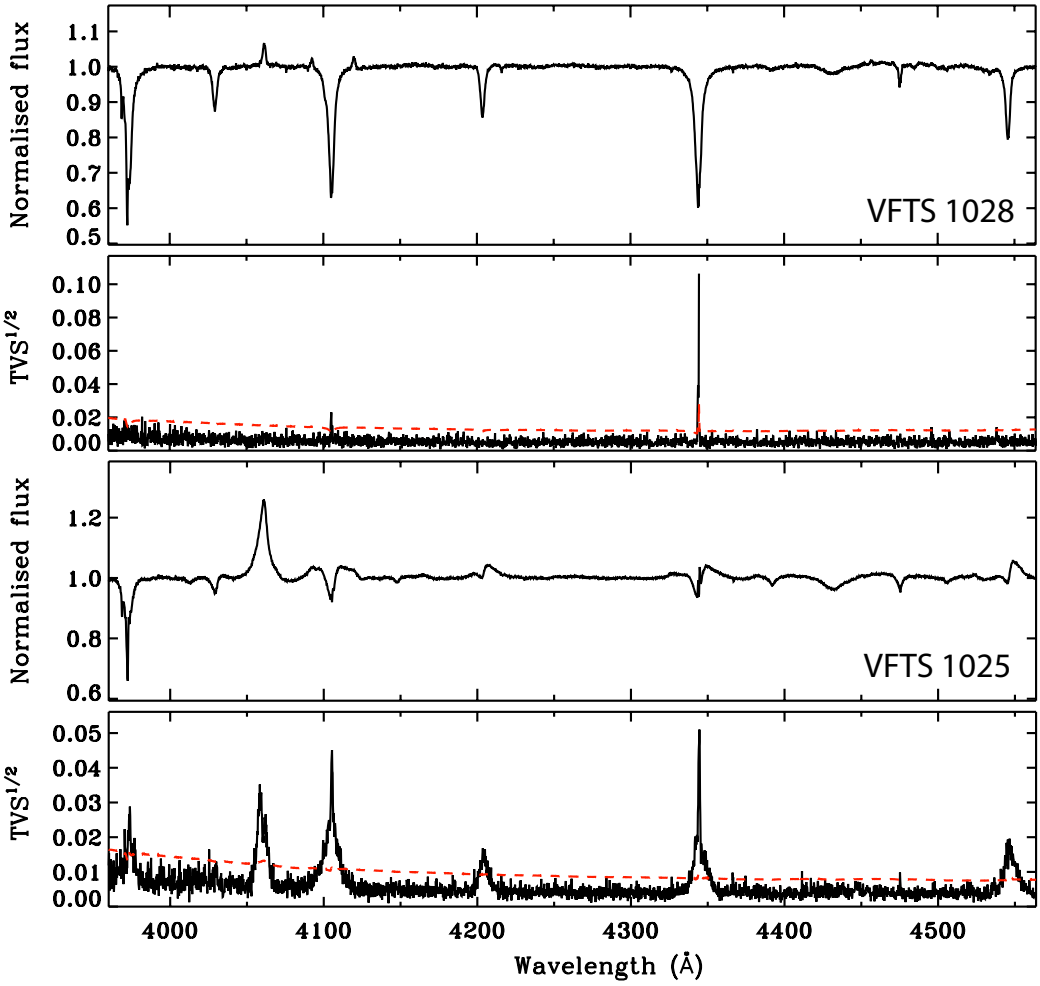

Figure 3.3 Weighted mean spectrum (first and third panels from the top) and Temporal Variance Spectrum ($TVS^{1/2}$; second and fourth panels from the top) for the ARGUS sources VFTS 1028 and VFTS 1025. The red dashed curves indicate the 99% confidence level for variability. Significant variability is only seen in the nebular emission lines of VFTS 1028, but it is detected in several stellar lines in VFTS 1025.

If none of the three tests above (equation 3.1, equation 3.3, and TVS) revealed variability in individual lines, we performed simultaneous Gaussian fits of He II λ4200, He II λ4542 and He I λ4388 (or a subset of these lines when one of them was too weak or simply not present) by forcing their central RV to be the same (see Figure 3.2 for an example). These three lines were adopted because they give reliable absolute RVs (see section 3.3.3). We can therefore fit them together to obtain more precise RV measurements. The series of RV measurements resulting from these simultaneous fits were then tested for variability using equations 3.1 and 3.3 again (see results in Table A.2). Stars still showing no sign of variability were then considered as suitable 'single stars' to study the dynamics of the cluster. The RVs of the ARGUS sources for all individual epochs are presented in Table A.3.

Out of 41 ARGUS sources, 16 are not detected as variable, 17 are variable (four SB2, 11 SB1, two emission-line stars with variability determined from the TVS), seven have too low a S/N for a meaningful variability analysis, and one is an emission-line star with no suitable absorption line for RV analysis and for which no significant variability was detected from the TVS.

3.3.3 Absolute radial velocities

For a given star, we want to use as many lines as possible to increase the precision of RV measurements, but at the same time we need to make sure that the selected lines give accurate results. In particular, all the lines fitted simultaneously to measure the RV of a star should give consistent results when fitted individually, and the selected lines should provide consistent absolute RVs if different subsets of lines are used for different stars (e.g. He I lines for late O-type stars and He II lines for early O-type stars).

To check the consistency of the absolute RVs measured from different lines, we compare in Figure 3.4 the RV of He II λ4542 with that of the other lines (of the same star) considered for the RV variability analysis. We choose this line as a reference for the comparison because it remains of reasonable strength across all O spectral subtypes. The He I and He II lines in a spectrum could be dominated by different components of a binary system and thus have different RVs, so we have only included the results from non-variable stars in that comparison. The RVs that we compare are the weighted means from all the individual epochs for each line and star. The rest wavelengths adopted to determine the absolute velocities are listed in Table 3.1.

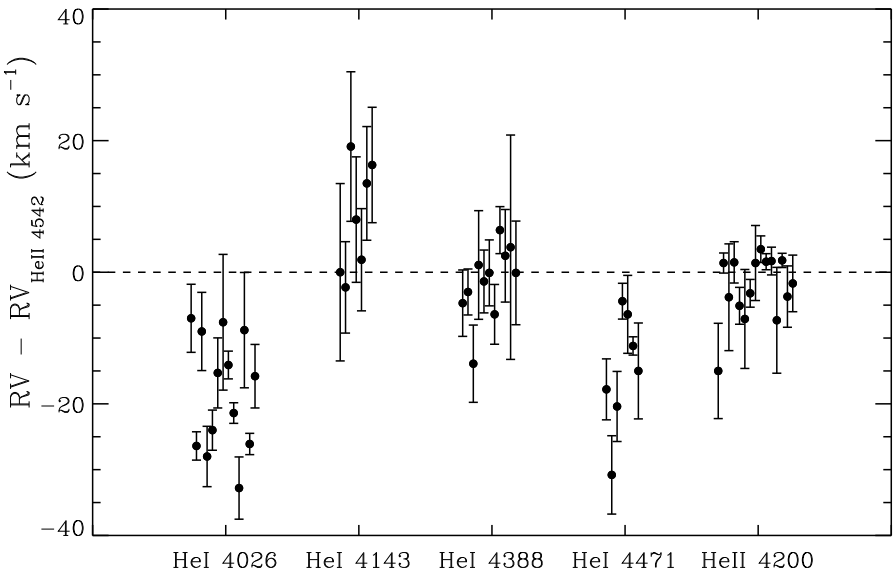

Figure 3.4 Difference between the absolute RVs measured from He II λ4542 and from the other stellar absorption lines considered in this study. Only stars showing no significant variability are included. The RVs are weighted means over all epochs of a given line and star.

Figure 3.4 shows that He I λ4388 and He II λ4200 have absolute velocities consistent with He II λ4542, with the expected number of measurements within $1\,\sigma$ of a zero RV shift between those lines. Because He I λ4143 is generally weak, the RV measurements of this line have large uncertainties. It is strong enough for our RV analysis in only a few ARGUS sources, making it harder to assess the reliability of this line for absolute RV measurements. For these reasons, we do not use He I λ4143 in our final absolute RV measurements. The comparison of Figure 3.4 also supports the contention

Table 3.1 Rest air wavelengths (λ_0) adopted for the principal helium lines in the ARGUS spectra. The lines suitable for accurate absolute RV measurements are highlighted in grey. Lines marked with a † symbol are blends, and the effective wavelength quoted in these cases are observed values. References: (1) Conti et al. (1977) ; (2) Peter van Hoof's Atomic Line List v2.04, http://www.pa.uky.edu/∼peter/atomic/ ; (3) NIST Atomic Spectra Data Base, www.nist.gov/pml/data/asd.cfm

Line	λ_0 [Å]	References
He I+He II λ4026	4026.072†	1
He I λ4143	4143.759	2
He I λ4388	4387.929	2
He I λ4471	4471.480†	3
He II λ4200	4199.832	2, 3
He II λ4542	4541.591	2, 3

that He I λ4471 and He I+He II λ4026 are not suitable for accurate absolute RV measurements. The RVs from these lines appear systematically shifted with respect to the RV of He II λ4542. For He I λ4471, the discrepancy can be attributed to the combination of the following factors: this line is a triplet transition with a forbidden component, it is susceptible to wind effects, for late O spectral subtypes it is blended with an O II line in its blue wing, and it also suffers the most from nebular contamination among the He I lines that we measured. The He I+He II λ4026 blend is dominated by He I λ4026.191 in late O-type stars and by He II λ4025.602 in early O-type stars. Since it is difficult to determine the level of contamination from the weaker component, which shifts the effective wavelength of this blend as a function of stellar temperature, the He I+He II λ4026 blend is not practical to use for absolute RV measurements.

Our choice of suitable lines for absolute RV measurements (He I λ4388, He II λ4200, and He II λ4542) is supported by the RV analysis performed in Sana et al. (2013a) on the O-type stars observed with MEDUSA as part of the VFTS (see Section 3.5). From similar comparisons to the one presented here, but with a larger sample, these authors concluded that the best consistency is observed between the lines He II λ4200, 4542, He I λ4388 and 4713, the latter being unavailable with the LR02 setting used for the ARGUS observations. The final RVs adopted for the non-variable ARGUS stars are therefore obtained from simultaneous fits of the three lines listed above, or a subset of them.

In stars with strong winds, infilling of photospheric absorption can modify the RV measured by Gaussian fitting for lines like He II λ4200 and He II λ4542 and also result in RV shifts between them. Comparison of Gaussian fitting measurements and values determined from CMFGEN models shows good consistency for O-type dwarfs and giants, but small shifts of a few tens of $\mathrm{km\,s^{-1}}$ for supergiants (P. Crowther, private communication). In our calculation of the velocity dispersion (Section 3.6.1), we therefore pay particular attention to the stars that are identified as possible supergiants (Section 3.4).

3.4 Spectral classification of ARGUS non-variable sources

To get a general idea of the content of our ARGUS sample in terms of spectral types, we classified the non-variable and presumably single stars. We did not attempt the complex task of classifying the binaries/variable stars, partly because the limited wavelength coverage of the ARGUS spectra makes it even more difficult, and because only the

apparently single stars are retained for the analysis of the dynamics anyway.

To assign spectral types, we visually inspected the ARGUS spectra degraded to an effective resolving power of 4 000 and, following the premises of Sota et al. (2011), we performed a morphological classification. In particular, for stars at intermediate and late subtypes, we used the eye-estimated line ratios of He I+II λ4026 to He II λ4200, He I λ4471 to He II λ4542, He I λ4388 to He II λ4542, He I λ4143 to He II λ4200 and Si III λ4552 to He II λ4542 in order to assign the spectral subtype. For the hottest stars (early subtypes), on the other hand, we were not able to exploit the primary criteria based on the nitrogen ionization equilibrium because our ARGUS spectra do not cover wavelengths longwards of $\sim$ 4570 Å and therefore do not include the crucial N III emission lines near 4640 Å. We thus concentrated on criteria related to the initial appearance of certain He I lines (such as He I λ4471, He I λ4143, and He I λ4388), and the presence and strength of N IV λ4058 and the Si IV doublet in emission. The morphological classification of our targets was furthermore constrained by comparing the degraded spectra to the spectra of O-type standards of solar metallicity compiled for the Tarantula Survey (Sana et al., in preparation) as well as to the spectra of VFTS targets obtained with MEDUSA-GIRAFFE which had already been classified (Walborn et al., in preparation).

Assigning a luminosity class to the ARGUS targets was more difficult because we could not exploit the selective emission effects in He II λ4686 and N III $\lambda\lambda$4634–4640–4642 (at subtypes earlier than O8), and the value of the He II λ4686/He I λ4713 ratio (at subtypes O9-9.7). While at late-O types one could still rely on secondary criteria, such as the ratio of Si IV λ4089 to He I λ4026, no alternative luminosity diagnostics exist at early- and mid-O types. Given this situation, we decided to follow Conti & Alschuler (1971) and exploit the increasing intensity of Si IV λ4089 relative to the nearby He I λ4143 (at subtypes later than O5 only).

The classification of the non-variable ARGUS targets, derived as outlined above, is presented in Table 3.2. In Section B of the appendix, we comment on specific sources, in particular those that have revised spectral types and the three that appear to have composite spectra. The accuracy of the spectral types reported in Table 3.2 for the ARGUS sources is typically between one and one and a half subtypes, with uncertainties caused by the effects of nebular emission, rotation (Markova et al. 2011), and metallicity (Markova et al. 2009). The uncertainty on the luminosity class is significantly larger as we were only able to separate the stars into two broad categories: high luminosity objects (luminosity class I/II) and low luminosity objects (luminosity class III/V). For completeness, we also include previously published spectral types in Table 3.2.

Table 3.2 Coordinates, RVs, and spectral types of ARGUS and MEDUSA sources showing no significant variability. Spectral types were determined in this work (see Section 3.4) for the ARGUS sources and by Walborn et al. (in preparation) for the MEDUSA sources, unless otherwise indicated. The sources are sorted by increasing projected radial distance (r_d) from R136-a1 ($\alpha = 5^h38^m42^s.39$, $\delta = -69°06'02.''91$, J2000). References: MH = Massey & Hunter (1998), WB97 = Walborn & Blades (1997). *Aliases are from Selman et al. 1999 (S99-), Hunter et al. 1997 (R136-), Malumuth & Heap 1994 (MH-), Parker 1993 (P93-) and Melnick 1985 (Mk).

ID		Data	α	δ	r_d	RV	Spectral type
VFTS	Aliases*		(2000)	(2000)	[pc]	[km s^{-1}]	
1024	S99-147, R136-226, MH-623	ARGUS	05 38 42.685	−69 06 07.03	1.1	263.7±2.3	O8.5 III/V
1014	S99-56, R136-29, MH-203, P93-863	ARGUS	05 38 41.515	−69 06 00.83	1.2	266.5±0.7	O2-4.5+mid/late O O3 V [MH98]
1012	S99-249, R136-151, MH-178	ARGUS	05 38 41.386	−69 06 02.49	1.3	264.6±2.8	O9 III/V
1009	S99-165, R136-88, MH-141	ARGUS	05 38 41.163	−69 06 02.83	1.6	274.2±1.4	O6.5 III/V
1007	S99-95, R136-60, MH-129, P93-827	ARGUS	05 38 41.077	−69 06 01.74	1.7	264.1±1.3	O6.5 III/V
1004	S99-193, R136-126, MH-95	ARGUS	05 38 40.848	−69 06 04.51	2.0	274.4±2.0	O9.5 III/V
1008	S99-163, R136-96, MH-134	ARGUS	05 38 41.108	−69 05 58.33	2.0	277.3±1.0	ON6.5 I/II
1023	S99-142, R136-83, MH-591	ARGUS	05 38 42.631	−69 06 10.91	2.0	266.4±2.0	O8 III/V O6 V [MH98]
1026	(S99-191), R136-41, MH-716, Mk35N	ARGUS	05 38 43.083	−69 06 11.26	2.2	265.0±0.9	O2-4.5+mid/late O O3 III(f*) [MH98] O8: V [WB97]
1002	S99-312, R136-194, MH-77	ARGUS	05 38 40.646	−69 06 05.73	2.4	272.7±5.6	O9.5 III/V
1018	S99-88, R136-37, MH-290, P93-900	ARGUS	05 38 41.887	−69 06 12.45	2.4	258.4±0.6	O2-4.5+mid/late O O3 III(f*) [MH98]
1020	S99-178, R136-101, MH-314	ARGUS	05 38 42.023	−69 06 16.75	3.4	267.4±0.9	O3-4
1006	S99-257	ARGUS	05 38 41.066	−69 06 15.16	3.4	264.2±3.9	O6.5 III/V
1028	S99-37, R136-23, P93-1036, Mk35S	ARGUS	05 38 43.274	−69 06 16.45	3.5	271.9±0.5	O3.5-4.5 O3 III(f*) [MH98] O4-5 V: [WB97]
1010	S99-189, R136-103, MH-156	ARGUS	05 38 41.268	−69 06 16.94	3.7	283.1±2.2	O7 III/V
468	S99-86, MH-17, P93-706, Mk36	MEDUSA	05 38 39.38	−69 06 06.39	4.0	272.0±0.8	O2 V((f*)) + OB

Table 3.2 continued

ID		Data	α	δ	r_d	RV	Spectral type
VFTS	Aliases*		(2000)	(2000)	[pc]	[km s^{-1}]	
477	S99-455	MEDUSA	05 38 39.75	−69 05 50.55	4.5	265.3±3.5	O((n))
1035	S99-169, R136-109	ARGUS	05 38 44.321	−69 05 45.05	5.0	268.5±2.2	O8.5 I/II
							O8 V [MH98]
601	S99-91, MH-986, P93-1317, Mk14N	MEDUSA	05 38 46.29	−69 05 59.25	5.1	266.8±0.6	O5-6 V((n))z
							O5 V((f)) [MH98]
							O4 V [WB97]
484	S99-124	MEDUSA	05 38 40.37	−69 05 43.72	5.3	284.2±1.0	O6-7 V((n))
611	S99-270	MEDUSA	05 38 46.90	−69 05 58.71	5.9	265.4±2.2	O8 V(n)
554	S99-343	MEDUSA	05 38 43.79	−69 05 38.70	6.1	275.6±1.4	O9.7 V
446	S99-194	MEDUSA	05 38 38.26	−69 06 17.29	6.4	258.9±5.0	O Vnn((f))
607	S99-294	MEDUSA	05 38 46.76	−69 05 48.75	6.6	257.8±1.0	O9.7 III
476	S99-206	MEDUSA	05 38 39.75	−69 05 39.21	6.7	270.1±2.2	O((n))
505	S99-265	MEDUSA	05 38 41.49	−69 05 34.52	7.0	265.5±3.4	O9.5 V-III
536	S99-295	MEDUSA	05 38 42.82	−69 06 32.43	7.2	248.4±1.4	O6 Vz
582	S99-414	MEDUSA	05 38 45.19	−69 05 37.43	7.2	270.2±2.3	O9.5 V((n))
615	S99-218	MEDUSA	05 38 47.33	−69 06 17.70	7.3	256.4±7.6	O9.5 IInn
515	S99-434	MEDUSA	05 38 41.86	−69 05 32.40	7.4	267.4±2.0	O6-9p
513	S99-266	MEDUSA	05 38 41.81	−69 05 31.91	7.6	266.3±1.3	O6-7 III-II(f)
622	S99-333	MEDUSA	05 38 48.12	−69 06 12.27	7.8	272.0±1.6	O9.7 III
498	S99-347	MEDUSA	05 38 41.19	−69 06 35.17	8.0	265.9±7.2	O9.5 V
451	S99-346	MEDUSA	05 38 38.52	−69 06 29.92	8.3	277.3± 10.8	O9: III:(n)
483	S99-309	MEDUSA	05 38 40.24	−69 05 30.78	8.3	275.4±2.7	O9 V
540	S99-372	MEDUSA	05 38 43.08	−69 06 36.88	8.3	242.7±1.1	B0 V
560	S99-350, P93-1139	MEDUSA	05 38 44.35	−69 06 40.73	9.5	259.7±0.9	O9.5 V
465	S99-365, P93-700	MEDUSA	05 38 39.28	−69 06 38.93	9.6	255.8±4.4	O5: Vn

3.5 Supplementary MEDUSA data

To complement our RV measurements of the ARGUS sources, we also include the RV measurements of the non-variable O-type stars observed with MEDUSA-GIRAFFE (Sana et al. 2013a) in the inner 10 pc of R136. This gives us 22 additional stars, 20 of which are located between 5 and 10 pc in projection from the centre of the cluster. We do not consider stars beyond 10 pc from the centre in our analysis of R136. Although partly arbitrary, this cutoff at 10 pc is a reasonable trade-off between increasing the number of stars in our sample and limiting the possible contamination from nearby clusters or other star formation events in the surroundings of R136.

The MEDUSA observations (see Chapter 2) were performed using three of the standard MEDUSA-GIRAFFE settings (LR02: $\lambda = 3960 - 4564$ Å, $\Delta\lambda = 0.61$ Å, $R \sim 7\,000$; LR03: $\lambda = 4499 - 5071$ Å, $\Delta\lambda = 0.56$ Å, $R \sim 8\,500$; HR15N: $\lambda = 6442 - 6817$ Å, $\Delta\lambda = 0.41$ Å, $R \sim 16\,000$). To detect RV variables, six epochs were observed for the LR02 setting with time constraints similar to those of the ARGUS observations (section 3.2 and Table A.1).

The RV and variability analysis of these stars is presented in Sana et al. (2013a) in the context of a study of the multiplicity of O-type stars in 30 Dor. The method is similar to the one we applied in Section 3.3.2. As a consistency check, we applied our method on the LR02 MEDUSA spectra of several O-type stars and found absolute RVs and $1\,\sigma$ uncertainties fully consistent with the results from the Sana et al. study. To illustrate this, we compare in Figure 3.5 the RV obtained with the method presented in this chapter with the RV measured by Sana et al. for the first epoch of the apparently single MEDUSA sources added to our sample (and listed in Table 3.2). The notable difference in the uncertainty found in some cases can be attributed to the different number of lines used in the fit. Because of the excellent consistency between both approaches, we do not repeat all the RV measurements of the MEDUSA stars, but adopt the values from the Sana et al. paper instead. For two of those additional MEDUSA stars, the luminosity class could not be constrained, but none of the others with well-defined luminosity classes are identified as supergiants (Walborn et al., in preparation). The RVs of these stars, obtained from Gaussian fitting, should therefore be reliable as discussed in section 3.3.3. The spectral types of the non-variable MEDUSA O-type stars used here, determined by Walborn et al. (in preparation), are given in Table 3.2.

Note that in parallel to the ARGUS observations, a few stars were also observed in the inner 10 pc of R136 with the Ultraviolet and Visual Echelle Spectrograph (UVES),

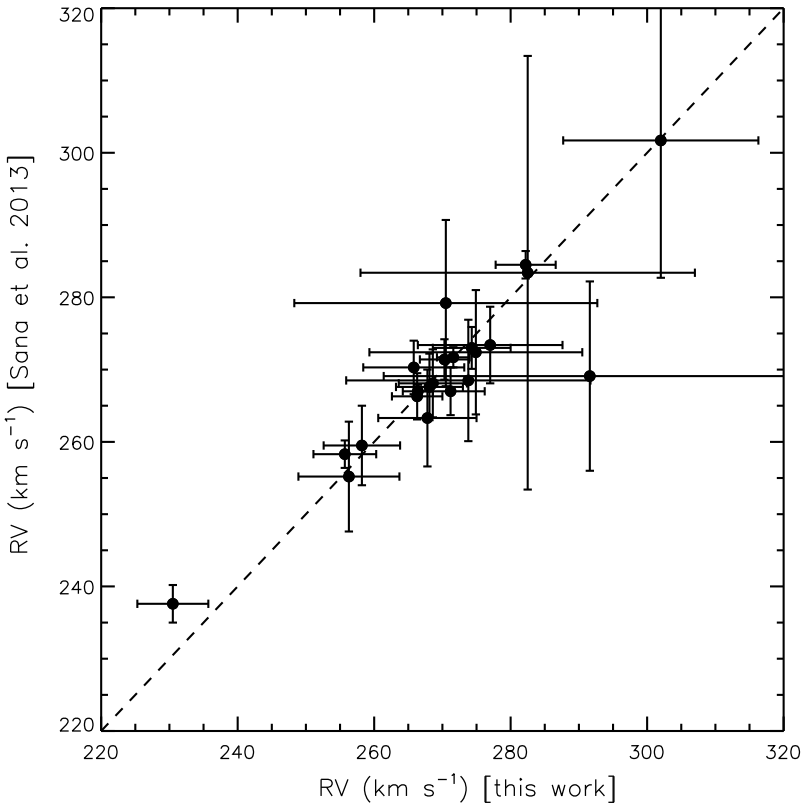

Figure 3.5 RVs obtained with the method presented in this chapter compared with the RVs measured by Sana et al. (2013a) for the first epoch of the apparently single MEDUSA sources added to our sample.

providing a greater resolving power than the GIRAFFE spectrograph. All the UVES targets but one in this region were also observed with ARGUS or MEDUSA, and these were already shown to be binaries/variable based on the ARGUS or MEDUSA observations alone. One star was observed only with UVES; Mk 39, an O2.5 If*/WN6 star (Crowther & Walborn 2011), which is not suitable for our RV analysis because the He II lines are wind contaminated.

Our final sample of apparently single ARGUS and MEDUSA stars within 10 pc from the centre of R136 is presented in Table 3.2. These are all the stars that we use for the analysis of the dynamics in the following sections. Their absolute RVs and their projected distance from the centre of the cluster (which we adopt to be the position of the very massive star R136-a1) are also listed. The projected distances are for an adopted distance modulus of 18.5 mag (see Evans et al. 2011). The absolute RV adopted for a given star is the weighted mean RV of all epochs. The spatial distribution of variable and non-variable ARGUS sources is shown in Figure 3.6, along with the positions of the non-variable MEDUSA O-type stars added to our sample.

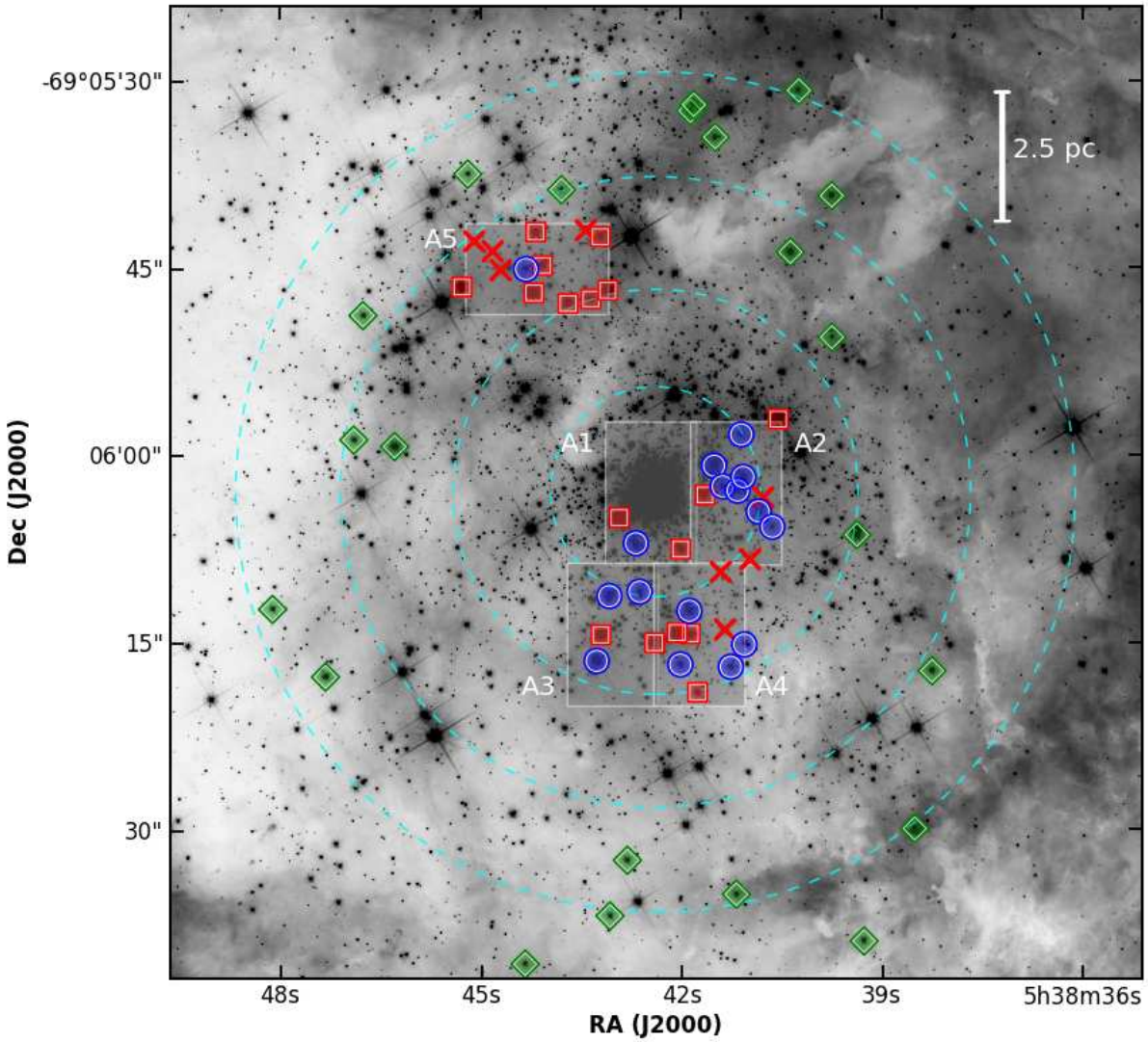

Figure 3.6 Distribution of ARGUS and MEDUSA sources used in this work overlaid on an F555W HST-WFC3 image of R136. ARGUS stars in which no variability was detected are shown as blue circles, variable ARGUS sources are represented by red squares, and ARGUS sources with too low S/N for RV analysis or no suitable absorption lines are indicated by red crosses. The ARGUS IFU pointings (A1 to A5) are also shown as transparent grey rectangles. MEDUSA non-variable stars added to the sample are represented by green diamonds. The dashed circles indicate projected radial distances of 2, 4, 6, and 8 pc from the centre of R136.

3.6 Velocity dispersion

3.6.1 Velocity dispersion upper limit

We can now determine the observed line-of-sight velocity dispersion (σ_{1D}) from the RV measurements of the non-variable stars. Because any effect not yet taken into account

(e.g. undetected binaries, intrinsic errors) would tend to increase the inferred σ_{1D}, we can consider that the results shown in this subsection represent an upper limit to the actual line-of-sight velocity dispersion of the cluster.

In what follows, the weighted mean radial velocity and the velocity dispersion (σ_{1D}), as well as their associated errors, are calculated by using the maximum likelihood estimators described by Pryor & Meylan (1993). This method assumes that the RV for each star is drawn from a normal distribution with the standard deviation being the quadrature sum of the individual RV uncertainty and the cluster line-of-sight velocity dispersion. Standard techniques for forming the likelihood of a set of velocities and finding its maximum lead to two equations that can be solved numerically for the mean velocity and the dispersion. Pryor & Meylan (1993) also provide equations for the variances of these quantities. Note that the velocity dispersion computed in this way is generally very similar to what is determined from basic equations, i.e. (Bevington 1969)

$$\mu = \frac{1}{\sum_i 1/\sigma_i^2} \sum_i \frac{RV_i}{\sigma_i^2}, \tag{3.6}$$

$$\mathrm{Var} = \frac{1}{\sum_i 1/\sigma_i^2} \sum_i \frac{(RV_i - \mu)^2}{\sigma_i^2}, \tag{3.7}$$

$$\sigma_{1D} = \sqrt{\mathrm{Var}\ \frac{N}{N-1}}, \tag{3.8}$$

where σ_i is the uncertainty on the RV measurement RV_i, μ is the weighted mean RV, Var is the variance, and N is the number of measurements. The method of Pryor & Meylan (1993) however has the advantage of providing a straightforward way of estimating the uncertainty on σ_{1D}.

In the upper panel of Figure 3.7, we present, as a function of projected radial distance from the centre of R136, the σ_{1D} of all the non-variable stars within that radius. Apart from an apparent increase in σ_{1D} in the inner region (likely not significant[1]), the velocity dispersion profile is relatively flat. However, note that what is shown in Figure 3.7 is not exactly the velocity dispersion profile (i.e. the velocity dispersion as a function of radius) due to the cumulative nature of the plot. For the stars within 5 pc from the centre, we find $\sigma_{1D} \lesssim 6\ \mathrm{km\,s^{-1}}$. Two stars dominate the increase in σ_{1D} between 5 and

[1]Also note that the low number of stars used to compute the dispersion in the inner region results in a less reliable associated error on σ_{1D}.

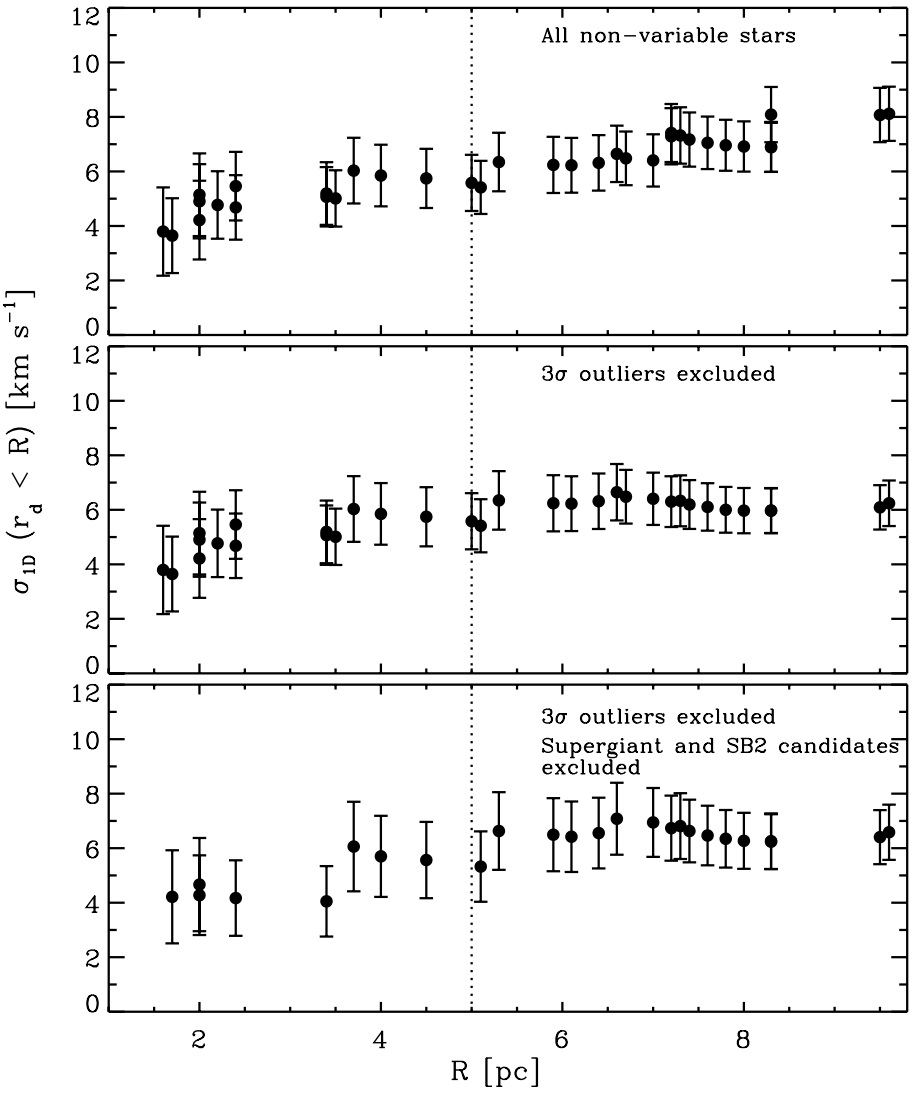

Figure 3.7 Observed line-of-sight velocity dispersion, as a function of R, for the stars within a projected radial distance R from the centre of R136. In the top panel, all the non-variable stars (see Table 3.2) are included. In the middle panel, two stars with a radial velocity more than 3σ away from the mean RV are excluded. In the bottom panel, supergiant and SB2 candidates are also excluded. In each panel, the first point from the left is the velocity dispersion of the four stars closest to the centre, the second point is the velocity dispersion of the innermost five stars, and so on.

10 pc: VFTS 536 ($r_d = 7.2$ pc; RV $= 248.4 \pm 1.4$ km s^{-1}) and VFTS 540 ($r_d = 8.3$ pc; RV $= 242.7 \pm 1.1$ km s^{-1}).

As a next step, to see the effect of possible outliers (slow runaways or massive stars along the line of sight but not members of R136), we exclude the stars with an RV more than $3\,\sigma$ away from the mean RV of our sample (268.3 ± 1.1 km s^{-1}). We choose σ to be 6 km s^{-1}, the observed velocity dispersion of the stars within 5 pc from the centre. VFTS 536 and VFTS 540 are indeed $>3\,\sigma$ outliers, and excluding them results

in an even flatter profile (Figure 3.7, middle panel).

When also excluding possible supergiants (I/II or no luminosity class attributed in Table 3.2), for which the RVs obtained from Gaussian fits could be problematic (see Section 3.3.3), and SB2 candidates (composite spectra, see Table 3.2 and Appendix B), the results do not change significantly, although more fluctuations are seen in the profile and the error bars are larger due to the smaller number of stars (Figure 3.7, bottom panel). The apparent increase in the inner $2-3$ pc also becomes even less significant when these supergiant and SB2 candidates are excluded.

In Section 3.6.5, we estimate the contribution of errors and undetected binaries to σ_{1D} and attempt to reproduce the observed velocity dispersion for the stars within 5 pc (in projection) from the centre, i.e. $\sigma_{1D} = 6$ km s^{-1}. We could choose a different radius, but because the velocity dispersion profile appears remarkably flat in the inner 10 pc, this would not change the results significantly. There is also a natural cut at ~ 5 pc if we consider the definition of a cluster proposed by Gieles & Portegies Zwart (2011), which states that stellar agglomerates for which the age of the stars exceeds the crossing time are bound and thus referred to as star clusters. The crossing time is roughly $2r/\sigma_{1D}$, where $2r$ is the distance for a star to travel from one side of the cluster to the other. Given an age of ~ 2 Myr for R136 and $\sigma_{1D} \sim 5$ km s^{-1} (after correcting for binaries; see Section 3.6.5), we can conclude that the stars that are physically within ~ 5 pc from the centre are part of the cluster following the above definition.

3.6.2 Contamination by "halo" stars

The surface brightness profile of R136 suggests that it is not a single-component cluster but the composite of a real cluster and a "halo", i.e. an OB association, with the latter contributing to more than 50% and possibly as much as 90% of its total integrated light (Maíz-Apellániz 2001; Mackey & Gilmore 2003). It is therefore worth asking how much could the OB association contaminate our velocity dispersion measurement for the cluster. In the double-component EFF fit (Elson et al. 1987, see Section 3.7) to the surface brightness profile of R136 by Mackey & Gilmore (2003), the projected radius where the two components contribute equally is at about 5 pc. If we consider the inner profile as the cluster and the outer profile as the halo, we can conclude from this fit that the contribution of halo stars projected on the cluster is negligible ($\lesssim 5\%$) in the inner 1.25 pc, but it could be significant beyond 5 pc.

We might expect the OB association to have a low velocity dispersion, as is observed in

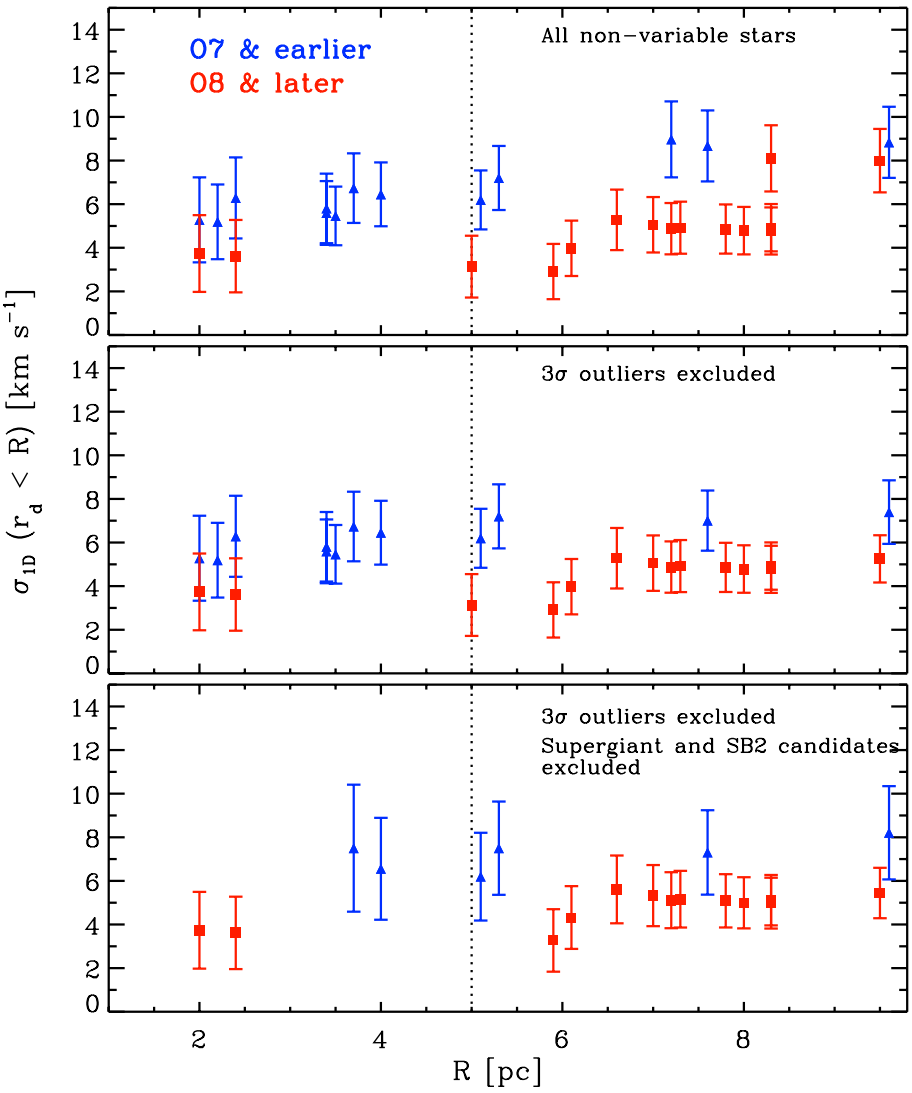

Figure 3.8 Same as Figure 3.7, but here the stars with known spectral subtypes are divided into two subsamples: O7 and earlier (blue triangles), and O8 and later (red squares). In each panel (and spectral subsample), the first point from the left is the velocity dispersion of the four stars (of that subsample) closest to the centre, the second point is the velocity dispersion of the innermost five stars, and so on.

Galactic cases once binaries and runaways are excluded (e.g. de Bruijne 1999). However, the latter are hard to identify if there is a massive cluster with a higher velocity dispersion embedded in the OB association. To explore the cluster/halo dichotomy, we divided our sample into two spectral subtype groups such that they had roughly the same number of stars, which resulted in these two subsamples: earlier than O7 and later than O8. We then computed the velocity dispersion as in Section 3.6.1 for the stars that could be placed in one of these groups (Figure 3.8). We would expect the earlier type stars to be more concentrated towards the centre as a result of mass segregation or due to an overall age difference between the cluster and halo populations. Figure 3.8 indeed

suggest a higher concentration of early-types towards the core, but this could well be due to the increasing crowding effects in the innermost regions favouring the detection of the brightest (most probably earliest) stars. In any case, there is no obvious difference in velocity dispersion between the two subsamples, and the contribution of halo stars to the velocity dispersion remains very difficult to identify. The velocity dispersion of the later subtypes is possibly slightly lower than that of the earlier subtypes, which would support the contention that the former are more likely associated with the halo, but this does not change the main result of the previous subsection about the line-of-sight velocity dispersion in the inner 5 pc of the cluster.

3.6.3 The contribution of cluster rotation

In Chapter 5, we present evidence for internal rotation of R136. From comparison of our RV measurements with simple rotation curves, we infer a rotational amplitude of $\sim 3\,\mathrm{km\,s^{-1}}$ and an optimal position angle for the rotation axis at an angle of $\sim 45^\circ$ east of north. To remove the anisotropy due to the suggested rotation and its contribution to the computed velocity dispersion, we subtracted from our measured RVs the rotation curve from these simple models. We find that the velocity dispersion obtained after this correction is typically $0.5\,\mathrm{km\,s^{-1}}$ lower than the values presented in Section 3.6.1. Thus, a small component of the observed line-of-sight velocity dispersion could be attributed to cluster rotation.

3.6.4 The velocity dispersion when including binaries/variable stars

It is interesting to see what the computed $\sigma_{1\mathrm{D}}$ would have been if we had not been careful about identifying and rejecting binaries and variable stars, or if we were not dealing with multi-epoch observations. To estimate this, we randomly selected one epoch for each ARGUS source on which the RV analysis was performed (variable and non-variable sources), and repeated the process to make 10 000 "single-epoch datasets". A median $\sigma_{1\mathrm{D}}$ of 25.0 $\mathrm{km\,s^{-1}}$ was obtained from all these combinations of single-epoch RV measurements, with a standard deviation of 5.9 $\mathrm{km\,s^{-1}}$ and values of $\sigma_{1\mathrm{D}}$ ranging from 12.9 to 48.0 $\mathrm{km\,s^{-1}}$. If we do a similar test but limit ourselves to the non-variable ARGUS sources (Table 3.2), we find a median $\sigma_{1\mathrm{D}}$ of 6.2 $\mathrm{km\,s^{-1}}$ (in good agreement with the results of section 3.6.1), with a standard deviation of 0.7 $\mathrm{km\,s^{-1}}$.

Note however that the velocity dispersion obtained when including all the RV variables cannot be directly compared with the velocity dispersion one would obtain from the

integrated light of a distant star cluster, as a few outliers could increase the velocity dispersion significantly without contributing much to the integrated light.

3.6.5 The contribution of errors and undetected binaries

To estimate the contribution of measurement errors and undetected binaries to the observed velocity dispersion, we performed a series of Monte Carlo simulations. These are adapted from the method presented by Sana et al. (2009) and refined in Sana et al. (2013a) to estimate the probability to detect binary systems. Bosch & Meza (2001) have also previously performed similar Monte Carlo simulations testing intrinsic and observed properties of binary stars. Our simulations mimic the process that we have been going through, i.e. identify variables from series of RV measurements and then compute the velocity dispersion from the remaining non-variable stars.

The general procedure goes as follows. We first adopt reasonable orbital parameter distributions (period, mass ratio, eccentricity) and an intrinsic binary fraction. Then, for 10 000 populations of N stars (where $N = 31$ is the size of the sample, i.e. all the ARGUS sources plus MEDUSA O-type stars within 5 pc from the centre of R136 on which the RV measurements and variability analysis were performed), we randomly draw which are binaries and which are single, and also randomly draw the parameters for the binaries from the adopted distributions. From these, we compute the orbital velocity at each epoch (based on the time sampling of the observations) for all the binaries assuming random orientations of the orbital planes and uncorrelated random time of periastron passage. We then add the measurement noise (based on the RV uncertainties of our sample) to the computed RVs of binaries and single stars. By applying the RV variability criteria of Section 3.3.2 (in particular the one based on the goodness of fit of a constant RV model), we can then eliminate the stars that we would have flagged as variable, compute the line-of-sight velocity dispersion of the apparently non-variable stars, and estimate the contribution from the orbital motion of binaries that were not detected. This procedure has the advantage that we not only take into account the long-period binaries (i.e. too long a period to be detected with the VFTS), but also all the shorter binary systems missed by our time sampling.

Before performing the full procedure outlined above, we estimated the contribution of measurement errors by taking a population with no binaries. For each star, we drew the RV at each epoch from a Gaussian distribution centered on zero and a sigma corresponding to the RV uncertainty at the corresponding epoch. We then applied the RV variability criteria of Section 3.3.2 to make sure that our adopted thresholds do not

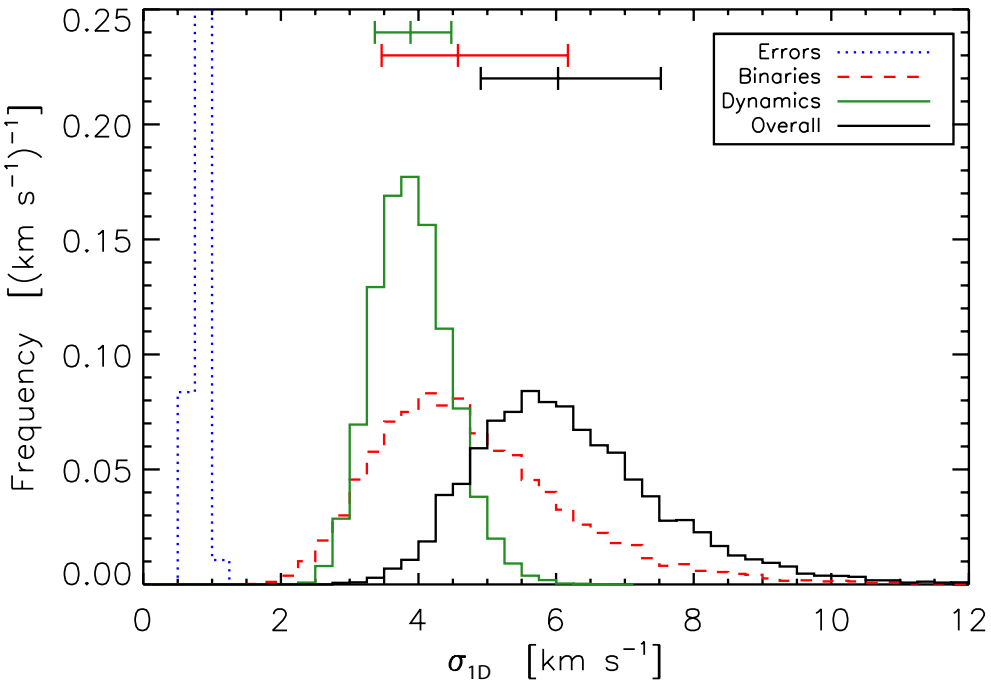

Figure 3.9 Estimate of the contributions to the line-of-sight velocity dispersion for massive stars in the inner 5 pc of R136. The blue dotted curve shows the distribution of the velocity dispersion from measurement errors only over 10 000 simulated populations. The red dashed curve is the distribution only from binaries undetected after applying our variability criteria (the initial input population has a binary fraction of 100%, and an Öpik-law distribution of the periods is adopted with period range of 0.15−6.85 in $\log P$ with P in units of days). The green dashed-dotted curve is the distribution for the dynamical velocity dispersion which best reproduces the observed velocity dispersion. The black solid curve takes into account measurement errors, undetected binaries, and the dynamical velocity dispersion. The median (central tick) and 68% confidence interval of the distributions are indicated on the upper part of the graph.

lead to false detections (the false detection rate was indeed found to be negligible). We finally computed the velocity dispersion of the population and repeated this for 10 000 populations. The resulting velocity dispersion distribution is represented by the blue dotted curve in Figure 3.9 (the peak of this blue curve is at 0.80 $(\mathrm{km\,s^{-1}})^{-1}$, out of the graph). It shows that, given the precision of our RV measurements, the intrinsic contribution of measurement errors to the observed velocity dispersion is very small. Note that we performed two tests on the population size: (i) we first used $N = 31$ stars, the full population size, and (ii) we randomly picked stars from the initial population following the results of a binomial test with a success rate of 50%, mimicking the fact that the dispersion is usually computed using an effective population of about half the size of the original one because of binary rejection. The two approaches made no difference on the resulting contribution of measurement errors.

The contribution of undetected binaries depends on what is assumed for the input distributions of orbital parameters. We focus here on the distribution of orbital periods, because the distributions of mass ratios and eccentricities have a limited impact (see Sana et al. 2013a). In what follows we adopt a flat distribution of mass ratios, as motivated by the recent results of Sana et al. (2012) and Kiminki & Kobulnicky (2012). For a more complete discussion of the current constraints on the distribution of orbital parameters of massive binaries, see Chapter 4.

As a first test to estimate the intrinsic contribution of undetected binaries, we adopted a conservative binary fraction of 100% and a commonly assumed standard Öpik-law distribution for the period (i.e. a flat distribution in $\log P$) with a period range of $0.15-6.85$ (in $\log P$, where P is in units of days). The maximum period adopted corresponds to the extrapolation of the Öpik law until a binary fraction of 100% is reached when considering the observed binary fraction and the overall detection rate of the VFTS (Sana et al. 2013a). We ran the full procedure outlined above, but without adding the measurement noise to the extracted orbital velocities. The resulting velocity dispersion distribution (from the stars that are not identified as RV variable) is shown with the red dashed curve in Figure 3.9. Under these assumptions, the velocity dispersion from undetected binaries is $4.6^{+1.6}_{-1.1}$ km s^{-1}. The quoted value is the median of 10 000 populations, and uncertainties correspond to the 68% confidence interval (equivalent to $\pm 1\,\sigma$ for Gaussian distributions). Note that within uncertainties, the undetected binaries alone could in principle produce the observed velocity dispersion of ~ 6 km s^{-1}.

To recover the true velocity dispersion of the cluster, we repeated the simulation, this time adding the measurement noise to the orbital RVs. We also included a contribution from the dynamical (i.e. cluster) velocity dispersion that was varied until the most probable velocity dispersion matched the observed velocity dispersion. For simplicity, we assumed that this dynamical contribution to the velocity dispersion did not vary as a function of radius. We estimate that the line-of-sight velocity dispersion attributable to the cluster dynamics is $3.9^{+0.6}_{-0.5}$ km s^{-1}. The errors on this value correspond to changes in the input dynamical velocity dispersion that result in median values of the output velocity dispersion distribution at percentiles 0.16 and 0.84 of the optimal output distribution (i.e. the 'overall' simulated distribution for which the median is the observed velocity dispersion). Note that we obtain a velocity dispersion of 26 ± 9 km s^{-1} from these simulations for a single epoch when including all binaries (i.e. without applying our variability criteria and thus without rejecting the binaries that would be detected), in keeping with the value of ~ 25 km s^{-1} that we found in Section 3.6.4 from

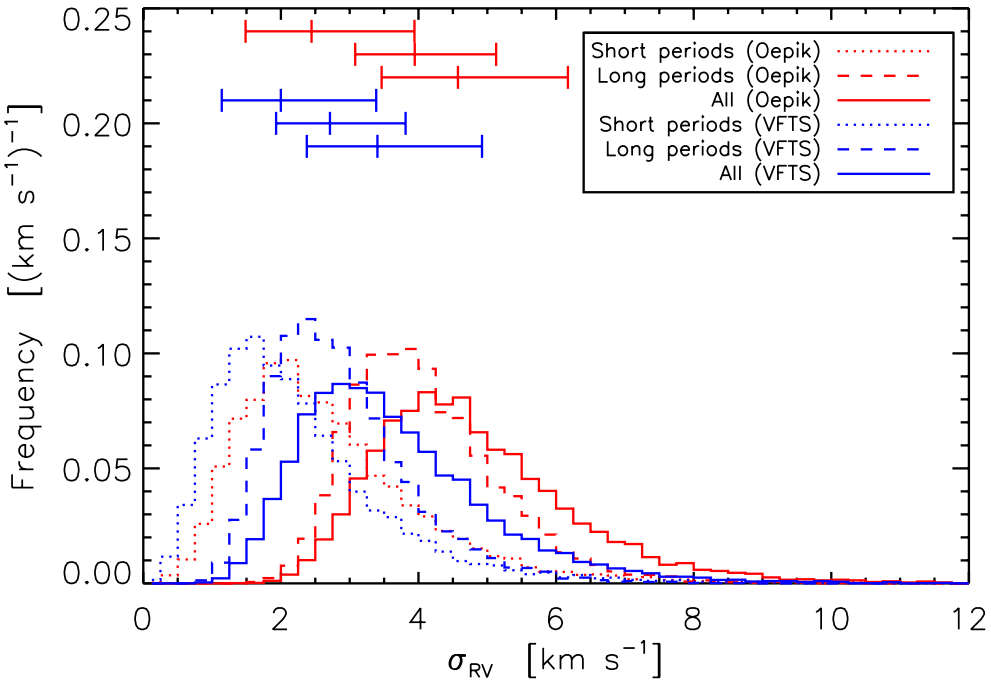

Figure 3.10 Same as Figure 3.9, but this time showing estimates of the contribution to the line-of-sight velocity dispersion of R136 from undetected binaries for different assumptions about the period distribution or range of periods considered. See the text for details.

the single-epoch RV measurements of all ARGUS sources (variable and non-variable).

We also ran simulations using different binary fractions and period distributions (see Figure 3.10). We first considered only periods shorter than $10^{3.5}$ days, i.e. the ones that could be detected given the time sampling of the VFTS (Sana et al. 2013a). Assuming a 50% binary fraction and a standard Öpik law for the period distribution, the estimated velocity dispersion from the undetected shorter period binaries alone is $2.4^{+1.5}_{-1.0}$ km s^{-1} (red dotted curve in Figure 3.10). If instead of the Öpik law we adopt the distribution found by Sana et al. (2013a) for the VFTS O-type binaries ($f(\log P) \propto (\log P)^{-0.45}$), we obtain a velocity dispersion from the undetected shorter period binaries of $2.0^{+1.4}_{-0.9}$ km s^{-1} (blue dotted curve in Figure 3.10). This is the minimal velocity dispersion contribution from undetected binaries. These values (to be compared with the red dashed curve in Figure 3.9) indicate that the contribution of undetected binaries is dominated by long period systems outside the sensitivity range of the VFTS.

To quantify the contribution of these longer period undetected binaries alone, we repeated the above exercise assuming a 50% binary fraction and considering only periods longer than $10^{3.5}$ days. For the Öpik law, we adopt the same maximum period as above ($10^{6.85}$ days), while for the period distribution of Sana et al. (2013a), we must

extrapolate to a maximum period of 10^{11} days[2]. The velocity dispersion from these long-period binaries is shown in Figure 3.10 (dashed curves). Note that the period distribution is uncertain in the long-period domain, so there is no evidence that the distribution from Sana et al. (2013a) is a better description of these systems than the Öpik law. Actually, if longer period systems are created by capture, then the Öpik law might be closer to reality.

Recall that the velocity dispersion from undetected binaries when including short and long-period systems (i.e. binary fraction 100%, Öpik-law distribution of periods ranging from 0.15 to 6.85 in $\log P$) is $4.6^{+1.6}_{-1.1}\,\mathrm{km\,s^{-1}}$. If we adopt the distribution with $f(\log P) \propto (\log P)^{-0.45}$ instead, the velocity dispersion from both short and long period undetected binary systems is $3.4^{+1.5}_{-1.0}\,\mathrm{km\,s^{-1}}$ (Figure 3.10, solid blue curve). In that case, the dynamical velocity dispersion that best reproduces the observed velocity dispersion would be around $5\,\mathrm{km\,s^{-1}}$. The Öpik law might therefore overestimate the contribution of binaries by $\sim$1 $\mathrm{km\,s^{-1}}$ compared to the period distribution measured in VFTS O-type binaries (Sana et al. 2013a), but we should again bear in mind that the extrapolation of the period distribution to long periods is uncertain.

In summary, we estimate that the velocity dispersion due to cluster dynamics alone (i.e. removing the effect of binarity but still including a small contribution from rotation) is likely somewhere between 4 and $5\,\mathrm{km\,s^{-1}}$, with a contribution of $\sim 0.5\,\mathrm{km\,s^{-1}}$ from rotation (see Section 3.6.3).

3.7 Discussion

Now that we have our measurement of the velocity dispersion at hand we can test the hypothesis that the cluster is in virial equilibrium. This is often done by deriving a dynamical, or virial mass, from the velocity dispersion which is then compared to the photometrically determined mass (see Chapter 1). To be able to derive the former we require knowledge about the mass distribution of the stars. For equilibrium models with an isotropic velocity dispersion the one-dimensional velocity dispersion, $\sigma_{1\mathrm{D}}$, relates to the mass, M, and the viral radius, r_v, as $M = 6 r_\mathrm{v} \sigma^2_{1\mathrm{D}}/G$. The virial radius is defined as $r_\mathrm{v} \equiv GM^2/(2W)$, with W the potential energy of the system. This relation is often expressed in terms of the radius containing half the light in projection, or effective

[2]This maximum period corresponds to the extrapolation of the period distribution until a binary fraction of 100% is reached when considering the observed binary fraction and the overall detection rate of the VFTS. We must however keep in mind that a period of 10^{11} days is much longer than the lifetime of an O-type star.

radius ($r_{\rm eff}$), as $M = \eta r_{\rm eff}\sigma_{\rm 1D}^2/G$, with $\eta \approx 10$. This is under the assumption that light traces mass, that the half-mass radius ($r_{\rm h}$) in projection is 3/4 times the 3D half-mass radius (Spitzer 1987) and that the ratio $r_{\rm v}/r_{\rm h} \approx 5/4$. The first two assumptions are not valid when a cluster is mass segregated (Fleck et al. 2006) as the 2D *light* radius can be twice as small as the 3D *mass* radius (Hurley 2007; Gaburov & Gieles 2008). For models with very flat density profiles, it is difficult to estimate the half-light radius. The surface brightness profiles of young clusters are often approximated by cored templates with a power-law decline of the form $I(r) = I(0)(1 + r^2/r_0^2)^{-\gamma/2}$, where r_0 is a scale radius. These profiles are often referred to as EFF profiles (Elson et al. 1987). For $\gamma > 2$ these models contain a finite amount of light, but diverge to infinite luminosity when $\gamma \leq 2$. The boundary at $\gamma = 2$ corresponds to 3D light profiles that decline as r^{-3}. For γ larger than, but close to 2, the ratio $r_{\rm v}/r_{\rm h}$ becomes very sensitive to the exact value of γ (Portegies Zwart et al. 2010). Additionally, determining $r_{\rm eff}$ becomes difficult as this quantity, and the total luminosity, can become unrealistically large when extrapolating to infinity.

The light profile of R136 has a profile close to $\gamma = 2$ (McLaughlin & van der Marel 2005), with indications for a 'bump' in the optical light profile at about 10 pc (Hunter et al. 1995; Maíz-Apellániz 2001; Mackey & Gilmore 2003). The presence of an additional component from the larger scale and near-constant-density OB association in which R136 is located (see section 3.6.2) has been interpreted as the reason for this relatively flat profile. In the near-infrared (NIR), the profiles are even flatter than the critical value (Andersen et al. 2009; Campbell et al. 2010) and the halo structure is not that obvious, but the NIR data did not extend very far into the OB association. Mass segregation, age differences between the core and halo, and differential extinction (which becomes important $\sim$ 10 pc away from the centre of R136) could explain the flatter profile in the NIR compared to the optical.

With the above caveats in mind, it is still interesting to see what dynamical mass we obtain for R136. If we assume $\eta \approx 10$, $3.4 \lesssim \sigma_{\rm 1D} \lesssim 6.0$ km s^{-1} (Section 3.6), and adopt a half-light radius of $r_{\rm eff} = 1.7$ pc (Hunter et al. 1995) which is consistent with the half-light radius obtained for the inner component of the double EFF fit discussed in Section 3.6.2, we get $M = 4.6 - 14.2 \times 10^4$ M$_\odot$. This is consistent with the estimated photometric mass of $\sim 10^5$ M$_\odot$ by Andersen et al. (2009), for which the cluster mass of $\sim 5 \times 10^4$ M$_\odot$ (computed for stellar masses between 25 M$_\odot$ and down to 2.1 M$_\odot$) was extrapolated assuming a Salpeter slope down to 0.5 M$_\odot$.

However, because of the difficulties outlined above, we decide to address whether R136 is in virial equilibrium by exploring an alternative method for which we do not need

to know the total mass. This relies on estimating the central velocity dispersion by following a very similar method to that presented by Richstone & Tremaine (1986). From the observations we find that the velocity dispersion is roughly constant with radius (Section 3.6.1). We can express the expected central dispersion $\sigma_{1\mathrm{D}}(0)$ of (self-consistent and isotropic) models with isothermal inner parts in terms of observed properties of the cluster

$$\sigma_{1\mathrm{D}}^2(0) = \alpha\pi G\Upsilon_V I(0) r_0, \tag{3.9}$$

where $G \approx 0.0043$ pc $\mathrm{M}_\odot^{-1}$ km^2 s^{-2} is the gravitational constant, Υ_V the mass-to-light ratio in $\mathrm{M}_\odot/\mathrm{L}_\odot$ in the V-band and α a constant that depends on the model.

We first consider the modified Hubble profile (Rood et al. 1972), which is an EFF profile with $\gamma = 2$, very close to the best fit to the surface brightness profile in the optical. From solving Jeans' equations assuming hydrostatic equilibrium and isotropic velocities, it can be shown that for this model $\alpha = 3 - 4\ln(2) \approx 0.227$. Secondly, we look at the Plummer (1911) model for which $\alpha = 1/6 \approx 0.167$. Finally, we can consider the isothermal sphere, which cannot be expressed in an EFF profile. For this model r_0 is defined as[3] $r_0^2 = 9\sigma_{1\mathrm{D}}^2/[4\pi G\rho(0)]$, where $\rho(0)$ is the central density. For the isothermal sphere $I(0) \approx 2\rho(0)r_0/\Upsilon_V$ (Binney & Tremaine 1987) and we thus have $\alpha \approx 2/9 \approx 0.222$. In conclusion, $\alpha \approx 0.2$ and the value is relatively insensitive to the choice of model (in contrast to the value of η).

The central surface brightness of R136 in the V-band is about $I(0) \approx 2.5 \times 10^6$ $\mathrm{L}_\odot$ pc^{-2} (McLaughlin & van der Marel 2005) and together with $r_0 \approx 0.3$ pc and $\Upsilon_V \approx 0.014$ (Mackey & Gilmore 2003; McLaughlin & van der Marel 2005) we find a predicted central velocity dispersion of $\sigma_{1\mathrm{D}} \approx 5.3$ km s^{-1} in virial equilibrium. Our measured dispersion is consistent with this value and we conclude that R136 is in virial equilibrium in the inner 5 pc (i.e. the region which, as we have argued, can be considered as bound and part of the cluster based on the definition discussed above). This is also consistent with a normal stellar initial mass function (IMF) for R136 (Andersen et al. 2009), as the expected velocity dispersion would be a factor of a few lower, for example, if the IMF was truncated at the low-mass end (the mass-to-light ratio would be lower in that case).

The expected velocity dispersion calculated above should actually be corrected for the fact that our stars are not at the centre of the cluster, unless we consider the cluster as an isothermal sphere in which case the dispersion is the same everywhere. For the

[3]The radius r_0 in the isothermal model is the radius where the projected density falls by roughly half its central value. For the EFF model with $\gamma = 2$ the projected density is exactly half the central value at r_0 and this is why we use the same symbol.

Plummer model and the modified Hubble profile, the velocity dispersion for an isotropic model decreases with radius. For example, in the modified Hubble profile, the velocity dispersion at 5 pc should be $\sim 40\%$ lower than at the centre for a core size of 0.3 pc, so in virial equilibrium we would expect to measure a dispersion of $\sim 3\,\mathrm{km\,s^{-1}}$ at 5 pc, which is still in relatively good agreement with our measured dispersion.

Other effects that we have not taken into account could also influence our estimate of the expected velocity dispersion in virial equilibrium. Mass segregation, for example, would result in a higher central surface brightness, a smaller core size, and a lower mass-to-light ratio. It is however not clear what would be the net effect on the velocity dispersion. Radial anisotropy would make the (projected) velocity dispersion profile decline more at larger radii with respect to an isotropic model with the same density profile (Wilkinson et al. 2004; Clarkson et al. 2012). On the other hand, tangential anisotropy could flatten the profile by reducing $\sigma_{1\mathrm{D}}$ in the core and increasing it in the outer parts, which is an interesting perspective considering the evidence for rotation (Chapter 5; Hénault-Brunet et al. 2012b) and the relatively flat velocity dispersion profile that we obtained for R136. A similarly flat profile was also found for the Arches cluster albeit within a much smaller radial extent (Clarkson et al. 2012). Detailed numerical modeling of R136 is required for a meaningful quantitative discussion of the complicated effects outlined above, but this is beyond the scope of the present work.

Other young massive clusters have recently been found to have a low velocity dispersion, suggesting that they are virial or even subvirial. Velocity dispersions of $4.5 \pm 0.8\,\mathrm{km\,s^{-1}}$ and $5.4 \pm 0.4\,\mathrm{km\,s^{-1}}$ were reported, respectively, for NGC 3603 (Rochau et al. 2010) and the Arches cluster (Clarkson et al. 2012) using proper motion measurements. From RV measurements of five yellow hypergiants and one luminous blue variable in Westerlund 1 showing little RV variations over 2 to 3 epochs, Cottaar et al. (2012a) estimated the velocity dispersion of this cluster to be $2.1^{+3.3}_{-2.1}\,\mathrm{km\,s^{-1}}$. From single-epoch near-infrared spectroscopy, Mengel & Tacconi-Garman (2007) found $5.8 \pm 2.1\,\mathrm{km\,s^{-1}}$ for the same cluster from the RVs of four red supergiants, $8.4\,\mathrm{km\,s^{-1}}$ from ten post-main-sequence stars (Mengel & Tacconi-Garman 2008), and finally $9.2\,\mathrm{km\,s^{-1}}$ from a sample of four red supergiants, five yellow hypergiants, and one B-type emission-line star (Mengel & Tacconi-Garman 2009). Note that these studies of Westerlund 1 use stars of spectral types and luminosity classes that are known to be pulsators or intrinsic RV variables (e.g. Ritchie et al. 2009; Clark et al. 2010), which along with the small number statistics (both in terms of number of stars and number of epochs) might explain the range of values obtained for the velocity dispersion.

Given the young age of these clusters for which low velocity dispersions were found,

including R136, this might look somewhat surprising if we expect the clusters to be expanding following gas expulsion. However, if the age of a cluster is at least few crossing times it might have had time to re-virialize, in which case the low velocity dispersions measured are not so surprising (e.g. Banerjee & Kroupa 2013). A consequence of the low velocity dispersions found is that these young massive clusters are certainly not being disrupted by gas expulsion, and in fact appear to be stable from a very young age. From now on, gas expulsion will not have a significant effect on the dynamical evolution of the cluster. A gas-free cluster in virial equilibrium is therefore a reasonable initial condition for dynamical simulations of the long-term evolution of these massive clusters. The gas expulsion scenario would also predict strong radial orbits in the outer parts of the cluster, which would result in a steep decline in σ_{1D} (Clarkson et al. 2012; Wilkinson et al. 2004), and this is not observed. As was alluded to in Chapter 1, several factors could potentially explain this apparent unimportance of gas expulsion in early cluster evolution, including a high star-formation efficiency (e.g. Goodwin & Bastian 2006), the formation of these clusters from the merging of dynamically cool (subvirial) substructures (e.g. Allison et al. 2009), and/or a cluster formation process resulting in a de-coupled distribution of gas and stars that offsets the disruptive effect of gas expulsion (e.g. Fellhauer et al. 2009; Moeckel & Clarke 2011; Kruijssen et al. 2012). In their analysis of a smoothed particle hydrodynamics (SPH) simulation of cluster formation, Kruijssen et al. (2012) indeed found that the gas and stars decouple dynamically as the stellar component accretes and shrinks, allowing it to already attain virial equilibrium while embedded in a cocoon of gas. Another consequence of our results is that even if it were true that gas expulsion had a very large dynamical effect ~ 1 Myr ago, then R136 would have had to be incredibly dense in the past.

R136 is often considered as an extremely dense cluster, but it is interesting to compare the low velocity dispersion that we found to the much larger line-of-sight velocity dispersion of a dense globular cluster like 47 Tucanae (11.6 $\mathrm{km\,s^{-1}}$; McLaughlin et al. 2006). R136 is still very young, and it will lose mass and expand due to stellar evolution. For an adiabatic mass loss, the radius will grow as $1/M$, so the velocity dispersion will go down by at least a factor of two ($\sigma_{1D} \propto (M/r)^{1/2} \propto M$), but in reality there is going to be even more significant expansion (Gieles et al. 2010a) which will reduce the velocity dispersion even more by the time R136 is as old as 47 Tucanae.

3.8 Summary

In an effort to determine the dynamical state of the young massive cluster R136, we used multi-epoch spectroscopy of stars in the inner regions of 30 Dor. We measured RVs with a Gaussian fitting procedure on selected key helium lines and performed a quantitative assessment of the variability. Out of 41 sources for which spectra were extracted from the ARGUS IFU data cubes, 16 were identified as non-variable. All of these were classified as O-type stars, three of which were also revealed to have composite spectra. To this sample of 16 ARGUS sources, we added measurements from 22 apparently single stars observed in the surrounding regions with MEDUSA-GIRAFFE, also as part of VFTS.

Using this sample of 38 non-variable massive stars within 10 pc from the centre of R136, we computed the velocity dispersion of the cluster. For the stars within 5 pc, we place an upper limit of 6 $\mathrm{km\,s^{-1}}$ on the line-of-sight velocity dispersion. This result does not change significantly if we exclude the few $3\,\sigma$ outliers, supergiant candidates, and stars having composite spectra. We also noted that the measured velocity dispersion of the cluster includes a small contribution of ~ 0.5 $\mathrm{km\,s^{-1}}$ from rotation.

From Monte Carlo simulations, we established that the contribution of measurement errors to the observed velocity dispersion is almost negligible. We also estimated the contribution of undetected binaries, which is relatively small and dominated by long period systems beyond the detectability range of the VFTS. When taking errors and undetected binaries into account, we estimate that the true velocity dispersion of the cluster (i.e. attributable only to cluster dynamics) is likely between 4 and 5 $\mathrm{km\,s^{-1}}$ for the stars within 5 pc from the centre.

Under basic assumptions, the expected central velocity dispersion in virial equilibrium was found to be ≈ 5.3 $\mathrm{km\,s^{-1}}$, in good agreement with our measurement, and we conclude that R136 is in virial equilibrium. Combined with the low velocity dispersions found in a few other young massive clusters, our results suggest that gas expulsion did not have a disruptive effect for these clusters. We would have obtained a velocity dispersion of ~ 25 $\mathrm{km\,s^{-1}}$ if binaries had not been identified and rejected, which supports the suggestion that the alleged super-virial state of young star clusters can be explained by the orbital motions of binary stars (Gieles et al. 2010b, see also Chapter 1). Our kinematic measurements in R136 also pave the way for a more detailed investigation and modeling of this young massive cluster, as we will briefly discuss in Chapter 7.

Chapter 4

The velocity dispersion of OB stars in young clusters from a single epoch of radial velocities: R136 as a test case

4.1 Introduction

Accurately measuring the velocity dispersion of a star cluster is essential to constrain its virial state, which is needed to determine if the cluster is currently stable or if it is expanding into the field. As discussed in the previous chapter, recent observations of resolved young massive clusters suggest that the majority of these have velocity dispersions of a few $\mathrm{km\,s^{-1}}$. These are based both on proper motion studies (e.g. Rochau et al. 2010; Clarkson et al. 2012) and multi-epoch radial velocity studies (e.g. Cottaar et al. 2012a; Hénault-Brunet et al. 2012a). The light of these young massive clusters is dominated by massive OB stars, a large fraction of which are spectroscopic binaries, so these radial velocity studies were designed to include multiple epochs. With this multi-epoch strategy, the significant effect of spectroscopic binaries on the observed radial velocity distribution can be reduced by identifying these binaries and removing them from the sample.

Alternatively, Cottaar et al. (2012b) presented a maximum likelihood procedure to recover the velocity dispersion of star clusters from a single epoch of radial velocity

data, despite the large effect on the observed radial velocity distribution from the orbital motions of spectroscopic binaries. By simultaneously fitting the intrinsic velocity distribution of the single stars and centres of mass of the binaries along with the radial velocities caused by orbital motions, this technique allows one to study the dynamical state of clusters having a low velocity dispersion without the need for multi-epoch observations to identify the spectroscopic binaries.

Cottaar et al. (2012b) showed that this method could successfully reproduce the velocity dispersion of 0.5 $\mathrm{km\,s^{-1}}$ of the old open cluster NGC 188 (Geller et al. 2008, 2009; Geller & Mathieu 2011) using a single epoch of radial velocity data and adopting the observed distribution of orbital parameters (i.e. period, mass ratio, and eccentricity) for the solar-type field stars. Due to the fact that (1) the O and B stars dominating the light of young massive clusters have a high spectroscopic binary fraction (e.g. Sana et al. 2012, and references therein) and (2) the distributions of orbital parameters of massive binaries are relatively loosely constrained, it is not obvious that the same method can be applied to successfully recover the velocity dispersion of these systems. It is therefore desirable to test it on a cluster for which the velocity dispersion was measured from an intensive dataset of multi-epoch radial velocities (i.e. after selecting out spectroscopic binaries).

In this chapter, we take advantage of the unique dataset provided by the VFTS (Evans et al. 2011). From multi-epoch spectroscopic data of massive stars in the 30 Doradus region of the Large Magellanic Cloud, the velocity dispersion of the young massive cluster R136, corrected for the orbital motions of binaries, was obtained in Chapter 3 (see also Hénault-Brunet et al. 2012a). The spectroscopic binary fraction and distribution of orbital parameters of the O-type stars in the broader 30 Doradus region were also constrained by Sana et al. (2013a). Using the radial velocities obtained in these previous studies, we can apply the procedure of Cottaar et al. (2012b) and check if the correct velocity dispersion can be recovered from a single epoch of radial velocities, even though the orbital parameter distributions of massive binaries are more loosely constrained and different from those of solar-type stars. In addition, we test the systematic and statistical uncertainties in the procedure through Monte Carlo simulations.

In Section 4.2, we briefly outline the maximum likelihood method presented by Cottaar et al. (2012b) and discuss available constraints on the binary properties of OB stars. We describe the radial velocity data of R136 as well as our mock datasets generated for the Monte Carlo simulations in Section 4.3. We present the results obtained when applying the maximum likelihood method to these data in Section 4.4, discuss the

general implications of these results in Section 6.5, and finally summarize our findings in Section 4.6.

4.2 Method

4.2.1 Outline of the maximum likelihood method

We use a maximum likelihood procedure to fit the observed radial velocity distribution. The details of this procedure can be found in Cottaar et al. (2012b). Briefly, we compute the likelihood to reproduce the observed radial velocity given an intrinsic velocity distribution, a set of binary orbital parameter distributions, and measurement uncertainties and we maximize this over the whole dataset. The observed radial velocity of a cluster member is the sum of three components: the velocity of the centre of mass, the measurement uncertainty and the velocity offset between the observed star in a binary and the centre of mass of the binary. The likelihood function for the observed radial velocity is therefore given by the convolution of the probability density functions (pdfs) of these three components.

Assuming a Gaussian velocity distribution for the cluster and Gaussian measurement uncertainties, the convolution of the pdfs of the velocity of the centre of mass and the measurement uncertainty is given by another Gaussian:

$$\mathrm{pdf}_{\mathrm{single}}(v_i, \sigma_i) = \frac{1}{\sqrt{2\pi(\sigma_v^2 + \sigma_i^2)}} \exp\left(-\frac{(v_i - \mu)^2}{2(\sigma_v^2 + \sigma_i^2)}\right), \tag{4.1}$$

where μ and σ_v are the mean velocity and velocity dispersion of the cluster and v_i and σ_i are the observed velocity and corresponding uncertainty for star i. For a single star this pdf directly gives the likelihood of reproducing the observed velocity, as there is no orbital motion.

To compute the velocity distribution for spectroscopic binaries we will have to convolve this pdf with the pdf of velocity offsets due to binary orbital motions. As no analytic form of this pdf is available, we compute the convolution between this pdf and the pdf of single stars (equation 4.1) numerically. First, we generate a large number (10^6) of random binaries from the assumed orbital period, mass ratio, and eccentricity distributions and calculate for each one the unprojected velocity v_k. As these velocities are randomly orientated with respect to the line of sight, the projected velocity offset will be a random value between $-v_k$ and $+v_k$, which gives us for the pdf of velocity

offsets projected along the line of sight:

$$\mathrm{pdf}_{\mathrm{offset}}(v_j) = \frac{1}{N} \sum_k \begin{cases} 0 & \text{if } v_k < v_j \\ \frac{1}{2v_k} & \text{if } v_k > v_j, \end{cases} \tag{4.2}$$

where k runs from 1 to N (the number of random binaries generated). The pdf for the observed velocity distribution can then be computed by numerically convolving the pdf for the measurement uncertainty and centre of mass velocity (equation 4.1) and the pdf for the velocity offset due to the binary orbital motions (equation 4.2):

$$\mathrm{pdf}_{\mathrm{binary}}(v_i, \sigma_i) = \int \mathrm{pdf}_{\mathrm{single}}(v', \sigma_i) \mathrm{pdf}_{\mathrm{offset}}(v_i - v') dv', \tag{4.3}$$

where v' is the sum of the velocity of the centre of mass of the binary and the offset due to the measurement uncertainty, and $v_i - v'$ is the velocity offset due to the binary orbital motion. We pre-computed equation 4.2 on a dense grid, which allowed for the repeated rapid computation of the integral in equation 4.3.

Finally the total likelihood $\mathcal{L}_i$ of observing a given velocity is obtained by summing equations 4.1 and 4.3 in the following way:

$$\mathcal{L}_i = f_{\mathrm{bin}}\ \mathrm{pdf}_{\mathrm{binary}}(v_i, \sigma_i) + (1 - f_{\mathrm{bin}})\ \mathrm{pdf}_{\mathrm{single}}(v_i, \sigma_i), \tag{4.4}$$

where f_{bin} is the binary fraction and $1 - f_{\mathrm{bin}}$ is the fraction of systems that are single stars.

For a given set of binary orbital parameter distributions (section 4.2.2), we vary the binary fraction (f_{bin}), the velocity dispersion (σ_v) and the mean velocity (μ_v) to find the maximum likelihood to reproduce all observed radial velocities (i.e. $\max(\prod_i \mathcal{L}_i)$). A simple Metropolis-Hastings implementation of Markov Chain Monte Carlo (MCMC) simulations is used to explore the probability distribution of the best-fit parameters and determine uncertainties on each of these marginalized over all the other free parameters (see Cottaar et al. 2012b). Figure 4.1 shows an example where we have fitted a single epoch of the multi-epoch radial velocities observed for R136 (for more details on this dataset see section 4.3.1). The binary orbital motions of the OB stars greatly affect the observed radial velocity distribution, as indicated by the large difference between the best-fit radial velocity distribution in green and the corresponding underlying Gaussian distribution in red.

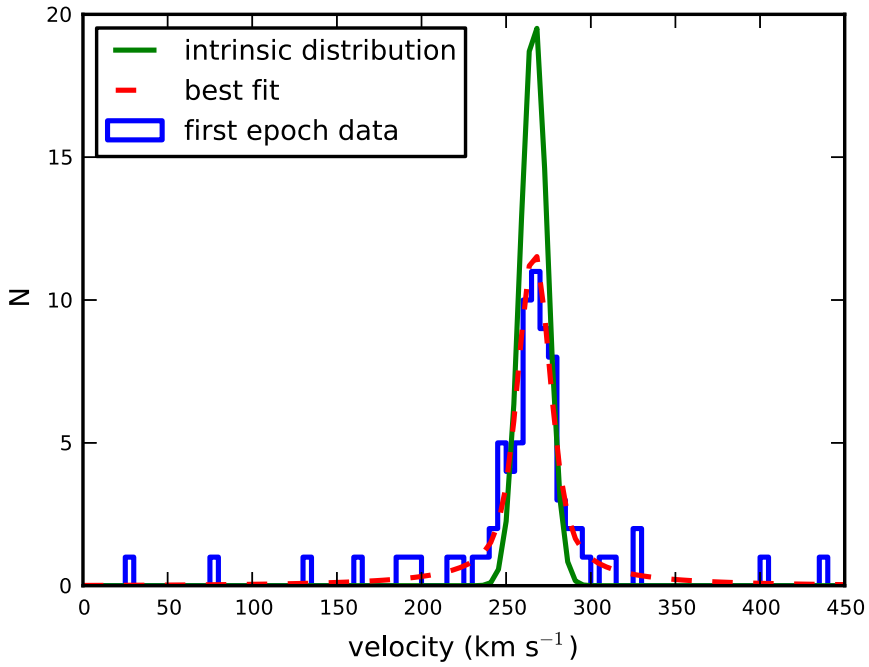

Figure 4.1 *Blue*: The observed radial velocity distribution for a single epoch drawn from the multi-epoch radial velocity dataset of R136 (Hénault-Brunet et al. 2012a; Sana et al. 2013a, see section 4.4.2 for details). *Red dashed*: the best-fit radial velocity distribution, including the effect of the orbital motions of spectroscopic binaries. *Green*: The intrinsic velocity distribution of the cluster, corrected for the orbital motions of binaries. This intrinsic distribution is assumed to be a Gaussian whose width and mean have been optimized to fit the data (section 4.2.1).

4.2.2 Current constraints on the binary properties of OB stars

In what follows, we focus on short-period (up to tens of years) close binaries, i.e. the ones which have the largest orbital velocities, the largest impact on the measured line-of-sight velocity dispersion, and which are probed efficiently by Doppler shifts of spectral lines. As we review in Section 4.2.3, there is now ample evidence that massive stars are preferentially found in binary systems, and in particular in these close spectroscopic binaries.

Unfortunately, the intrinsic distributions of orbital parameters of these binaries are still relatively poorly constrained, despite their fundamental importance to stellar evolution, star formation, and the early dynamical evolution of massive star clusters. Even when studies include a relatively large number of systems (e.g. Garmany et al. 1980; Mason et al. 2009), often only a small fraction of the identified binaries have well-constrained

Table 4.1 Constraints on the distributions of orbital parameters of massive binaries from the literature. The intrinsic binary fractions inferred for these distributions of orbital parameters and their corresponding domain are listed. The intrinsic binary fractions corresponding to an extrapolation of the period distribution to 300 years are also given. References: (1) Sana et al. (2012), (2) Sana et al. (2013a), (3) Kiminki & Kobulnicky (2012).

Parameter	*pdf*	Domain	Variable	Value	Sample	Reference
$\log_{10}(P/\mathrm{day})$	$(\log_{10} P)^{\pi}$	0.15 — 3.5	π	-0.55±0.22	Galactic clusters	(1)
		0.15 — 3.5		-0.45±0.30	30 Doradus	(2)
		0.0 — 3.0		0.2±0.4	Cyg OB2	(3)
$q = M_2/M_1$	q^{κ}	0.1 — 1.0	κ	-0.1±0.6	Galactic clusters	(1)
		0.1 — 1.0		-1.0±0.4	30 Doradus	(2)
		0.005 — 1.0		0.1±0.5	Cyg OB2	(3)
e	e^{η}	0 — 0.9	η	-0.45±0.17	Galactic clusters	(1)
		0 — 0.9		-0.5 (fixed)	30 Doradus	(2)
		0.0001 — 0.9		-0.6±0.3	Cyg OB2	(3)
Binary fraction				$69 \pm 9\%$	Galactic clusters	(1)
				$51 \pm 4\%$	30 Doradus	(2)
				$44 \pm 8\%$	Cyg OB2	(3)
Binary fraction				$85 \pm 11\%$	Galactic clusters	(1)
for extrapolated				$65 \pm 5\%$	30 Doradus	(2)
period distribution				$82 \pm 15\%$	Cyg OB2	(3)

orbital properties (see Sana & Evans 2011). A few recent studies have however achieved a better completeness in characterizing the identified binaries, in addition to correcting for observational biases in a more systematic way through Monte Carlo simulations (e.g. to translate the observed binary fraction into an intrinsic binary fraction).

Kobulnicky & Fryer (2007) attempted to constrain the distributions of orbital parameters of massive binaries by using a sample of 900 RV measurements of 32 O-type and 88 B-type stars in the Cyg OB2 association and comparing the raw velocities with the expectations of Monte Carlo simulations. They were however forced to make several simplifying assumptions about the orbital parameter distributions. Building upon this work and taking advantage of an extended dataset, Kiminki & Kobulnicky (2012) used 12 years of spectroscopic observations of 114 massive stars (B3–O5 primary stars) in Cyg OB2 and modeled the observed mass ratio, orbital period, and eccentricity distributions composed from the well-constrained orbital properties of 24 known binaries in the association (22 of which have periods shorter than 30 days; see caveats about this in Section 4.2.3). Sana et al. (2013a) analysed the multiplicity properties of the O-type star population of 30 Doradus through multi-epoch spectroscopy obtained as part of the VFTS. With 360 O-type stars surveyed, this is the largest homogenous sample of massive stars analysed to date. However, given the limited number of epochs obtained (typically six), the orbital parameters could not be determined for individual binary systems. The intrinsic binary fraction and period and mass ratio distributions in this case were therefore constrained by modeling simultaneously the observed binary fraction, the distribution of the amplitudes of radial

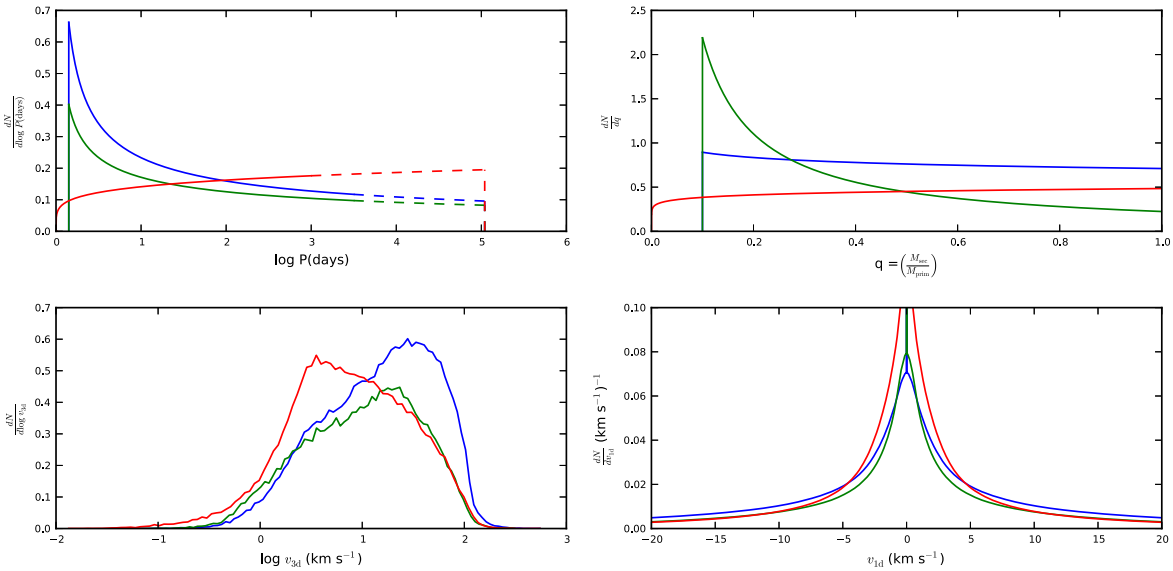

Figure 4.2 The assumed period distributions (upper left) and mass ratio distributions (upper right), as well as the unprojected logarithmic velocity distributions (lower left) and the projected velocity distributions (lower right). The extrapolation of the period distributions from the observed range to an upper limit of 300 years are plotted as dashed lines. The distributions have been normalized so that the fraction of binaries in the range of non-extrapolated periods match the intrinsic binary fractions inferred over the range of periods from the observations. The blue lines show the distributions from Sana et al. (2012), the green lines from Sana et al. (2013a) and the red lines from Kiminki & Kobulnicky (2012), as detailed in Table 4.1.

velocity variations and the distribution of the time scales of these variations. Sana et al. (2012) homogeneously analysed the O-type star population of six nearby Galactic open clusters and simultaneously measured all the relevant intrinsic multiplicity properties. The larger average number of epochs allowed for a more complete binary detection compared to the other studies. Over 75% of the 40 binaries identified in this sample have measured orbital properties, which also made it possible for the authors to directly model and fit the orbital parameter distributions. More details about the studies mentioned in this section and other pioneering works are presented in Section 4.2.3.

The distributions of orbital parameters from the three main studies discussed above are illustrated in Figure 4.2 and summarized in Table 4.1 along with the intrinsic spectroscopic binary fractions. The domains for which the period, mass ratio, and eccentricity have been considered and to which the quoted intrinsic binary fractions apply are also listed. Power laws are used to describe the probability density functions of orbital periods (in $\log_{10}$ space), mass ratios and eccentricities with exponents π, κ, and η, respectively. In the following sections, we use the values of the power-law exponents from these different studies to explore how sensitive the velocity dispersion

and binary fraction are to these assumptions when they are fitted from a single epoch of radial velocities.

We focus on the binary properties from the three papers listed in Table 4.1 because these studies are based on large samples and correct for observational biases in a systematic way through Monte Carlo simulations. In contrast to some other studies, they also have the advantage that they do not a priori assume a fixed distribution for the periods or mass ratios (apart from assuming a power-law functional form). Moreover, they sample different combinations of period and mass ratio distributions, cover a relatively wide range of values of π and κ, and together are therefore representative of the current uncertainties on the binary properties of massive stars. These studies also each sample a different environment in terms of cluster mass and density. The clusters considered by Sana et al. (2012) have relatively low masses ($1000 - 5000$ $M_\odot$), and it is currently unknown if the binary fraction and orbital parameter distributions should be affected in the more energetic environment of a $\sim 10^5$ $M_\odot$ cluster like the 30 Doradus region, where the stars in the sample of Sana et al. (2013a) are located. We do not necessarily expect all the scenarios encompassed by the values in Table 4.1 to be applicable to the young massive cluster R136, but it is interesting to test how the maximum likelihood method behaves under different assumptions about the binary properties.

It is important to note that given the limited baselines of the observations on which the above studies are based, only binaries with a period of up to ~ 10 years could be detected. However, wider binaries might still significantly alter the observed velocity distribution. To accurately measure the velocity dispersion of a cluster, we need to accurately predict how many binaries might cause velocity offsets of similar amplitude to the velocity dispersion of the cluster. Figure 4.3 illustrates that large velocity offsets are likely to be caused by close binaries and small velocity offsets are more likely to be caused by wider binaries, as expected. At the velocity dispersion of R136 (~ 6 km s^{-1}; Hénault-Brunet et al. 2012a, see also Section 4.4.2), the velocity offsets are dominated by binaries between ~ 1 and ~ 100 years, thus extending beyond the period range covered by spectroscopic surveys. To account for all the relevant binaries in our fits of the R136 data, we extrapolate the orbital period distribution to an upper limit of 300 years. We increase the binary fraction to match the intrinsic binary fraction determined over the period range covered by the observations (last row in Table 4.1).

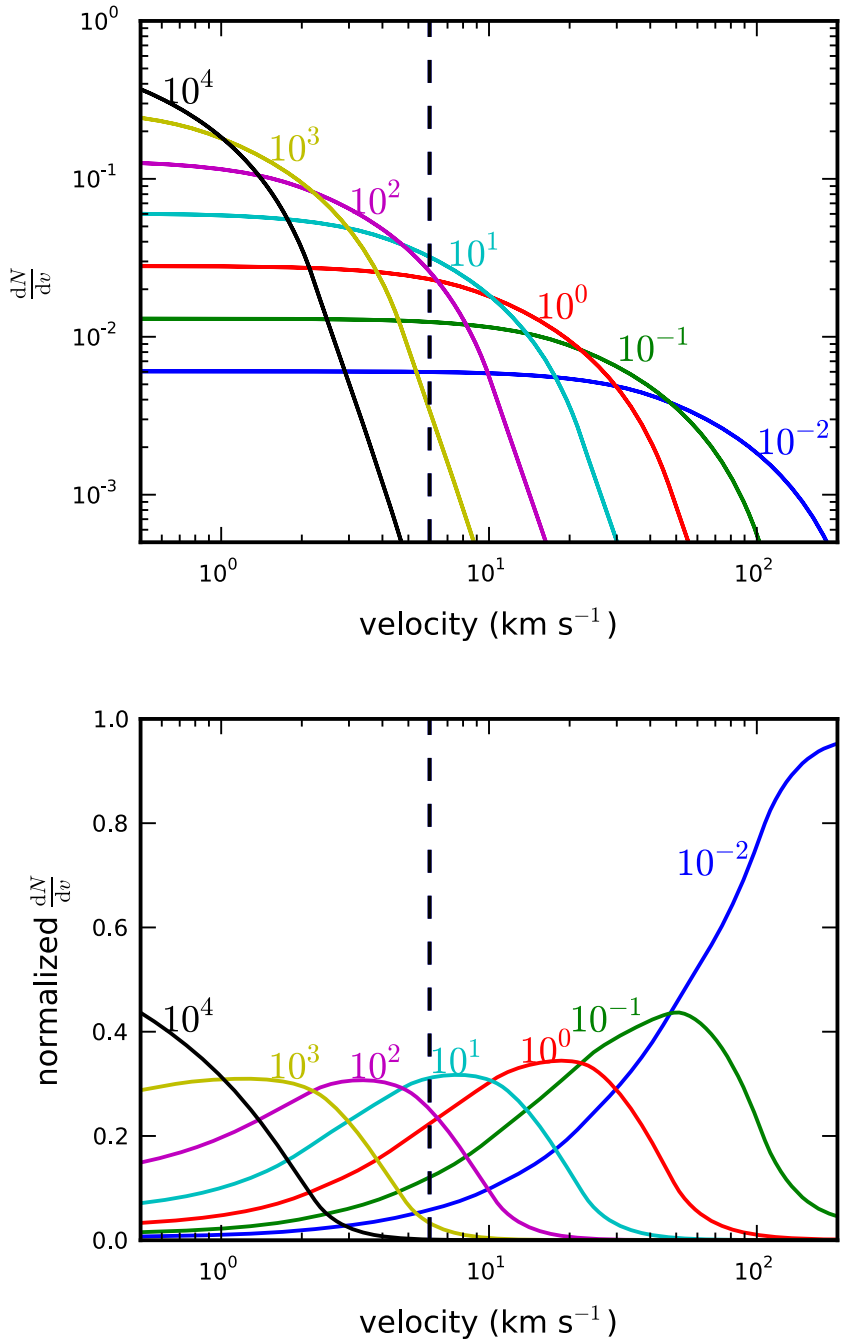

Figure 4.3 *Top*: The probability distribution ($\frac{dN}{dv}$) for the radial velocity difference between the primary star in a binary and its centre of mass. Every line represents a binary with a fixed period and primary mass of 20 $M_\odot$, but random mass ratios, eccentricities, and phases drawn from a flat distribution, as well as a random orientation with the periods increasing by factors of 10. The periods have been labeled in the figure in years. The vertical dashed line marks the velocity dispersion within 10 pc of R136 (~ 6 km s^{-1}). *Bottom*: Same as top panel, but with the probability at every velocity offset renormalized so that the sum of the probabilities is 1.

4.2.3 Review of the binary properties of OB stars

For completeness, the constraints on the binary fraction and distributions of orbital parameters of massive binaries presented in the literature are reviewed below.

Period distribution

Sana et al. (2012) showed that the intrinsic period distribution of their Galactic open clusters sample does not follow the widely used Öpik law (i.e., a flat distribution in the logarithm of the separation or, equivalently, of the period; Öpik 1924) but is instead overabundant in short period systems. They found an exponent $\pi = -0.55 \pm 0.22$ for the power law of the period distribution for lower and upper bounds of 0.15 and 0.35 on $\log_{10} P/\mathrm{d}$. For the same period range, Sana et al. (2013a) also found from the 30 Doradus dataset a stronger preference for short periods than previously assumed, with a comparable value of $\pi = -0.45 \pm 0.30$. This is in contrast with the best-fit value of $\pi = 0.2 \pm 0.4$ from Kiminki & Kobulnicky (2012) for Cyg OB2 binaries, which is consistent with the Öpik law to within $1\,\sigma$, although these authors argued that no single power law adequately reproduces the data at the shortest periods ($P < 14$ days). Although Kiminki & Kobulnicky assume a power law distribution valid between 1 and 1000 days, we must also highlight that their sample does not probe this full range of periods. The power law exponent of the period distribution was determined from 22 binaries having periods shorter than 30 days, so the results had to be extrapolated over almost two orders of magnitude.

Mass ratio distribution

It has been reported that the mass ratio distribution of massive binaries tends to peak towards unity (Bosch & Meza 2001; Pinsonneault & Stanek 2006), but this has since been contested (Lucy 2006) and more recent studies tend to favor a flat distribution of mass ratios. Kiminki & Kobulnicky (2012) indeed inferred a value of $\kappa = 0.1 \pm 0.5$ for the exponent of the power-law distribution of mass ratios for the known massive binaries in Cyg OB2. Similarly, Sana et al. (2012) found no preference for equal-mass binaries ($\kappa = -0.1 \pm 0.6$) in Galactic open clusters. In 30 Doradus, Sana et al. (2013a) even found a mass ratio distribution that is slightly skewed towards systems with low mass ratios ($\kappa = -1.0 \pm 0.4$), although this only provides a weak constraint on the distribution of mass ratios, and these results are still in agreement within $2\,\sigma$ with the two previous studies reporting flat distributions. These results are all incompatible

with a random pairing from a classical mass function (i.e. $\kappa = -2.35$; see Sana et al. 2013a).

Eccentricity distribution

Because measuring the eccentricity of a spectroscopic binary requires many epochs of radial velocity data, we are only beginning to probe the eccentricity distribution of massive binaries. As expected from tidal dissipation that tends to circularize their orbit (Zahn 1977, 1978), a large fraction of the short-period massive binary systems are found to have low eccentricities (Sana & Evans 2011; Kiminki & Kobulnicky 2012). Kiminki & Kobulnicky (2012) found a value of $\eta = -0.6 \pm 0.3$ for the exponent of the power-law distribution of eccentricities, while Sana et al. (2012) obtained $\eta = -0.45 \pm 0.17$. Sana et al. (2013a) could not constrain η in the 30 Doradus study and instead adopted the eccentricity distribution inferred by Sana et al. (2012) for the Galactic open clusters sample.

Binary fraction

A number of studies have investigated the observed fraction of spectroscopic binaries among massive stars. Mason et al. (2009) compiled results from the literature to show that 51% of the Galactic O-type stars investigated by multi-epoch spectroscopy are in fact spectroscopic binaries, while this fraction goes up to 56% for objects in clusters or OB associations. Barbá et al. (2010) obtained a similar fraction, with 60% of the 240 Galactic O and WN stars in their survey of the southern sky displaying significant radial velocity variations (i.e. >10 km s^{-1}). Chini et al. (2012) also observed a high binary fraction in their spectroscopic survey of O and B stars in the southern Milky Way. Studies focusing on individual young open clusters or OB associations have reported observed binary fractions between 30 and 60% (e.g. De Becker et al. 2006; Hillwig et al. 2006; Sana et al. 2008, 2009; Mahy et al. 2009; Rauw et al. 2009; Sana et al. 2011; Mahy et al. 2013), with variations from one cluster to the other compatible with the statistical fluctuations expected given the size of the samples (Sana & Evans 2011). Thus, although it has been proposed that the spectroscopic binary fraction might be related to the cluster density (e.g. García & Mermilliod 2001), the current data is consistent with a common binary fraction in all clusters, at least for O-star rich clusters (for details see Sana & Evans 2011).

To constrain the intrinsic fraction of spectroscopic binaries, one has to correct the

observed fraction for observational biases, which depend on the underlying distributions of orbital parameters. Kobulnicky & Fryer (2007) opted to fix the period distribution to the standard Öpik law because the solution of their Monte Carlo simulations for the period and mass-ratio distributions was degenerate. They inferred an intrinsic binary fraction of over 80%, but note that the range of separations considered in this study (up to 10 000 AU) extends well beyond the sensitivity domain of their spectroscopic observations, which can be misleading. Kiminki & Kobulnicky (2012) observed a binary fraction of 21% in Cyg OB2 (24/114 objects) and inferred an intrinsic fraction of 44±8% considering binaries with periods between 1 and 1000 days. Sana et al. (2012) identified 40 spectroscopic binaries for an observed binary fraction of 56% in their Galactic open clusters sample and found an intrinsic fraction of $69 \pm 9\%$ for periods in the range $0.15 < \log_{10} P/\mathrm{d} < 3.5$. Sana et al. (2013a) observed a spectroscopic binary fraction of $35 \pm 3\%$ in 30 Doradus, compatible with what Bosch et al. (2009) found from a different but overlapping sample of 54 O and early B-type stars, and inferred an intrinsic binary fraction of $51 \pm 4\%$ for periods again in the range $0.15 < \log_{10} P/\mathrm{d} < 3.5$. This binary fraction appears mostly uniform across the 30 Doradus region and independent of the spectral type and luminosity class.

4.3 Data

4.3.1 R136

The dataset that we use to test the maximum likelihood method outlined in Section 4.2.1 consists of multiple epochs (at least five) of RV measurements for 81 O-type systems in the inner 10 pc (in projection) of R136 obtained as part of the VFTS. These 81 systems include both apparently single stars and objects showing RV variability. Most of the stars in the inner 5 pc have been observed with ARGUS (see Chapter 3), while the vast majority of stars between 5 and 10 pc were observed with MEDUSA. In both cases, the RVs were measured by fitting Gaussians to helium absorption lines using a similar approach and the same rest wavelengths (Chapter 3, Hénault-Brunet et al. 2012a; Sana et al. 2013a). Our sample of 81 objects excludes the B-type and emission-line stars observed by the VFTS in the inner 10 pc of R136, but it includes a few supergiants (or supergiant candidates) for which the absolute radial velocities might be less accurate due to the effect of stellar winds on the line profiles. These were however shown to have a negligible impact on the velocity dispersion of the apparently single stars of the sample (see Chapter 3). The RV measurements for

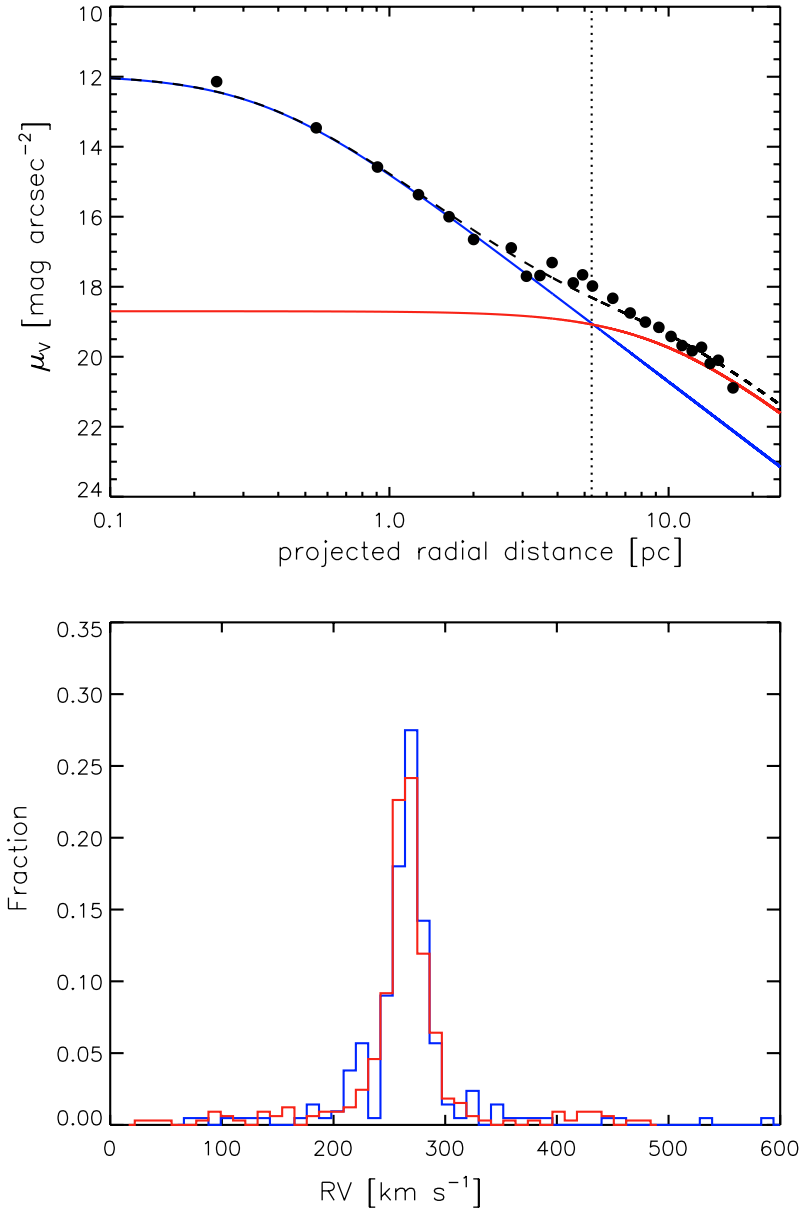

Figure 4.4 *Top:* Two-component EFF fit to the surface brightness profile of R136 as in Mackey & Gilmore (2003). The data points shown are Mackey and Gilmore's recalibrated surface brightnesses from McLaughlin & van der Marel (2005). Stars that are further out than ~ 5 pc (marked by the dotted line) from the cluster centre are more likely to be part of the OB association. Within this radius stars are more likely to belong to the R136 cluster itself. *Bottom:* Normalized histograms showing the velocity distribution of the 32 stars within 5 pc in blue (211 velocities), and the 49 stars between 5 and 10 pc in red (327 velocities).

individual epochs are listed in Hénault-Brunet et al. (2012a) and Sana et al. (2013a). The median RV uncertainty of the single-epoch measurements for the objects of our

sample is $\sim$ 4 $\mathrm{km\,s^{-1}}$. Note that we do not include stars observed by the VFTS further out than 10 pc to limit possible contamination from nearby clusters or other star formation events in the surroundings of R136.

Recall that Mackey & Gilmore (2003) found that the light profile of R136 is best fitted with a double-component EFF (Elson et al. 1987) profile, suggesting that the cluster is superimposed on an OB association contributing to a significant fraction of its total integrated light (Maíz-Apellániz 2001). In this double-component EFF fit, the projected radius where the two components contribute equally is at about 5 pc, as illustrated in Figure 4.4 (top panel). To see if these two distinct components have any effect on the velocity distribution of our sample, we also show in Figure 4.4 (bottom panel) the velocity distribution of the stars more likely to be part of the inner component (i.e. the cluster) compared to the velocity distribution of the stars more likely to be part of the outer component (i.e. the OB association). We see no evidence for a difference in the velocity distribution between the two components. Similarly, we showed in Chapter 3 that velocity dispersion profile is relatively flat between 1 and 10 pc from the centre of R136[1]. Because the two components are essentially indistinguishable (at least kinematically) in the inner 10 pc, we conclude that it is justified to try to fit a single velocity dispersion for all the stars of our sample.

4.3.2 Simulated data

Using Monte Carlo simulations we hope to (1) show the self-consistency of the method, (2) determine how the accuracy is limited by the loosely constrained binary orbital parameter distributions (Section 4.2.2), and (3) determine limitations to the precision of the method due to small-number statistics. In these simulations, we create a mock dataset of radial velocities through a two-step procedure. First, we assign every star an intrinsic radial velocity from a Gaussian distribution with given mean velocity and velocity dispersion, then for a subset of these stars (whose size is set by the binary fraction) we assign an additional velocity representing the effect of the binary orbital motions. These additional velocities are computed using randomly drawn binary orbital parameters from one of the period, mass ratio, and eccentricity distributions listed in Table 4.1. In all cases we use the extrapolated period distribution out to 300 years and the corresponding binary fraction (last row in Table 4.1). In these simulations, we do not look at the effect that measurement uncertainties or a non-Gaussian velocity distribution have on the best-fit parameters.

[1]Even though only the inner $\sim 5-6$ pc are more than a crossing time old and can be considered to be bound, and thus strictly speaking part of the cluster (see Gieles & Portegies Zwart 2011).

These mock radial velocity datasets are then fitted using our maximum likelihood procedure, assuming one of the three binary orbital parameter distributions listed in Table 4.1. This can either be the same binary orbital parameter distributions used to generate the data to test for self-consistency and constrain the precision of the method, or a different set of orbital parameter distributions to test the accuracy of the procedure when the orbital parameter distributions in the cluster do not match those assumed. We repeat these experiments for various sample sizes and intrinsic velocity distributions in the cluster.

4.4 Results

4.4.1 Systematic biases: Monte Carlo simulations

The uncertainty in the orbital parameter distributions of OB stars, encapsulated by the different sets of distributions that we are considering, induces systematic offsets in the observed velocity dispersion (and binary fraction) when an assumption about the underlying binary properties is made to fit the observed velocity distribution. Figure 4.5 shows the systematic offset in the radial velocity dispersion induced when we fit the randomly generated radial velocity datasets (Section 4.3.2) assuming each of the sets of binary orbital parameter distributions listed in Table 4.1.

In Figure 4.5, we have crossed out the simulations for which we find a best-fit binary fraction of 100%. Such a high best-fit binary fraction indicates that there are more high velocity outliers in the dataset than can be explained by the assumed binary orbital parameter distributions. These high-velocity outliers could have many causes, such as ejected stars, contaminating field stars, or bad radial velocity measurements. In the case of Figure 4.5 (top panel), the radial velocity datasets were generated using the binary properties from Sana et al. (2012), which result in a large fraction of close and equal-mass binaries. This leads to many high-velocity outliers in these datasets, which cannot be matched by the other orbital parameter distributions considered here (even for a binary fraction of 100%). This situation, where the assumed orbital parameter distributions cannot explain the large number of high-velocity outliers, will cause the velocity dispersion to be systematically overestimated, as this reduces the number of outliers. So, irrespective of the nature of the high-velocity outliers, when a binary fraction of 100% is found the measured velocity dispersion is unreliable. Therefore, below we will only consider the cases where we find a best-fit binary fraction below 100%.

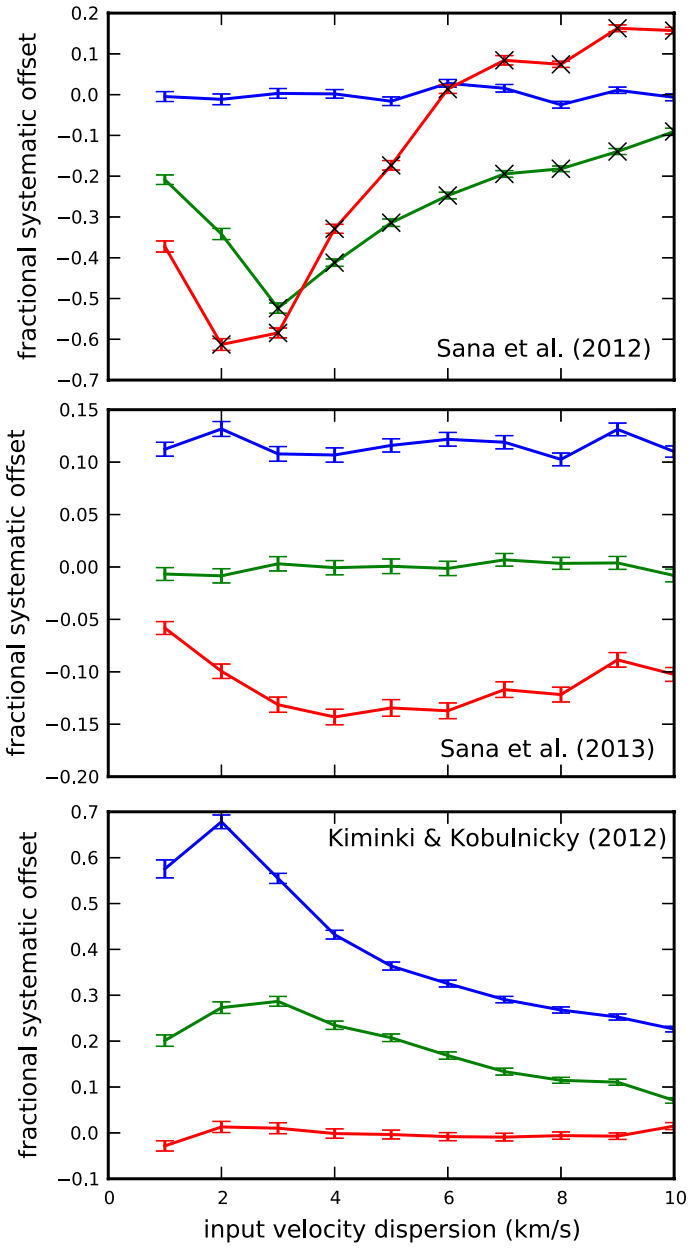

Figure 4.5 The systematic offset induced in the best-fit velocity dispersion due to the uncertainties in the orbital parameter distributions of OB stars. From top to bottom we have generated the data using the orbital parameter distributions from Sana et al. (2012), Sana et al. (2013a), and Kiminki & Kobulnicky (2012). The colors indicate the set of orbital parameter distributions assumed for the fit: blue for Sana et al. (2012); green for Sana et al. (2013a); red for Kiminki & Kobulnicky (2012). When the orbital parameter distributions used to generate the data are the same as those assumed in the fit, there is no systematic offset in the measured velocity dispersion. The error bars represent the remaining uncertainty on the systematic offset after our $\sim$ 30 Monte Carlo simulations, each of which included 2000 radial velocities. The simulations for which we find a best-fit binary fraction of 100% in the majority of cases are crossed out in black (see upper panel) to indicate that the measured velocity dispersion is likely to be overestimated in this case (see the main text).

When we use the same orbital parameter distributions to fit the data as we used to generate the data, no systematic offset between the input and observed velocity dispersion are found (Figure 4.5; blue in the upper panel, green in the middle panel, red in the bottom panel) from which we conclude that the procedure is self-consistent (i.e. it gives the right result if a dataset is generated which matches all the assumptions).

Significant systematic offsets are found when different orbital parameter distributions are used to generate the data than to fit the data. For the sets of orbital parameter distributions under study here, these systematic biases in the velocity dispersion range from up to 60% for small velocity dispersions ($\sim 2\,\mathrm{km\,s^{-1}}$) to as low as 25% for velocity dispersions of 10 $\mathrm{km\,s^{-1}}$ (other lines in Figure 4.5). This suggests that without precise knowledge of the binary properties of massive stars in a given environment, we are limited to an accuracy of tens of percent when determining the velocity dispersion using a single epoch of radial velocities from OB stars. Most OB stars will form in massive clusters, whose virial velocity dispersion is generally expected be above 4 $\mathrm{km\,s^{-1}}$. In this range the velocity dispersion can be measured to an accuracy better than $\sim 40\%$, which allows a cluster in virial equilibrium to be distinguished from an unbound cluster from a single epoch of observations.

If it is larger than the statistical uncertainties due to small-number statistics, this systematic uncertainty of $\sim$ 40% will limit the accuracy of a measured velocity dispersion. Figure 4.6 shows the dependence of the random uncertainties (on the velocity dispersion) on the sample size. From this figure we find that a $2\,\sigma$ statistical uncertainty of $\sim 40\%$ is reached for a sample size of ~ 100 stars (for a cluster with a velocity dispersion of 5 $\mathrm{km\,s^{-1}}$).

4.4.2 Analysis of R136 radial velocity data

After selecting out identified binaries and estimating the effect of undetected binaries, we determined in Chapter 3 a velocity dispersion of $\sim 6\,\mathrm{km\,s^{-1}}$ for the O-type stars within 10 pc in projection from the centre of R136[2]. To test our procedure, we fit single-epoch radial velocity datasets extracted from the full multi-epoch dataset presented in Section 4.3.1. One such fit is shown in Figure 4.1.

Because every star in the sample has been observed for at least five epochs, we were able to extract five single-epoch radial velocity datasets without any overlap. Note that

[2]The velocity dispersion was slightly smaller ($\sim 5\,\mathrm{km\,s^{-1}}$) when considering only the stars within 5 pc from the centre. Note that we ignore here the small potential contribution ($\sim 0.5\,\mathrm{km\,s^{-1}}$) to the velocity dispersion coming from cluster rotation (Chapter 5 Hénault-Brunet et al. 2012b).

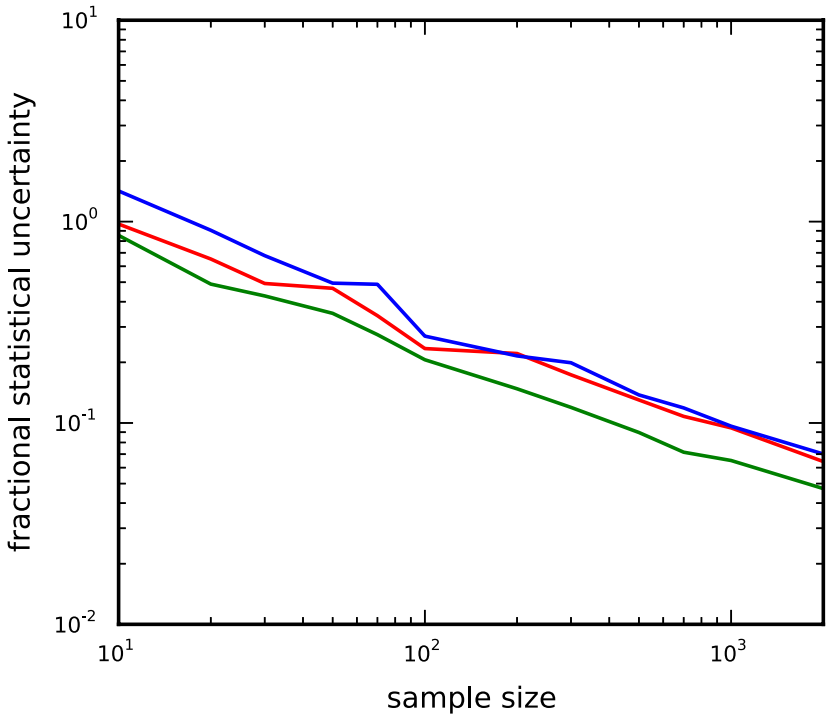

Figure 4.6 The random uncertainties in the measured velocity dispersion as a function of the sample size N for single-epoch observations of a cluster with a velocity dispersion of 5 $\mathrm{km\,s^{-1}}$. The colors indicate the set of orbital parameter distributions assumed for the fit: blue for Sana et al. (2012); green for Sana et al. (2013a); red for Kiminki & Kobulnicky (2012), i.e. same color coding as in Figure 4.5. The random uncertainties are given relative to the input velocity dispersion of 5 $\mathrm{km\,s^{-1}}$.

these datasets are not independent, as they all include observations of the same stars, albeit at different epochs.

The best-fit binary fraction, velocity dispersion and mean velocity for each of these five datasets are shown in Figure 4.7. The three different colors again represent the three sets of orbital parameter distributions assumed. The $1\,\sigma$ error bars are somewhat larger than predicted from the Monte Carlo simulations for a sample of ~ 80 RVs (see Figure 4.6). This is because a significant subset of the observed radial velocities in R136 have a measurement uncertainty comparable or larger than the velocity dispersion. These more uncertain radial velocities provide (nearly) no information about the velocity dispersion of the cluster, so the effective sample size is smaller than suggested by the ~ 80 RVs.

Depending on the assumed binary properties, we find very different binary fractions. In general, we find lower binary fractions for the orbital parameter distributions where an

individual binary has a larger likelihood of causing a significant radial velocity offset. This explains the low binary fraction found for the parameters from Sana et al. (2012, blue in Figure 4.7), which has relatively many close and equal-mass binaries (see Table 4.1 and Figure 4.2). In contrast the distribution described by Sana et al. (2013a) has more low-mass binary companions, while the distribution described by Kiminki & Kobulnicky (2012) has a larger proportion of wide binaries.

The velocity dispersion is less sensitive to the exact parameters assumed than the binary fraction, albeit we do still find variations of $\sim 2-3$ km s^{-1}, which is comparable to the $\sim 40\%$ systematic uncertainty found from Monte Carlo simulations (Sec. 4.4.1). In general, the velocity dispersion of R136 fitted from single-epoch RVs is consistent with what was derived from the multi-epoch approach (Hénault-Brunet et al. 2012a).

Finally the best-fit mean velocity is hardly sensitive to the assumed orbital parameter distributions, because as long as the projections of the binaries on the sky are random, the velocities from the binary orbital motions will be symmetrically distributed around the mean velocity. This suggests that measurements that depend on the mean velocity, such as cluster rotation, may be determined with only a single epoch of radial velocity data.

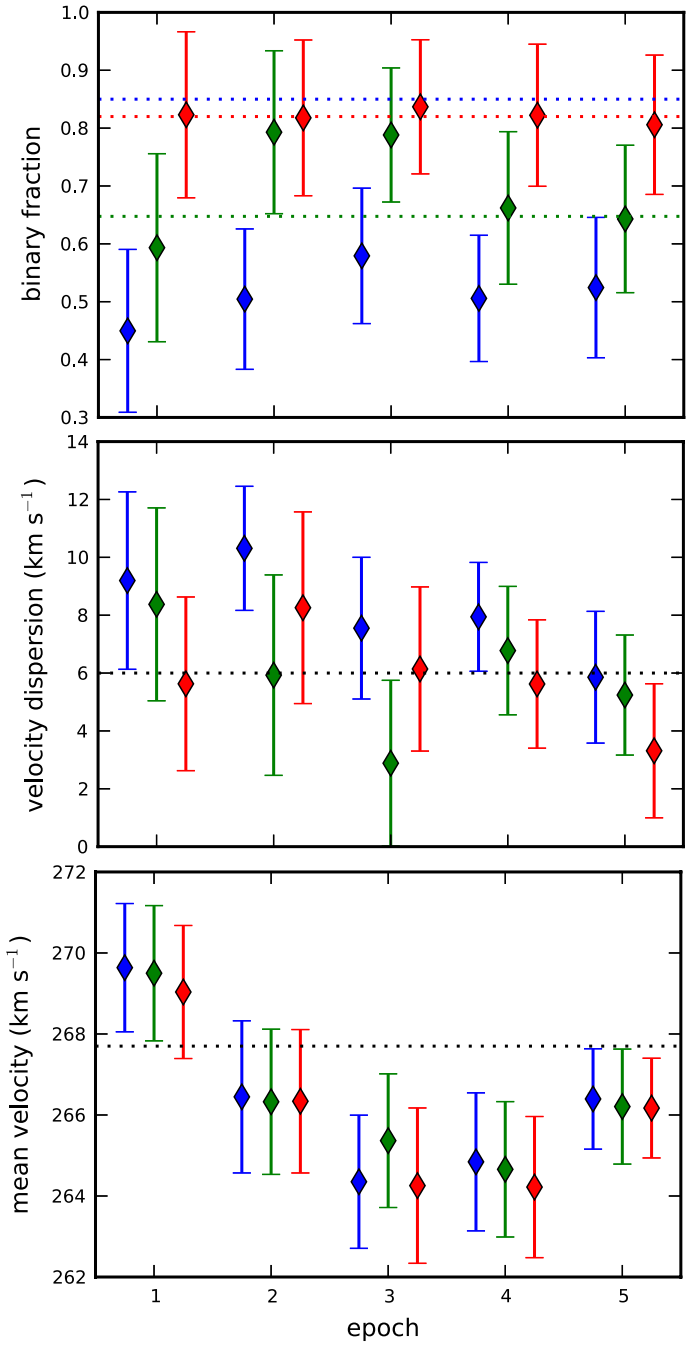

Figure 4.7 The best-fit binary fraction, velocity dispersion, and mean velocity for five single-epoch radial velocity datasets of the O-type stars in R136. The colors indicate the set of orbital parameter distributions assumed in the fit: blue from Sana et al. (2012); green from Sana et al. (2013a) ; and red from Kiminki & Kobulnicky (2012). The error bars show the 1σ uncertainties on the best-fit values, as estimated through Markov Chain Monte Carlo simulations. The dashed lines in the middle and lower panels show the values found after removing the spectroscopic binaries identified from multi-epoch data (Hénault-Brunet et al. 2012a). The dashed lines in the upper panel indicate the intrinsic binary fractions (extrapolated to a period of 300 days) listed in Table 4.1, the green one corresponding to the 30 Doradus sample.

4.5 Discussion

Given the present-day uncertainties on the orbital parameter distributions of OB spectroscopic binaries (e.g. Table 4.1 and Figure 4.2), we found that the velocity dispersion can be measured from a single epoch of radial velocity data with an accuracy ranging from $\sim$ 60% for a cluster velocity dispersion of $\sim$ 2 $\mathrm{km\,s^{-1}}$ to $\sim$ 25% for $\sigma_{1\mathrm{D}} \sim 10$ $\mathrm{km\,s^{-1}}$. For typical velocity dispersions of young massive clusters ($\gtrsim$ 4 $\mathrm{km\,s^{-1}}$) we find that an accuracy of better than 40% can be reached, which is sufficient to distinguish a cluster in virial equilibrium from an unbound cluster. Compared to the factor of ~ 5 difference that we would get if we just blindly computed the velocity dispersion from a single epoch of RVs without taking into account binaries (see Chapter 3), this is a significant improvement. The systematic uncertainty will dominate over the statistical uncertainties from small-number statistics for a sample size larger than about 100 radial velocities. This means that after observing 100 stars for a single epoch, the accuracy of the measured velocity dispersion will in principle no longer increase when more stars are observed due to the uncertainty in the binary orbital parameter distributions of OB stars. Observing the same stars for only one more epoch might make it possible to push down the systematic uncertainties and increase the accuracy with which the velocity dispersion is measured under the 40% level. We are currently exploring an extension of the method presented in this chapter to the case of two epochs of RVs.

To explain the systematic offset we directly compare the fits of the single-epoch R136 data for the orbital parameter distributions of Sana et al. (2012) and Kiminki & Kobulnicky (2012). In the case of Sana et al. (2012) the binaries typically orbit each other with tens of $\mathrm{km\,s^{-1}}$, an order of magnitude larger than for Kiminki & Kobulnicky (2012) (Figure 4.3). Thus, an individual binary in the case of Sana et al. (2012) will have a much large probability of causing a high-velocity outlier. To reproduce the high-velocity outliers in the R136 data we thus need a lower binary fraction for the binary orbital parameter distribution of Sana et al. (2012) than for Kiminki & Kobulnicky (2012), which explains the trend in the binary fraction found for the R136 data (left panel in Figure 4.7).

The fitted velocity dispersion on the other hand is affected by the abundance of wider binaries with orbital velocities comparable to the velocity dispersion of the cluster (~ 6 $\mathrm{km\,s^{-1}}$), as these binaries are more likely to really broaden the observed peak in the velocity distribution, instead of just creating a high-velocity tail. We can see in Figure 4.2 that these binaries are much more common for the orbital parameter distributions

of Kiminki & Kobulnicky (2012) than for those of Sana et al. (2012), even before we take into account the fact that we find a lower overall binary fraction for Sana et al. (2012). This much higher fraction of wide binaries broadening the observed velocity distribution when assuming the binary orbital parameter distributions of Kiminki & Kobulnicky (2012) leads to a significantly smaller best-fit velocity dispersion (central panel in Figure 4.7) compared to Sana et al. (2012). The fact that this systematic offset in the velocity dispersion is smaller than a factor of 2 is surprising given that the typical orbital velocities differ by an order of magnitude (see lower left panel in Figure 4.2).

Note that the differences between the sets of binary properties listed in Table 4.1 might be real to some extent (i.e. not only reflect uncertainties in our knowledge of these properties). There are reasons to believe that the binary properties of massive stars might depend on the environment and the age of the region in which they are located. For example, the intrinsic fraction of O-type spectroscopic binaries seems lower in 30 Doradus[3] than in the relatively low-density Galactic clusters (see Table 4.1), although both results still agree within $2\,\sigma$. As discussed by Sana et al. (2013a), this might suggest that the binary properties in the 30 Doradus region have already been significantly affected by dynamical and/or stellar evolution which would induce merger events or binary disruption and decrease the observed number of binaries. This is to be expected given the presence of different populations in the region, some already quite old, and the fact that a fraction of the O-star population consists of runaways. For the Galactic open clusters sample, cluster dynamics and stellar evolution are not expected to have significantly altered the orbital properties of the binaries (Sana et al. 2012). Given the young age of the clusters in this sample, the parameters reported in this case are probably a good representation of the properties of massive binaries at birth.

As discussed in Section 4.2.3, there is a wide variety of possible period, mass ratio, and eccentricity distributions for OB binaries considered in the literature. We have chosen to limit our analysis to the three orbital parameter distributions in Table 4.1, which we felt were the most representative of our present-day knowledge about these distributions. The method presented here can however be used to fit any radial velocity distribution, as well as to explore the systematic offsets in the measured velocity dispersion between any sets of orbital parameter distributions.

[3]The binary fraction quoted by Kiminki & Kobulnicky (2012) is even lower than that found by Sana et al. (2013a) in 30 Doradus, but note that Kiminki & Kobulnicky considered a shorter period range extending to 1 000 days, compared to a maximum period of about 3 000 days for the two other studies listed in Table 4.1. When the binary fractions from all these studies are considered over the same extrapolated period range of 300 years, only 30 Doradus appears to have a significantly lower binary fraction.

4.6 Summary

We explored the applicability of the maximum likelihood method presented by Cottaar et al. (2012b) to recover the velocity dispersion of massive stars in young clusters from a single epoch of radial velocity data. By using Monte Carlo simulations and multi-epoch stellar radial velocity data in the young massive cluster R136 as a test case, we showed that the method works reasonably well, the main limitation being uncertainties in the binary properties of OB stars which can lead to a systematic uncertainty of tens of percent in the fitted velocity dispersion ($< 40\%$ for typical young massive cluster velocity dispersions, i.e. $\gtrsim 4$ km s^{-1}).

Although we have tested the method on a sample of RVs of O-type stars in R136 and considered binary properties that were derived mainly from spectroscopic surveys of O-type stars (including early B-type stars in the case of Kiminki & Kobulnicky 2012), it should also be applicable to samples of B-type stars as they appear to have similar binary properties (Dunstall et al., in preparation). This opens the door to using a single epoch of RVs to estimate the velocity dispersion of the massive star population in a large number of young Galactic open clusters which may contain at most a few O-type stars but a much larger number of B-type stars.

Chapter 5

Evidence for rotation of the young massive cluster R136

5.1 Introduction

Little is known about rotation in young star clusters, partially because it is already very challenging to accurately measure σ_{1D} given the high multiplicity fraction of massive stars, as we have seen in the previous chapters. Frenk & Fall (1982) reported an age-ellipticity relation for clusters in the LMC with older clusters presenting less elongated shapes, which was interpreted as internal evolution erasing any asymmetry stemming from the violent relaxation process of the formation[1]. However, rotation and ellipticity are not necessarily equivalent. Ellipticity can be due to rotation (e.g. ω Cen; Meylan & Mayor 1986) but also to velocity anisotropy (Stephens et al. 2006; Hénon 1973), and rotating clusters can be spherical (Lynden-Bell 1960; Meza 2002).

Marginal evidence for rotation was found for the young (few 100 Myrs) Galactic cluster GLIMPSE-C01 with an amplitude of $V_{\rm rot} \sin i \ /\sigma_{1D} \simeq 0.2$ (Davies et al. 2011). A rotational signal in the RVs was also detected in the $\sim$ 100 Myr cluster NGC 1866 (Fischer et al. 1992) and in the $\sim$ 50 Myr binary cluster NGC 1850 (Fischer et al. 1993), both in the LMC. To really confirm whether clusters form with a significant amount of angular momentum, we need to look for rotation in an even younger cluster. The young massive cluster R136 is an ideal target to establish this. With an estimated

[1]There is however some debate upon the existence of this correlation, with van den Bergh & Morbey (1984) arguing that it is not statistically significant and Kontizas et al. (1989) and Goodwin (1997) reporting that it is only a weak correlation.

mass of about 10^5 $M_\odot$ (Andersen et al. 2009, see also Chapter 3) and its sub solar metallicity, it may at some stage resemble a typical metal-rich globular cluster (GC) as we find them in the Milky Way Bulge. With an age of less than 2 Myr (de Koter et al. 1998; Massey & Hunter 1998; Crowther et al. 2010), it is so young that any rotation needs to be attributed to the formation process, be it from merging of sub-clusters or directly from the angular momentum of the progenitor cloud. A rough estimate of the half-mass relaxation time ($t_{\rm rh}$) of R136 can be obtained by assuming $N = 10^5$ stars and a half-mass radius of 2.3 pc, which is found from multiplying the half-light radius of 1.7 pc (Hunter et al. 1995) by 4/3 (Spitzer 1987). Following the formula of Spitzer & Hart (1971, see also Chapter 1), we obtain $t_{\rm rh} \simeq 366\,{\rm Myr}$, so relaxation would not have had time to erase the original signature of rotation.

In this chapter, we report on evidence for rotation of R136 deduced from the RV measurements of massive stars obtained as part of the VFTS, a result originally published in Hénault-Brunet et al. (2012b). We briefly present the sample on which this study is based in Section 5.2 and describe our analysis of the rotational signature in Section 5.3. We discuss the implications of the rotation of R136 for cluster evolution in Section 5.4, and summarize our results in Section 5.5.

5.2 Data

The main data used in this chapter consist of RV measurements and their uncertainties for 36 apparently single O-type stars within a projected radius of 10 pc from the centre[2] of R136 (again adopted here as the position of the star R136-a1: $\alpha = 5^{\rm h}38^{\rm m}42^{\rm s}.39$, $\delta = -69°06'02.''91$, J2000). These data and measurements, based on observations from the VFTS, have been described extensively in previous chapters. We retain here only the RVs of stars showing no significant variability throughout all epochs, and we apply a $3\,\sigma$ clipping centered on the mean velocity of the cluster, with $\sigma = 6$ km s^{-1}, the observed line-of-sight velocity dispersion of the cluster (i.e. before correction of the velocity dispersion for undetected binaries; see Chapter 3). This yields a total of 16 ARGUS sources, all within 5 pc from the centre, and 20 Medusa sources, all between 5 and 10 pc except two between 4 and 5 pc. These are all the sources listed in Table 3.2 minus the $3\,\sigma$ outliers VFTS 536 and VFTS 540. In Figure 5.1, we schematically present the positions of all the stars of this sample and their distribution of RVs with respect to the mean RV of the cluster.

[2]Note that the results presented below are not sensitive to changes (within reasonable uncertainties) in the adopted position for the centre of the cluster.

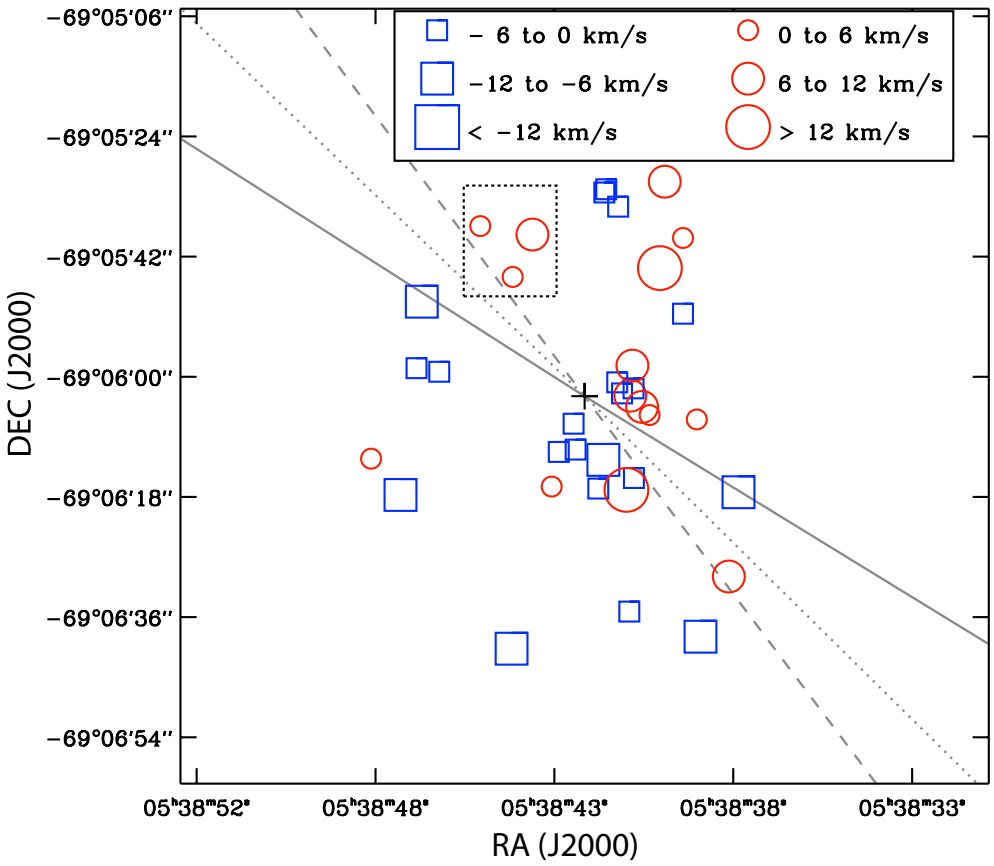

Figure 5.1 Illustration of the positions and RVs of the stars considered in this chapter. Symbol sizes denote the magnitude of the stellar velocities with respect to the average cluster velocity. The solid, dotted, and dashed lines correspond to the optimal rotation axis determined for models with a constant rotational velocity, a constant rotation rate, and a more realistic rotation curve (see Section 5.3), respectively. The dotted rectangle indicates the stars that coincide with the clump reported by Sabbi et al. (2012, see sections 5.3 and 5.4).

5.3 Analysis

5.3.1 The "globular cluster" method

As a first step to explore the presence of internal rotation in R136, we applied a method commonly used to detect rotation in globular clusters (e.g. Côté et al. 1995; Bellazzini et al. 2012). We divided our sample in two using a dividing line passing through the centre of the cluster, and we computed the difference in the weighted mean RV between the two subsamples of stars. We then rotated the dividing line by 20° and repeated the calculation. We recorded the difference in the mean RV between the two subsamples for each position angle (PA) of the dividing line, and plotted the difference in mean RV as a

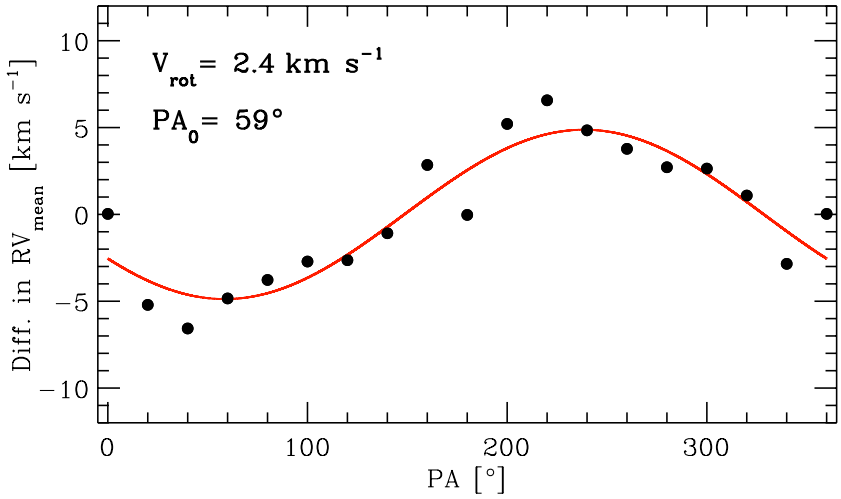

Figure 5.2 Difference between the mean radial velocities on each side of the cluster with respect to a line passing through the centre (R136-a1) with position angle PA (measured from north to east, north = 0°, east = 90°), as a function of PA. The continuous line is the sine curve that best fits the observed pattern.

function of PA (Figure 5.2). In studies of globular clusters, a coherent sinusoidal signal pattern like that seen in Figure 5.2 is generally interpreted as a clear sign of rotation (although see our caveats below). Note that we adopted a PA increasing anti-clockwise in the plane of the sky from north (PA = 0°) towards east (PA = 90°). We fitted the observed pattern with the simple sine law:

$$\Delta \mathrm{RV}_{\mathrm{mean}} = A_{\mathrm{rot}} \sin(\mathrm{PA} + \Phi), \tag{5.1}$$

where $\Phi = 270° - \mathrm{PA}_0$, PA_0 is the position angle of the dividing line (in degrees) corresponding to the maximum rotation amplitude and coinciding with the rotation axis, and A_{rot} is two times the actual mean rotation amplitude in $\mathrm{km\,s^{-1}}$ ($V_{\mathrm{rot}} = A_{\mathrm{rot}}/2$, see e.g. Lane et al. 2010b). Note that the difference in mean RV is averaged over the full range of radii of our sample. V_{rot} should therefore be considered as a lower limit to the maximum rotational amplitude because the amplitude is expected to vary with distance from the centre of the cluster. It is also a projection of the 3D amplitude onto the plane of the sky, but we do not know the inclination. The best-fit parameters that we obtained are $V_{\mathrm{rot}} = 2.4\ \mathrm{km\,s^{-1}}$ and $\mathrm{PA}_0 = 59°$. The uncertainties associated to these parameters ($\sim 0.1\ \mathrm{km\,s^{-1}}$ and $\sim 5°$ respectively) from the simple fit however appear unrealistically small. For example, the uncertainty on PA_0 is significantly smaller than the typical difference in position angle between two nearby stars (i.e. with similar position angles). This illustrates one of the drawbacks of the method above. While it does suggest that R136 might be rotating, and despite being widely used to detect

and quantify the amount of rotation in globular clusters, the method is indeed less than ideal. Because every data point in Figure 5.2 effectively contains all the RV measurements of the sample, all the data points are correlated. This likely explains why the uncertainties on $V_{\rm rot}$ and PA_0 obtained when fitting a sine curve to the data are unrealistically small. The fact that the data is extremely smoothed even makes it possible to obtain a sinusoidal signal pattern in cases where there is no genuine and significant cluster rotation. The method also does not allow comparison of the data with a specific rotation curve and instead implicitly assumes a constant rotational amplitude. In addition, it does not offer a systematic way to test the significance of the detected rotation signal. We therefore judged it desirable to investigate the possible rotation of R136 further and in the next subsection present a straightforward maximum likelihood approach that compares the data (without any binning) to simple models with a given velocity dispersion and rotational velocity amplitude.

5.3.2 Maximum likelihood method

In this section, we fit rotating models to our set of measured RVs by maximizing the logarithm of the likelihood function (Bevington 1969)

$$M = \ln \mathcal{L} = \ln \left[\prod_{i=1}^{N} P_i \right] = \sum_{i=1}^{N} \ln P_i, \tag{5.2}$$

where P_i is the probability density function of a measurement RV_i. Given our relatively small dataset, we only consider three simple models: (1) a constant rotational velocity amplitude, (2) a constant rotation rate, and finally (3) a more realistic model with solid body rotation in the inner parts peaking near 2 half-mass radii followed by a decline (see e.g. Lynden-Bell 1967; Gott 1973). For these models, the probability density function of a measurement RV_i with uncertainty σ_i given a position angle PA_0 for the rotation axis and a line-of-sight velocity dispersion $\sigma_{\rm 1D}$ can be written as

$$P_i = \frac{1}{\sqrt{2\,\pi}\sqrt{\sigma_i^2 + \sigma_{\rm 1D}^2}} \exp\left[-\frac{1}{2} \left(\frac{\mathrm{RV}_i - V_{\rm rot} \sin i}{\sqrt{\sigma_i^2 + \sigma_{\rm 1D}^2}} \right)^2 \right], \tag{5.3}$$

where $V_{\rm rot} \sin i$ is a constant for the model with fixed rotational velocity. For the model with constant rotation rate, $V_{\rm rot} \sin i$ depends on the rotation rate (Ω) and the distance from the rotation axis (X_j) such that $[V_{\rm rot} \sin i]_j = \Omega\ X_j$. For the physically

motivated model, we adopt a function of the form $[V_{\rm rot}\sin i]_j = A/2 \cdot X_j/(1+(X_j/4)^2)$, where X_j is the distance to the rotation axis in pc and A is the maximum rotational velocity which we assume is at 4 pc for simplicity (the half-mass radius of R136 is about 2 pc). This rotation curve captures the general behaviour seen in simulations of rotating clusters (e.g. Kim et al. 2002). Note that because the velocity dispersion profile of R136 appears relatively flat (Chapter 3), this function also describes $V_{\rm rot}/\sigma$. The position angle (with respect to the centre of the cluster) is defined as increasing from north to east, as in Section 5.3.1. We adopt negative rotational velocities for position angles between PA_0 and $\mathrm{PA}_0 + 180°$. For simplicity, we assume that $\sigma_{\rm 1D}$ is constant across the radius range considered. This $\sigma_{\rm 1D}$ is largely due to cluster dynamics, but contains a small contribution from the orbital motions of undetected binaries (~ 1 km s^{-1}; see Chapter 3), effectively adding noise to the rotational signature that we are trying to detect.

Given that the parameter space to be explored is not so vast, we simply search for the best-fit parameters using a grid approach. The values of the parameters that are found to maximize the likelihood function are $\mathrm{PA}_0 = 57 \pm 26°$, $V_{\rm rot}\sin i = 2.8 \pm 0.9$ km s^{-1} and $\sigma_{\rm 1D} = 5.6 \pm 0.8$ km s^{-1} for the constant rotational velocity model, $\mathrm{PA}_0 = 44 \pm 28°$, $\Omega = 0.66 \pm 0.28$ Myr^{-1} and $\sigma_{\rm 1D} = 5.8 \pm 0.8$ km s^{-1} for the constant rotation rate model, and $\mathrm{PA}_0 = 36 \pm 21°$, $A = 3.4 \pm 1.3$ km s^{-1} and $\sigma_{\rm 1D} = 5.6 \pm 0.8$ km s^{-1} for the final model. Note that the parameters obtained for the constant rotational velocity model are consistent with those found in Section 5.3.1 with the method commonly used in studies of globular clusters, but the maximum likelihood method still has the advantage of directly comparing the data to models without binning. We see that see that when the rotation and velocity dispersion are fitted simultaneously, the velocity dispersion is, as expected, slightly lower (by ~ 0.5 km s^{-1}) than what was measured without considering rotation (6.3 km s^{-1} for all the stars of the sample considered here; see Figure 3.7). The best-fit rotation curves are shown in Figure 5.3.

The uncertainties on the best-fit parameters were first estimated using Monte Carlo simulations of mock datasets comparable to our measured data (i.e. with the same rotational signal). For each of the simple models considered, we applied the maximum likelihood method above to 10 000 distributions of velocities. The adopted size and spatial distribution of the simulated populations were taken to be the same as the observed sample in order to be sensitive to possible biases introduced by our non-uniform spatial sampling. Radial velocities were first drawn randomly from a Gaussian distribution with σ taken as the value of σ_{1D} quoted above. For each simulated RV, observational noise was added based on the RV uncertainty of the observed star at the

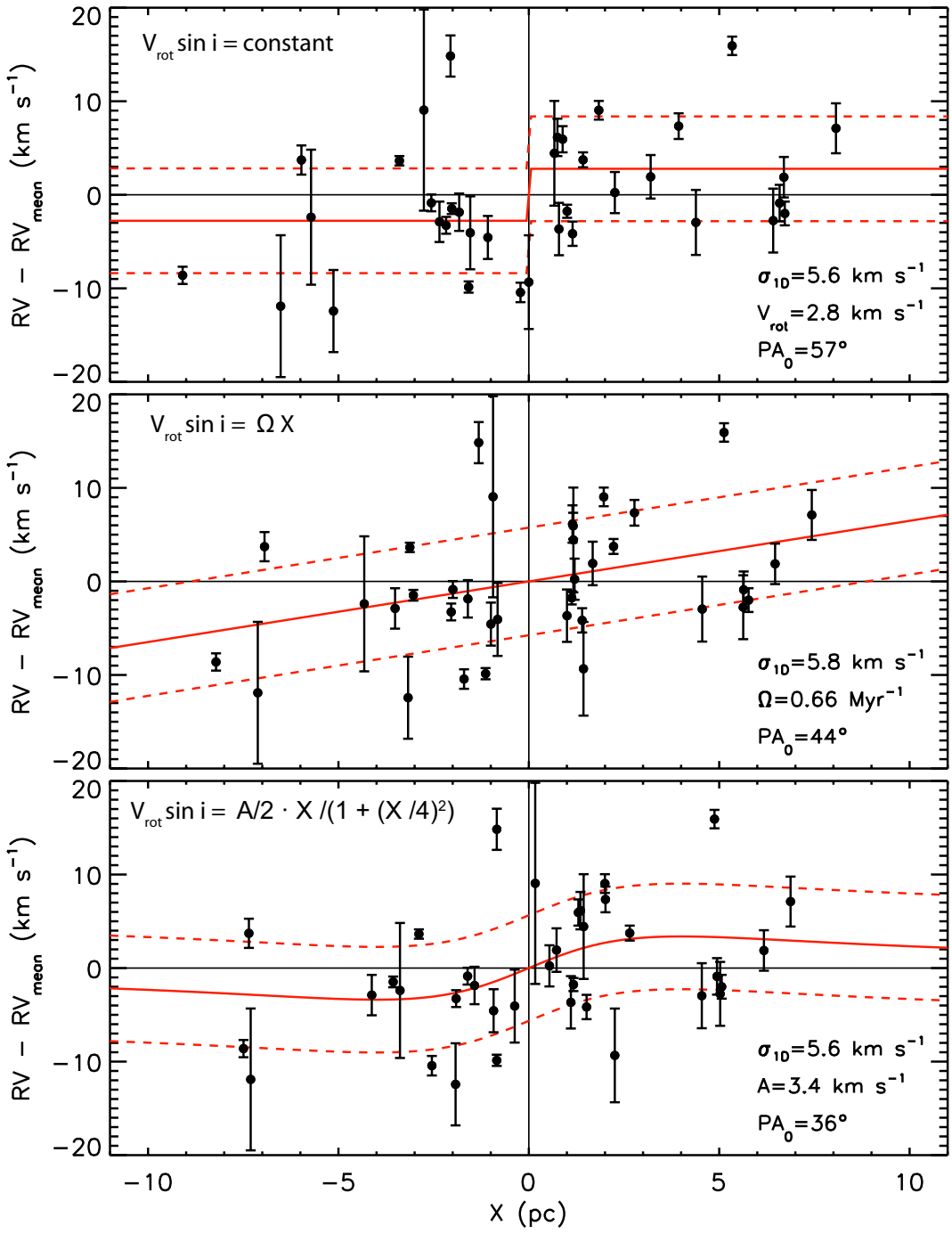

Figure 5.3 RV (in the system of the cluster) as a function of distance X from the optimal rotation axis for models with constant rotational velocity rate (top), constant rotation rate (middle), and the more realistic rotation curve with $V_{\rm rot} \sin i = A/2 \cdot X/(1 + (X/4)^2)$ (bottom). The best-fit rotation curves are shown as solid lines, and $\pm\sigma_{\rm 1D}$ envelopes are represented by dashed lines.

same location, again to take into account the biases introduced by our non-uniform dataset. We then added an extra velocity component due to the rotation of the cluster as prescribed by the best-fit rotation curves presented above, and finally fitted the three

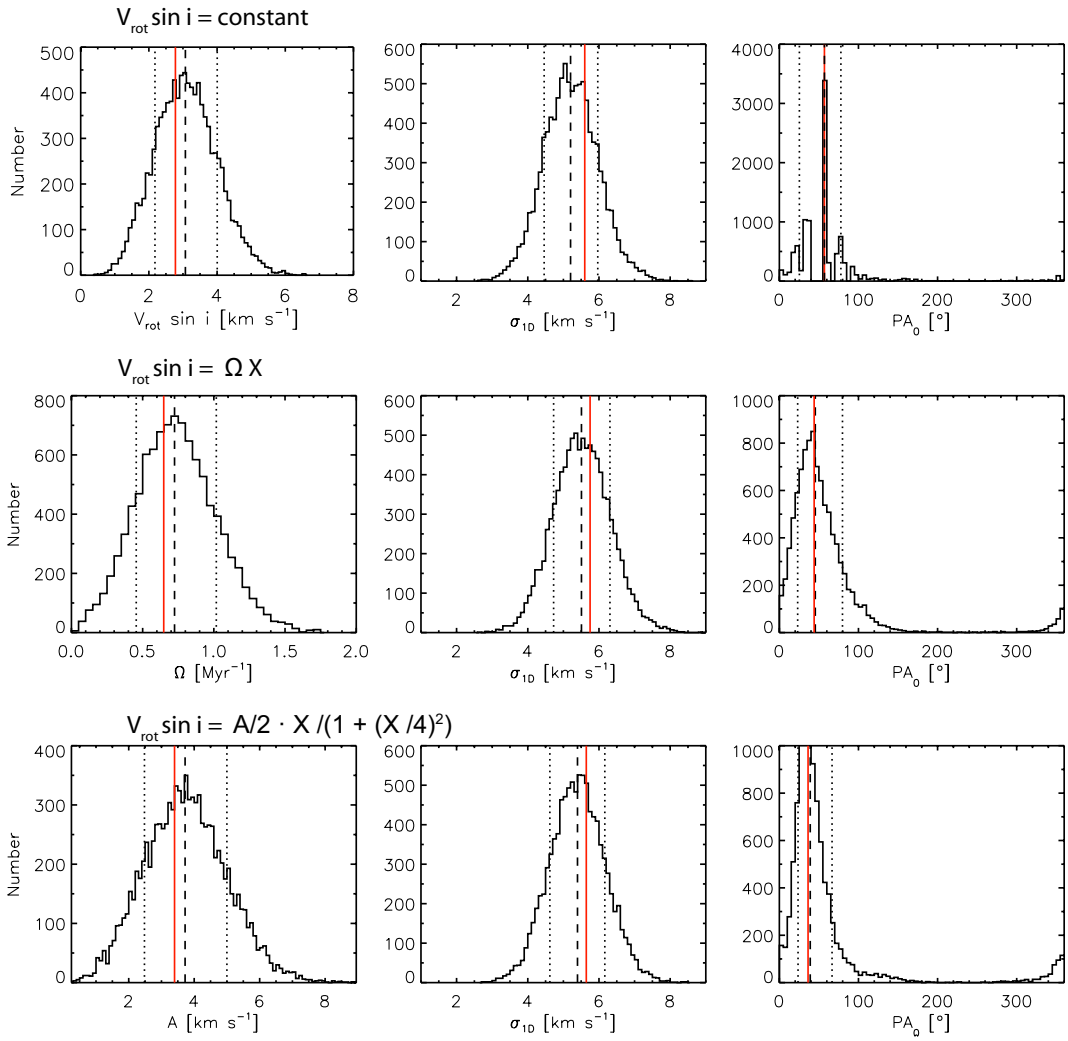

Figure 5.4 Distributions of fitted parameters from 10 000 simulated datasets with the same rotation curves as the best-fit rotation curves determined from the R136 dataset. The parameters used to generate the simulated datasets are indicated by vertical red lines. The median of each distribution is shown as a dashed line and the 68% confidence intervals are represented by dotted lines. From top to bottom, the distributions are for models with constant rotational velocity, constant rotation rate, and the more realistic rotation curve with $V_{\rm rot} \sin i = A/2 \cdot X/(1 + (X/4)^2)$.

rotating models to the mock RV distributions.

The distributions of best-fit parameters from these simulations are shown in Figure 5.4. We estimated the $1\,\sigma$ errors on the best-fit parameters of the R136 dataset by considering the 0.16 and 0.84 percentiles of the distributions obtained from the Monte Carlo simulations. While the rotation curve parameters assumed to generate the simulated datasets appear to be recovered very well, these tests make it possible to investigate potential biases in our fitting procedure. From Figure 5.4, we can see for example that the amplitude of the rotation curve (or the rotation rate) appears to

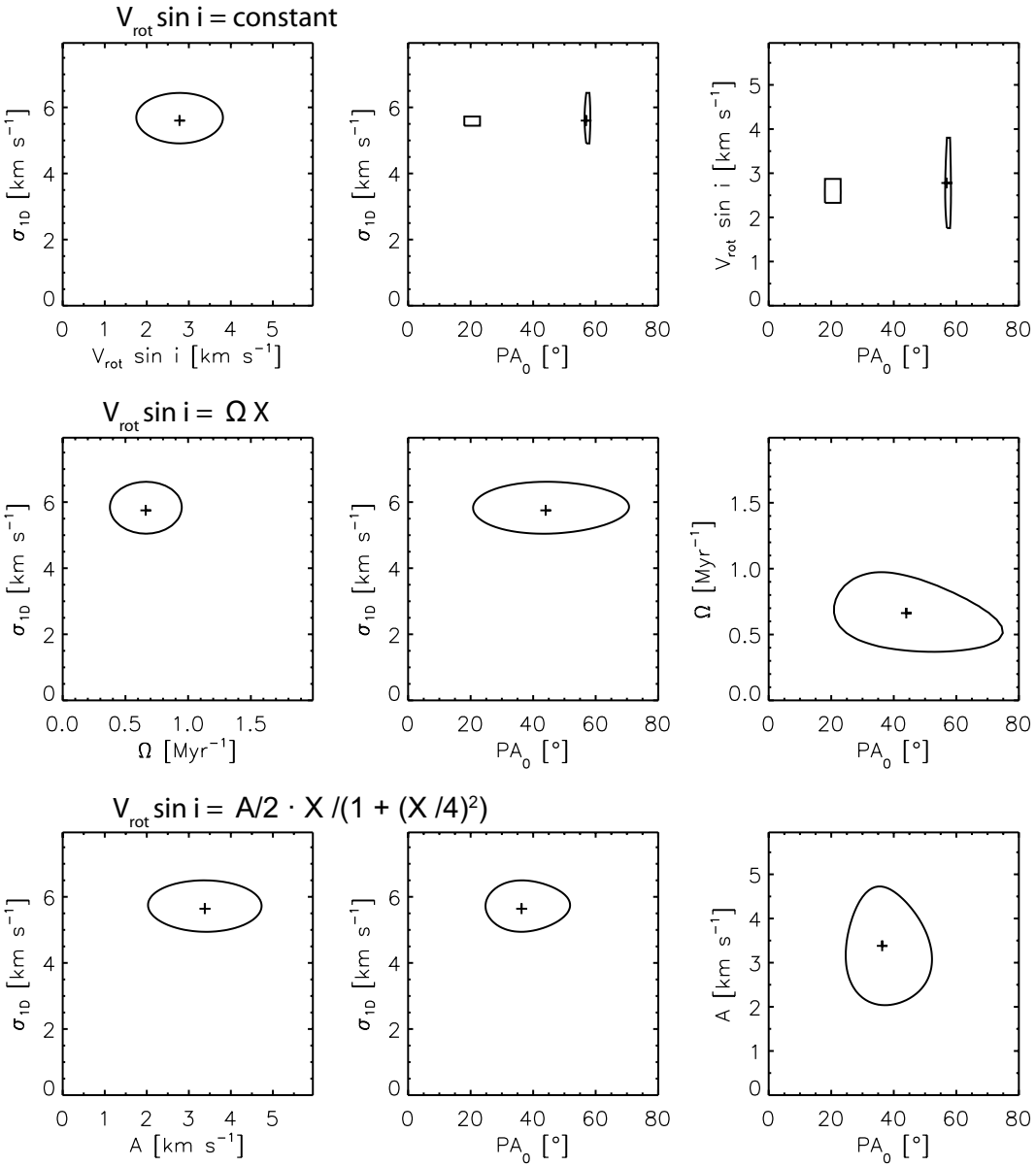

Figure 5.5 Likelihood contours around the best-fit parameters for the rotation curve of the R136 dataset for the three different models considered. The best-fit parameters are indicated by a cross, and the contours trace where $\Delta M = \frac{1}{2}$ from the maximum value of M.

be systematically slightly overestimated, and σ_{1D} tends to be slightly underestimated. These biases however generally remain much smaller than the estimated uncertainties on the parameters. The structure in the distribution of best-fit PA_0 from the simulated datasets with constant rotational velocity also suggests some non-trivial biases towards certain position angles for the rotation axis (see below).

We also obtained consistent uncertainties with the ones estimated from Monte Carlo simulations by considering the change in parameters necessary to decrease M by $\Delta M =$

$\frac{1}{2}$ from its value at the maximum, which should be valid if the likelihood function follows a Gaussian form (Bevington 1969). Figure 5.5 shows such likelihood contours for the different pairs of parameters and for the three different models. Note the peculiar shape of the contours for PA_0 for the constant rotational velocity model (to be compared with the upper right distribution of Figure 5.4), indicating that the likelihood function is not varying smoothly in this case. The maximum value of M is slightly higher for the constant rotational velocity model (-83.63) compared to the two other models (which have a maximum M of -84.45 and -84.08), but likelihood ratio tests on the simulated datasets above showed that the difference is not significant. Thus, we currently cannot favour one model over the others.

To establish the significance of the detected rotational signal, we performed another set of Monte Carlo simulations and applied the maximum likelihood method above to 10 000 random distributions of velocities (i.e. non-rotating systems). We again adopted the same size and spatial distribution as the observed sample for the simulated RV distributions (i.e. same number of stars with the same coordinates as those observed, but with new velocities). The velocities were drawn from a Gaussian distribution with $\sigma = 6$ km s^{-1}, the observed line-of-sight velocity dispersion, and observational noise was again added based on the RV uncertainty of the observed star at the same location before fitting the data. The distribution of $V_{\rm rot} \sin i$, Ω, and A from 10 000 such simulations is shown in Figure 5.6. The distributions do not peak at zero because the limited number of stars and the measurement noise generally result in a non-zero amplitude. Our best-fit values for the observed set of RVs are located in the right tail of these distributions and the corresponding confidence level of the detection is near 95% (94.6% for the constant rotation rate model, 91.3% for the constant rotational velocity model, and 94.6% for the third model). This might not seem like a very solid detection, but given the current lack of constraints on the rotation of very young clusters, a relatively high confidence level like this is definitely worth reporting and should stimulate further studies.

We can also use the simulated datasets with no rotation to explore potential biases in the fitted position angle of the rotation axis. Figure 5.7 shows for the three models considered the distribution of PA_0 from the 10 000 simulated random RV distributions with no built-in rotation. These distributions are not uniform like we might expect, indicating that some angles are preferred, which is most likely due to the non-uniform and limited spatial distribution of the sample. Some tests were performed with much larger and more uniformly distributed simulated samples and in these cases a uniform distribution of PA_0 is indeed obtained. Fortunately, the right panels of Figure 5.4 still

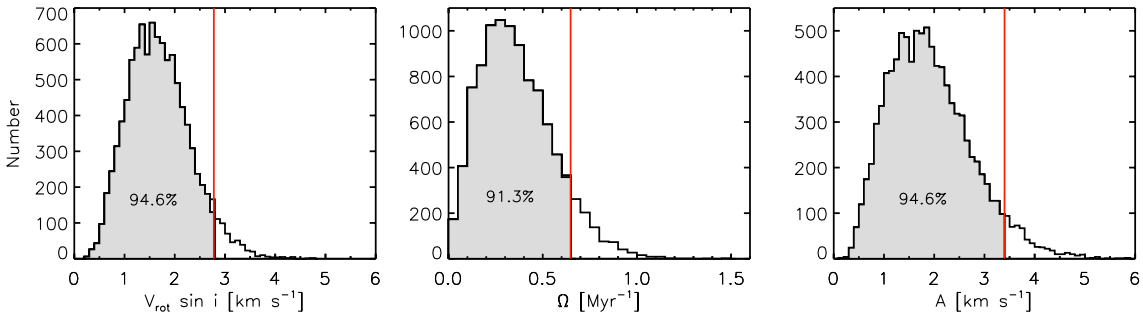

Figure 5.6 Distribution of amplitudes $V_{\rm rot} \sin i$, Ω, and A from 10 000 Monte Carlo simulations of RV distributions with no rotation. The optimal values for the observed RV configuration are indicated by red vertical lines. Confidence levels of 94.6%, 91.3% and 94.6% are found respectively for the best-fit amplitude of each model.

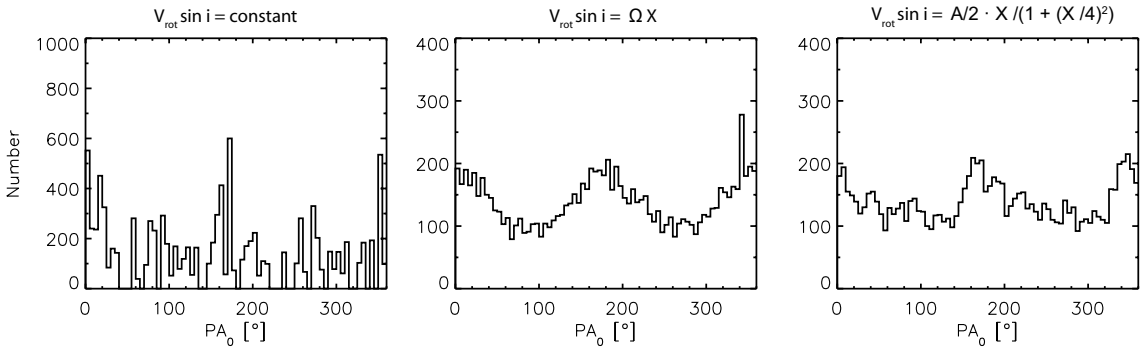

Figure 5.7 Distribution of PA_0 from 10 000 Monte Carlo simulations of RV distributions with no rotation for the three models considered.

suggest that these biases towards certain angles are not strong enough to prevent us from recovering the correct value of PA_0, although they might contribute to increase the uncertainty on this parameter.

To test the validity of the detected signal, the analysis presented above was also performed on different subsamples (see Table 5.1). For simplicity, we focus here on results for the model with a physically motivated rotation curve. First, we analysed a subsample from which supergiant candidates and stars with possible composite spectra were excluded, as their RVs might be inaccurate (see Chapter 3). Secondly, Sabbi et al. (2012) found a dual structure in the density of low mass stars in R136 indicating that a second smaller clump or cluster is present ~ 5.4 pc from the core of R136. Only three of our targets coincide with this second clump (see Figure 5.1), but we performed our analysis without including those stars in case a different mean RV of the clump with respect to the main cluster leads to the spurious detection of a rotational signal. The best-fit parameters obtained for these two subsamples are in excellent agreement with those of the main sample, albeit the confidence level drops to $\sim 90\%$ due to the lower

number of RV measurements. These results suggest that the rotational signal detected is not dominated by supergiant/SB2 candidates or by the stars that might belong to the smaller clump from Sabbi et al. (2012).

As an additional check, we ran the analysis on different subsamples of apparently single O-type stars from the VFTS using the measurements of Sana et al. (2013a), including stars farther away from R136 than in our main sample. The analysis of these subsamples suggests that the rotation signal is dominated by the stars in the inner regions and does not result from a velocity gradient across the field on a larger scale in the surrounding OB association. For example, when considering the sample of stars between 10 and 20 pc in projection from the centre (37 stars), we find that A goes down to 2.6 $\mathrm{km\,s^{-1}}$ and the confidence level is only 35% in this case, so no rotational signature is found in the outer regions.

Note that stars that are part of the surrounding 30 Doradus region and not members of R136 could contaminate our sample. If we assume that the outer component of the double-component EFF fit (Elson et al. 1987) to the light profile of R136 (Mackey & Gilmore 2003) is due to the surrounding association, then we may expect these stars to contribute to $> 50\%$ of the sample beyond 5 pc from the centre and to dilute the rotational signal in the outer regions of the cluster.

Table 5.1 Best-fit parameters for the rotation curve and confidence level for the detection of rotation for different subsamples of stars in and around R136. N_{stars} indicates the number of RVs used for each subsample.

Sample	N_{stars}	$\mathrm{PA_0}$	σ_{1D}	A	Confidence level
		[°]	$[\mathrm{km\,s^{-1}}]$	$[\mathrm{km\,s^{-1}}]$	%
< 10 pc	36	36 ± 21	5.6 ± 0.8	3.4 ± 1.3	94.6
< 10 pc; no supergiants/SB2	29	35 ± 30	5.8 ± 0.9	3.4 ± 1.4	90.4
< 10 pc; -3 stars from Sabbi et al. clump	33	32 ± 44	5.9 ± 0.8	3.2 ± 1.3	89.6
$10 - 20$ pc	37	314 ± 109	7.0 ± 1.0	2.6 ± 1.1	34.7

5.4 Discussion

Given that $\sigma_{1\mathrm{D}} \simeq 5 \pm 1$ $\mathrm{km\,s^{-1}}$ for R136 after correcting for undetected binaries (Chapter 3) and that the mean rotational velocity in the radius range considered is $\simeq 3 \pm 1\,\mathrm{km\,s^{-1}}$ for the three best-fit rotation curves shown above, our analysis implies that $V_{\mathrm{rot}} \sin i \,/\sigma_{1\mathrm{D}} \simeq 0.6 \pm 0.3$, which is somewhat larger than what is typically observed in globular clusters (e.g. Meylan & Heggie 1997). We have to keep in mind that $V_{\mathrm{rot}} \sin i$ is itself a projected quantity, and so is $\sigma_{1\mathrm{D}}$. We would like to know how these quantities

relate to the 3D quantities $\langle v_\phi \rangle$ and $v_{\rm rms}$. Here $\langle v_\phi \rangle$ is the mean tangential velocity component in the ϕ direction, used as the rotational component of the velocity vector in spherical coordinates for a cluster rotating about the z axis, and $v_{\rm rms}$ is the root-mean square of the velocities.

We can estimate that $V_{\rm rot}/\sigma_{\rm 1D}$ is typically about 10% larger than $\langle v_\phi \rangle / v_{\rm rms}$. This can be understood as follows. For a circular orbit with unit velocity and the line of sight along the orbital plane ($\sin i = 1$) the mean RV component is $2/\pi$. For an isotropic velocity dispersion the observed component is $\sigma_{\rm 1D} = v_{\rm rms}/\sqrt{3}$. This means that $[V_{\rm rot}/\sigma_{\rm 1D}]/[\langle v_\phi \rangle / v_{\rm rms}] \simeq 2\sqrt{3}/\pi \simeq 1.1$. If $\sin i = 1$ then we would have $\langle v_\phi \rangle / v_{\rm rms} \simeq 0.9\ V_{\rm rot}/\sigma_{\rm 1D}$ and a lower limit on $\langle v_\phi \rangle / v_{\rm rms}$ of 0.5 ± 0.2. A ratio of $\langle v_\phi \rangle / v_{\rm rms} = 0.5$ implies a ratio of kinetic energy in rotation over kinetic energy in random motions of 0.25, which in turn implies that at least 20% of the total kinetic energy is in rotation. If instead we assume that $\sin i = 2/\pi$ (the average of $\sin i$ assuming a random distribution of inclination angles), we have $\langle v_\phi \rangle / v_{\rm rms} = 0.9$ and 45% of the total kinetic energy in rotation. The approximate criterion for stability against non-axisymmetric perturbations provided by Ostriker & Peebles (1973) states that the ratio of the rotational kinetic energy over the potential energy should not exceed $|T_{\rm rot}/W| < 0.14$. If we assume virial equilibrium, then $T = -0.5W$, so for $T_{\rm rot} = 0.20\ T$ and $T_{\rm rot} = 0.45\ T$ this implies $|T_{\rm rot}/W| = 0.1$ and 0.225, respectively. Although not a rigorous test, this suggests that a low inclination is perhaps more reasonable.

If the cluster was flattened by rotation (although recall our previous words of caution about ellipticity and rotation), we would expect to see peaks in the azimuthal density profile, with density minima coinciding with the rotation axis (i.e. $\rm PA_0 \sim 45°$ and 225°) and density maxima 90° away from the rotation axis (i.e. $\rm PA_0 \sim 135$ and 315°). However, only one minimum is seen at a position angle of $\sim 100 - 120°$ in the K_s- and H-band azimuthal density profiles of R136 by Campbell et al. (2010).

Given the very young age of R136, the cause of the rotation needs to be looked for in the details of the formation process of the cluster. This is a short and complicated phase in which various physical processes, with their respective timescales, operate simultaneously. A logical starting point is to see whether giant molecular clouds (GMCs), the birth sites of YMCs, rotate. Rosolowsky et al. (2003) found that GMCs in M33 have non-zero angular momentum. From simple arguments based on differential rotation in a galactic potential and self gravity we expect that the rotation of GMCs should be prograde with the orbit in the galaxy. However, Rosolowsky et al. (2003) found that 40% of the GMCs have retrograde motions, which supports a scenario

in which GMCs form through both agglomeration and self gravity and the angular momentum is the result of the clumpiness of the gas (Dobbs et al. 2011). As we pointed out previously, a merger is another way to give rise to rotation. Interestingly, the dual structure found by Sabbi et al. (2012) in the density of low mass stars in R136 possibly hints at a relatively recent merger event of the main core of R136 and a second clump or cluster. Note however that cluster mergers with a small mass ratio[3] and high angular momentum do not happen fast enough compared to the age of R136 (Gieles et al., in preparation), so this cannot be the cause of the observed rotation, although it is still suggestive of an ongoing merger.

To establish whether the rotation in old GCs is a remnant of their formation, we need to know if the angular momentum can survive for a Hubble time of dynamical evolution. During the evolution, angular momentum is diffused outward (Fall & Frenk 1985; Einsel & Spurzem 1999) and ultimately lost through the escape of stars with high angular momentum (Agekian 1958; Shapiro & Marchant 1976). This process operates on a relaxation time and the angular momentum reduces after a fixed number of elapsed relaxation times. The relaxation time of expanding clusters grows roughly linearly in time, which makes the number of elapsed relaxation times grow slowly, namely as a logarithm of the age. Because the majority of GCs are in this expansion phase (Gieles et al. 2011), we may expect rotational signatures to still be present after a Hubble time because they have not evolved enough. For clusters that have entered the 'mass-loss' phase, we do not expect the rotation to survive.

5.5 Summary

We presented evidence that the young massive cluster R136 is rotating with a rotational velocity amplitude of about 3 $\mathrm{km\,s^{-1}}$, which implies that at least $\sim 20\%$ of its total kinetic energy is in rotation. Obviously, RV measurements of more stars in this cluster would be desirable to establish whether the rotation signal is genuine with a higher confidence than the current 95%, and if so to better populate the rotation curve. Plans to this effect will be presented in Chapter 7, along with possible constraints that this might allow us to place on scenarios for the formation of R136. Given the young age of R136, our results suggest that star clusters may form with a significant amount of angular momentum. We finally argued that the rotation of globular clusters could originate from their formation, but this is clearly a topic where more detailed numerical investigations are welcome.

[3]The second clump found by Sabbi et al. appears much less massive than R136.

Chapter 6

Discovery of a Be/X-ray pulsar binary and associated supernova remnant in the Wing of the SMC

6.1 Introduction

The formation of massive stars and clusters and its dependance on the conditions of the host environment are topics of perennial interest and ongoing debate. The star-forming region NGC 602 offers a unique opportunity to study massive star formation and associated feedback at the low metallicity characteristic of the SMC. This motivated the FLAMES spectroscopic survey of the massive star population in and around NGC 602 from which the results presented in this chapter (and initially published in Hénault-Brunet et al. 2012c) partly originate.

The survey was conducted as part of a multi-wavelength study concentrating on the supergiant shell SGS-SMC 1 and the star-forming region NGC 602. Along with the optical spectroscopy, observations of the far eastern region of the SMC Wing have been conducted with Chandra and XMM-Newton (PI: L.M. Oskinova). The data have already been used to reveal a rare early-type (O3) star of ~ 50 $M_{\odot}$ in the SMC (Evans et al. 2012) as well as to study the X-ray emission and feedback from the young stellar population in NGC 602 (Oskinova et al. 2013).

In this chapter, we concentrate on one bright X-ray source that was detected with these observations. The source, located near NGC 602 in projection (see Figure

6.1) and coinciding with the emission-line star 2dFS 3831 (RA $=1^{\rm h}27^{\rm m}46.03^{\rm s}$, Dec. $= -73°32'56.42''$, J2000.0), is revealed as a Be/X-ray binary thanks to the synergy between the FLAMES optical spectroscopy and the X-ray data. Based on the results of section 6.3.2, we will refer to this X-ray source as SXP 1062 following the nomenclature of Coe et al. (2005) for SMC X-ray pulsars. The discovery of such an object near NGC 602 provides important clues to the star formation history in this region of the SMC. As we will also see, its properties make it a rare and ideal object to better understand the spin evolution and accretion physics of neutron stars.

This chapter is organised as follows. We first present background information about Be/X-ray binaries and the NGC 602 region in section 6.2. We describe the X-ray observations of SXP 1062 and their analysis in section 6.3. In section 6.4, we characterise the spectrum of 2dFS 3831, the optical companion to the X-ray pulsar. We finally discuss the properties and environment of this newly discovered Be/X-ray binary as well as the implications of our findings in section 6.5.

6.2 Background

6.2.1 Be/X-ray binaries

Stars with an initial mass in excess of ~ 8 $M_\odot$ end their life in a core-collapse supernova explosion giving birth to a degenerate compact object – either a neutron star or a black hole. While the majority of massive stars are born in binary systems, only a small fraction ($\sim$10%) of binaries are thought to survive the supernova explosion, leaving a normal star and a compact object orbiting each other (e.g. Iben & Tutukov 1996; Popov & Prokhorov 2006). At some point in the evolution of such a binary system, the compact object will accrete matter from its companion and the system will enter the high-mass X-ray binary (HMXB) stage. The detection of coherent pulsations from the accreting X-ray source then provides strong evidence that the compact object is a rotating neutron star. The pulses of high-energy radiation are due to a misalignment of the rotation axis and the magnetic axis of the neutron star. Gas that is accreted from the stellar companion is accelerated as it moves into the gravitational potential well of the neutron star and channeled by the magnetic field of the neutron star onto its magnetic poles. The accreted matter then rapidly decelerates when it reaches the surface and potential energy is converted to heat. This energises the plasma and produces localised X-ray hot spots which move into and out of view as the neutron star spins, giving rise to regular X-ray pulses (Davidson & Ostriker 1973). The period of these pulsations is the

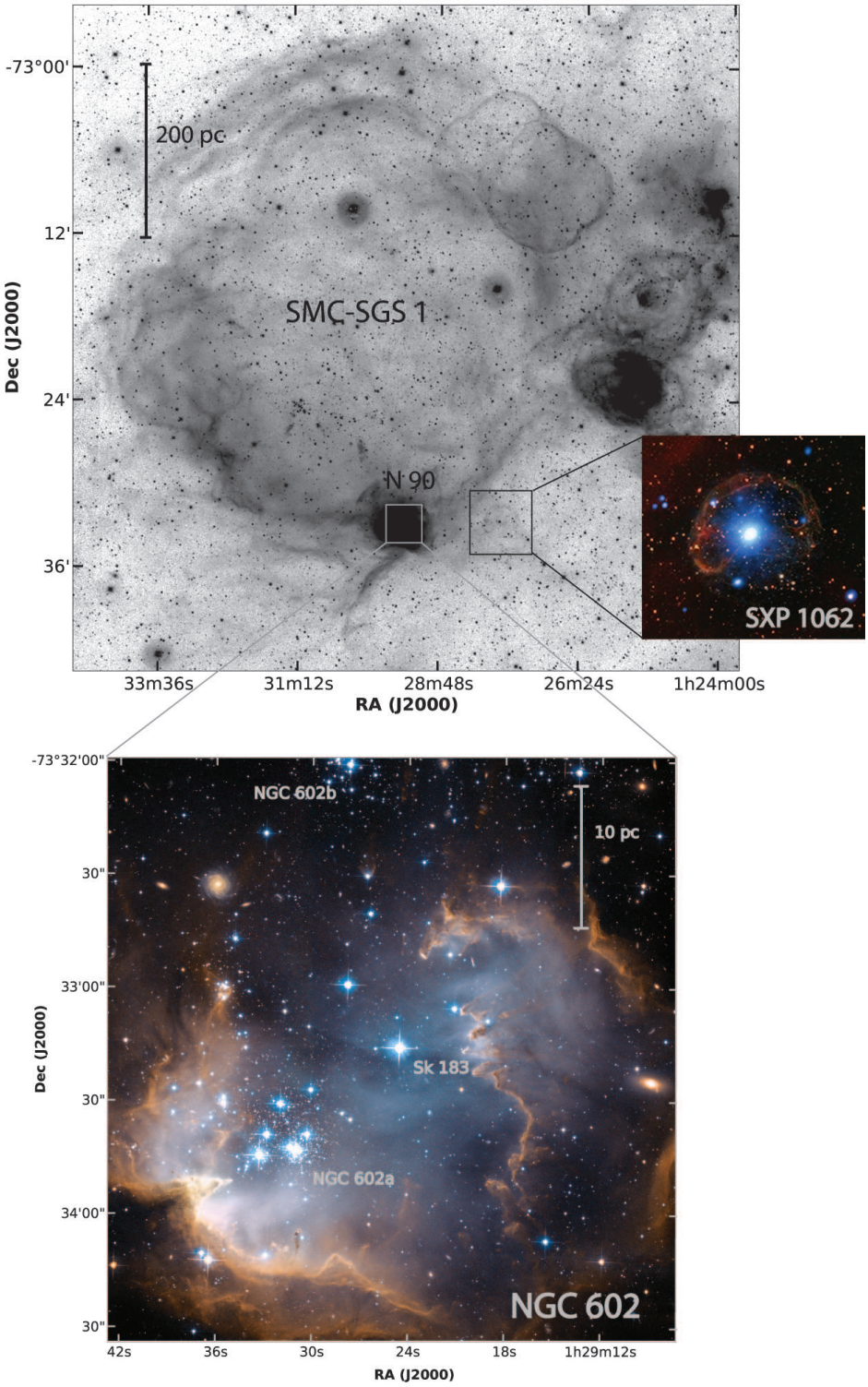

Figure 6.1 *Top:* Hα image of the supergiant shell SGS-SMC 1 from the Magellanic Cloud Emission-line Survey (MCELS; Smith & MCELS Team 1999). *Right:* Composite X-ray (blue) and optical (red, green) image of the supernova remnant around SXP 1062 (data from Chandra, XMM, CTIO-MOSAIC, and MCELS). *Bottom:* HST-ACS Wide Field Channel (WFC) F555W, F814W, F658N color composite image of NGC 602 (Carlson et al. 2007).

rotation period of the crust of the neutron star, and its value changes with time as accreted matter transfers angular momentum to or from the neutron star. The details of the spin evolution of the neutron star in a HMXB depend on the initial strength of its magnetic field and on the mass accretion rate history (Urpin et al. 1998).

HMXBs are subdivided into two categories based on the luminosity class of the optical companion. If the companion is a supergiant (luminosity class I–II) they are simply called supergiant X-ray binaries (SGXBs), while Be/X-ray binaries (BeXRBs) contain a dwarf, subgiant or giant Be (or Oe) star (spectral type O9–B5 and luminosity class III–V). In these BeXRB systems, which form the majority of HMXBs (e.g. Reig 2011), the Be (Oe) stars are rapidly rotating B-type (O-type) stars which at some point in their lives show spectral lines in emission, hence the qualifier "e" in their spectral type (e.g. Porter & Rivinius 2003). The most obvious lines are the hydrogen Balmer and Paschen series lines, but Be stars can show He or Fe lines in emission as well (e.g. Hanuschik 1996). They also display an excess of infrared radiation compared to what is expected from an absorption-line B-type star of the same spectral type. Both the emission lines and the infrared excess are thought to originate from a decretion disc formed as the rapidly rotating Be star ejects material into its equatorial plane (Okazaki 2001). This disc, along with the wind of the Be star, feeds the X-ray pulsar (see the recent review by Reig 2011). The formation of these systems can be understood by assuming that the progenitor of the neutron star transferred mass an angular momentum to its companion before it exploded as a supernova (Rappaport & van den Heuvel 1982).

6.2.2 BeXRBs in the SMC

Because of their relatively low galactic foreground extinction, known distance, and proximity, the Magellanic Clouds are ideal targets to study populations of X-ray binaries. The SMC is host to a large population of $\sim$ 60 HMXBs, comparable to the number known in the Galaxy (e.g. Haberl & Pietsch 2004; Coe et al. 2005; Laycock et al. 2010; Reig 2011; Sturm et al. 2013). However, unlike the Galactic population where about half of the HMXBs are BeXRBs, all of these systems but one are BeXRB systems, SMC-X1 being the only known SGXB in the SMC (Webster et al. 1972).

It was recently suggested that the BeXRB population of the SMC can be used as a tracer of relatively recent star formation and therefore provide insight into the history of the galaxy. Antoniou et al. (2010) found that BeXRBs are preferentially located in regions with star formation rate (SFR) bursts around 25 to 60 Myr ago, and additionally that the number of BeXRBs in a region correlates with the SFR in that region $\sim$ 40 Myr

ago. Most SMC BeXRBs are indeed found in the Bar where increased star formation ~ 40 Myr ago must have created them in large number. This is consistent with the finding that Be stars develop their decretion disks at ages of $\sim 25 - 80$ Myr, with a maximum occurrence at ~ 40 Myr (McSwain & Gies 2005).

Based on the above, we do not expect regions with a low SFR at ~ 40 Myr to host a significant number of BeXRBs. This appears to be true in the Wing of the SMC, the region linking the eastern side of the SMC to the Bridge, which itself connects the SMC and LMC. Despite its lower content of gas, dust, and stars, it shows strong but more recent star formation with a burst ~ 10 Myr ago (Harris & Zaritsky 2004), and it is indeed apparently deficient in BeXRBs (Antoniou et al. 2010). While the lower number of BeXRBs in this region is consistent with expectations, it must be noted that the coverage of the SMC Wing by X-ray observations has been sparser than that of the Bar. Three BeXRB pulsars with a spin period ($P_{\rm spin}$) less than 40 s are known in the Wing area (Chakrabarty et al. 1998; Macomb et al. 1999; Corbet et al. 2003) compared to only one (SXP 1062; presented in this chapter) with $P_{\rm spin} > 40$ s. This is in contrast to the whole SMC population, for which Knigge et al. (2011) found a bimodal spin distribution with more systems having $P_{\rm spin} > 40$ s, likely caused by a bimodal distribution of orbital periods associated with the two distinct types of neutron-star-forming supernovae (iron core collapse and electron capture supernovae). Identifying previously unknown systems in the Wing of the SMC (e.g. McGowan et al. 2007; Sturm et al. 2013) is important to enable the best statistical comparison of the Wing and Bar populations and eventually obtain a full picture of the history of the SMC.

6.2.3 The NGC 602 region

A particularly interesting region of the Wing is SGS SMC-1, the only known supergiant shell in the SMC (see Figure 6.1). This large structure of ~ 600 pc in diameter was discovered by Meaburn (1980) using deep Hα+[N II] images. The H II region N 90 (Henize 1956) is located at the southern rim of SGS-SMC 1. It comprises two young star clusters, NGC 602a and NGC 602b. Another cluster, NGC 602c, is found $\sim 11'$ to the northeast. The region encompassing the three clusters is commonly referred to as NGC 602 (Westerlund 1964). The Wing is mostly characterised by extremely low gas and dust densities, but NGC 602 displays the properties of a very active and complex star-forming environment.

The stellar population of NGC 602 has been studied in detail with optical images from the Hubble Space Telescope and deep infrared images from the Spitzer Space

Telescope. In addition to very old stars of $6 - 8$ Gyr, likely the SMC field population, NGC 602 contains young stars of $\sim 4 - 5$ Myr concentrated in the densest central region, i.e. NGC 602a (Westerlund 1964; Hutchings et al. 1991; Cignoni et al. 2009). A rich population of pre-main sequence stars with a maximum age of 5 Myr was also revealed and found preferentially towards the centre (Carlson et al. 2007; Cignoni et al. 2009). These results and the significant number of young stellar objects detected along the outskirts of the central cluster (Carlson et al. 2007; Gouliermis et al. 2007) suggest that star formation began ~ 5 Myr ago in NGC 602a and gradually propagated outward where it is still ongoing. As for what initially triggered the formation of these clusters, the low density environment in the Wing of the SMC hints at an additional mechanism acting along with gravitational collapse. Schmalzl et al. (2008) proposed that star formation was possibly induced by encounters with the LMC or the Milky Way. NGC 602 is located at the intersection of three H I shells, and Nigra et al. (2008) suggested that its formation is instead the result of the interaction of two expanding shells ~ 7 Myr ago. These authors also found that the photoionised gas in N 90 has a low radial velocity gradient and dispersion across the nebula. Carlson et al. (2011) therefore concluded that the ionising radiation, and not feedback from stellar winds and supernovae, is the primary trigger of the current star formation around NGC 602a. The quiescence of the gas in N 90 also suggests that a supernova explosion has yet to occur within NGC 602, but the discovery of a relatively nearby BeXRB presented in this chapter shows that supernovae are definitely part of the broader landscape.

6.3 X-ray observations

The X-ray data were obtained with the ACIS-I camera on the Chandra X-ray Observatory (CXO) and with the EPIC cameras onboard XMM-Newton. The Chandra observations consisted of 11 separate exposures acquired between 2010-03-31 and 2010-04-29 (effective exposure time of 290.7 ks), while 4 separate exposures were obtained with XMM-Newton between 2010-03-25 and 2010-04-12 (EPIC-pn effective exposure time of 162.5 ks). The data were reduced using the most up-to-date versions of the corresponding data reduction software. The X-ray source CXO J012745.97-733256.5 (=SXP 1062) coinciding with the optical emission-line star 2dFS 3831 is detected in each of these 15 exposures. In the Chandra observations, the positional uncertainty ($1\,\sigma$) of the X-ray source is $0.9''$. The average background-subtracted count rates are 0.0548 ± 0.0004 and 0.1227 ± 0.0019 counts s^{-1} respectively for the Chandra pointings in the $0.5 - 10.0$ keV band and the XMM-Newton EPIC-pn observations

in the $0.2 - 12.0$ keV band. The source was previously detected during an XMM-Newton slew on 2009-11-16, with the X-ray flux at the same level as during the 2010 observations. The object was also detected by the ASCA X-ray observatory in May 1999. Interestingly, the source remained undetected in the short 700 s off-axis exposure during the ROSAT All Sky Survey in 1990, although at its present luminosity it would have been bright enough at an expected ROSAT PSPC count rate of 0.01 counts s^{-1}. It was also not detected by a 10 ks exposure with the Einstein X-ray observatory in 1980. This suggests that SXP 1062 exhibits some level of long-term X-ray variability.

6.3.1 Spectral analysis

Figure 6.2 shows the background-subtracted Chandra and XMM-Newton spectra of SXP 1062 with all exposures combined for a given instrument. The Chandra spectra were extracted from a $12\farcs8$ circular region and the background was extracted from a

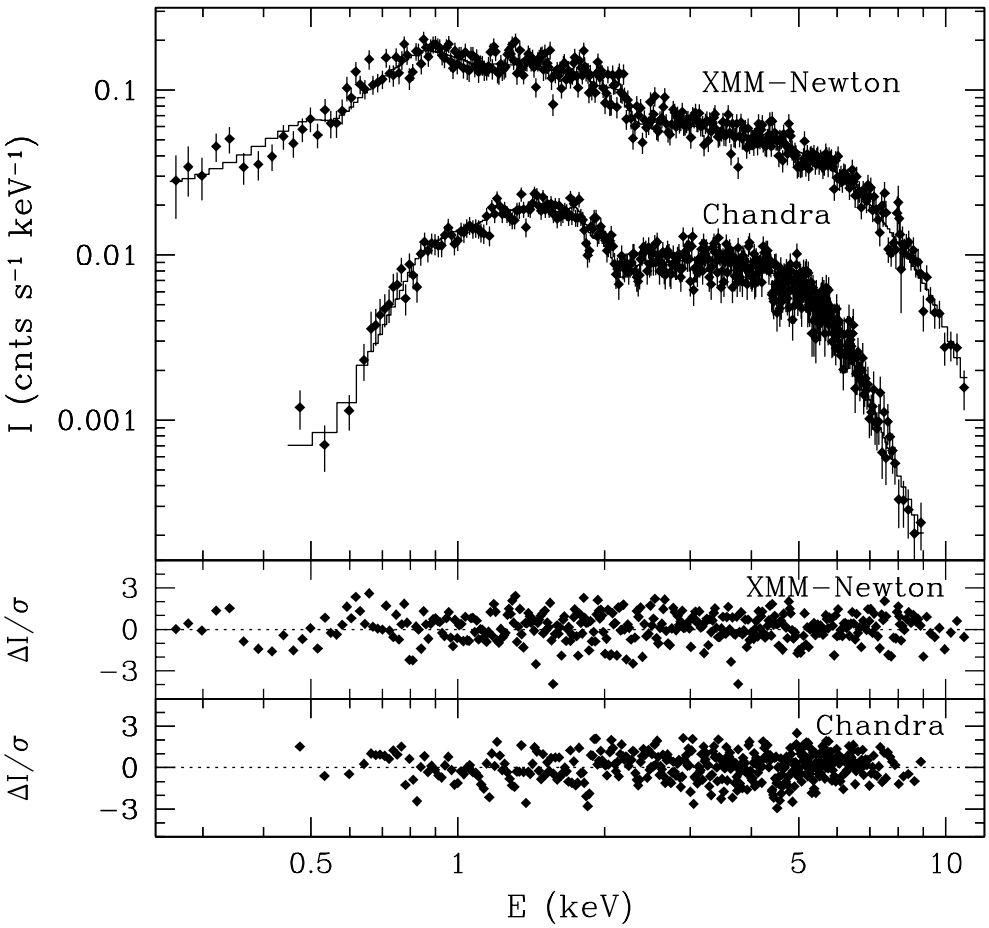

Figure 6.2 Chandra ACIS-I and XMM-Newton EPIC-pn spectra of SXP 1062. Overplotted is the best-fit model including power-law, thermal, and blackbody components. The lower panels show the residuals of the fit.

Table 6.1 Best-fit parameters of the spectral models. The code for the different components of each model is **P** for power-law, **B** for blackbody, and **T** for optically thin thermal emission with SMC abundances.

	P	**PB**	**PT**	**PBT**
$N_{\rm H}$ (10^{21} cm^{-2})	1.18±0.06	1.48±0.12	1.63±0.04	1.35±0.12
Γ	0.746±0.011	1.185±0.022	0.732±0.011	0.767±0.027
$A_{\rm powerlaw}$ ($\frac{\rm phot}{\rm keV\ cm^2\ s}$)	(6.60±0.11)×10^{-5}	(6.35±0.35)×10^{-5}	(6.48±0.12)×10^{-5}	(4.87±0.30)×10^{-5}
kT (keV)	...	2.13±0.05	...	1.54±0.16
$A_{\rm blackbody}$ ($\frac{10^{39}\ \rm erg}{\rm s\ kpc^2}$)	...	(1.11±0.20)×10^{-5}	...	(4.5±0.9)×10^{-6}
kT (keV)	...	...	0.589±0.032	0.648±0.029
$A_{\rm thermal}$ (10^9 cm^{-5})	...	...	2.60±0.32	2.80±0.30
χ^2/DoF	1.30	1.21	1.19	1.07

concentric annular region of radii 12.″8 and 19.″2 which was free of sources. Likewise, the XMM-Newton spectra were extracted from a 32″ circular region and the background from four adjacent circular regions free of sources with radius 45″.

As a first step, the background-subtracted Chandra and XMM-Newton spectra of SXP 1062 were simultaneously fitted using a simple absorbed power-law model (Figure 6.3, left panel). The best-fit parameters are listed in Table 6.1, where $N_{\rm H}$ is the hydrogen column density, Γ is the power-law index, $A_{\rm powerlaw}$ is a normalisation factor[1], and χ^2/DoF is the reduced χ^2. All uncertainties in Table 6.1 and in the text below correspond to 90% confidence intervals. The best-fit results for the absorbed power-law model imply an absorbed flux in the energy range $0.2 - 12.0$ keV of $f_{\rm X} = 1.8 \times 10^{-12}$ erg cm^{-2} s^{-1}. This corresponds to an intrinsic X-ray luminosity (i.e. corrected for absorption) in this same energy range of $L_{\rm X} = 6.9 \times 10^{35}$ erg s^{-1} assuming a distance modulus of 18.7 appropriate for the Wing (e.g. Cignoni et al. 2009), or $L_{\rm X} = 8.2 \times 10^{35}$ erg s^{-1} for the 'standard' SMC distance modulus of 18.9 (e.g. Harries et al. 2003). The photon index Γ of ~ 0.75 is typical of X-ray pulsar binaries and a signature of accretion onto a strongly magnetized neutron star. BeXRBs indeed have hard $1 - 10$ keV spectra with a power-law index Γ of $0 - 1$ (e.g. Yokogawa et al. 2003).

From the residuals of the fit, the simple power-law model suggests some emission excess below 1 keV and at high energies, so as a next step we added a blackbody component (Figure 6.3, central panel), which gives a better match to the data at high energies and statistically improves the fit. The temperature (kT) and normalisation factor[2]

[1] $F(E)dE = A_{\rm powerlaw}\ E^{-\Gamma}dE$, where $F(E)$ is the flux of the power-law component as a function of photon energy in units of counts/keV/cm^2/s.

[2] Defined such that $A_{\rm blackbody} = L_{39}/D_{10}^2$, where L_{39} is the luminosity of the blackbody source in units of 10^{39} erg s^{-1}, D_{10} is the distance to the source in units of 10 kpc, and $A_{\rm blackbody}$ is in units of 10^{39} erg/s/kpc^2.

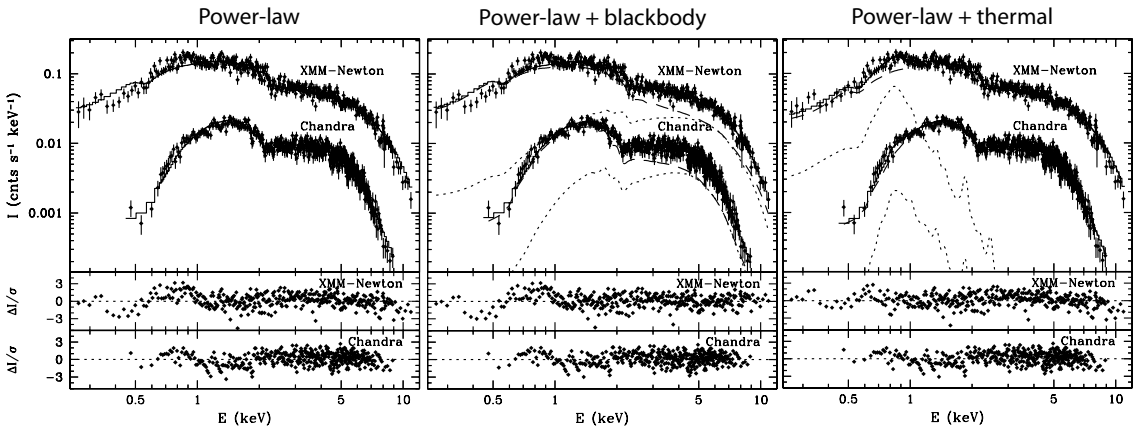

Figure 6.3 Same as Figure 6.2 but for the power-law, power-law+blackbody and power-law+thermal component models (from left to right **P**, **PB**, and **PT** from Table 6.1). For the models with two components, the power-law component is shown as a dashed line, the other component as a dotted line, and the sum of the two components as a solid line.

($A_{\rm blackbody}$) for the blackbody component are listed in Table 6.1 along with the other parameters of the best-fit model. The observed X-ray flux is similar to that of the previous model (simple power-law), but the X-ray luminosity decreases by $\sim 10\%$. To improve the situation in the low-energy range, we also tried a model for which an optically thin thermal plasma component with SMC abundances is included instead of a blackbody (Figure 6.3, right panel). The best-fit temperature (kT) and normalisation factor[3] ($A_{\rm thermal}$) for the thermal component are listed in Table 6.1. As in the case of adding a blackbody component, the addition of a thermal component to the power-law model improves the fit. The resulting intrinsic X-ray luminosity in this case is only marginally greater by $\sim 1\%$ compared to the simple power-law model.

Finally, the best fit is achieved by adding simultaneously a thermal plasma and a blackbody component to the power-law (see Table 6.1 and Figure 6.2). The flux for this model (PBT in Table 6.1) is $f_{\rm X} = 1.66^{+0.19}_{-0.25} \times 10^{-12}$ erg cm^{-2} s^{-1}, corresponding to an intrinsic luminosity $L_{\rm X} = 6.3^{+0.7}_{-0.8} \times 10^{35}$ erg s^{-1} for a distance modulus of 18.7.

The column densities are well constrained by spectral fitting, albeit the values slightly differ depending on the model. Using the best-fit values, we note that the H column densities in Table 6.1 imply $A_V = 0.66 - 0.91$ mag for the $N_{\rm H}/A_V$ ratio of 1.79×10^{21} cm^{-2} mag^{-1} (Predehl & Schmitt 1995), i.e. $E_{B-V} = 0.21 - 0.29$ assuming $R_V = 3.1$. This range is in good agreement with the $E_{B-V} = 0.19$ value computed by

[3]Defined such that $A_{\rm thermal} = \frac{10^{-14}}{4\pi D_A^2 (1+z)^2} \int n_e n_H dV$, where D_A is the angular diameter distance to the source (in cm), z is the redshift, n_e and n_H are the electron and H densities (in cm^{-3}), and $A_{\rm thermal}$ is in units of 10^9 cm^{-5}.

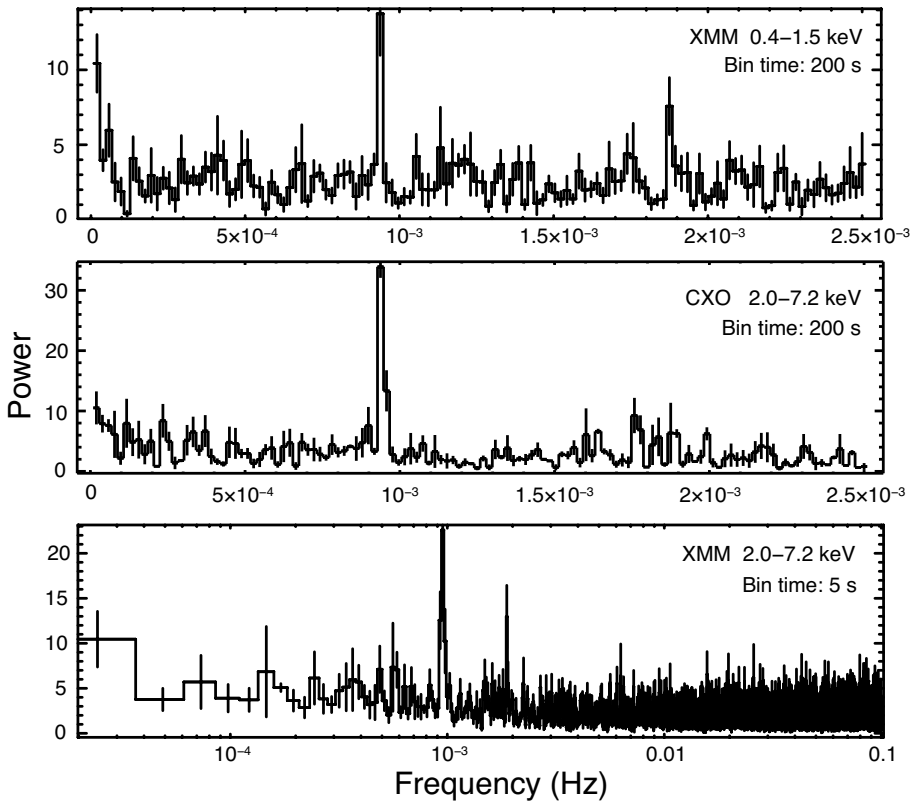

Figure 6.4 XMM-Newton and Chandra power density spectra in the soft and hard energy bands for different bin times.

comparing the value $(B-V) = -0.04$ of 2dFS 3831 (Massey 2002) with the intrinsic value $(B-V)_0 = -0.23$ of a B0-0.5III star (Wegner 1994) considering the uncertainties on the photometry and spectral type (see section 6.4 for the optical spectroscopy of 2dFS 3831, the optical companion of the X-ray pulsar).

6.3.2 Timing analysis

The arrival times of X-ray photons were corrected for the Solar System barycentre. A search for pulsations in the X-ray light curves of the soft and hard energy bands ($0.4-1.5$ keV, $2.0-7.2$ keV) and a total energy band ($0.4-7.2$ keV) was performed using fast Fourier transform and light-curve folding techniques as implemented in the Timing analysis software *xronos*.

Figure 6.4 shows the resulting Chandra and XMM-Newton power density spectra in the soft and hard energy bands with a clear peak at a frequency of 9.4×10^{-4} Hz ($P = 1\,062$ s). This coherent X-ray pulse period establishes the source as a binary X-ray pulsar. The pulse profiles folded with this period are shown in Figure 6.5.

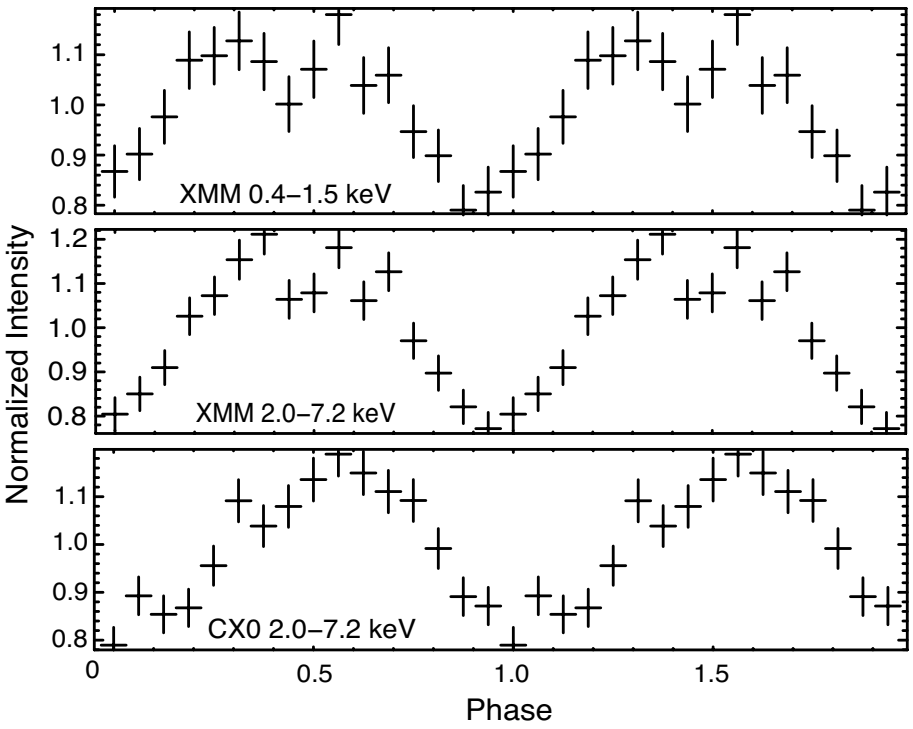

Figure 6.5 Pulse profiles folded with a period of 1 062 s in different energy bands.

The light-curves used to compute the XMM-Newton power spectrum in the hard energy band, the XMM-Newton power spectrum in the soft energy band, and the Chandra power spectrum in the hard energy band were binned by respectively 5 s, 200 s, and 200 s. The 5 s bin time for one of these was chosen to make sure that a shorter pulse was not missed. No pulse was found in the soft band Chandra observations, possibly because the count rate in this case is too low. Because of the softer response of the EPIC-pn camera, the pulse in the soft band is the most obvious in the light-curves obtained with this instrument.

Note that in addition to the pulse period discussed above, X-ray variability was also detected at a level of $\sim$ 20% peak-to-peak on a timescale of several days in both XMM-Newton and Chandra light-curves. Given that this variability does not appear regular and that the sampling on this timescale is very sparse, we do not analyse these variations further.

6.4 Optical spectroscopy

From its X-ray position with subarcsecond precision from Chandra images, the optical counterpart to SXP 1062 is unambiguously identified as 2dFS 3831 (Evans et al. 2004).

We observed this star with the VLT FLAMES instrument (Pasquini et al. 2002) on 2010 October 25 as part of our spectroscopic survey of massive stars in NGC 602. The reduction of the data from this survey was performed following the procedure described in Chapter 2 for the VLT-FLAMES Tarantula Survey (see also Evans et al. 2011), i.e. following the standard data processing procedure (bias subtraction, fibre location, summed extractions, division by flat-field, wavelength calibration) using the ESO Common Pipeline Library FLAMES reduction routines (v.2.8.7). Heliocentric correction and subtraction of a median sky spectrum was also performed. Spectra of 2dFS 3831 were obtained in the MEDUSA-fibre mode of FLAMES using the LR02 setting of the GIRAFFE spectrograph (3960−4564 Å, $R = 7\,000$, e.g. Evans et al. 2011). Five pairs of 1 800 s exposures were obtained. As the signal-to-noise ratio of spectra from individual pairs of exposures was too low, the spectra from all the exposures were normalized and merged.

Archival 2dF spectra of this star were also retrieved. These two spectra cover the regions from $\sim 3\,800$ to $4\,900$ Å and $\sim 6\,000$ to $7\,000$ Å, with resolving powers of 1 500 and 2 500 respectively (Evans et al. 2004). Figure 6.6 shows the VLT-FLAMES and 2dF spectra of 2dFS 3831. The VLT-FLAMES spectrum has been smoothed and rebinned to an equivalent resolving power of $R = 4\,000$.

A weak He II λ4542 absorption line is visible in the VLT-FLAMES spectrum and there is a hint of a weak He II λ4686 line in the 2dF spectrum, but He II λ4200 is absent, suggesting a spectral type around B0-0.5 following the classification adopted by Evans et al. (2004).

Several characteristics attributable to a circumstellar disc indicate that 2dFS 3831 is a classical Be star. Fe II λ4179 and Fe II λ4233 emission lines typical of some early Be stars (e.g. Slettebak 1982) are visible in the VLT-FLAMES spectrum. The Hα emission seen in the 2dF spectrum is relatively strong with an equivalent width (EW) of -23 Å. There is significant Hβ emission, plus emission in the core of the other Balmer lines (double-peaked in the VLT-FLAMES spectrum) and apparent infilling of the He I absorption lines. By comparison with the spectrum prior to sky subtraction, we can confirm that the double-peaked emission in the Balmer lines is not due to oversubtraction of nebular features present in the median sky spectrum. Also, given the relative weakness of the nebular emission lines in the mean sky spectrum, the emission in the core of the Balmer lines is most likely dominated by circumstellar material and not by nebular contamination. Two Micron All Sky Survey (2MASS; Skrutskie et al. 2006) JHK_s photometry also indicates a clear infrared excess when compared with expected colors for a B0-0.5 spectral type (Wegner 1994). Given this spectral type, recall that we

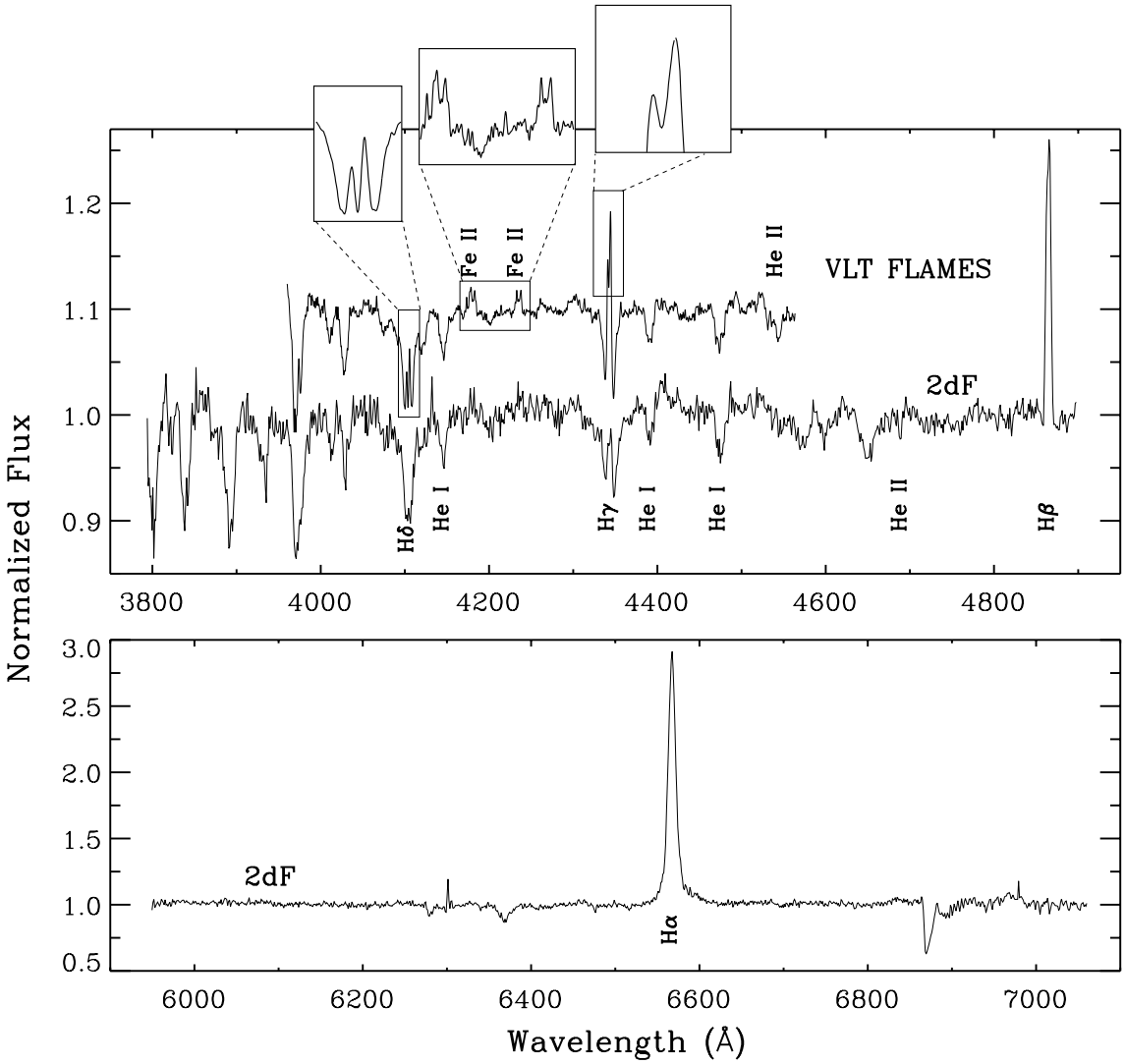

Figure 6.6 Optical VLT-FLAMES and 2dF spectra of 2dFS 3831 with key spectral features identified. The VLT-FLAMES spectrum is offset vertically.

estimated in section 6.3.1 that $E_{B-V} = 0.19$, which for a standard extinction curve corresponds to $E_{J-K_s} \approx 0.1$. A normal B0-0.5 star (without circumstellar disc) has an intrinsic $(J - K_s)_0$ of about -0.19, so we would expect the observed $(J - K_s)$ to be -0.09 if there was no infrared excess, but $(J - K_s) = 0.33$ is actually observed for 2dFS 3831.

The observed magnitude ($V = 14.36$, $B = 14.32$; Massey 2002) combined with a distance modulus of 18.7 lead to an absolute magnitude consistent with a B0-0.5 giant (Walborn 1972; Vacca et al. 1996). We thus determine the spectral type of 2dFS 3831 as B0-0.5(III)e+, where '+' signifies the presence of Fe II. This corresponds to a typical effective temperature $T_{\rm eff} \sim 26\,000$ K and an evolutionary mass $M \sim 15\,M_\odot$ at SMC metallicity (cf. Trundle et al. 2007). A more quantitative atmospheric analysis would

require spectra of higher quality and is beyond the scope of this work.

Since the density of early-type stars is relatively low in the Wing of the SMC, a correlation with the X-ray source by chance is unlikely, and we are very confident that 2dFS 3831 is the companion of the X-ray pulsar. We can get a very rough estimate for the probability of a chance alignment by following the arguments below. Assuming that the total mass of the SMC is $\sim 7 \times 10^9$ $M_\odot$ (including dark matter, see Bekki & Stanimirović 2009) and that $\sim 85\%$ of the mass is in dark matter, we estimate that it contains about 10^9 stars. About one star in 800 is a B-type star (Binney & Merrifield 1998), and $\sim 35\%$ of B stars are Be stars in the SMC (e.g. Martayan et al. 2010), which gives about 4×10^5 Be stars in the SMC. Given the area of ~ 10 square degrees covered by the SMC on the sky, this leads to about 6 Be stars per square arcminute and a 0.8% chance probability of finding a serendipitous Be star in our 1σ Chandra error circle. Note that this does not even take into account the lower density of the Wing, the fact that not all Be stars show Hα at a given time and that some percentage of them might not be observable because of absorption effects, so the actual probability is even lower. Also, Be stars in BeXRBs cover a narrower range in spectral type compared to isolated Be stars (O9–B2; Negueruela 1998), and the spectral type of 2dFS 3831 happens to be in that range.

We estimated the radial velocity of 2dFS 3831 from the VLT-FLAMES spectrum by following a method similar to that of Chapter 3 and fitting Gaussian profiles, this time only to the wings of Hγ, Hδ, Hϵ, He I λ4143, and He I λ4388. The signal-to-noise ratio of individual exposures/epochs was not sufficient to check for radial velocity variations so we only performed these measurements on the mean spectrum. The average radial velocity of all the lines used is 167 km s^{-1} with a standard deviation of 13 km s^{-1}. This is consistent with the mean velocity of massive stars in the SMC (Evans & Howarth 2008), and also with the gas velocities measured by Nigra et al. (2008) across the N 90 H II region ionized by NGC 602A. Thus, we do not see any evidence that the HMXB acquired a high space velocity following the supernova explosion.

6.5 Discussion

6.5.1 The properties of SXP 1062

Out of a sample of a little over 60 known X-ray pulsars in the SMC, a total of nine have been confirmed to have spin periods in excess of 500 s (Laycock et al. 2010). SXP 1062

has the second longest period known and is only the third with a spin period larger than 1000 s. These slowly rotating pulsars are particularly interesting because they represent a challenge for the theory of spin evolution of a neutron star in a close binary system (see section 6.5.3).

According to the Corbet diagram for SMC BeXRBs, relating the spin of the neutron star and the orbital period of the binary (Corbet et al. 2009), we expect SXP 1062 to have an orbital period of $\sim$ 300 days. Such a long orbital period is also expected from the $P_{\rm orb}$-EW(Hα) diagram (Reig et al. 1997), from which our measured EW(Hα) suggests an orbital period of $\sim$ 100 days. Note however that the maximum EW(Hα) of the system, which probes the maximum size of the disc (and indirectly the orbital period), could be higher than our instantaneous measurement, so this period estimate should be taken as a lower limit.

SXP 1062 shares many characteristics with the class of persistent BeXRBs (e.g. Reig 2011): a low X-ray luminosity $\sim 10^{34} - 10^{35}$ erg s^{-1}, a slowly rotating pulsar with $P_{\rm spin} > 200$ s, a relatively flat light-curve with possible sporadic and unpredicted increases in intensity by less than an order of magnitude, and a lack of iron lines at $\sim$ 6.4 keV indicative of small amounts of material in the vicinity of the neutron star. These properties suggest that the neutron star in these systems orbits the Be star in a wide and nearly circular orbit, continuously accreting material from the low-density outer regions of the circumstellar envelope.

A thermal excess of blackbody type, with a high temperature ($kT > 1$ keV) and a small emission area ($R < 0.5$ km, consistent with a hot spot at the polar cap of the neutron star) has recently been suggested as another common feature of persistent BeXRBs (La Palombara et al. 2009, 2013). The X-ray spectrum of the pulsar in these systems cannot be described with a single-component model. The fits with only a power-law or only a blackbody are affected by large residuals, other models are rejected by the data, but a good fit is obtained with a power-law+blackbody model. Such a blackbody component is also identified in the X-ray spectrum of SXP 1062 (section 6.3.1). Given that we know the temperature of the blackbody and its flux (from our best-fit models) as well as the distance to the source, we can easily calculate its luminosity and use the Stefan-Boltzmann law to estimate a radius of $\sim$ 0.4 km for the blackbody source, in keeping with what has been found in other persistent BeXRBs.

6.5.2 The environment of SXP 1062

We detected a shell nebula around SXP 1062 in the Magellanic Cloud Emission-line Survey (MCELS; Smith & MCELS Team 1999) Hα image and in a higher resolution CTIO 4m MOSAIC (Muller et al. 1998) Hα image (see Figure 6.7). This shell is also detected in the MCELS [O III] image, but hardly in [S II]. We again adopt a distance modulus of 18.7 in the calculations below, which we perform to constrain the nature of the shell.

The shell does not appear uniform, with radii varying from $\sim 75''$ at the sharp rim to the northeast to $\sim 94''$ at the diffuse edge to the southwest. The peak surface brightness of the northeast rim is $\sim 6 \times 10^{-17}$ erg s^{-1} cm^{-2} arcsec^{-2}, corresponding to an emission measure[4] of ~ 30 cm^{-6} pc. The width of the rim suggests that the shell thickness (ΔR) is $5-10\%$ of the shell radius (R) and the longest emitting length at the shell rim is $2R[2\Delta R/R - (\Delta R/R)^2]^{1/2}$. Thus, taking into account uncertainties on the shell thickness and radius, we can estimate that the rms density in the shell is 1.3 ± 0.3 H-atom cm^{-3} and the gas mass in the shell is 250 ± 100 M$_\odot$. This large mass indicates that the shell gas must be dominated by interstellar material (as opposed to stellar ejecta).

The shell morphology resembles supernova remnants (SNRs) in the Magellanic Clouds (e.g. Mathewson et al. 1983). The X-ray images also suggest that diffuse X-ray emission possibly associated with a SNR may be present in the vicinity of SXP 1062 (Figure 6.1; also see Oskinova et al. 2013; Haberl et al. 2012). As the shell mass is much larger than the typical supernova ejecta mass, we assume that the shell is a SNR in the Sedov-Taylor (adiabatic) phase, such that the kinetic energy in the shell would be $\sim 30\%$ of the supernova explosion energy (Taylor 1950; Sedov 1959). Adopting a canonical explosion energy of 10^{51} ergs, the current shell kinetic energy is 3×10^{50} ergs, and implies a shell expansion velocity of 350 ± 100 km s^{-1} and an age of $0.4(R/V) = (2-4) \times 10^4$ yr. This age is much smaller than the cooling timescale of the low density gas inside the shell, justifying an adiabatic shock for the Sedov-Taylor phase. The inferred pre-shock interstellar gas density, 1/4 of the shell density, is 0.3 ± 0.1 H-atom cm^{-3}, consistent with the low density expected in the SMC Wing. The bright [O III] emission can easily be produced by a 350 km s^{-1} shock (cf. Hartigan et al. 1987) and the ionising flux of the B0–0.5III star is sufficient to photoionise the shell gas and its surrounding pre-shock

[4]The emission measure, EM, is defined as $\int_0^L n_e^2 dl$, where n_e is the electron density and L is the total path length in ionised gas. The EM is related to the H_α surface brightness, I_{H_α}, by EM(pc cm^{-6}) = 4.908×10^{17} I_{H_α}(erg s^{-1} cm^{-2} arcsec^{-2}), where the numerical constant given here is for $T = 10^4$ K (e.g. Rozas et al. 2000).

medium. Furthermore, the diffuse [O III] emission to the northeast exterior of the shell indicates the existence of a harsh radiation field. Therefore, the ionisation stage of the pre-shock medium may be too high to produce strong post-shock [S II] emission. We thus conclude that the shell nebula detected around SXP 1062 is most likely a SNR. This is supported by the recent findings of Haberl et al. (2012) who also argued for the supernova remnant nature of the nebula based on its radio and X-ray emission. From the radius of the SNR and the temperature of its extended diffuse X-ray emission, these authors estimated an age of $(1 - 2.5) \times 10^4$ yr for the SNR, which is slightly shorter than our estimate, albeit fully compatible. They also argued that the strong [O III] emission suggests an oxygen-rich SNR (Arbutina & Urosević 2005), indicating that it would have developed from a type Ib supernova event (the explosion of a massive O, B, or Wolf-Rayet star).

The extent of the shell, which has not reached the NGC 602 region, and its young kinematic age suggest that this supernova event did not trigger the formation of NGC 602. The fact that SXP 1062 is almost but not exactly centered in the shell

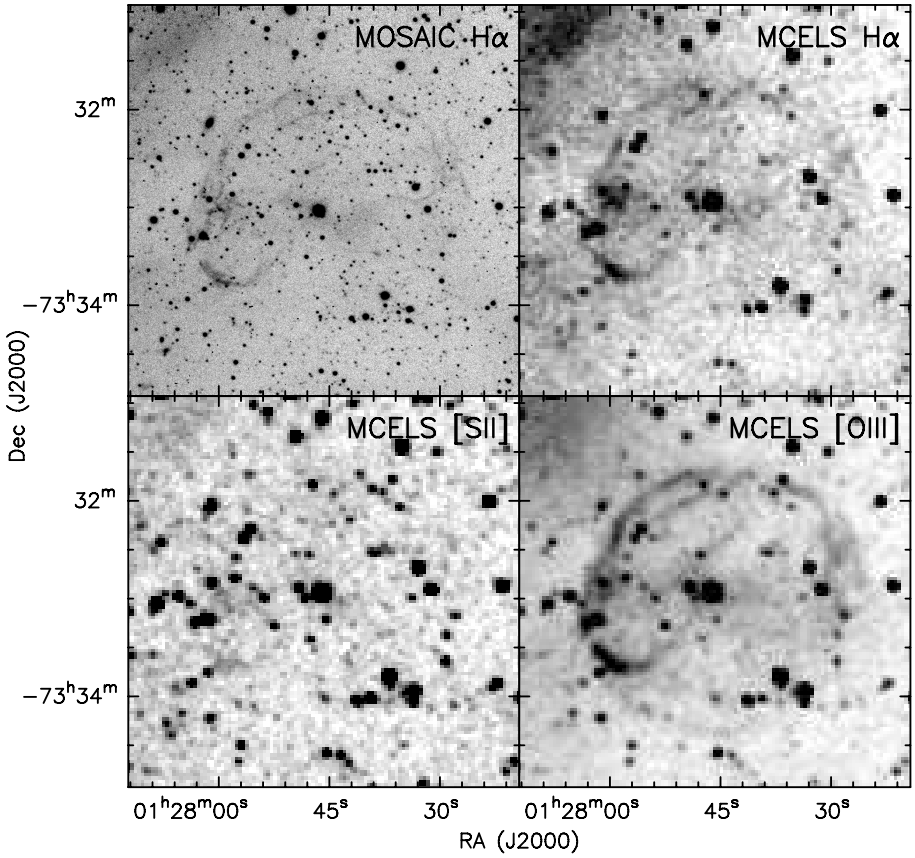

Figure 6.7 MOSAIC Hα image and MCELS Hα, [S II], and [O III] images of a region centered on the position of 2dFS 3831=SXP 1062 and showing the supernova remnant shell nebula detected around the target.

might indicate that the ambient density is higher on one side, or could also mean that if the star is moving with respect to the surroundings, its velocity cannot be very large. We estimate that the star is ~ 4 pc offset from the centre of the shell, which implies an upper limit to the velocity in the plane of the sky of $100 - 200$ km s^{-1} based on the dynamical age estimated above. Note that the radial velocity was shown to be consistent with the typical velocity of stars in the SMC (section 6.4).

6.5.3 A slowly rotating pulsar in a young supernova remnant

The association of SXP 1062 with a supernova remnant shell makes it an exceptional case of a young neutron star with a known age in a HMXB. Only two other X-ray binaries have been discovered within observable SNRs; SS 433 is a galactic HMXB with a B or A giant primary star located within the remnant W50, and a HMXB with an O5III(f) star primary was recently revealed in the LMC remnant DEM L241 (Seward et al. 2012). SXP 1062 is the first instance where the age of the neutron star in a BeXRB can be estimated. The short age estimated for the SNR also qualifies SXP 1062 as the youngest known X-ray pulsar in a binary system.

In addition to the known age, spin period, X-ray luminosity, and X-ray spectrum that we presented above for SXP 1062, Haberl et al. (2012) reported a very large average spin-down rate of 0.26 s per day over an observing period 18 days by further analysing the XMM-Newton observations of this object. With the unique combination of all these constraints, SXP 1062 is quickly emerging as a key system to probe the physics of accretion and the spin evolution of neutron stars in binary systems.

The long spin period of the pulsar is particularly interesting given that periods longer than $\sim$ 1000 s are difficult to accommodate in our current understanding of these systems. Spin periods in the rage $1 - 1000$ s can be explained in the standard theory for the spin evolution of a neutron star in a close binary system (see Reig 2011, and references therein). In this scenario, the spin evolution is divided into three main phases, each characterised by a different energy release mechanism and corresponding to a different evolutionary stage of the neutron star. These phases are termed (1) the pulsar (or ejector) phase, (2) the propeller phase, and (3) the accretor phase.

1. Following a supernova explosion, a rapidly rotating radio pulsar is formed. In this first evolutionary phase, the spin period is $\sim$10 ms for magnetic fields in the typical range $\sim 10^{12} - 10^{13}$ G. The neutron star radiates at the expense of its rotational energy.

2. At the propeller stage, infalling matter is stopped by the centrifugal barrier caused by the rapidly rotating magnetosphere. As ionised matter cannot penetrate into the magnetic field, stable accretion is impossible. Part of the infalling matter is accelerated outward, taking away some of the angular momentum of the neutron star. The spin-down continues until gravity and the centrifugal force balance. In the canonical scenario this occurs at the so-called equilibrium period (Davies & Pringle 1981):

$$P_{\rm eq} \approx 17\ \mu_{30}^{6/7}\ \dot{M}_{15}^{-3/7}\ \left(\frac{M_{\rm X}}{\rm M_\odot}\right)^{-5/7}\ {\rm s}, \tag{6.1}$$

where μ_{30} is the magnetic moment in units of 10^{30} G cm^3, $\dot{M}_{15}$ is the mass accretion rate in units of 10^{15} g s^{-1}, and $M_{\rm X}$ is the mass of the neutron star.

3. In the third phase, when the spin period becomes larger than $P_{\rm eq}$, the centrifugal barrier ceases to be effective, and plasma is able to reach the surface of the neutron star by moving along the magnetic field lines towards the magnetic poles. Since the material carries angular momentum, the neutron star will experience a strong spin-up. In principle, $P_{\rm eq}$ is therefore the maximum spin period for a given mass-accretion rate.

In this canonical model, long periods in excess of 1000 s could be achieved if $B > 10^{14}$ G or $\dot{M} < 10^{12}$ g s^{-1}, but such a strong magnetic field is unlikely and a low mass accretion rate like this would imply an X-ray luminosity two to three orders of magnitude lower than observed (Reig 2011).

To explain the existence of long-period pulsars ($P_{\rm spin} > 1000$ s), another phase in the spin-period evolution has been suggested. This phase, called the subsonic propeller phase, occurs before the accretion phase and can delay the onset of accretion until a much longer period is reached (e.g. Ikhsanov 2007). Davies & Pringle (1981) showed that the magnetosphere of the neutron star during the propeller phase is surrounded by a hot spherical envelope. The interaction between the magnetosphere and the envelope leads to a spin-down of the neutron star, and the energy loss by the star is convected up through the envelope and lost through its outer boundary. The neutron star remains in the propeller state as long as this energy input to the envelope dominates over the radiative losses from the plasma in the envelope. In the subsonic propeller phase scenario, steady accretion can happen for $P_{\rm spin} > P_{\rm eq}$ if the cooling of the envelope plasma dominates the energy input from the star. However, as long as the temperature of the envelope remains higher than the free-fall temperature, no accretion is possible

(Reig 2011). We must however note that the canonical picture presented above, which is obviously simplified, has started to be challenged by new and more complex models. For example, Shakura et al. (2012) presented a modification of the spherical accretion scenario in which the neutron star is assumed to accrete material from a hot turbulent envelope surrounding its magnetosphere. This model allows long spin periods as high as $\sim$ 1000 s and large period derivatives even for the standard magnetic fields $B \sim 10^{12} - 10^{13}$ G and mass accretion rates $\dot{M} \sim 10^{16}$ g s^{-1} expected in BeXRBs.

The young age of SXP 1062 and its large spin-down rate make it stand out even more among presently known X-ray pulsars with long spin periods. In that respect, it is important to note that the arguments above about $P_{\rm eq}$ implicitly rely on the assumption that the neutron star is old enough to have already entered the propeller stage. Unless the accretion rate is unusually large, a neutron star in a BeXRB with $B \gtrsim 10^{12}$ G starts its evolution in the pulsar (ejector) phase, for which the duration can be roughly estimated as (Popov & Turolla 2012)

$$\tau_{\rm ej} \gtrsim 10^{6} \left(\frac{B}{10^{12}\ {\rm G}} \right)^{-1} \left(\frac{\dot{M}}{10^{15}\ {\rm g\ s^{-1}}} \right)^{-1/2} \ {\rm yr}. \tag{6.2}$$

For typical values of B and $\dot{M}$, it would be impossible for the neutron star to enter the propeller phase (and then become an accretor) in a time of only a few 10^4 yr, the estimated age of the SNR associated to SXP 1062. The accretion rate in SXP 1062 is $\dot{M} = L_{\rm X}/\eta c^2 \sim 6 \times 10^{15}$ g s^{-1} for an efficiency $\eta = 0.1$ (c is the speed of light), which combined with the above suggests that the magnetic field is (or has been) quite strong.

Since the publication of our discovery (Hénault-Brunet et al. 2012c), four different explanations have been proposed for the nature of SXP 1062. Assuming the extreme case where the neutron star has constantly spun down at the measured rate of -2.6×10^{-12} Hz s^{-1} over its whole lifetime, Haberl et al. (2012) speculated that it was born with a spin period of at least 0.5 s, which is unusually slow if we compare to the spin periods of a few tens of milliseconds expected for newly born neutron stars. Note that the duration of the observations used by these authors is only 18 days, and the very large spin-down rate measured is actually unlikely to be sustained over the whole lifetime of SXP 1062. To reconcile the long spin period and young age, Popov & Turolla (2012) instead assumed that the neutron star is spinning at the equilibrium period and estimated the current magnetic field to be $B \lesssim 10^{13}$ G according to the model of Shakura et al. (2012). They showed that if SXP 1062 was born as a magnetar ($B > 10^{14}$ G, which then decayed to its present value), it could have spun down to

~ 1000 s within a few 10^4 years due to strong magnetic braking, thereby also producing the large spin-down observed. Ikhsanov (2012) proposed that the large spin-down rate and long spin period of such a young pulsar can only be explained within the magnetic accretion scenario in which the neutron star is assumed to accrete from a magnetized wind. In this scenario, a surface magnetic field of $B \sim 4 \times 10^{13}$ G is sufficient. As some B-type stars have strong magnetic fields (Oskinova et al. 2011), accretion from a magnetized stellar wind cannot be excluded. Finally, Fu & Li (2012) suggested that SXP 1062 may still be an accreting magnetar with a present-day magnetic field $B \gtrsim 10^{14}$ G.

In summary, no consensus has been reached yet regarding the nature of SXP 1062, but it is clear that it represents a special object which has already attracted a lot of attention. Further monitoring will be welcome in order to discriminate between the proposed models. In section 7.5, we will briefly outline future strategies that would help to better understand SXP 1062 and thereby the physics of accretion and spin behaviour of neutron stars.

Chapter 7

Conclusions and future prospects

In this short concluding chapter, the main results of this thesis are summarized and the outstanding questions or future projects that these results might trigger are discussed.

7.1 New constraints on the dynamics of R136

The VFTS is a fine example of what we can learn about the evolution of young star clusters by studying massive stars, and vice versa. Beside understanding the evolution of massive stars, one of the two main goals of the VFTS was to investigate the dynamical state and evolution of the important cluster that is R136. As the results presented in this thesis testify, this has certainly now been achieved.

In order to gain insight into the importance of gas expulsion in the early evolution of star clusters, we presented a detailed kinematic study of R136 using multi-epoch spectroscopic data from the VFTS. This represents, to the best of our knowledge, the first successful attempt at measuring the velocity dispersion of this cluster. By applying quantitative criteria to establish whether or not our observed stars displayed significant RV variability, we were able to define a sample of apparently single stars. These were used to place an upper limit of 6 $\mathrm{km\,s^{-1}}$ on the line-of-sight velocity dispersion of stars within a projected distance of 5 pc from the centre of R136. Thanks to our well-defined variability criteria, we were able to run Monte Carlo experiments on simulated datasets and implement the same variability analysis as used on the real data. This allowed us to account for the contribution of measurement errors and investigate the contribution of undetected (mostly long-period) binaries to the velocity dispersion. We concluded that the true velocity dispersion of R136 (between 1 and 5 pc from the centre) is

most likely between 4 and 5 $\mathrm{km\,s^{-1}}$ given a range of reasonable assumptions about the period distribution of massive binaries. We found that we would have measured a velocity dispersion of $\sim$ 25 $\mathrm{km\,s^{-1}}$ (a factor of $\sim$ 5 too high) if binaries had not been identified and rejected, confirming the advantage of the multi-epoch strategy and the risk of interpreting velocity dispersion measurements of unresolved extragalactic young massive clusters. We are certainly not the first to advance that ignoring the contribution of massive binaries to the stellar velocity dispersion of young clusters (in both integrated-light observations of distant systems and studies of resolved clusters) can lead to significantly overestimate this velocity dispersion. This idea has indeed been discussed previously in the literature (e.g. Bosch et al. 2009; Gieles et al. 2010b). Our study of R136 however provides a very clear and detailed illustration of the effect of massive binaries.

Although we have admittedly made many simplifying assumptions when addressing the dynamical state of R136, the velocity dispersion that we obtained is fully consistent with the velocity dispersion that we would expect if the cluster is in virial equilibrium. This adds a significant data point to a currently limited list of resolved young massive clusters in the Local Group (all of them in the Galaxy except R136) for which kinematic measurements have been performed (see Chapter 3). Among radial velocity studies, ours is the only one to truly estimate the velocity dispersion, not just an upper limit on this dispersion. In any case, all recent dynamical studies of resolved young massive clusters (either from proper motions or radial velocities) have shown that they have low velocity dispersions consistent with them being in virial equilibrium. This implies that they show no signs of violent gas removal and any resulting expansion, and suggests that once clusters emerge from their embedded state they are long-lived objects. These results support what has been found in an analysis of a smoothed particle hydrodynamics (SPH) simulation of cluster formation (Kruijssen et al. 2012), where most clusters (or sub-clusters) are found to be gas-poor and close to being virialized before gas expulsion, indicating that they will not be strongly affected by gas expulsion.

As another application (although originally not planned) of our multi-epoch RV measurements in R136, we investigated the internal rotation of the cluster. Using the radial velocities of 36 apparently single O-type stars (based on the same variability analysis as the velocity dispersion study) within a projected radius of 10 pc from the centre of the cluster, we found evidence for rotation of the cluster as a whole with a confidence level of about 95%. By fitting simple rotation curves to our data, we found a typical rotational velocity of $\sim 3\ \mathrm{km\,s^{-1}}$. When compared to the low velocity dispersion that we inferred for R136, this result suggests that star clusters may form with at least

$\sim 20\%$ of their kinetic energy in rotation. As we will briefly discuss below, establishing empirically whether star clusters show signs of rotation can put strong constraints on models of cluster formation and evolution. For very young (few Myr old) clusters, this is largely unexplored. Even though the rotation of R136 needs to be confirmed to a higher confidence level, our result remains exciting and will hopefully draw a renewed attention to the role of angular momentum in cluster formation and evolution.

7.2 Towards quantitative dynamical analysis of young massive clusters

Perhaps even more important than the specific results on R136 is the progress made towards quantitative dynamical analysis of resolved young massive clusters.

In Chapters 3 and 4, we have quantified the interplay between the orbital motions of massive binary stars and the observed kinematics of young massive star clusters. We now have the knowledge of what is required to measure the true velocity dispersion of a cluster, as well as the statistical tools to perform such measurements. Given any new multi-epoch RV dataset of massive stars in a cluster, the method applied in Chapter 3 could directly be applied to recover the velocity dispersion and the contribution of binaries.

Alternatively, we have tested in Chapter 4 a maximum likelihood procedure to recover the true velocity dispersion of a star cluster from a single epoch of radial velocity data. This is achieved by simultaneously fitting the intrinsic velocity distribution of the single stars and the centres of mass of the binaries along with the velocity shifts caused by orbital motions. The method had been shown in the past to accurately reproduce velocity dispersions below 1 $\mathrm{km\,s^{-1}}$ for solar-type stars in old open clusters, but we endeavoured to test its applicability to young massive clusters dominated by massive binary stars. We did this by using Monte Carlo simulations and our R136 RV data as an example for which the velocity dispersion of O-type stars is known from a multi-epoch approach, and taking into account the large uncertainties in the binary orbital parameter distributions of OB stars. We showed that the method must be applied with care given the higher spectroscopic binary fraction and more loosely constrained distributions of orbital parameters of OB stars compared to solar-type stars. However, for typical velocity dispersions of young massive clusters ($\gtrsim 4\ \mathrm{km\,s^{-1}}$), we demonstrated that the velocity dispersion can be estimated to within 40% or better from a single epoch of RVs, making it possible to distinguish between a cluster in virial equilibrium and an

unbound cluster. This offers an efficient mean of estimating the velocity dispersion of the massive star population in other young clusters and associations, in particular in young massive clusters, whose light is dominated by OB stars.

We may even speculate that the method tested in Chapter 4 could eventually be used to study the dynamics of massive stars in systems where this has been almost impossible up to now. There has been an increasing interest in near-infrared spectroscopy of massive stars in recent years (e.g. Hanson et al. 2005), as this wavelength regime offers the possibility of analysing these stars in embedded regions and near the Galactic centre given the substantially lower extinction compared to the optical. Quantitative atmospheric analysis of early-type stars from near-infrared spectral lines is now giving promising results (e.g. Stap et al. 2011). Assuming that precise radial velocities can also be obtained from near-infrared spectra, then the results of Chapter 4 might offer a way of studying the dynamics of massive embedded clusters, or even the dynamics of the significant number of Galactic YMCs (e.g. Davies et al. 2012) which are strongly affected by extinction and for which we currently have very little kinematic information.

Although very simple, the maximum likelihood method presented in Chapter 5 to investigate the rotation of R136 also represents an improvement over the method commonly used to detect rotation in star clusters, which involves significant smoothing of the data. Both of the approaches used in Chapters 4 and 5 are based on assuming probability density functions for the velocities and fitting discrete kinematic data (in this case RVs). In the future, a natural extension would therefore be to combine both aspects, i.e. fit the kinematics of a rotating cluster with a binary population from a single-epoch of RVs, and check if the rotation can be detected. It would also be interesting, for example, to allow the velocity dispersion to vary as a function of radius and see how well more complicated (and self-consistent) dynamical models can be fitted.

Note that while focussing on massive binaries, there are several other aspects that we have intentionally not taken into account and which could influence the dynamics of clusters and the expected velocity dispersion in virial equilibrium. More work is definitely needed to understand the effects of mass segregation and velocity anisotropy on the observed kinematics, for example. By building upon the work presented in this thesis and combining these efforts with detailed numerical modeling of R136-like clusters, we will hopefully gain a more quantitative insight into some of the complicated effects outlined above. In this era of large radial velocity surveys and upcoming proper motions and distances from GAIA, lessons learned from this work towards quantitative dynamical analysis of young clusters will prove useful to understand the details of their dynamical evolution.

7.3 Confirming the rotation of R136 and unveiling its formation

Following the detection of a relatively large rotational amplitude in R136 with a confidence level of 95%, an obvious follow-up study will be to establish whether the rotation signal is genuine with a much higher confidence level. As explained below, such a study could also give clues about the formation of R136.

Prompted by the possible rotation of R136, we explored with N-body models different ways for the cluster to gain angular momentum (Gieles et al., in preparation). We show in Figure 7.1 (right panel) the resulting rotation curve for two different scenarios with the same total angular momentum: (1) an equal mass merger of two sub-clusters and (2) the collapse of a uniform sphere with angular momentum (Gott 1973). From these models, an important signature can readily be seen in the rotation curves: the location of the peak is at about the half-mass radius ($r_h \approx 1.7$ pc) for the merger and around 2 r_h (i.e. 3.4 pc) for the uniform collapse. This offers a straightforward way to discriminate between these two scenarios. We tried to determine the location of the peak with the current data by fitting the same function as we used to fit the amplitude (see below), but now letting the peak radius as a free parameter (it was fixed in the paper). As a result we find $R_{\rm peak} = 3.7 \pm 1.6$ pc. The uncertainty ($\approx \pm r_h$) is currently too large to favour one or the other scenario. More RV measurements are needed to tell the difference. We know $V_{\rm rot} \sin i/\sigma_{\rm 1D}$, but ideally we also want to know the amount of kinetic energy in rotation and the total angular momentum of the cluster. This also requires more precise constraints on the location of the peak (where most of the angular momentum is located).

The best way to show whether the rotational signal is genuine with high confidence as well as bring down the uncertainty on the position of the peak of the rotation curve is to increase the number of stars with measured RVs in R136. To estimate the number of additional RVs needed, we performed the following simulations. We augmented our set of measured RVs with a mock RV data set with the same velocity dispersion as the cluster and a built-in rotational signal given by our best-fit rotation curve (the physically motivated rotation curve in Chapter 5) and best-fit rotation axis. Note that we previously fitted a rotation curve of the form $V_{\rm rot} \sin i = A\ x/(1 + (x/R_{\rm peak})^2)$ (see Lynden-Bell 1967) to our measured RVs using a maximum likelihood method. The positions of the stars for the mock RV data were randomly sampled within the possible positions of additional ARGUS pointings (Figure 7.1, left panel) and typical

uncertainties of 2 $\mathrm{km\,s^{-1}}$ were assumed for these stars. We fitted the rotation curve to our augmented RV sample and repeated the procedure for a large number of mock samples. We estimate that RVs for 20 additional single stars in the inner 5 pc would be sufficient to bring down the $1\,\sigma$ uncertainty on the position of the peak to ~ 1 pc ($\sim 0.6\ r_h$), allowing us to discriminate between the two models (see Figure 7.1, right panel).

By doing a similar exercise on mock samples with the same properties (velocity dispersion and measurement noise) as our observed sample but without any rotation (i.e. random RVs), we also estimate that the confidence level for the rotational signal would be increased to $\sim 99\%$ by adding these 20 stars. That is, assuming that the rotational signature is real and well described by our current best fit, the probability of obtaining a higher rotational velocity amplitude than the one measured purely by chance would be only $\sim 1\%$.

To add these 20 new single stars, about four additional ARGUS pointings could be

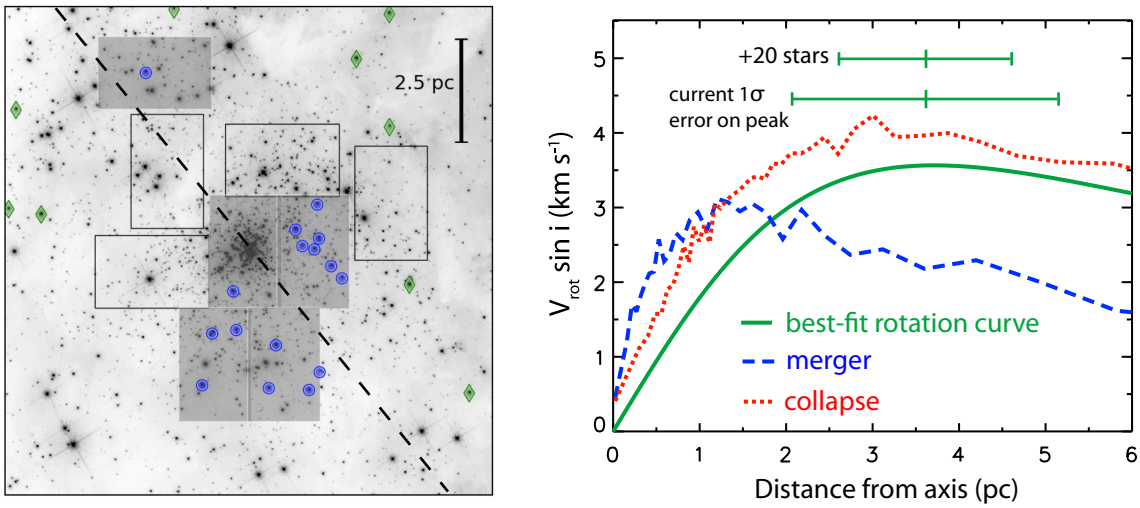

Figure 7.1 *Left:* ARGUS pointings from the VFTS (grey rectangles) with apparently single stars from our sample represented by blue circles (ARGUS) and green diamonds (MEDUSA), along with possible positions of additional ARGUS pointings (empty rectangles), overlaid on an HST-WFC3 F555W image (De Marchi et al. 2011). The approximate position of the rotation axis from our analysis of the VFTS data is indicated by the dashed line. *Right:* Rotational velocity as a function of distance from the rotation axis. The green solid curve shows the best-fit rotation curve for the physically motivated rotation curve discussed in Chapter 5. The rotation curves obtained from N-body models (Gieles et al., in preparation) are shown for an equal-mass merger and for the collapse of a uniform sphere, both with the same amount of angular momentum. Note that rotation curves plotted for these two models are for $\sin i = 1$. We also illustrate the decrease in the $\pm 1\sigma$ uncertainty on the position of the peak that is expected when adding 20 new RVs.

observed in a region of the cluster that was not covered by our previous observations, between 1 and 5 pc (where we expect the peak of the rotation curve to be) to the north, west and east of R136 (Figure 7.1, left panel). We could also make use of the UVES fibres to simultaneously collect additional spectra in the surrounding region.

From the VFTS data, we were able to extract $\sim$ 30 spectra suitable for RV analysis from four ARGUS pointings (i.e. excluding the fifth pointing in the core of R136, not well suited for the extraction of individual sources). After rejection of binaries, we were left with 16 apparently single stars. From inspection of an HST-WFC3 F555W image (e.g. Figure 7.1, left panel), there should be a similar number of suitable spectra of bright stars from the four possible new pointings. Assuming that $\sim$ 50% will be identified as binaries, we would be left with 15 to 20 new single stars. By monitoring additional stars with UVES fibres, the desired number of single stars would be reached. By measuring RVs at three different epochs and applying variability criteria as we did in Chapter 3, we would be able to reject most short-period binaries such that the contribution of undetected binaries to the observed velocity dispersion of non-variable stars remains negligible.

7.4 Binaries, velocity dispersion, and rotation: connecting the dots

One of the ways to get angular momentum into the cluster that was explored with N-body simulations (Gieles et al., in preparation) is a major merger with two clusters of 50 000 $M_\odot$ forming a 10^5 $M_\odot$ cluster. In this particular case, although the velocity dispersion a few parsec away from the centre is comparable to what we measured for R136 ($\sim$ 5 km s^{-1}), the central velocity dispersion (in the inner parsec) is significantly higher, reaching about 10 km s^{-1}. Measuring such a high central velocity dispersion would be another indication that R136 formed and got its angular momentum from a major merger event. Solving this problem would require measuring radial velocities for a large number of stars in the central parsec of R136, but unfortunately we could not extract any source in that region from the VFTS ARGUS data. However, the data that will eventually allow us to test this scenario might have already been obtained. A new HST spectroscopic programme (PI: P.A. Crowther) currently underway aims to determine the physical properties of a large number of massive stars in the dense central parsec of R136, which can only be observed from space or with adaptive optics. This will provide UV and optical spectra for several tens of massive stars, but with a very limited number of epochs. Therefore, assuming that the radial velocities of these

stars can be measured from the optical spectra to better than 10 $\mathrm{km\,s^{-1}}$ (such that the uncertainties do not prevent a velocity dispersion of 10 $\mathrm{km\,s^{-1}}$ from being resolved), this could constitute a perfect application of the method discussed in Chapter 4. Our tests indeed indicate that even without a precise knowledge of the binary properties of massive stars, a velocity dispersion of 10 $\mathrm{km\,s^{-1}}$ can be measured with an accuracy of $\sim 20\%$ or better from a single epoch of radial velocities.

Another way to explore the importance of mergers for cluster rotation would be to study apparent double clusters and verify how many of those are bound and form actual binary cluster systems, such that they might eventually merge. One example of an apparent double cluster is NGC 1850, in the LMC, where a young ($4-5$ Myr) and relatively low-mass cluster ($\sim 7\,500$ $\mathrm{M_\odot}$) is located at projected distance of ~ 7.5 pc from the main cluster, which is $50-60$ Myr old and has a total current mass of $\sim 50\,000$ $\mathrm{M_\odot}$ (Fischer et al. 1993). The geometry of the LMC, which is almost face-on, makes it unlikely that these clusters are chance alignments along the line of sight, and their similar ages also suggest a common origin. However, to find out if they are bound, their relative radial velocity has to be determined. An observational programme has been proposed to test this scenario by obtaining radial velocities of several stars with FLAMES in the poorly studied and younger of the two clusters (PI: M. Andersen). Again, the tools developed in the context of the present thesis will be useful to take into account the effect of massive binaries and accurately measure the systemic velocity and velocity dispersion of the cluster. This might lead to more studies of binary clusters, which are expected to be relatively common. For example, an apparent binary cluster frequency of 10% (for separations less than 18 pc) has been estimated by Dieball & Grebel (2000) for Magellanic Cloud clusters, less than half of which are expected to be chance alignments.

7.5 SXP 1062: the Rosetta Stone of accreting neutron stars?

In Chapter 6, we reported the discovery of a BeXRB, SXP 1062, containing one of the slowest rotating X-ray pulsars in the SMC. The discovery of a supernova remnant shell around the object allowed us to constrain the age of the pulsar to $(2-4)\times 10^4$ yr, which is surprisingly young for such a slowly rotating pulsar. There is currently no favoured explanation for the long spin period found, but SXP 1062 is quickly becoming a key object to understand the physics of accreting neutron stars. Despite 50 years of X-ray astronomy and hundreds of known X-ray binaries, there are still huge gaps in our understanding of accretion on neutron stars in binary systems, of field decay in

these objects, of their initial properties, and of the possible formation of magnetars in binaries. A HMXB in which the neutron star is young and has a known age makes it possible to address some of these issues. SXP 1062 is therefore a truly unique system and possibly a missing link.

In order to disentangle the different scenarios discussed in Chapter 6, further monitoring of SXP 1062 will be needed. It will be important to obtain new measurements of the spin period and establish correlations between spin period variations, the X-ray luminosity, and spectral properties. In particular, monitoring the relation between the spin period and the X-ray luminosity would be a powerful tool for distinguishing between different accretion and evolutionary scenarios. Recall that Shakura et al. (2012) presented a scenario in which the neutron star accretes material from a hot turbulent envelope surrounding its magnetosphere, in which case long spin periods and large period derivatives are possible even for the standard magnetic fields and mass accretion rates expected in BeXRBs. This model predicts a very specific relation between the period derivative, the X-ray luminosity, and the mass accretion rate (Figure 1 of Shakura et al. 2012). If this relation was verified, then a very strong magnetic field would not be required. On the other hand, a proton cyclotron absorption line is predicted at 0.3 keV in the case of a magnetar, and if such a line was detected it would lend support to the model proposed by Fu & Li (2012).

Finally, the discovery of SXP 1062 nicely illustrates the synergy between multi-object optical spectroscopic surveys of young clusters or massive-star forming regions and observations in other wavelength regimes (X-rays in this case). It does suggest that tantalising discoveries about binary interaction and the late stages of massive star evolution could be made if a deep X-ray survey of the 30 Doradus region was performed and complemented the VFTS.

Appendix A

Log of radial velocity measurements and variability tests

Table A.1 Individual epochs of the ARGUS observations. The modified Julian date (MJD) represents the central time of all the exposures of a given epoch. The nomenclature of individual exposures follows that presented in Evans et al. (2011).

Field	Epoch #	Exposures	MJD
A1	1	01[a-f]	54761.237
	2	02 [a-f]	54761.287
	3	03 [g-l]	54767.283
	4	03 [a-f]	54845.177
	5	04 [a-f]	54876.131
	6	05 [c+d]	55173.310
	7	05 [a+b]	55178.167
A2	1	01 [a+b]	54790.290
	2	02 [a+b]	54791.140
	3	03 [a+b]	54846.095
	4	04 [a+b]	54889.102
	5	05 [a+b]	55173.232
A3	1	01 [a+b]	54791.200
	2	02 [a+b]	54791.247
	3	03 [a+b]	54846.256
	4	04 [a+b]	54890.094
	5	05 [a]	55202.149
A4	1	01 [a+b]	54791.317
	2	02 [a+b]	54792.176
	3	03 [a+b]	54847.161
	4	04 [c+d]	54892.102
	5	04 [e+f]	54894.039
	6	04 [g+h]	54896.040
	7	04 [a+b]	54898.057
	8	05 [a+b]	55201.187
A5	1	01 [a+b]	54803.172
	2	02 [a+b]	54803.216
	3	03 [a+b]	54851.099
	4	04 [c+d]	54893.045
	5	04 [a+b]	54907.085
	6	05 [a+b]	55204.144

Table A.2 Results of the variability tests for the ARGUS sources. The apparently single stars are indicated by shaded IDs. For SB2 systems, the values presented here refer to the primary component. Note that source VFTS 1022 was extracted in ARGUS pointings A3 and A4.

ID	Field	Line	SB2	Epoch(s)	$\left\lvert\frac{RV_i-\mu}{\sigma_i}\right\rvert_{\max}$	$P(\chi^2,\nu)$	$\Delta\mathrm{RV}_{\max}$ [km s^{-1}]	TVS	Notes
542	A5	He I+He II λ4026	...	...	12.7	1.0000	181.9±11.4	✓	TVS also shows significant variability in Balmer lines and N IV λ4058.
		He II λ4200	...	...	28.9	1.0000	185.9±5.5	✓	Double peak in TVS indicative of binary motion. Weak P Cygni emission.
		He II λ4542	...	...	36.8	1.0000	148.5±4.2	✓	Double peak in TVS indicative of binary motion. Weak P Cygni emission.
545	A3	He I+He II λ4026	...	...	1.0	0.3484	...	...	
		He II λ4200	...	...	1.1	0.5688	...	...	
		He II λ4542	...	...	4.9	1.0000	14.4±3.0	...	
570	A5	...	...	...	...	...	...	...	Too low S/N for RV analysis.
585	A5	He I+He II λ4026	...	...	0.9	0.3268	...	...	
		He II λ4200	...	...	2.7	0.9991	...	...	
		He II λ4542	...	...	2.5	0.9867	...	...	
		4200+4542	...	...	3.2	1.0000	32.7±9.1	...	
1001	A2	...	...	...	...	...	...	...	Emission-line star, no suitable absorption line for RV analysis. Variability in He II λ4542 emission from TVS.
1002	A2	He I λ4388	...	...	2.4	0.9136	...	...	
1003	A2	...	...	...	...	...	...	...	B[e] star, no suitable absorption line for RV analysis.
1004	A2	He I+He II λ4026	...	...	2.1	0.9600	...	...	
		He I λ4388	...	...	2.3	0.9771	...	...	
		He II λ4200	...	...	2.4	0.9196	...	...	
		He II λ4542	...	...	1.6	0.8421	...	...	
		4200+4388+4542	...	...	3.3	0.9986	...		

Table A.2 continued

ID	Field	Line	SB2	Epoch(s)	$\left\lvert\frac{RV_i-\mu}{\sigma_i}\right\rvert_{\max}$	$P(\chi^2,\nu)$	$\Delta\mathrm{RV}_{\max}$ [km s^{-1}]	TVS	Notes
1005	A2	...	...	...	...	...	...	...	Too low S/N for RV analysis.
1006	A4	He I+He II λ4026	...	...	1.2	0.0869	...	...	
		He II λ4200	...	...	1.9	0.6553	...	...	
		He II λ4542	...	...	3.7	0.9992	...	...	
		4200+4542	...	...	3.5	0.9997	...		
1007	A2	He I+He II λ4026	...	...	1.9	0.9766	...	...	
		He I λ4388	...	...	0.8	0.1244	...	...	
		He II λ4200	...	...	2.1	0.8986	...	...	
		He II λ4542	...	...	0.8	0.1502	...	...	
		4200+4388+4542	...	...	1.4	0.5402	...		
1008	A2	He II λ4200	...	...	1.0	0.1854	...	...	
		He II λ4542	...	...	1.2	0.4761	...	...	
		4200+4542	...	...	1.6	0.5707	...	...	
1009	A2	He I+He II λ4026	...	...	0.7	0.1257	...	...	
		He I λ4471	...	...	0.7	0.1607	...	...	
		He II λ4200	...	...	1.6	0.4610	...	...	
		He II λ4542	...	...	2.3	0.8584	...	...	
		4200+4542	...	...	2.1	0.7858	...	...	
1010	A4	He I+He II λ4026	...	...	1.2	0.3767	...	...	
		He II λ4200	...	...	1.2	0.2252	...	...	
		He II λ4542	...	...	1.0	0.1728	...	...	
		4200+4542	...	...	1.5	0.4831	...	...	
1011	A4	...	...	...	...	...	...	...	Too low S/N for RV analysis.
1012	A2	He I+He II λ4026	...	...	2.0	0.8506	...	...	

Table A.2 continued

ID	Field	Line	SB2	Epoch(s)	$\left\lvert\frac{RV_i-\mu}{\sigma_i}\right\rvert_{\max}$	$P(\chi^2,\nu)$	$\Delta\mathrm{RV}_{\max}$ [km s^{-1}]	TVS	Notes
		He I λ4388	...	...	2.7	0.9949	...	...	
		He I λ4471	...	...	1.3	0.3517	...	...	
		He II λ4200	...	...	1.8	0.7524	...	...	
		He II λ4542	...	...	1.1	0.2058	...	...	
		4200+4388+4542	...	...	2.9	0.9826	...	...	
1013	A4	...	...	...	...	...	...	...	Too low S/N for RV analysis.
1014	A2	He I+He II λ4026	...	...	1.2	0.5620	...	...	
		He I λ4388	...	...	1.5	0.4265	...	...	
		He II λ4200	...	...	2.2	0.9645	...	...	
		He II λ4542	...	...	2.4	0.9268	...	...	
		4200+4388+4542	...	...	3.0	0.9926	...		
1015	A2	He I+He II λ4026	...	...	1.1	0.2398	...	...	
		He I λ4143	...	...	1.1	0.1787	...	...	
		He I λ4388	...	...	1.9	0.8445	...	...	
		He II λ4200	...	...	2.7	0.9953	...	...	
		He II λ4542	...	...	3.8	1.0000	69.9±16.1	...	
		4200+4542	...	...	4.5	1.0000	77.7±13.9	...	
1016	A4	He I+He II λ4026	?	4?, 5?	1.6	0.5778	...	...	
		He II λ4200	✓	2, 3, 6?	12.9	1.0000	166.4±11.4	✓	Double peak in TVS indicative of binary motion.
		He II λ4542	?	6?	19.2	1.0000	148.5±7.6	✓	Double peak in TVS indicative of binary motion.
1017	A4	He I+He II λ4026	...	...	1.7	0.4677	...	...	
		He II λ4200	...	...	3.7	1.0000	44.0±9.1	...	Weak P Cygni emission?
		He II λ4542	...	...	6.2	1.0000	42.1±5.7	✓	Weak P Cygni emission?
1018	A4	He I+He II λ4026	...	...	1.8	0.7663	...		

Table A.2 continued

ID	Field	Line	SB2	Epoch(s)	$\left\lvert\frac{RV_i-\mu}{\sigma_i}\right\rvert_{\max}$	$P(\chi^2,\nu)$	$\Delta\mathrm{RV}_{\max}$ [km s^{-1}]	TVS	Notes
		He II λ4200	...	...	2.1	0.5696	...	...	
		He II λ4542	...	...	1.7	0.5315	...	...	
		4200+4542	...	...	1.9	0.8805	...	...	
1019	A1	He II λ4200	✓	1-4, 6, 7	31.6	1.0000	287.5±7.2	✓	Double peak in TVS indicative of binary motion.
		He II λ4542	✓	1-4, 6, 7	47.4	1.0000	301.5±4.8	✓	Double peak in TVS indicative of binary motion.
1020	A4	He I+He II λ4026	...	...	1.7	0.7254	...	...	
		He II λ4200	...	...	1.8	0.4695	...	...	
		He II λ4542	...	...	1.3	0.2682	...	...	
		4200+4542	...	...	1.4	0.5039	...	...	
1021	A4	He I+He II λ4026	...	...	2.8	0.9950	...	...	
		He I λ4471	...	...	3.1	0.9997	...	...	
		He II λ4200	...	...	4.7	1.0000	17.3±3.1	...	
		He II λ4542	...	...	5.3	1.0000	11.0±1.9	...	
1022	A3, A4	He I+He II λ4026	...	...	3.7	0.9994	...	...	
		He II λ4200	...	...	3.4	0.9998	...	...	
		He II λ4542	...	...	3.6	1.0000	14.2±3.2	...	
1023	A3	He I λ4388	...	...	1.8	0.8739	...	...	
		He II λ4200	...	...	1.2	0.5073	...	...	
		He II λ4542	...	...	0.5	0.0229	...	...	
		4200+4388+4542	...	...	1.5	0.6155	...	...	
1024	A1	He I+He II λ4026	...	...	3.1	0.9923	...	...	
		He I λ4388	...	...	2.4	0.7910	...	...	
		He II λ4200	...	...	1.3	0.3178	...	...	
		He II λ4542	...	...	2.9	0.9937	...	...	

Table A.2 continued

ID	Field	Line	SB2	Epoch(s)	$\left\lvert\frac{RV_i-\mu}{\sigma_i}\right\rvert_{\max}$	$P(\chi^2,\nu)$	$\Delta\mathrm{RV}_{\max}$ [km s^{-1}]	TVS	Notes
		4200+4388+4542	...	...	2.2	0.9284	...	...	
1025	A1	He I λ4388	...	...	1.3	0.4262	...	...	Emission-line star. Significant variability in emission lines and P Cygni profiles from TVS.
1026	A3	He I+He II λ4026	...	...	1.5	0.4289	...	...	
		He I λ4388	...	...	0.8	0.1612	...	...	
		He II λ4200	...	...	0.8	0.0743	...	...	
		He II λ4542	...	...	2.2	0.9254	...	...	
		4200+4388+4542	...	...	1.9	0.9063	...	...	
1027	A5	He I+He II λ4026	...	...	1.7	0.7245	...	...	
		He II λ4200	...	...	4.4	1.0000	90.3±16.4	...	
		He II λ4542	...	...	5.3	1.0000	74.7±12.4	...	
		4200+4542	...	...	6.7	1.0000	75.2±9.9	...	
1028	A3	He I+He II λ4026	...	...	1.8	0.7310	...	...	
		He II λ4200	...	...	1.2	0.2051	...	...	
		He II λ4542	...	...	1.5	0.6237	...	...	
		4200+4542	...	...	1.3	0.3646	...	...	
1029	A5	He I+He II λ4026	...	...	13.0	1.0000	113.1±7.1	✓	
		He II λ4200	...	...	18.0	1.0000	97.5±4.1	✓	Double peak in TVS indicative of binary motion.
		He II λ4542	...	...	30.6	1.0000	102.5±2.5	✓	Double peak in TVS indicative of binary motion.
		4200+4542	...	...	35.6	1.0000	101.0±2.1	...	
1030	A5	...	...	...	...	...	...	...	Too low S/N for RV analysis.
1031	A5	He I+He II λ4026	✓	1-3, 5-6	...	...	...	...	SB3 at epochs #1 and 2?
		He II λ4200	✓	1-3, 5-6	...	...	...	✓	SB3 at epochs #1 and 2?
		He II λ4542	✓	1-3, 5-6	3.3	1.0000	35.6±10.6	✓	SB3 at epochs #1 and 2?

Table A.2 continued

ID	Field	Line	SB2	Epoch(s)	$\left\lvert\frac{RV_i-\mu}{\sigma_i}\right\rvert_{\max}$	$P(\chi^2,\nu)$	$\Delta\mathrm{RV}_{\max}$ [km s^{-1}]	TVS	Notes
1032	A5	He I+He II λ4026	...	...	3.8	0.9995	...	...	
		He I λ4388	...	...	1.3	0.3758	...	...	
		He II λ4200	...	...	8.5	1.0000	45.9±5.4	...	
		He II λ4542	...	...	11.8	1.0000	39.3±3.4	✓	
		4200+4542	...	...	14.5	1.0000	40.7±2.9	...	
1033	A5	He I+He II λ4026	✓	1, 5	...	...	...	...	
		He I λ4143	✓	1	...	...	...	...	
		He I λ4388	✓	1	...	...	...	...	
		He II λ4200	✓	1, 2	...	...	...	...	
		He II λ4542	✓	1, 2, 4	3.4	1.0000	27.6±5.8	...	
1034	A5	He I+He II λ4026	...	...	4.7	1.0000	13.3±2.1	...	
		He I λ4143	...	...	3.9	0.9999	...	...	
		He I λ4388	...	...	3.7	0.9984	...	...	
		He I λ4471	...	...	5.9	1.0000	7.5±1.6	...	
		He II λ4200	...	...	1.8	0.7640	...	...	
		He II λ4542	...	...	3.3	0.9996	...	...	
		4200+4388+4542	...	...	4.9	1.0000	7.3±1.4	...	
1035	A5	He II λ4200	...	...	1.1	0.2005	...	...	
		He II λ4542	...	...	0.8	0.0504	...	...	
		4200+4542	...	...	1.3	0.2300	...	...	
1036	A5	...	...	...	...	...	...	...	Too low S/N for RV analysis.
1037	A5	...	...	...	...	...	...	...	Too low S/N for RV analysis.

Table A.3 RVs (in $\mathrm{km\,s^{-1}}$) for individual epochs for all the ARGUS sources suitable for RV analysis. The lines used for the final RV measurements of a given star are indicated. RVs for the Medusa targets are presented in Sana et al. (2013a).

ID	line	RV_1	RV_2	RV_3	RV_4	RV_5	RV_6	RV_7	RV_8
542	He II 4542	254.1 ± 2.6	256.9 ± 3.4	158.4 ± 2.5	227.6 ± 3.5	229.7 ± 2.5	108.4 ± 2.4		
545	He II 4542	230.5 ± 1.5	230.1 ± 1.8	228.4 ± 2.0	232.2 ± 2.1	242.8 ± 2.2			
585	He II 4200+He II 4542	280.8 ± 6.6	...	248.1 ± 6.3	273.3 ± 4.5	273.7 ± 4.0	249.9 ± 5.3		
1002	He I 4388	257.6 ± 12.0	275.2 ± 13.6	264.9 ± 13.3	264.6 ± 11.8	302.1 ± 12.3			
1004	He I 4388+He II 4200+He II 4542	285.7 ± 4.7	278.5 ± 5.2	276.2 ± 4.1	258.4 ± 4.8	273.4 ± 3.9			
1006	He II 4200+He II 4542	249.5 ± 9.8	245.4 ± 11.3	294.4 ± 8.5	251.4 ± 13.6	275.0 ± 16.4	284.0 ± 17.9	284.3 ± 13.6	246.5 ± 8.3
1007	He I 4388+He II 4200+He II 4542	264.9 ± 2.6	261.0 ± 2.8	262.9 ± 3.2	263.1 ± 2.9	268.1 ± 2.8			
1008	He II 4200+He II 4542	277.3 ± 2.0	281.0 ± 2.4	275.0 ± 2.7	277.7 ± 2.1	275.8 ± 1.8			
1009	He II 4200+He II 4542	277.6 ± 3.0	275.2 ± 3.3	266.9 ± 3.5	274.3 ± 3.7	274.9 ± 2.5			
1010	He II 4200+He II 4542	284.2 ± 5.0	287.1 ± 6.5	279.2 ± 5.3	273.7 ± 7.4	277.3 ± 7.5	278.7 ± 7.5	287.0 ± 6.4	292.2 ± 6.0
1012	He I 4388+He II 4200+He II 4542	275.0 ± 6.4	266.1 ± 6.4	267.2 ± 6.2	247.8 ± 5.8	269.9 ± 6.2			
1014	He I 4388+He II 4200+He II 4542	269.3 ± 1.4	266.9 ± 1.7	268.1 ± 1.7	266.7 ± 1.4	262.3 ± 1.4			
1015	He II 4200+He II 4542	253.1 ± 7.9	279.7 ± 9.5	217.2 ± 9.6	294.9 ± 10.1	265.4 ± 9.0			
1016	He II 4542	316.9 ± 4.4	296.3 ± 5.4	329.0 ± 4.5	186.1 ± 6.1	342.6 ± 5.5	181.3 ± 6.2	329.8 ± 4.4	320.5 ± 4.1
1017	He II 4542	203.2 ± 3.3	213.3 ± 3.8	191.7 ± 3.6	217.7 ± 3.1	212.7 ± 3.6	227.2 ± 3.0	202.8 ± 2.9	185.1 ± 4.3
1018	He II 4200+He II 4542	255.4 ± 1.6	260.9 ± 1.6	259.8 ± 1.5	259.0 ± 2.0	254.6 ± 2.0	258.2 ± 2.3	260.0 ± 1.7	258.1 ± 1.4
1019	He II 4542	362.2 ± 5.6	381.9 ± 6.9	134.8 ± 4.0	117.8 ± 4.1	266.3 ± 3.8	86.5 ± 3.1	388.0 ± 3.6	
1020	He II 4200+He II 4542	265.3 ± 2.1	266.8 ± 2.8	270.8 ± 2.5	266.4 ± 3.0	265.6 ± 3.1	263.7 ± 3.4	271.0 ± 2.7	268.0 ± 2.2

Table A.3 continued

ID	line	RV_1	RV_2	RV_3	RV_4	RV_5	RV_6	RV_7	RV_8
1021	He II 4542	248.6 ± 1.2	256.8 ± 1.3	249.8 ± 1.2	245.8 ± 1.4	247.2 ± 1.4	251.2 ± 1.5	250.0 ± 1.2	249.6 ± 1.1
1022	He II 4542 (A3 pointing)	222.2 ± 1.6	222.5 ± 1.6	227.0 ± 1.7	230.4 ± 1.8	226.0 ± 2.3			
1022	He II 4542 (A4 pointing)	219.6 ± 2.0	216.2 ± 2.6	229.6 ± 2.1	219.9 ± 2.5	227.6 ± 2.6	228.2 ± 2.5	221.5 ± 2.1	217.7 ± 2.2
1023	He I 4388+He II 4200+He II 4542	270.2 ± 4.4	260.4 ± 3.9	267.4 ± 4.7	266.1 ± 4.5	272.0 ± 5.6			
1024	He I 4388+He II 4200+He II 4542	272.3 ± 6.1	267.6 ± 6.1	245.5 ± 8.1	269.2 ± 8.1	272.6 ± 7.3	262.8 ± 4.7	255.6 ± 5.5	
1026	He I 4388+He II 4200+He II 4542	264.9 ± 1.7	268.4 ± 1.8	265.7 ± 2.1	262.3 ± 2.1	260.8 ± 2.6			
1027	He II 4200+He II 4542	292.3 ± 4.2	293.3 ± 5.9	265.5 ± 5.2	218.1 ± 8.0	237.9 ± 4.2	260.4 ± 3.9		
1028	He II 4200+He II 4542	272.1 ± 0.9	272.7 ± 1.0	271.6 ± 1.1	270.3 ± 1.2	272.1 ± 1.4			
1029	He II 4200+He II 4542	290.7 ± 1.3	292.7 ± 1.2	227.0 ± 1.7	287.7 ± 2.9	262.5 ± 1.7	328.0 ± 1.3		
1031	He II 4542	274.7 ± 8.0	278.0 ± 7.0	242.4 ± 8.1	256.5 ± 3.2	251.6 ± 5.3	275.4 ± 4.0		
1032	He II 4200+He II 4542	263.9 ± 1.7	264.2 ± 1.8	272.7 ± 2.7	285.6 ± 3.3	259.9 ± 2.2	300.6 ± 1.9		
1033	He II 4542	268.3 ± 3.8	266.2 ± 3.8	240.7 ± 4.4	248.8 ± 7.9	251.2 ± 4.3	251.2 ± 3.3		
1034	He I 4388+He II 4200+He II 4542	263.7 ± 1.0	263.2 ± 1.0	263.8 ± 1.2	270.3 ± 1.8	264.4 ± 1.2	270.5 ± 1.0		
1035	He II 4200+He II 4542	268.1 ± 4.1	262.7 ± 4.6	272.1 ± 6.5	271.3 ± 9.2	271.9 ± 4.8	269.7 ± 5.8		

Appendix B

Notes on individual ARGUS sources

We comment here on selected individual sources, paying particular attention to those with previous identifications, composite spectra, or which appear multiple in the WFC3 image. For reference, the spectra of the ARGUS sources that did not show spectroscopic variability are also displayed in Fig. B.1.

- *VFTS 542:* This star is identified as a definite variable with a large amplitude from both ARGUS and Medusa observations. Its He II λ4200 and He II λ4542 lines show a weak P Cygni component and it is classified as O2 If*/WN5 (Evans et al. 2011), so even if it was not variable, its absolute RV could not be trusted. RV discrepancies as large as $\sim$ 40 km s^{-1} are found at some epochs between He II λ4200 and He II λ4542.

- *VFTS 545:* It is also known as Mk35 (Melnick 1985) and classified as O2 If*/WN5 (Evans et al. 2011). There is a discrepancy of $\sim$ 20 km s^{-1} between He II λ4200 and He II λ4542, and its absolute RV also cannot be trusted. Low-amplitude variability is only detected in He II λ4542, which is stronger and has smaller RV uncertainties compared to He II λ4200.

- *VFTS 570:* The ARGUS spectra of this source were not analysed for RV variability because their S/N was too low, but from the Medusa spectra it was found to be a definite RV variable with a large amplitude (Sana et al. 2013a). Two stars appear to contribute significantly to the ARGUS source when comparing with the WFC3 image.

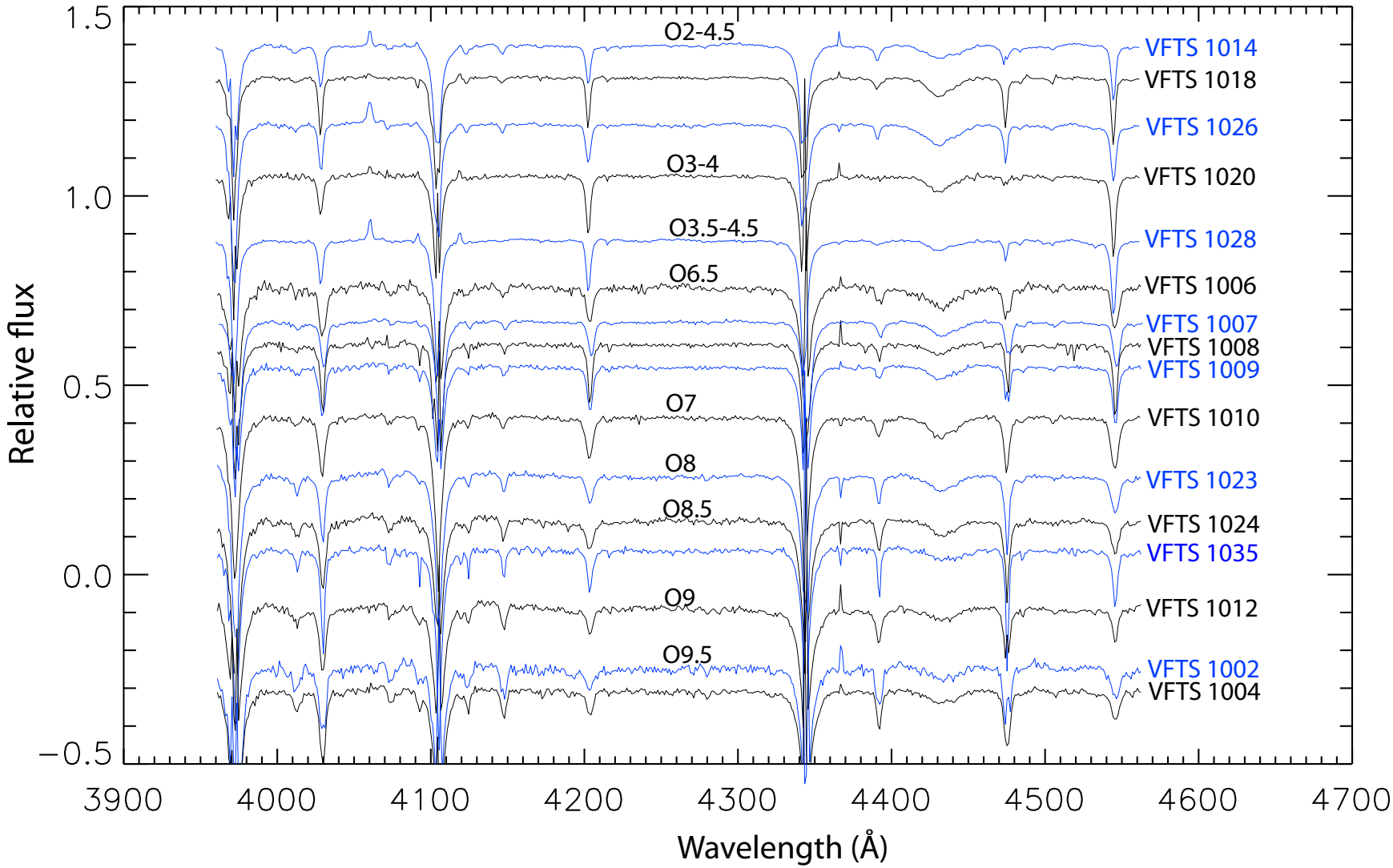

Figure B.1 Spectra of ARGUS sources that did not show spectroscopic variability, ordered from earliest to latest spectral types. These spectra are the result of merging the multiple epochs and exposures and have been rebinned to an equivalent resolving power of $R = 4\,000$ to perform spectral classification.

- *VFTS 585:* This source was also found to be variable from the Medusa spectra (Sana et al. 2013a). Significant RV variability was detected from the relatively low S/N ARGUS spectra only once He II λ4200 and He II λ4542 were fitted simultaneously.

- *VFTS 1001:* This source corresponds to a known Wolf-Rayet star, R134 (Feast et al. 1960), classified as WN6(h) (e.g. Massey & Hunter 1998). Although it was detected as an X-ray source and suggested as a possible colliding-wind binary by Portegies Zwart et al. (2002), it is not known to be a binary. Interestingly, our TVS analysis reveals significant variability in the He II λ4542 emission, but it is unclear if this is due to a normalisation problem in a spectral range dominated by several emission lines, where the continuum is harder to define.

- *VFTS 1003:* This source was found to be a new B[e]-type star in Evans et al. (2011). The TVS analysis performed in the present work did not reveal any significant variability other than in the nebular emission lines (due to sky subtraction).

- *VFTS 1004:* The WFC3 image suggests that two sources are contributing to VFTS 1004, but it does not display a composite spectrum, it is not found to be variable, and the He I λ4388, He II λ4200 and He II λ4542 lines all have consistent absolute RVs.

- *VFTS 1007:* Similarly to VFTS 1004, VFTS 1007 appears multiple when inspecting the WFC3 image, but it is not variable, it does not have a composite spectrum, and He I λ4388, He II λ4200 and He II λ4542 all have consistent absolute RVs.

- *VFTS 1008:* The well-developed N III absorption lines suggest that nitrogen is overabundant, hence the ON classification.

- *VFTS 1014:* The presence of N IV λ4058 and Si IV λ4089/4116 emission together with weak but well developed He I singlet lines at 4121, 4143 and 4388 Å suggests a composite spectrum (see Fig. B.2). Based on the helium line diagnostics and the absence of Si III λ4552, the later component is identified as a mid/late O-type star. From the relative strength of N IV and Si IV, the other component is O2-4.5 (we cannot be more precise because our the ARGUS spectrum does not include the N V absorption region), in agreement with the O3 V classification of Massey & Hunter (1998). Even though its spectrum appears composite, this source did not show significant variability. The He I λ4388, He II λ4200 and He II λ4542 lines all have consistent absolute RVs.

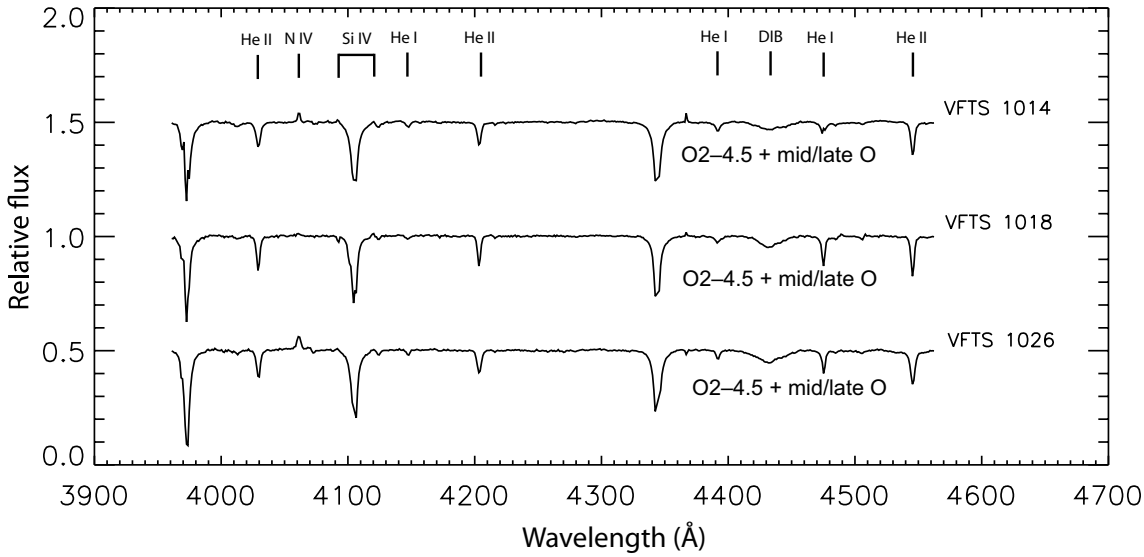

Figure B.2 Non-variable ARGUS sources displaying composite spectra. Emission lines labelled are N IV λ4058 and Si IV $\lambda\lambda$4089, 4116. Absorption lines labelled are He I λ4026, He I λ4143, He II λ4200, He I λ4388, He I λ4471, He II λ4542 and a diffuse interstellar band at 4428 Å.

- *VFTS 1015:* This source is clearly multiple by comparison with the WFC3 image and significant RV variability is found in He II λ4542. For some epochs, the RV of the He I λ4388 line is clearly different from that of He II λ4200 and He II λ4542 lines.

- *VFTS 1017:* This source is variable. Its He II λ4200 and He II λ4542 lines have a weak P Cygni component. A discrepancy of up to ~ 30 km s^{-1} is found in the RVs of He II λ4200 and He II λ4542 at different epochs.

- *VFTS 1018:* The presence of weak N IV λ4058 and Si IV λ4116 emission in combination with weak but well developed He I singlet lines suggests a composite spectrum (see Fig. B.2). Based on the helium line diagnostics and the absence of Si III λ4552, the later component is identified as a mid/late O-type star.. From the relative strength of the N IV and Si IV emission, the other component is classified as O2-4.5, in relatively good agreement with the O3 III(f*) classification of Massey & Hunter (1998). Even though its spectrum appears composite, this source did not show significant variability. The He I λ4388, He II λ4200 and He II λ4542 lines all have consistent absolute RVs.

- *VFTS 1019:* This is a known high-mass binary (R136-038) classified as O3 III(f*) + O8 by Massey & Hunter (1998), then revised as O3 V + O 6 V by Massey et al. (2002). The ARGUS spectra show obvious variability, a large RV amplitude, and SB2 profiles at several epochs.

- *VFTS 1022:* This source corresponds to Mk37a=R136-014 (Melnick 1985; Massey & Hunter 1998), classified as O4 If+ by Massey & Hunter (1998), but suggested as O3.5 If*/WN7 by Crowther & Walborn (2011). 13 epochs (the source is on the edge of the A3 and A4 ARGUS pointings) made it possible to detect low-amplitude RV variability in He II λ4542. However, even if it had not been flagged as variable, this star would not have been suitable for our analysis of the dynamics. A discrepancy of $\sim$ 15 $\mathrm{km\,s^{-1}}$ is found between the RVs of He II λ4200 and He II λ4542, and the RV of He I λ4388 is significantly larger than that of the He II lines.

- *VFTS 1023:* We classified this star as O8 III/V. Massey & Hunter (1998) classified it as O6, but at this subtype He I+II λ4026 should be as deep as He II λ4200 while He I λ4471 should be significantly weaker than He II λ4542. Also, He I λ4143 and He I λ4388 should be much weaker than He II λ4200 and He II λ4542 respectively, which is not what we see. A possible explanation for the discrepancy between our classification and that of Massey & Hunter (1998) is that this source is an undetected single-lined spectroscopic binary.

- *VFTS 1025:* This source appears multiple and the centre of the ARGUS position is offset between two stars in the WFC3 image, with the much brighter star being R136c. It is interesting to note that we find significant variability in the TVS of this source (see Fig. 3.3). R136c was identified as a probable binary (Schnurr et al. 2009) and suspected to be a colliding-wind massive binary (Crowther et al. 2010).

- *VFTS 1026:* When comparing with the WFC3 image, the centre of the ARGUS source appears offset between two stars. One of these is MH41, O3 III(f*) (Massey & Hunter 1998), also classified as O8: V by Walborn & Blades (1997). The light is probably dominated by MH41 (the brighter of the two stars), although we flagged VFTS 1026 as having a composite spectrum (see Fig. B.2), as suggested by the presence of N IV λ4058 and Si IV λ4089/4116 emission together with weak but well developed He I singlet lines at 4121, 4143 and 4388 Å. Based on the helium line diagnostics and the absence of Si III λ4552, the later component is identified as a mid/late O-type star. From the relative strength of the N IV and Si IV emission, the other component is classified as O2-4.5, in agreement with the classification of Massey & Hunter (1998). This source is however not variable, and its He I λ4388, He II λ4200 and He II λ4542 lines have consistent absolute RVs.

- *VFTS 1031:* This corresponds to R136-025 (O3 V; Massey & Hunter 1998), which was flagged as a suspected variable by Massey et al. (2002). In our ARGUS spectra, the He I+He II λ4026, He II λ4200 and He II λ4542 lines seem to display three components at some epochs.

- *VFTS 1034:* This corresponds to Mk32, which is itself a blend of R136-013 (O8 III(f), Massey & Hunter 1998; O7.5 II, Walborn & Blades 1997) and R136-074 (O6 V, Massey & Hunter 1998). The variability in this source is more obvious in the He I+He II λ4026 and He I λ4471 lines, but also significant when He I λ4388, He II λ4200 and He II λ4542 are fitted simultaneously.

Bibliography

Agekian, T. A. 1958, Soviet Ast., 2, 22

Aguilar, L. A. & Merritt, D. 1990, ApJ, 354, 33

Allison, R. J., Goodwin, S. P., Parker, R. J., et al. 2009, ApJL, 700, L99

Andersen, M., Zinnecker, H., Moneti, A., et al. 2009, ApJ, 707, 1347

Anderson, J. & van der Marel, R. P. 2010, ApJ, 710, 1032

Antoniou, V., Zezas, A., Hatzidimitriou, D., & Kalogera, V. 2010, ApJ, 716, L140

Arbutina, B. & Urosević, D. 2005, MNRAS, 360, 76

Banerjee, S. & Kroupa, P. 2013, ApJ, 764, 29

Banerjee, S., Kroupa, P., & Oh, S. 2012, ApJ, 746, 15

Barbá, R. H., Gamen, R., Arias, J. I., et al. 2010, in Revista Mexicana de Astronomia y Astrofisica, vol. 27, Vol. 38, Revista Mexicana de Astronomia y Astrofisica Conference Series, 30–32

Bastian, N. 2011, arXiv:1107.2140

Bastian, N. 2012, arXiv:1208.3403

Bastian, N., Covey, K. R., & Meyer, M. R. 2010, ARA&A, 48, 339

Bastian, N., Emsellem, E., Kissler-Patig, M., & Maraston, C. 2006, A&A, 445, 471

Bastian, N. & Gieles, M. 2006, eprint arXiv, 9669

Bastian, N., Gieles, M., Goodwin, S. P., et al. 2008, MNRAS, 389, 223

Bastian, N. & Goodwin, S. P. 2006, MNRAS, 369, L9

Bastian, N., Saglia, R. P., Goudfrooij, P., et al. 2006, A&A, 448, 881

Baumgardt, H. & Kroupa, P. 2007, MNRAS, 380, 1589

Baumgardt, H., Kroupa, P., & Parmentier, G. 2008, MNRAS, 384, 1231

Baumgardt, H., Makino, J., Hut, P., McMillan, S., & Portegies Zwart, S. 2003, ApJL, 589, L25

Bekki, K. 2010, ApJL, 724, L99

Bekki, K. & Stanimirović, S. 2009, MNRAS, 395, 342

Bellazzini, M., Bragaglia, A., Carretta, E., et al. 2012, A&A, 538, A18

Bestenlehner, J. M., Vink, J. S., Gräfener, G., et al. 2011, A&A, 530, L14

Bevington, P. R. 1969, Data reduction and error analysis for the physical sciences, ed. Bevington, P. R.

Binney, J. & Merrifield, M. 1998, Galactic Astronomy

Binney, J. & Tremaine, S. 1987, Galactic dynamics (Princeton, NJ, Princeton University Press, 1987)

Bonnell, I. A. & Bate, M. R. 2006, MNRAS, 370, 488

Bosch, G. & Meza, A. 2001, in Revista Mexicana de Astronomia y Astrofisica Conference Series, Vol. 11, Revista Mexicana de Astronomia y Astrofisica Conference Series, 29

Bosch, G., Selman, F., Melnick, J., & Terlevich, R. 2001, A&A, 380, 137

Bosch, G., Terlevich, E., & Terlevich, R. 2009, AJ, 137, 3437

Bressert, E., Bastian, N., Evans, C. J., et al. 2012, A&A, 542, A49

Bressert, E., Bastian, N., Gutermuth, R., et al. 2010, MNRAS, 409, L54

Bromm, V., Coppi, P., & Larson, R. 1999, ApJ, 527, L5

Brott, I., de Mink, S. E., Cantiello, M., et al. 2011, A&A, 530, A115

Campbell, M. A., Evans, C. J., Mackey, A. D., et al. 2010, MNRAS, 405, 421

Cantiello, M., Brocato, E., & Blakeslee, J. P. 2009, A&A, 503, 87

Carlson, L. R., Sabbi, E., Sirianni, M., et al. 2007, ApJ, 665, L109

Carlson, L. R., Sewiło, M., Meixner, M., et al. 2011, ApJ, 730, 78

Cassinelli, J. P., Mathis, J. S., & Savage, B. D. 1981, Science, 212, 1497

Castor, J. I., Abbott, D. C., & Klein, R. I. 1975, ApJ, 195, 157

Cerviño, M., Valls-Gabaud, D., Luridiana, V., & Mas-Hesse, J. M. 2002, A&A, 381, 51

Chakrabarty, D., Levine, A. M., Clark, G. W., & Takeshima, T. 1998, IAU Circ., 7048, 1

Chini, R., Hoffmeister, V. H., Nasseri, A., Stahl, O., & Zinnecker, H. 2012, MNRAS, 424, 1925

Chu, Y.-H. & Kennicutt, R. C. 1994, ApJ, 425, 720

Cignoni, M., Sabbi, E., Nota, A., et al. 2009, AJ, 137, 3668

Cioni, M.-R. L., Clementini, G., Girardi, L., et al. 2011, A&A, 527, A116

Clark, J. S., Ritchie, B. W., & Negueruela, I. 2010, A&A, 514, A87

Clarkson, W. I., Ghez, A. M., Morris, M. R., et al. 2012, ApJ, 751, 132

Coe, M. J., Edge, W. R. T., Galache, J. L., & McBride, V. A. 2005, MNRAS, 356, 502

Conti, P., Crowther, P., & Leitherer, C. 2008, From Luminous Hot Stars to Starburst Galaxies,Cambridge University Press, Cambridge, UK

Conti, P. S. & Alschuler, W. R. 1971, ApJ, 170, 325

Conti, P. S., Leep, E. M., & Lorre, J. J. 1977, ApJ, 214, 759

Corbet, R., Markwardt, C. B., Marshall, F. E., et al. 2003, IAU Circ., 8064, 4

Corbet, R. H. D., Coe, M. J., McGowan, K. E., et al. 2009, A Massive Star Odyssey: From Main Sequence to Supernova, 4, 361

Côté, P., Welch, D. L., Fischer, P., & Gebhardt, K. 1995, ApJ, 454, 788

Cottaar, M., Meyer, M. R., Andersen, M., & Espinoza, P. 2012a, A&A, 539, A5

Cottaar, M., Meyer, M. R., & Parker, R. J. 2012b, A&A, 547, A35

Crowther, P. A., Schnurr, O., Hirschi, R., et al. 2010, MNRAS, 408, 731

Crowther, P. A. & Walborn, N. R. 2011, MNRAS, 416, 1311

Davidson, K. & Ostriker, J. P. 1973, ApJ, 179, 585

Davies, B., Bastian, N., Gieles, M., et al. 2011, MNRAS, 411, 1386

Davies, B., de La Fuente, D., Najarro, F., et al. 2012, MNRAS, 419, 1860

Davies, R. E. & Pringle, J. E. 1981, MNRAS, 196, 209

De Becker, M., Rauw, G., Manfroid, J., & Eenens, P. 2006, A&A, 456, 1121

de Bruijne, J. H. J. 1999, MNRAS, 310, 585

de Grijs, R. & Anders, P. 2006, MNRAS, 366, 295

de Koter, A., Heap, S. R., & Hubeny, I. 1998, ApJ, 509, 879

De Marchi, G., Paresce, F., Panagia, N., et al. 2011, ApJ, 739, 27

de Mink, S. E., Langer, N., Izzard, R. G., Sana, H., & de Koter, A. 2013, ApJ, 764, 166

Dieball, A. & Grebel, E. K. 2000, A&A, 358, 897

Dobbs, C. L., Burkert, A., & Pringle, J. E. 2011, MNRAS, 417, 1318

Douglas, L. S., Bremer, M. N., Lehnert, M. D., Stanway, E. R., & Milvang-Jensen, B. 2010, MNRAS, 409, 1155

Duquennoy, A. & Mayor, M. 1991, A&A, 248, 485

Einsel, C. & Spurzem, R. 1999, MNRAS, 302, 81

Elmegreen, B. G. & Efremov, Y. N. 1997, ApJ, 480, 235

Elson, R. A. W., Fall, S. M., & Freeman, K. C. 1987, ApJ, 323, 54

Ernst, A., Glaschke, P., Fiestas, J., Just, A., & Spurzem, R. 2007, MNRAS, 377, 465

Evans, C., Hunter, I., Smartt, S., et al. 2008, The Messenger, 131, 25

Evans, C., Lennon, D., Smartt, S., & Trundle, C. 2006, A&A, 456, 623

Evans, C., Smartt, S., Lee, J., et al. 2005a, A&A, 437, 467

Evans, C., Smartt, S., Lennon, D., et al. 2005b, The Messenger, 122, 36

Evans, C., Walborn, N., Crowther, P., et al. 2010, ApJ, 715, L74

Evans, C. J., Hainich, R., Oskinova, L. M., et al. 2012, ApJ, 753, 173

Evans, C. J. & Howarth, I. D. 2008, MNRAS, 386, 826

Evans, C. J., Howarth, I. D., Irwin, M. J., Burnley, A. W., & Harries, T. J. 2004, MNRAS, 353, 601

Evans, C. J., Taylor, W. D., Hénault-Brunet, V., et al. 2011, A&A, 530, 108

Fall, S. M. & Frenk, C. S. 1985, in IAU Symposium, Vol. 113, Dynamics of Star Clusters, ed. J. Goodman & P. Hut, 285–296

Fall, S. M., Krumholz, M. R., & Matzner, C. D. 2010, ApJL, 710, L142

Farouki, R. T. & Salpeter, E. E. 1982, ApJ, 253, 512

Feast, M. W., Thackeray, A. D., & Wesselink, A. J. 1960, MNRAS, 121, 337

Fellhauer, M., Wilkinson, M. I., & Kroupa, P. 2009, MNRAS, 397, 954

Fischer, P., Welch, D. L., Cote, P., Mateo, M., & Madore, B. F. 1992, AJ, 103, 857

Fischer, P., Welch, D. L., & Mateo, M. 1993, AJ, 105, 938

Fleck, J.-J., Boily, C. M., Lançon, A., & Deiters, S. 2006, MNRAS, 369, 1392

Frenk, C. S. & Fall, S. M. 1982, MNRAS, 199, 565

Fu, L. & Li, X.-D. 2012, ApJ, 757, 171

Fujii, M. S. & Portegies Zwart, S. 2011, Science, 334, 1380

Fullerton, A. W., Gies, D. R., & Bolton, C. T. 1996, ApJ Supp., 103, 475

Gaburov, E. & Gieles, M. 2008, MNRAS, 391, 190

García, B. & Mermilliod, J. C. 2001, A&A, 368, 122

Garmany, C. D., Conti, P. S., & Massey, P. 1980, ApJ, 242, 1063

Geller, A. M. & Mathieu, R. D. 2011, Nature, 478, 356

Geller, A. M., Mathieu, R. D., Harris, H. C., & McClure, R. D. 2008, AJ, 135, 2264

Geller, A. M., Mathieu, R. D., Harris, H. C., & McClure, R. D. 2009, AJ, 137, 3743

Geyer, E. H., Nelles, B., & Hopp, U. 1983, A&A, 125, 359

Geyer, M. P. & Burkert, A. 2001, MNRAS, 323, 988

Gibson, B. K. 2000, Mem. Soc. Astron. Italiana, 71, 693

Gieles, M., Baumgardt, H., Heggie, D. C., & Lamers, H. J. G. L. M. 2010a, MNRAS, 408, L16

Gieles, M., Heggie, D. C., & Zhao, H. 2011, MNRAS, 413, 2509

Gieles, M., Moeckel, N., & Clarke, C. J. 2012, MNRAS, 426, L11

Gieles, M. & Portegies Zwart, S. F. 2011, MNRAS, 410, L6

Gieles, M., Sana, H., & Portegies Zwart, S. F. 2010b, MNRAS, 402, 1750

Goodwin, S. P. 1997, MNRAS, 286, L39

Goodwin, S. P. & Bastian, N. 2006, MNRAS, 373, 752

Gott, III, R. J. 1973, ApJ, 186, 481

Gouliermis, D. A., Quanz, S. P., & Henning, T. 2007, ApJ, 665, 306

Grebel, E. K. & Chu, Y.-H. 2000, AJ, 119, 787

Haberl, F. & Pietsch, W. 2004, A&A, 414, 667

Haberl, F., Sturm, R., Filipović, M. D., Pietsch, W., & Crawford, E. J. 2012, A&A, 537, L1

Haiman, Z. & Loeb, A. 1997, ApJ, 483, 21

Hanson, M. M., Kudritzki, R.-P., Kenworthy, M. A., Puls, J., & Tokunaga, A. T. 2005, ApJ Supp., 161, 154

Hanuschik, R. W. 1996, A&A, 308, 170

Harries, T. J., Hilditch, R. W., & Howarth, I. D. 2003, MNRAS, 339, 157

Harris, J. & Zaritsky, D. 2004, AJ, 127, 1531

Hartigan, P., Raymond, J., & Hartmann, L. 1987, ApJ, 316, 323

Hénault-Brunet, V., Evans, C. J., Sana, H., et al. 2012a, A&A, 546, A73

Hénault-Brunet, V., Gieles, M., Evans, C. J., et al. 2012b, A&A, 545, L1

Hénault-Brunet, V., Oskinova, L. M., Guerrero, M. A., et al. 2012c, MNRAS, 420, L13

Henize, K. G. 1956, ApJ Supp., 2, 315

Hénon, M. 1973, A&A, 24, 229

Hills, J. G. 1980, ApJ, 235, 986

Hillwig, T. C., Gies, D. R., Bagnuolo, Jr., W. G., et al. 2006, ApJ, 639, 1069

Holtzman, J. A., Faber, S. M., Shaya, E. J., et al. 1992, AJ, 103, 691

Hong, J., Kim, E., Lee, H. M., & Spurzem, R. 2013, MNRAS

Hunter, D. A., Shaya, E. J., Holtzman, J. A., et al. 1995, ApJ, 448, 179

Hunter, D. A., Vacca, W. D., Massey, P., Lynds, R., & O'Neil, E. J. 1997, AJ, 113, 1691

Hunter, I., Brott, I., Lennon, D. J., et al. 2008a, ApJ, 676, L29

Hunter, I., Dufton, P. L., Smartt, S. J., et al. 2007, A&A, 466, 277

Hunter, I., Lennon, D. J., Dufton, P. L., et al. 2008b, A&A, 479, 541

Hurley, J. R. 2007, MNRAS, 379, 93

Hutchings, J., Cartledge, S., & Pazder, J. 1991, AJ

Iben, Jr., I. & Tutukov, A. V. 1996, ApJ, 456, 738

Ikhsanov, N. R. 2007, MNRAS, 375, 698

Ikhsanov, N. R. 2012, MNRAS, 424, L39

Johansson, L. E. B., Greve, A., Booth, R. S., et al. 1998, A&A, 331, 857

Kamann, S., Wisotzki, L., & Roth, M. M. 2013, A&A, 549, A71

Kennicutt, Jr., R. C. & Chu, Y.-H. 1988, AJ, 95, 720

Kim, E., Einsel, C., Lee, H. M., Spurzem, R., & Lee, M. G. 2002, MNRAS, 334, 310

Kiminki, D. C. & Kobulnicky, H. A. 2012, ApJ, 751, 4

King, I. 1962, AJ, 67, 471

Knigge, C., Coe, M. J., & Podsiadlowski, P. 2011, Nature, 479, 372

Kobulnicky, H. A. & Fryer, C. L. 2007, ApJ, 670, 747

Kontizas, E., Kontizas, M., Sedmak, G., & Smareglia, R. 1989, AJ, 98, 590

Kouwenhoven, M. B. N. & de Grijs, R. 2008, A&A, 480, 103

Kroupa, P. & Boily, C. M. 2002, MNRAS, 336, 1188

Kruijssen, J. M. D., Maschberger, T., Moeckel, N., et al. 2012, MNRAS, 419, 841

Krumholz, M. R., Klein, R. I., McKee, C. F., Offner, S. S. R., & Cunningham, A. J. 2009, Science, 323, 754

La Palombara, N., Mereghetti, S., Sidoli, L., Tiengo, A., & Esposito, P. 2013, ArXiv:1301.5120

La Palombara, N., Sidoli, L., Esposito, P., Tiengo, A., & Mereghetti, S. 2009, A&A, 505, 947

Lada, C. J. & Lada, E. A. 2003, ARA&A, 41, 57

Lane, R. R., Brewer, B. J., Kiss, L. L., et al. 2010a, ApJL, 711, L122

Lane, R. R., Kiss, L. L., Lewis, G. F., et al. 2010b, MNRAS, 401, 2521

Lane, R. R., Kiss, L. L., Lewis, G. F., et al. 2010c, MNRAS, 406, 2732

Larsen, S. S. 2004, A&A, 416, 537

Larsen, S. S. 2010, Royal Society of London Philosophical Transactions Series A, 368, 867

Laycock, S., Zezas, A., Hong, J., Drake, J. J., & Antoniou, V. 2010, ApJ, 716, 1217

Leitherer, C., Schaerer, D., Goldader, J. D., et al. 1999, ApJ Supp., 123, 3

Lucy, L. B. 2006, A&A, 457, 629

Lützgendorf, N., Kissler-Patig, M., de Zeeuw, T., et al. 2012, The Messenger, 147, 21

Lynden-Bell, D. 1960, MNRAS, 120, 204

Lynden-Bell, D. 1967, MNRAS, 136, 101

Mackey, A. D., Da Costa, G. S., Ferguson, A. M. N., & Yong, D. 2013, ApJ, 762, 65

Mackey, A. D. & Gilmore, G. F. 2003, MNRAS, 338, 85

Macomb, D. J., Finger, M. H., Harmon, B. A., Lamb, R. C., & Prince, T. A. 1999, ApJL, 518, L99

Mahy, L., Nazé, Y., Rauw, G., et al. 2009, A&A, 502, 937

Mahy, L., Rauw, G., De Becker, M., Eenens, P., & Flores, C. A. 2013, A&A, 550, A27

Maíz-Apellániz, J. 2001, ApJ, 563, 151

Makino, J., Akiyama, K., & Sugimoto, D. 1991, Ap&SS, 185, 63

Malumuth, E. M. & Heap, S. R. 1994, AJ, 107, 1054

Markova, N., Bianchi, L., Efremova, B., & Puls, J. 2009, Bulgarian Astronomical Journal, 12, 21

Markova, N., Puls, J., Scuderi, S., Simón-Díaz, S., & Herrero, A. 2011, A&A, 530, A11

Markwardt, C. B. 2009, Astronomical Data Analysis Software and Systems XVIII, 411, 251

Martayan, C., Baade, D., Frémat, Y., & Zorec, J. 2010, in IAU Symposium, Vol. 266, IAU Symposium, ed. R. de Grijs & J. R. D. Lépine, 470–473

Mason, B. D., Hartkopf, W. I., Gies, D. R., Henry, T. J., & Helsel, J. W. 2009, AJ, 137, 3358

Massey, P. 2002, ApJ Supp., 141, 81

Massey, P. & Hunter, D. A. 1998, ApJ, 493, 180

Massey, P., Penny, L. R., & Vukovich, J. 2002, ApJ, 565, 982

Mathewson, D. S., Ford, V. L., Dopita, M. A., et al. 1983, ApJ Supp., 51, 345

McGowan, K. E., Coe, M. J., Schurch, M., et al. 2007, MNRAS, 376, 759

McLaughlin, D. E., Anderson, J., Meylan, G., et al. 2006, ApJ Supp., 166, 249

McLaughlin, D. E. & van der Marel, R. P. 2005, ApJ Supp., 161, 304

McSwain, M. V. & Gies, D. R. 2005, ApJ Supp., 161, 118

Meaburn, J. 1980, MNRAS, 192, 365

Melnick, J. 1985, A&A, 153, 235

Mengel, S. & Tacconi-Garman, L. E. 2007, A&A, 466, 151

Mengel, S. & Tacconi-Garman, L. E. 2008, in IAU Symposium, Vol. 246, IAU Symposium, ed. E. Vesperini, M. Giersz, & A. Sills, 113–114

Mengel, S. & Tacconi-Garman, L. E. 2009, Ap&SS, 324, 321

Meurer, G. R., Heckman, T. M., Leitherer, C., et al. 1995, AJ, 110, 2665

Meylan, G. & Heggie, D. C. 1997, A&A Rev., 8, 1

Meylan, G. & Mayor, M. 1986, A&A, 166, 122

Meynet, G. & Maeder, A. 2000, A&A, 361, 101

Meza, A. 2002, A&A, 395, 25

Miller, B., Whitmore, B., Schweizer, F., & Fall, S. 1997, AJ, 114, 2381

Moeckel, N. & Clarke, C. J. 2011, MNRAS, 410, 2799

Moffat, A. F. J. & Seggewiss, W. 1983, A&A, 125, 83

Mokiem, M. R., de Koter, A., Evans, C. J., et al. 2007a, A&A, 465, 1003

Mokiem, M. R., de Koter, A., Evans, C. J., et al. 2006, A&A, 456, 1131

Mokiem, M. R., de Koter, A., Vink, J. S., et al. 2007b, A&A, 473, 603

Morgan, W. W., Keenan, P. C., & Kellman, E. 1943, An atlas of stellar spectra, with an outline of spectral classification

Muller, G. P., Reed, R., Armandroff, T., Boroson, T. A., & Jacoby, G. H. 1998, in Society of Photo-Optical Instrumentation Engineers (SPIE) Conference Series, Vol. 3355, Society of Photo-Optical Instrumentation Engineers (SPIE) Conference Series, ed. S. D'Odorico, 577–585

Negueruela, I. 1998, A&A, 338, 505

Nigra, L., Gallagher, J. S., Smith, L. J., et al. 2008, PASP, 120, 972

Oey, M. S., King, N. L., & Parker, J. W. 2004, AJ, 127, 1632

Okazaki, A. T. 2001, PASJ, 53, 119

Öpik, E. 1924, Publications of the Tartu Astrofizica Observatory, 25, 1

Oskinova, L. M., Sun, W., Evans, C. J., et al. 2013, ArXiv e-prints

Oskinova, L. M., Todt, H., Ignace, R., et al. 2011, MNRAS, 416, 1456

Ostriker, J. P. & Peebles, P. J. E. 1973, ApJ, 186, 467

Parker, J. W. 1993, AJ, 106, 560

Pasquini, L., Avila, G., Blecha, A., et al. 2002, The Messenger, 110, 1

Pietrzyński, G., Graczyk, D., Gieren, W., et al. 2013, Nature, 495, 76

Pinsonneault, M. H. & Stanek, K. Z. 2006, ApJL, 639, L67

Plummer, H. C. 1911, MNRAS, 71, 460

Popov, S. B. & Prokhorov, M. E. 2006, MNRAS, 367, 732

Popov, S. B. & Turolla, R. 2012, MNRAS, 421, L127

Portegies Zwart, S. F., Makino, J., McMillan, S. L. W., & Hut, P. 1999, A&A, 348, 117

Portegies Zwart, S. F., McMillan, S. L. W., & Gieles, M. 2010, ARA&A, 48, 431

Portegies Zwart, S. F., Pooley, D., & Lewin, W. H. G. 2002, ApJ, 574, 762

Porter, J. M. & Rivinius, T. 2003, PASP, 115, 1153

Predehl, P. & Schmitt, J. H. M. M. 1995, A&A, 293, 889

Pryor, C. & Meylan, G. 1993, in Astronomical Society of the Pacific Conference Series, Vol. 50, Structure and Dynamics of Globular Clusters, ed. S. G. Djorgovski & G. Meylan, 357

Rappaport, S. & van den Heuvel, E. P. J. 1982, in IAU Symposium, Vol. 98, Be Stars, ed. M. Jaschek & H.-G. Groth, 327–344

Rauw, G., Nazé, Y., Fernández Lajús, E., et al. 2009, MNRAS, 398, 1582

Reig, P. 2011, Ap&SS, 332, 1

Reig, P., Fabregat, J., & Coe, M. J. 1997, A&A, 322, 193

Richstone, D. O. & Tremaine, S. 1986, AJ, 92, 72

Ritchie, B. W., Clark, J. S., Negueruela, I., & Crowther, P. A. 2009, A&A, 507, 1585

Rochau, B., Brandner, W., Stolte, A., et al. 2010, ApJL, 716, L90

Rood, H. J., Page, T. L., Kintner, E. C., & King, I. R. 1972, ApJ, 175, 627

Rosolowsky, E., Engargiola, G., Plambeck, R., & Blitz, L. 2003, ApJ, 599, 258

Rozas, M., Zurita, A., & Beckman, J. E. 2000, A&A, 354, 823

Sabbi, E., Lennon, D. J., Gieles, M., et al. 2012, ApJL, 754, L37

Sana, H., de Koter, A., de Mink, S. E., et al. 2013a, A&A, 550, A107

Sana, H., de Mink, S. E., de Koter, A., et al. 2012, Science, 337, 444

Sana, H., Dunstall, P. R., Hénault-Brunet, V., et al. 2013b, in Astronomical Society of the Pacific Conference Series, Vol. 465, Proceedings of a Scientific Meeting in Honor of Anthony F. J. Moffat, ed. L. Drissen, C. Rubert, N. St-Louis, & A. F. J. Moffat, 284

Sana, H. & Evans, C. J. 2011, in IAU Symposium, Vol. 272, IAU Symposium, ed. C. Neiner, G. Wade, G. Meynet, & G. Peters, 474–485

Sana, H., Gosset, E., & Evans, C. J. 2009, MNRAS, 400, 1479

Sana, H., Gosset, E., Nazé, Y., Rauw, G., & Linder, N. 2008, MNRAS, 386, 447

Sana, H., James, G., & Gosset, E. 2011, MNRAS, 416, 817

Savage, B. D., Fitzpatrick, E. L., Cassinelli, J. P., & Ebbets, D. C. 1983, ApJ, 273, 597

Schmalzl, M., Gouliermis, D. A., Dolphin, A. E., & Henning, T. 2008, ApJ, 681, 290

Schnurr, O., Chené, A.-N., Casoli, J., Moffat, A. F. J., & St-Louis, N. 2009, MNRAS, 397, 2049

Sedov, L. I. 1959, Similarity and Dimensional Methods in Mechanics

Selman, F., Melnick, J., Bosch, G., & Terlevich, R. 1999, A&A, 341, 98

Seward, F. D., Charles, P. A., Foster, D. L., et al. 2012, ApJ, 759, 123

Shakura, N., Postnov, K., Kochetkova, A., & Hjalmarsdotter, L. 2012, MNRAS, 420, 216

Shapiro, S. L. & Marchant, A. B. 1976, ApJ, 210, 757

Sirianni, M., Nota, A., Leitherer, C., De Marchi, G., & Clampin, M. 2000, ApJ, 533, 203

Skrutskie, M. F., Cutri, R. M., Stiening, R., et al. 2006, AJ, 131, 1163

Slettebak, A. 1982, ApJ Supp., 50, 55

Smith, R. C. & MCELS Team. 1999, in IAU Symposium, Vol. 190, New Views of the Magellanic Clouds, ed. Y.-H. Chu, N. Suntzeff, J. Hesser, & D. Bohlender, 28

Sota, A., Maíz Apellániz, J., Walborn, N. R., et al. 2011, ApJ Supp., 193, 24

Spitzer, L. 1987, Dynamical evolution of globular clusters (Princeton, NJ, Princeton University Press, 1987, 191 p.)

Spitzer, L. 1987, Princeton, NJ, Princeton University Press, 1987, 191 p., -1

Spitzer, Jr., L. 1969, ApJL, 158, L139

Spitzer, Jr., L. & Hart, M. H. 1971, ApJ, 164, 399

Stap, F. A., Sana, H., & de Koter, A. 2011, Journal of Physics Conference Series, 328, 012025

Stephens, A. W., Catelan, M., & Contreras, R. P. 2006, AJ, 131, 1426

Sturm, R., Haberl, F., Pietsch, W., & Udalski, A. 2013, ArXiv:1301.3362

Taylor, G. 1950, Royal Society of London Proceedings Series A, 201, 159

Taylor, W. D. 2012, PhD thesis, University of Edinburgh

Townsley, L. K., Broos, P. S., Feigelson, E. D., et al. 2006, AJ, 131, 2140

Trundle, C., Dufton, P. L., Hunter, I., et al. 2007, A&A, 471, 625

Urpin, V., Konenkov, D., & Geppert, U. 1998, MNRAS, 299, 73

Vacca, W. D., Garmany, C. D., & Shull, J. M. 1996, ApJ, 460, 914

van den Bergh, S. & Morbey, C. L. 1984, ApJ, 283, 598

van Leeuwen, F., Le Poole, R. S., Reijns, R. A., Freeman, K. C., & de Zeeuw, P. T. 2000, A&A, 360, 472

Vink, J. S., de Koter, A., & Lamers, H. J. G. L. M. 2001, A&A, 369, 574

Walborn, N. R. 1971, ApJ Supp., 23, 257

Walborn, N. R. 1972, AJ, 77, 312

Walborn, N. R., Barbá, R. H., Brandner, W., et al. 1999, AJ, 117, 225

Walborn, N. R., Barbá, R. H., & Sewiło, M. M. 2013, AJ, 145, 98

Walborn, N. R. & Blades, J. C. 1997, ApJ Supp., 112, 457

Walborn, N. R., Howarth, I. D., Lennon, D. J., et al. 2002a, AJ, 123, 2754

Walborn, N. R., Maíz-Apellániz, J., & Barbá, R. H. 2002b, AJ, 124, 1601

Wang, Q. D. 1999, ApJL, 510, L139

Webster, B. L., Martin, W. L., Feast, M. W., & Andrews, P. J. 1972, Nature, 240, 183

Wegner, W. 1994, MNRAS, 270, 229

Weidner, C., Kroupa, P., & Bonnell, I. A. D. 2010, MNRAS, 401, 275

Weigelt, G. & Baier, G. 1985, A&A, 150, L18

Werner, M. W., Becklin, E. E., Gatley, I., et al. 1978, MNRAS, 184, 365

Westerlund, B. 1964, MNRAS, 127, 429

Westmoquette, M. S., Exter, K. M., Smith, L. J., & Gallagher, J. S. 2007, MNRAS, 381, 894

White, R. E. & Shawl, S. J. 1987, ApJ, 317, 246

Whitmore, B., Zhang, Q., Leitherer, C., et al. 1999, AJ, 118, 1551

Wilkinson, M. I., Kleyna, J. T., Evans, N. W., et al. 2004, ApJL, 611, L21

Woosley, S. & Bloom, J. 2006, Annual Review of A&A, 44, 507

Yokogawa, J., Imanishi, K., Tsujimoto, M., Koyama, K., & Nishiuchi, M. 2003, PASJ, 55, 161

Yoon, S.-C., Langer, N., & Norman, C. 2006, A&A, 460, 199

Zahn, J.-P. 1977, A&A, 57, 383

Zahn, J.-R. 1978, A&A, 67, 162

List of publications

Published in refereed journals

Hénault-Brunet, V., Evans, C. J., Sana, H., Gieles, M., Bastian, N., Maíz Apellániz, J., Markova, N., Taylor, W.D., Bressert, E., Crowther, P. A., van Loon, J. Th., *The VLT-FLAMES Tarantula Survey. VII. A low velocity dispersion for the young massive cluster R136*, 2012, A&A, 546, A73

Hénault-Brunet, V., Gieles, M., Evans, C. J., Sana, H., Bastian, N., Maíz Apellániz, J., Taylor, W. D., Markova, N., Bressert, E., de Koter, A., van Loon, J. Th., *The VLT-FLAMES Tarantula Survey. VI. Evidence for rotation of the young massive cluster R136*, 2012, A&A, 545, L1

Hénault-Brunet, V., Oskinova, L. M., Guerrero, M. A., Sun, W., Chu, Y.-H., Evans, C. J., Gallagher III, J. S., Gruendl, R. A., Reyes-Iturbide, J., *Discovery of a Be/X-ray pulsar binary and associated supernova remnant in the Wing of the Small Magellanic Cloud*, 2012, MNRAS, 420, L13

Torres-Flores, S., Barbá, R. H., Maíz Apellániz, J., Rubio, M., Bosch, G., **Hénault-Brunet, V.**, Evans, C. J., *Studying the kinematics of the giant star-forming region 30 Doradus I. The data*, 2013, accepted for publication in A&A

Oskinova, L. M., Sun, W., Evans, C. J., **Hénault-Brunet, V.**, Chu, Y.-H., Gallagher III, J. S., Guerrero, M. A., Gruendl, R. A., Güdel, M., Silich, S., Chen, Y., Nazé, Y., Reyes-Iturbide, J., Hainich, R., *Discovery of X-ray emission from young suns in the Small Magellanic Cloud*, 2013, ApJ, 765, 73

van Loon, J. Th., Bailey, M., Tatton, B.L., Maíz Apellániz,J., Crowther, P. A., de Koter, A., Evans, C. J., **Hénault-Brunet, V.**, Howarth, I. D., Richter, P., Sana,

H., Simón-Díaz, S., Taylor, W. D., Walborn, N. R., *The VLT-FLAMES Tarantula Survey IX. The interstellar medium seen through Diffuse Interstellar Bands and neutral sodium*, 2012, A&A, 550, A108

Sana, H., de Koter, A., de Mink, S.E., Dunstall, P.R., Evans, C.J., **Hénault-Brunet, V.**, Maíz Apellániz, J., Ramírez-Agudelo, O. H., Taylor, W. D., Walborn, N. R., Clark, J. S., Crowther, P. A., Herrero, A., Gieles, M., Langer, N., Lennon, D. J., Vink, J. S., *The VLT-FLAMES Tarantula Survey VIII. Multiplicity properties of the O-type star population*, 2012, A&A, 550, A107

Evans, C. J., Hainich, R., Oskinova, L. M., Gallagher, J. S., III, Chu, Y.-H., Gruendl, R. A., Hamann, W.-R., **Hénault-Brunet, V.**, Todt, H., *A Rare Early-type Star Revealed in the Wing of the Small Magellanic Cloud*, 2012, ApJ, 753, 173

Bressert, E., Bastian, N., Evans, C.J., Sana, H., **Hénault-Brunet, V.**, Goodwin, S. P., Parker, R. J., Gieles, M., Bestenlehner, J. M., Vink, J. S., Taylor, W. D., Crowther, P. A., Longmore, S. N., Gräfener, G., Maíz Apellániz, J., de Koter, A., Cantiello, M., Kruijssen, J. M. D., *The VLT-FLAMES Tarantula Survey. IV. Candidates for isolated high-mass star formation in 30 Doradus*, 2012, A&A, 542, A49

Dufton, P. L., Dunstall, P. R., Evans, C. J., Brott, I., Cantiello, M., de Koter, A., de Mink, S. E., Fraser, M., **Hénault-Brunet, V.**, Howarth, I. D., Langer, N., Lennon, D. J., Markova, N., Sana, H., Taylor, W. D., *The VLT-FLAMES Tarantula Survey: The fastest rotating O-type star and shortest period LMC pulsar - remants of a supernova disrupted binary?*, 2011, ApJ, 743, L22

Bestenlehner, J. M., Vink, J. S., Gräfener, G., Najarro, F., Evans, C. J., Bastian, N., Bonanos, A. Z., Bressert, E., Crowther, P. A., Doran, E., Friedrich, K., **Hénault-Brunet, V.**, Herrero, A., de Koter, A., Langer, N., Lennon, D. J., Maíz Apellániz, J., Sana, H., Soszynski, I., Taylor, W. D., *The VLT-FLAMES Tarantula Survey. III. A very massive star in apparent isolation from the massive cluster R136*, 2011, A&A, 530, L14

Taylor, W. D., Evans, C. J., Sana, H., Walborn, N. R., de Mink, S. E., Stroud, V. E., Alvarez-Candal, A., Barbá, R. H., Bestenlehner, J. M., Bonanos, A. Z., Brott, I., Crowther, P. A., de Koter, A., Friedrich, K., Gräfener, G., **Hénault-Brunet, V.**, Herrero , A., Kaper, L., Langer, N., Lennon, D. J., Maíz Apellániz, J., Markova, N.,

Morrell, N., Monaco, L., Vink, J. S., *The VLT-FLAMES Tarantula Survey. II. R139 revealed as a massive binary system*, 2011, A&A, 530, L10

Evans, C. J., Taylor, W. D., **Hénault-Brunet, V.**, Sana, H., de Koter, A., Simón-Díaz, S., Carraro, G., Bagnoli, T., Bastian, N., Bestenlehner, J. M., Bonanos, A. Z., Bressert, E., Brott, I., Campbell, M. A., Cantiello, M., Clark, J. S., Costa, E., Crowther, P. A., de Mink, S. E., Doran, E., Dufton, P. L., Dunstall, P. R., Friedrich, K., Garcia, M., Gieles, M., Gräfener, G., Herrero, A., Howarth, I. D., Izzard, R. G., Langer, N., Lennon, D. J., Maíz Apellániz, J., Markova, N., Najarro, F., Puls, J., Ramirez, O. H., Sabín-Sanjulián, C., Smartt, S. J., Stroud, V. E., van Loon, J. Th., Vink, J. S., Walborn, N. R., *The VLT-FLAMES Tarantula Survey. I. Introduction and observational overview*, 2011, A&A, 530, A108

Evans, C. J., Walborn, N. R., Crowther, P. A., **Hénault-Brunet, V.**, Massa, D., Taylor, W. D., Howarth, I. D., Sana, H., Lennon, D. J., van Loon, J. Th., *A massive runaway star from 30 Doradus*, 2012, ApJ, 715, L74

Conference proceedings and other publications (selected)

Evans, C.J. Taylor, W. D., Sana, H., **Hénault-Brunet, V.** & the VLT-FLAMES Tarantula consortium, *The VLT-FLAMES Tarantula Survey*, ESO Messenger No. 145, September 2011

Hénault-Brunet, V., Evans, C. J., Taylor, W. D., Gieles, M. & the VLT-FLAMES Tarantula consortium, *A project to study stellar and gas kinematics in 30 Dor with the VLT-FLAMES Tarantula Survey*, 2011, Bulletin de la Société Royale des Sciences de Liège, 80, 376